Australian Government

Wine Australia

THE UNIVERSITY of ADELAIDE

Plant sensor-based precision irrigation for improved vineyard water use efficiency, grape and wine composition and quality, and vineyard profitability

FINAL REPORT TO WINE AUSTRALIA

Project Number: **UA 1803-1.3**

Principal Investigator: **DR VINAY PAGAY**

Research Organisation: **THE UNIVERSITY OF ADELAIDE**

Date: **31/08/2022**

Table of Contents

Abstract

Prudent water management in Australian vineyards has become increasingly important in light of current energy market prices, potential oversupply of grapes and wine leading to low farmgate prices paid for grapes, as well as inefficiencies in ageing irrigation infrastructure in many vineyards. Increasing the efficiency of irrigation water use to maximise yield and/or quality is one strategy to address some of these issues, and can be done by precise monitoring of soil and vine moisture levels, and applying irrigation based on cultivar-specific thresholds relevant to each metric based on phenological stage. We evaluated the benefits associated with implementing irrigation schedules on Cabernet Sauvignon (CAS) and Shiraz (SHI) grapevines in Coonawarra based on non-data-driven (CONV) and data-driven metrics including crop evapotranspiration (ET_c), soil moisture thresholds (SWS), and two plant-based water status thresholds (PWS/PWS1, PWS2). SWS and PWS strategies were informed by remote monitoring of the respective parameters using continuous moisture sensors. Our results indicated that using data-driven approaches was generally superior to non-data-driven methods, and that water use efficiency (WUE=yield/irrigation) could be enhanced, particularly when using metrics that were associated with the vine itself, i.e. ET_c and PWS. Despite inter-annual variations in the results that were attributed to weather conditions, we observed 3- to 6-fold increases in WUE based on data-driven methods compared to the conventional (non-data driven) method in CAS, and a doubling of WUE in SHI. Comparing various irrigation schedules, PWS1, based on proximal thermal sensors, had the highest WUE in SHI during the final season, while ET had the highest WUE in CAS in the same season. The PWS group consistently outperformed the conventional group every season. Despite reductions in irrigation in the data-driven treatments, no significant impacts to yield or grape composition parameters were observed. High resolution remote sensing was utilised to generate spatial and temporal information of all three vineyard blocks; this data was used to develop predictive models of soil and vine water status, gas exchange, and crop coefficients. Financial (cost-benefit) analysis revealed that the economic water productivity (gross margin $ per ML of water applied) for CAS was 4-fold higher in the ET and PWS treatments, and CONV was highest in SHI due to the high yields obtained in the final season. Finally, an irrigation practices survey conducted in 2021 across the Limestone Coast region revealed that over 70% of growers used experience or historical schedules to irrigate, and only 6% of growers used plant-based sensors to inform their irrigation decisions. The greatest barriers to adoption of new technology for irrigation decision-making were a lack of understanding of their value and high cost. This study has demonstrated the potential of several direct, proximal and remote irrigation sensors and tools to determine irrigation schedules in order to increase water use efficiency in grapevine through precision irrigation.

1 Executive summary

The overarching objective of this project was to assess the value of plant-sensor based precision irrigation on grapevine performance, water use efficiency, and grape and wine composition of Cabernet Sauvignon (CAS) and Shiraz (SHI) grapevines. The project was conducted in the Coonawarra viticultural region of South Australia. In the first three seasons, five irrigation strategies were investigated: conventional or grower-driven approach (CONV), 2x CONV for “well-watered” vines (CONV+), and three data-driven (sensor-based) irrigation strategies: vine water status based on proximal thermal sensors (PWS/PWS1), soil water status (SWS), and crop evapotranspiration (ET_c). In the fourth season (2021/2022), an additional plant sensor-based irrigation strategy based on continuous measurement of trunk water potential (PWS2) was also evaluated. Additionally, UAV-based remote sensing was used to obtain high resolution (vine-level) estimates of grapevine crop coefficients, soil and water status, and canopy gas exchange.

For measuring plant performance and water status, various instruments for direct, proximal and remote sensing were used at key phenological stages of grapevine development. The evidence- or sensor-based irrigation strategies had a clear advantage of saving irrigation water in CAS and SHI grown in Terrarossa soil and Rendzina soils (SHI in Terrarossa only). For instance, in 2020/2021 season (S3) in CAS (in lighter Terrarossa soil), ET- and PWS-treated vines received only 38% and 67% of the total irrigation of CONV+ treated vines. However, despite significantly lower soil and plant water status, ET- and PWS-treated vines showed similar net carbon assimilation (A_N), stomatal conductance (g_s), leaf intrinsic water use efficiency (WUE_i), yield, and berry anthocyanin and phenolics concentrations relative to CONV+ vines. Reduction of irrigation by 38% in SWS treatments led to significant reductions of soil and plant water status, g_s and A_N however, vines maintained similar WUE_i relative to CONV+ treatment. The reduction of irrigation did not result in a yield penalty, nor reduced berry and juice composition in the CAS vines on Terrarossa soils.

In the 2020/2021 season in CAS on heavier Rendzina soils, sensor-based irrigation reduced water supply by 30-40% relative to CONV+. Despite significantly lower plant water status and g_s, all vines maintained similar WUE_i to CONV+. ET and PWS treatments did not result in yield penalties, a positive result, however, yield was significantly reduced in the SWS treatment relative to CONV+ vines.

In SHI grapevines on Terrarossa soils, plant sensor-based irrigation (PWS) reduced irrigation by 40-60% compared to CONV+ treated vines. Even though, reduced water supply significantly reduced plant water status and leaf gas exchange, PWS1, PWS2 and SWS treatments significantly improved WUE_i relative to CONV+ vines during 2021/2022 season, without yield penalties or decreases in berry/juice composition parameters.

Overall, our results suggest that both ET- and plant sensor-based irrigation scheduling are superior approaches for high-quality grape/wine production for CAS, while the plant sensor-based irrigation scheduling approach is superior in SHI in order to increase water use efficiency without yield or quality penalties.

Using high-resolution (UAV-based) thermal and multispectral remote sensing in conjunction with machine learning modelling, we obtained spatial (vine-level) and temporal (phenology-specific) information on soil moisture (Ψ_{pd}) and vine physiological parameters (Ψ_s, A_n, g_s, WUE_i, K_c) for the entire vineyard block and beyond the trial sub-block. These predictive models can aid practitioners in implementing precision irrigation, i.e. irrigating blocks at the sub-block level, based on water requirements as determined by the various sensors such as those evaluated in this project. The spatial maps can also be used to inform the placement of proximal or direct plant and soil sensors for improved decision-making at the sub-block level.

Financial analysis of the various data-driven options (PWS, SWS, ET) versus the non-data driven-option (CONV/CONV+) indicated that there was a strong dependence of gross margin and payback period on yield and/or irrigation application rates. Hence, the ET (in CAS and SHI) and PWS (in SHI) treatments had the highest financial returns to the grower based on lower water application rates as yields were similar across the different strategies. These differences would be even higher, if growers had to pay for water, increasing the impetus for using sensors to inform irrigation decisions.

The project has successfully met the objectives and delivered:

- a comprehensive evaluation of various irrigation scheduling methods available to grape growers that are based on subjective and objective assessments. Vine performance and fruit/wine level assessments were carried out for each irrigation regime.

- an evaluation of two new commercial crop water status sensors and determination of their thresholds to increase water use efficiency.

- a new high-resolution remote sensing platform for assessment of canopy performance, and spatial and temporal prediction of the same parameters.

- a financial analysis of the different irrigation scheduling strategies evaluated in this study.

- a comprehensive industry survey of current irrigation practices in the Limestone Coast.

- knowledge dissemination to the industry via seminars and scientific papers.

2 Background

As a perennial crop, grapevines (*Vitis vinifera* L.) are vulnerable to changing environmental conditions, both within a growing season and interannually. Predictions of climatic conditions across many Australian viticultural regions indicate that average growing season temperatures are likely to increase and precipitation is likely to decrease (Webb et al. 2007). In South Australia, the largest winegrape producing state in Australia (Wine Australia 2022), the annual mean maximum temperature is predicted to increase by 2.1 °C by 2050 while annual precipitation is predicted to decrease by between 6.6-15% by the same time (Green and Pannell, 2020). Superimposed on this climate background are extreme weather events such as heatwaves, which are predicted to increase in both frequency and severity, e.g. the number of days per year above 40 °C is projected to double by 2050 compared to the baseline period of 1981-2010. These conditions will result in higher rates of evapotranspiration (ET) with a consequent decrease in soil moisture and increase in soil salinity (Schultz and Stoll 2010). As grapevine phenology, grape yield, chemical composition and quality, and consequent wine quality are all intimately tied to the prevailing environmental conditions, the predicted shifts in climate across Australian viticultural regions will undoubtedly impact on future winegrape production, grape/wine quality, and profitability (Webb and Jones, 2010). In this context, some vineyards within existing viticultural regions may become economically unviable (White et al., 2006), and regional cultivars and wine styles may become undesirable (Jones et al., 2005).

Several strategies exist to mitigate against the negative impact of increasing temperatures and decreasing rainfall including soil management, irrigation, use of undervine and interrow cover crops (Santos et al., 2020, Marks et al. 2022), canopy management practices (Santos et al., 2020), vineyard cooling strategies (Bayer et al., 2017; Pagay 2018), and use of heat- and drought-tolerant cultivars and rootstocks (Fraga et al. 2012). In semi-arid regions such as the Murray-Darling Basin, supplemental irrigation (i.e. irrigation in excess of rainfall; henceforth termed 'irrigation') is not only essential, but a powerful tool to manipulate canopy development and vigour, yield, fruit composition, and wine quality. Under heatwave conditions, which are becoming increasingly frequent during the grape growing season in inland Australian viticultural regions, irrigation can also aid in mitigating against heat stress in grapevines, and provide ancillary benefits such as maintaining soil structure, soil microbial activity, and cover crop function. A critically important aspect that motivated the present work, increasing ET across Australian viticultural regions have placed increased pressure on freshwater for irrigation, which has compelled irrigators to seek approaches to increase the efficiency of water use, or water use efficiency (WUE) such that greater productivity is obtained from their vineyards through prudent irrigation management. Irrigation scheduling, which refers to the timing and quantum of irrigation water applied to crops, is a useful tool to increase the WUE at the vine and vineyard scales. Strategies such as regulated deficit irrigation (Fereres and Soriano, 2007; Romero et al. 2022) and partial rootzone drying (Dry et al. 2001) have been shown to be useful irrigation scheduling tools to increase the WUE of vineyards.

Irrigation strategies can be broadly categorised as those based on: i) historical applications or experiential; ii) evaporative demand (e.g., crop evapotranspiration, ET_c); iii) soil moisture (either matric potential (tension) or volumetric water content) thresholds; and, iv) plant water status thresholds. A number of review papers have been published that describe each of these approaches in detail; see, for example, Jones, 2004; Cifre et al., 2005, Jones, 2007; Williams, 2017, Fernández, 2017, Rienth and Scholasch, 2019, Mirás-Avalos and Araujo, 2021.

Irrigation scheduling tools are typically based on the interpretation of soil moisture, with their popularity ascribed to the well-established relationship between vine physiological parameters and soil water availability (Centeno et al., 2010). Common methods for soil moisture monitoring generally include a variety of sensors and probes aimed at measuring either volumetric water content (%VWC) or soil matric potential (kPa) (Munoz-

Carpena et al., 2004). However, despite their prevalence, an accurate measure of soil moisture is limited by soil heterogeneity and uncertain rooting depths (Lebon et al., 2003), both of which represent limitations to soil moisture-based irrigation scheduling. In contrast, plant-based methods for irrigation scheduling are thought to take the whole soil-plant-atmosphere into account, and as such, have been suggested as the most direct way to measure plant water stress (Shackel, 2011). There are several techniques for measuring plant water status as described by Fernández (2017); however, for the majority of strategies discussed, a degree of interpretation is required for a given species and cultivar (Collins and Loveys, 2010). In addition, despite being considered effective and accurate detectors of vine water stress, strategies involving plant water status have historically lacked commercial applicability (Jones, 2004), and, until only recently, had largely been confined to the research domain. Presently, only a handful of Australian vineyards utilise plant water status sensors to determine irrigation schedules, and typically these are vineyards > 100 ha (AWRI, 2019). Irrigation scheduling based on evaporative demand involves the quantitative determination of vine water consumption, typically, crop evapotranspiration (ET_c) to dictate how much water needs to be replaced in a subsequent irrigation cycle. One of the strengths of ET-based irrigation scheduling is the ability to quantitatively determine how much water to apply based on the Penman-Monteith energy balance model (Allen et al., 1998). However, this methodology has limitations depending on the method and data used to calculate reference evapotranspiration (ET_0), in addition to obtaining and using accurate crop coefficients (Gautam et al., 2021). Although each of the aforementioned strategies has been successfully used to carry out irrigation scheduling, the efficacy of each of these strategies is dependent on the thresholds used, with the choice of threshold potentially being influenced by factors such as production goals, cultivar traits, and environmental conditions.

Considering that the effectiveness of commonly used decision metrics for irrigation scheduling can be impacted by a range of environmental, production, physiological, and operator-driven factors, it is difficult to compare strategies based on existing research, which has motivated the present work. To the best of our knowledge, the aforementioned irrigation scheduling strategies have not been directly compared against one another in a single study in grapevine that also assesses WUE as a primary objective. We therefore conducted such a study on Cabernet Sauvignon and Shiraz grapevines in the Coonawarra viticultural region of South Australia between 2018-2022. As part of the study, we assessed a variety of continuous soil moisture and plant water status sensors that are commercially available, and utilised these sensors to determine irrigation schedules targeted at increasing leaf and crop WUEs. Furthermore, we utilised high resolution remote sensing to build a spatial and temporal predictive model of vine water status and WUE, which can be utilised to implement precision irrigation in vineyards down to the single vine level.

In a recent review of climate change and viticultural adaptation strategies, Santos et al. (2020) highlight the value in utilising new technologies including drones and automatic plant-based irrigation systems to determine the most appropriate irrigation practices in the future; this foresight was provided two years after the commencement of this study and underscoring its relevance.

3 Project Aims

The following aims and deliverables were defined for each of the four seasons, S1-S4, from 2018 to 2022:

Table 1: Project outputs and activities, 2018-2022

Season	Outputs	Activities
S1 - 2018/2019	A. Vineyard blocks identified and setup for irrigation trial. B. Proximal plant sensors developed and deployed. C. Identification, purchase, and operation of the UAS-based remote sensing platform. D. Remote, proximal, and direct field data collection. E. Winemaking, juice/wine chemical composition analysis.	Identify trial sites and set up experiment. Deploy plant and soil moisture sensors. Purchase and tested/used remote sensing equipment. Collect seasonal soil moisture and vine performance data. Conduct juice and wine chemical analysis.
S2 - 2019/2020	A. Validation of plant sensor data against a different level of irrigation. B. Data of vine performance against conventionally-scheduled irrigation. C. Economic (cost-benefit) analysis of sensor-driven irrigation vs conventional irrigation. D. Present findings of study through articles, presentation, and conferences.	Plant sensor data collected and validated vs direct plant measures. Collect seasonal soil moisture and vine performance data. Economic model development begun for Cabernet Sauvignon. Write and publish two papers on irrigation scheduling.
S3 - 2020/2021	A. Validation of data on vine performance, yield, water use efficiency, grape quality and wine quality, and comparison of sensor-driven irrigation vs conventionally scheduled irrigation B. Validation of industry irrigation practices benchmarks. C. Wireless connectivity of sensors to Cloud based data platforms.	Collect and analyse grape and wine data. Conduct survey of Limestone Coast wine industry of irrigation practices. Implement wireless (4G) connectivity to the Cloud.
S4 - 2021/2022	A. Assessment of the impact of sensor-driven vs conventionally scheduled irrigation on vine performance, yield, water use efficiency, grape quality and wine quality of SHI B. Economic (cost-benefit) analysis of sensor-driven irrigation vs conventional irrigation. C. Present findings of study through articles, presentation, and conferences.	Grape and wine data collection and analysis. Analyse financials of Shiraz and Cabernet under different irrigation regimes. Data dissemination through industry workshops and conferences.

4 Materials and methods

4.1 Design of irrigation trials

In 2017/2018, the field trial was conducted at Wynns Coonawarra Estate's Alex88-East vineyard for Cabernet Sauvignon (CAS) on Schwarzmann rootstock. A conventional (non-intervention) irrigation treatment was compared against evapotranspiration (ET)-based, plant status (PWS)-based and soil water status (SWS)-based treatments. In the 2018/2019 season, the irrigation trials were expanded from the existing 2017/2018 trials with clear aim to: i) increase statistical power by replication, ii) understand influence of soil type on water status, and, iii) understand influence of genotype/phenotype on water status. The trial was expanded from AX88-East to AX88-West and Katnook Estate Homestead Block (Shiraz/Teleki 5C). At Katnook, an additional Shiraz block, Prodigy, was monitored for benchmarking purposes as this is the highest quality Shiraz (SHI) vineyard at the estate; no irrigation treatments were applied in this block. In the 2019/2020 and 2020/2021 seasons, irrigation trials were repeated at all three locations. However, based on experience from the 2018/2019 season, the data collection was restricted to two replications (blocks), which was found suitable for available resources. In the fourth and final season, 2021/2022, due to budgetary constraints and already having three years of data from the Cabernet block, the trial was conducted only at Katnook (Shiraz) with additional treatments as mentioned bellow.

4.1.1 Location

Figure 1: The four vineyards in Coonawarra, SA used for this study

The irrigation trials were established at three vineyards: Cabernet Sauvignon/Schwarmann at TWE/Wynns-Alex88-east (Terrarossa soil), TWE/Wynns-Alex88-west (Rendzina soil), and Accolade/Katnook Estate Shiraz/Teleki 5C (Homestead Block) (Terrarossa soil). The Prodigy Shiraz vineyard at Katnook (Terrarossa soil) was observed for benchmarking purpose without any irrigation trial.

Alex88-East (AX88E) and Alex88-West (AX88W) both have CAS planted in the year 1988 with a total area of 17.3 ha. The east side of the vineyard consistently produces higher quality grape/juice in comparison, predominantly due to the soil type. The soil type in the AX88E is the red porous "TerraRossa" soil with an underlying bed of limestone rock. Moving towards the west, the soil gradually transforms into a much heavier and darker clay type called 'Rendzina'. The water holding capacity and regulation of water through these two soil types result in the different water status of the plant for the same level of irrigation and subsequently, the final quality of the wine. The setup in AX88E and AX88W helped assess the soil and vine water status of the CAS blocks with quite different soil types while keeping the rootstock and scion genotypes, and viticulture practices consistent.

The Katnook vineyard is a younger SHI (on Teleki 5C rootstock) planted in the year 2013 on porous “TerraRossa” soil type. The Prodigy vineyard is an older SHI block, which consistently produces high-quality wine. Vines regulate water differently with the age of the plant, thus resulting in different water status in Katnook and Prodigy for the same irrigation practice. The setup in Katnook and Prodigy will help us understand how the younger SHI at different irrigation treatment compare to the older high-quality SHI. By understanding the age effect, the quality of the younger vines could be improved by co-replicating the water status of the older vines. Moreover, comparing Katnook with Alex88-east, we intend to unravel the differences in water status between the SHI and CAS under similar treatment, terroir, and irrigation practices. We expect to understand the isohydric vs anisohydric behaviour of the plant to cope with the water stress and thus better manage the plant's water use efficiency without compromising the yield and quality of the wine.

4.1.2 Experimental design

All the irrigation trials (Alex88-east, Alex88-west, and Katnook) are set up similarly whereas the Prodigy does not contain any irrigation trials. The experimental design – Randomised Complete Block -- is as shown in Figure 2.

2018-2021 seasons (CAS, SHI)

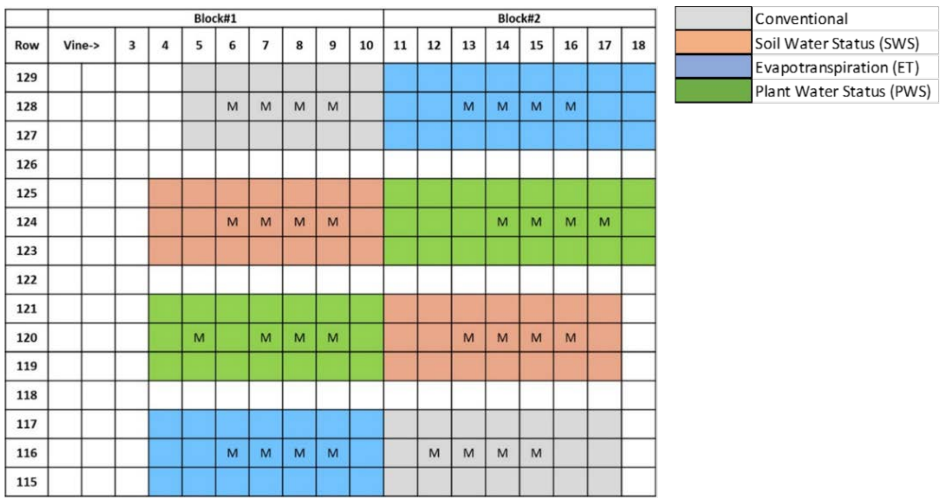

Figure 2: Experimental designs at Alex88-east, Alex88-west and Katnook.

2021-2022 season (SHI)

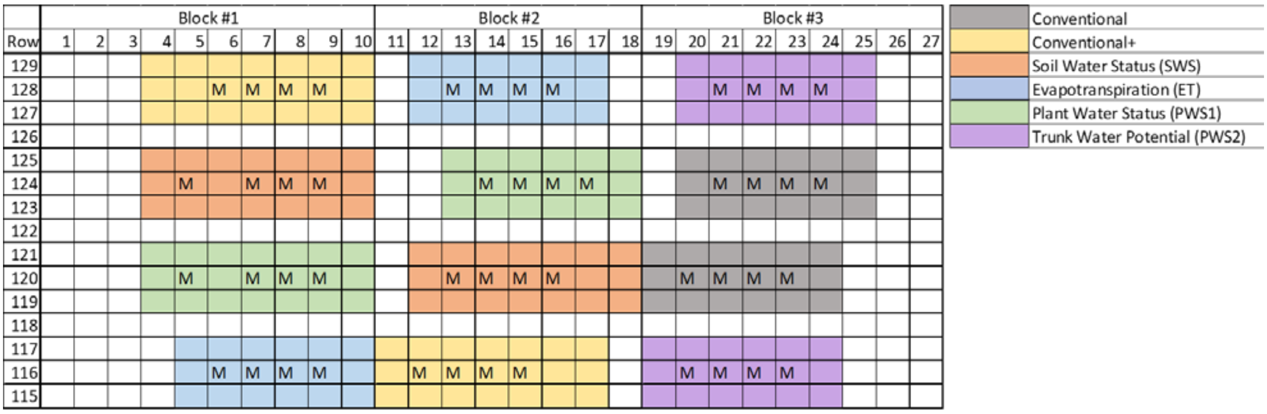

Figure 3: Experimental designs at Alex88-east, Alex88-west and Katnook.

The experimental design consisted of two blocks with four different treatment types (Conventional, ET, SWS and PWS). The conventional treatment is where the growers apply as much water they normally do; as such it was a non-intervention treatment. In the other treatments, SWS, PWS and ET, we scheduled irrigation based on quantitative (sensor-based) evidence of soil moisture, plant water status, and evapotranspiration, respectively. Each irrigation treatment in each block was separated by 1-2 buffer vine rows between them. A single treatment consisted of three rows where only the vines from middle row were measured (marked M in Figure 2). Thus, each set of measurement vines had buffers between rows and also within the row to ensure no irrigation overlap between treatments. Except for CONV, all data-driven irrigation treatments used thresholds before each irrigation cycle to decide whether irrigation should be applied**.**

In the 2020/2021 growing season, the conventional or grower-driven treatment (CONV) received the double the amount of irrigation relative to the previous season (CONV+), which represented an extra treatment. Other treatments SWS, PWS and ET were applied based on the measurement value of soil moisture, canopy conductance, and crop evapotranspiration (ET_c), respectively.

In the 2021/2022 season, in addition to the irrigation treatments applied in the previous season, two treatments (non-altered original grower-driven (CONV) and trunk water potential-based (PWS2)) were also assessed.

4.2 Scientific equipment and sensors

4.2.1 Direct, proximal, and continuous sensors

This category of sensors includes the sensors located on the ground including continuous measurement sensors such as weather station, infrared towers (plant-based sensors, PWS1), and soil moisture sensors (Figure 3).

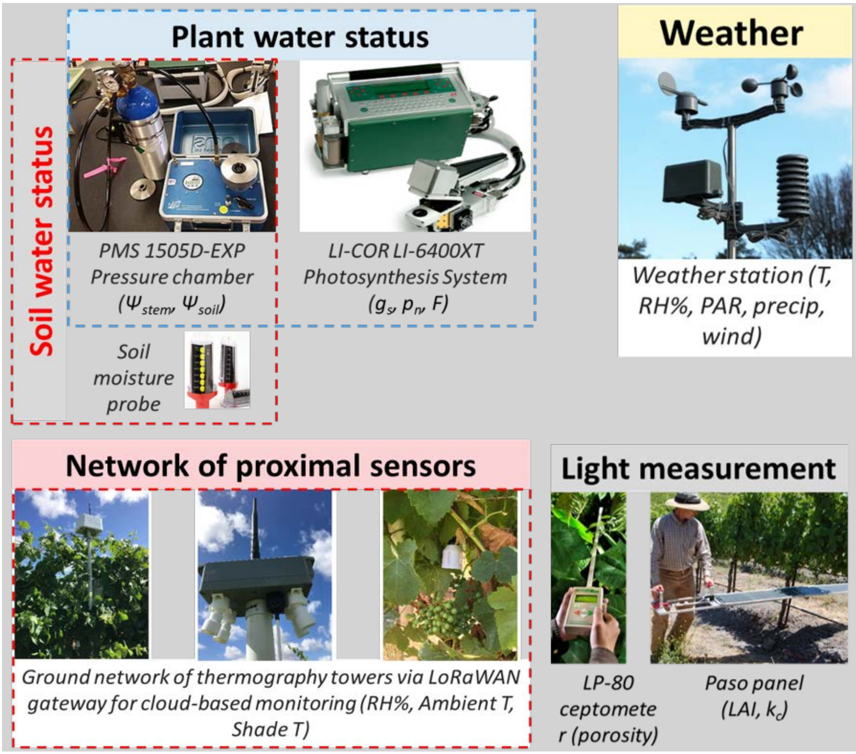

Figure 4: Direct, proximal, and continuous sensors used in this study of grapevine irrigation

4.2.1.1 Direct and proximal sensors

Multiple direct/proximal sensors were employed for this experiment. The sensors in this category "direct/proximal" include the sensors that required manual operation.

4.2.1.1.1 Pressure chamber

The pressure chamber (Figure 3) is used to measure the pre-dawn leaf water potential and mid-day stem water potential. The pre-dawn measurement is an indication of the total water that is accessible to the plant's rooting system. This information is reflected in the predawn measurement of the water potential. One measurement per plant was made using the pressure chamber between 0230-0500 h.

The midday stem water potential shows the water status of the plant when the plant is transpiring at full potential. For this, a mature leaf per sentinel vine was selected from the shoulder of the vine. The selection criterion for the leaves was neither too young, nor too mature, from within 1/3-2/3 shoot length, without obvious disease/discolouration, and from a full sunlit shoot. The selected leaf was bagged in the aluminium bag, at least 30 minutes before the measurement. The bagging enabled equilibrium of the leaf water potential to the overall water potential of the shoot. The measurement was carried out between 1100–1400 h.

4.2.1.1.2 Portable photosynthesis system

An infrared gas analyser (IRGA; Figure 3) was used to measure leaf gas exchange of sentinel vines: stomatal conductance, rate of transpiration, and net photosynthesis rate, among others. These measurements gives an indication of the plants' physiological performance in response to the given amount of soil water availability and environmental conditions. This measurement was carried out on fully sunlit leaves from the same shoot as the bagged leaf (for stem water potential) using a LI-COR 6400XT infrared gas analyser, between 1100–1400 h.

4.2.1.1.3 Ceptometer

An Accu-PAR LP-80 ceptometer (Figure 3) was used to measure the canopy light interception. The light interception measurements included the canopy porosity (T) and the leaf area index (LAI). Canopy porosity gives an indication of the amount of light penetrating the canopy reaching the fruits, which is also a good predictor of anthocyanin in the berries. The LAI is a measure of the number of leaves per square meter of the area. These measurements were also made at solar noon (1230-1400 h).

4.2.1.1.4 Crop coefficient measurement

A Paso-panel (Figure 3) was custom-built to measure the crop coefficient (K_c) of the canopy. The K_c is a measure of the canopy size to the vineyard macrostructure such as fractional cover. This crop coefficient, together with reference evapotranspiration (ET_0), is used to estimate crop evapotranspiration (ET_c), which is one of the irrigation strategies (treatments) evaluated in this study. Using an empirical relationship, K_c is estimated indirectly based on the sunlight intercepted by the Paso-panel (a flexible solar panel) when in the full sun vs when under the canopy (partially shaded). These measurements were also made at solar noon (1230-1400 h).

4.2.1.2 Continuous sensors

The continuous sensors employed in this trial include Transp-IR thermography sensors (Athena Irrigation Technologies, Adelaide, SA), soil moisture sensors (Teros-12, METER, Pullman, WA, USA), BOM weather station, and microtensiometers (FloraPulse, USA). These instruments measured data continuously without the necessity of operators, and the data was accessed remotely through various Cloud-based interfaces.

4.2.1.2.1 Thermography towers

Proximal infrared (IR/thermal) 'Transp-IR' (Gen 1) sensors were obtained from Athena Irrigation Technologies (Adelaide, SA) for continuous measurement of vine water status. Four sensors per vineyard were tested and deployed in the three trial sites in early January 2020. The sensor platform consists of sensor nodes (Figure 4.a) that are mounted over a wooden post (Figure 4.b), a temperature-humidity sensor for VPD measurement (Figure 4.c). The sensor nodes collect continuous canopy temperature as well as VPD data and transmit the data using 4G mobile network to an Amazon Web Services (AWS) Cloud platform. Each sensor node acquires canopy temperature from two vines per node on both sides of the canopy, as well as in-canopy temperature and humidity for the estimation of ambient VPD. The sensor data is collected every 10 min and a daily value of vine water index (VWI), a thermal water stress indicator, was provided as a measure of vine water status/stress. The data visualisation and download occurred through a web-based interface (dashboard).

Figure 5: 'Transp-IR' continuous water status sensors (Athena IR-Tech, Adelaide, SA).

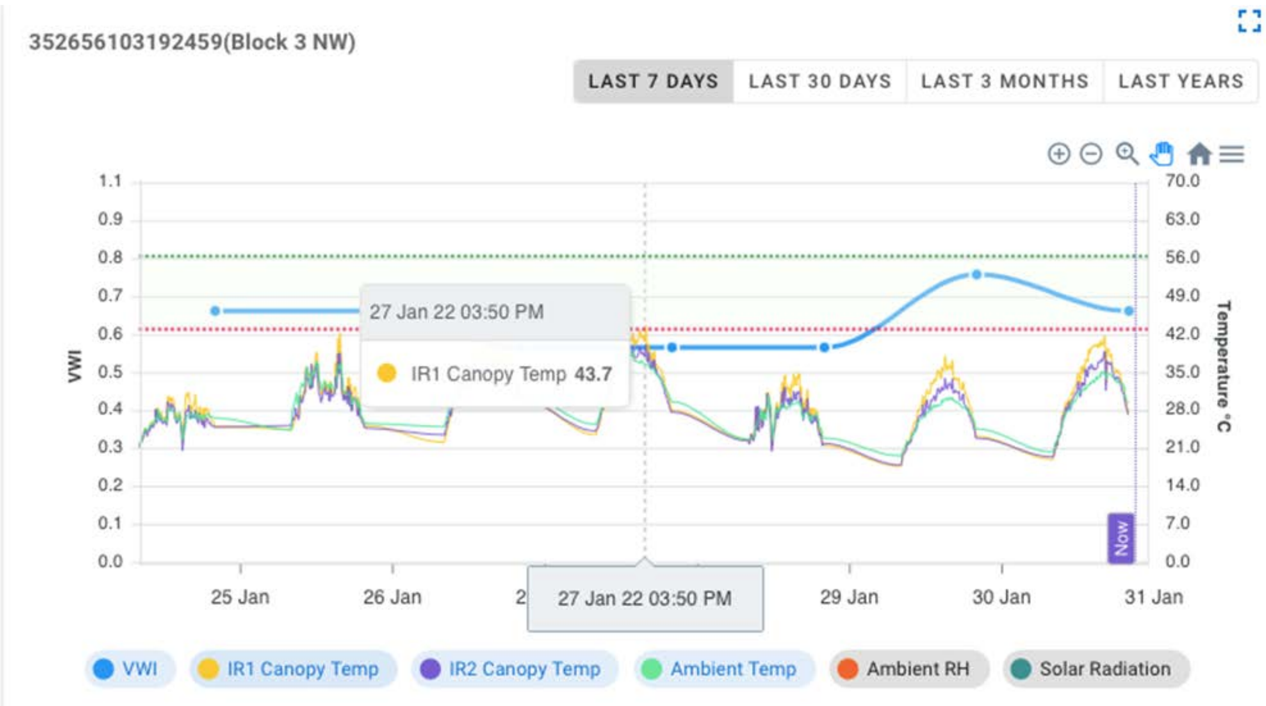

Figure 5: Dashboard providing data visualisation of Transp-IR sensor data. The Vine Water Index (VWI) is shown graphically as a coloured scale bar on the top of the dashboard. Individual sensor data is shown below the scale bar along with canopy temperature, ambient temperature, relative humidity, and solar radiation.

Continuous measurements of canopy temperature and VPD were used to derive an index of water stress, Vine Water Index (VWI). The VWI was mapped onto traditional metrics including g_s and Ψ_{stem} for validation. This mapping allowed the determination of thresholds of VWI based on known or established g_s or Ψ_{stem} thresholds to maximise WUE, yield or grape quality. In doing so, growers can target specific objectives of individual blocks through VWI thresholds (optimum ranges).

Optimised VWI thresholds to maintain 80-85% of the maximum photosynthetic rates (A_N) were derived from the non-linear relationships between g_s and A_N per cultivar. The VWI values were related to g_s through correlation analysis using data measured over the growing season under a range of vine water status.

4.2.1.2.2 Soil moisture sensors

In addition to the surrogate soil moisture, the pre-dawn leaf water potential measurement or matric potential, actual soil volumetric water content was measured using a network of soil moisture sensors. These sensors (TEROS-12, Meter Group, Pullman, WA, USA) were installed 30 cm below the ground and measured three parameters: soil salinity, soil temperature, and volumetric water content (%). One soil moisture sensor was installed per vineyard in each SWS treatment. The soil moisture was logged hourly onto an online dashboard (Greenbrain, MEA, Adelaide, SA).

4.2.1.2.3 Weather station

Daily meteorological data was acquired from the Bureau of Meteorology local weather station (Coonawarra Station ID: 94817) that was in proximity to the field (approximately 1 km south of the CAS block and 5 km north of the SHI block). The meteorological data included the daily minimum and maximum temperatures, minimum and maximum humidity, total solar radiation, and precipitation. This data, together with the K_c was used to compute ET_c.

4.2.1.2.4 Microtensiometers

Microtensiometers (Figure 6) were embedded into the trunk of SHI and CAS grapevines as described by Pagay et al., (2021). The data of trunk water potential was obtained every 20 min wirelessly transmitted to a Cloud-based server (Amazon Web Services, USA) and visually displayed on a user interface (FloraPulse, Davis, CA, USA).

Figure 6: Novel direct plant microtensiometers (FloraPulse) used during 2020/21 season for measuring trunk water potential

4.2.2 Remote sensing equipment

4.2.2.1 The unmanned aerial vehicle

A DJI Matrice 600 Pro hexacopter was used as the sensor carrier for this research. This UAV offered a flight time of about 16-20 mins and payload capacity of about 6 kg, easily accommodating the sensor payload which included a thermal, a multispectral, and an RGB camera (see Figure 7).

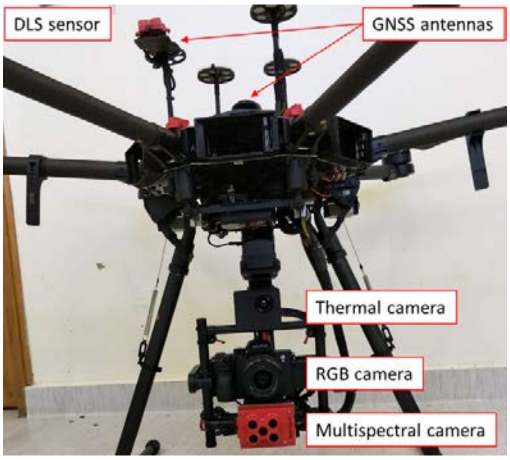

Figure 7: The UAV platform and the sensors for the remote sensing of vine water status.

The flight planning and data capturing strategy were determined before the field campaign. The flights took place at a height of 30 m in a regular mapping ("lawnmower") flight pattern. The camera was programmed to capture images once every second (maximum frame rate). The speed of the flight (3 m/s) was set to match with the image capture rate such that at least 80% forward overlap between subsequent images were achieved. The separation of the subsequent flight strips was set such that over 70% side overlap was achieved. With 80%, forward and 70% side overlap, the images were expected to produce high resolution maps via mosaicking (photogrammetry). Furthermore, consideration was provided to the total flight time (14 min battery life) balancing out with the flight altitude. For higher flight altitudes, the UAV could fly faster without compromise in the image overlap and complete the mission in a shorter time. The selected parameter was a compromise between the desired overlap, the maximum operating rate of the camera, the life of the battery and the size of the site. The flight planning and the flight operation was performed in the DJI Ground Station Pro software application (Fig. 8).

Figure 8: DJI GS Pro software to plan the UAV flight and capturing of the remote data.

The use of independent cameras (thermal, multispectral, and RGB) requires spatial overlay between the output products (e.g. maps) such that correct plants are observed in each map. For this, we use two-step processing to acquire maps with correct geographic location and with correctly overlayed layers. The first step is to use a GNSS antenna onboard the UAV that can provide a spatial reference to each image of at least one camera. The GNSS antenna of the multispectral camera was capable of geotagging the multispectral images. As a result, the products from the multispectral images were in a correct geographic location. The images were acquired in WGS84 coordinate frame, and the post-processed products were derived in MGA54 projected coordinate frame. The second step set in the field was to have permanent control points on the field. For this, we hammered about 15 wooden pegs (sized 35 x 5 x 5 cm) on each of the test sites, and manufactured ground targets (sized 30 cm diameter). The ground targets were placed at the peg location, for each of our field campaigns. This way, the targets are captured by all the cameras, and hence are used as tie-points to align and overlay the maps from the cameras.

4.2.2.2 RGB camera

A full-frame RGB camera (Sony α7RIII) was used to capture the high-resolution natural colour images from the UAV. The camera had a wide field of view of 65.3° x 46.4°, the focal length of 28 mm and the CCD chip had 7952 x 5304 pixels. Given the camera parameters, the proposed flying height resulted in a single image coverage of 38.5 x 25.7 m with a spatial resolution of 0.5 cm (at 30 m altitude). This level of spatial resolution was adequate to capture single leaves at high resolution, and for our application, which requires measurement at a single vine canopy level.

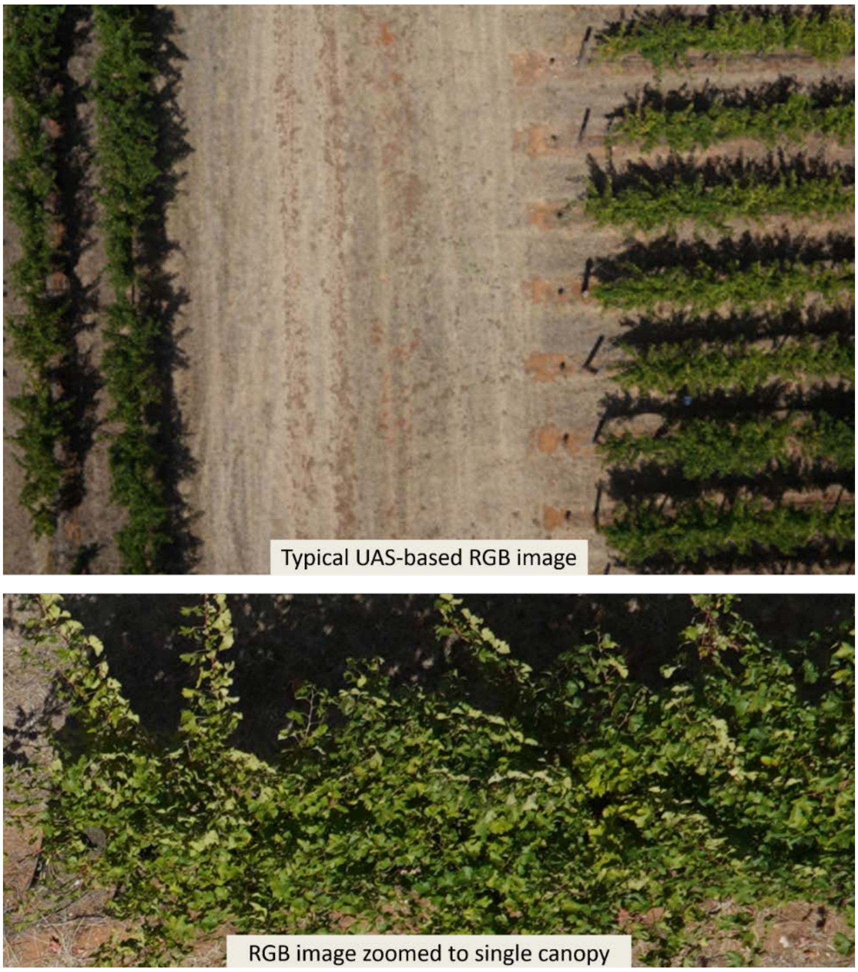

Figure 9: Typical single RGB image captured from a UAV. Note that leaf-level spatial resolution is achievable.

4.2.2.3 Multispectral camera

A five-band multispectral camera (MicaSense RedEdge-M) was used to co-capture the multispectral images. The five discrete bands captured five independent images at blue (475 nm), green (560 nm), red (670 nm), red edge (720 nm), and near infrared (840 nm) region of the electromagnetic spectrum. The camera had a field of view of 47.9° x 36.9°, focal length of 5.4 mm, and each discrete CCD chip had 1280 x 960 pixels. The resulting image for the proposed flying height had coverage of 26.7 x 20 m with a spatial resolution of 2.1 cm (at 30 m altitude).

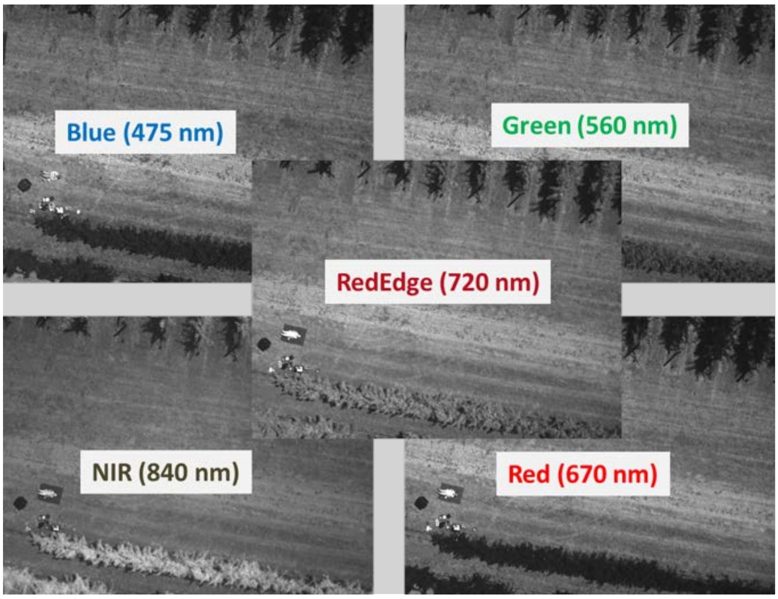

Figure 10: A typical single multispectral image. Note that the camera captures a discrete image for each discrete band.

4.2.2.4 Thermal camera

Thermal images were captured using a FLIR Tau2 640 core with TeAx acquisition board. The sensor captured, at 7.5 – 14 µm, the latent heat coming to the sensor from the scene. The camera had the field of view of 45.4° x 37°, the focal length of 13 mm, and contained 640 x 520 microbolometers arranged as pixels. The resulting thermal image for the proposed flying height had coverage of 25.1 x 20.1 m with a spatial resolution of 3.9 cm. The achievable resolution is sufficient for our application to measure a single canopy. At 3.9 cm resolution, a single canopy will still have several hundred pixels allowing accurate measurement of the pure canopy temperature.

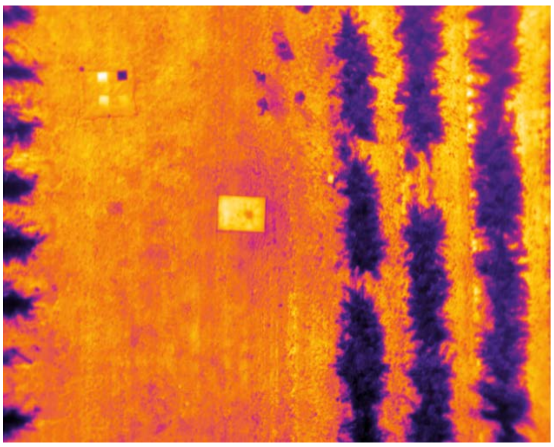

Figure 11: Typical single thermal image. Note the thermal image requires image-stretching techniques for visualisation purpose. The raw thermal image appears completely dark to human eyes.

4.2.3 Thresholds for irrigation scheduling

The four irrigation strategies used measurement of different factors to drive the irrigation. The strategies resulted in different total irrigation volumes (per season) as well as different times or schedules of irrigation each week. The decision to irrigate was based on historical (CONV, CONV+), measured (SWS, PWS) or calculated (ET) information. A set of thresholds based on quantitative measurement values were set for each of the non-control treatment. For each irrigation cycle, the measurements are compared against the predetermined threshold. Treatments were irrigated only, if the quantitative measurements dropped below the predetermined threshold (see below for details).

4.2.3.1 Conventional

The CONV irrigation treatment is the 'control' group of this study, which was irrigated by the growers without intervention by the trial researchers. The irrigation amount and timing incorporated a combination of historical irrigation schedules, weather conditions, visual inspection of the vines and occasional soil moisture measurements. In the 2020-21 growing season, due to the high levels of water stress observed in the CONV vines during the previous season (2019-20), the amount of irrigation was doubled for the CONV irrigation treatment (CONV+) to ensure the vines were well-watered. In the 2021/2022 season, both CONV and CONV+ treatments were compared with other sensor-driven treatments.

4.2.3.2 Plant water status

The PWS treatment received irrigation based on the measurement of plant water status specifically the VWI value derived from the Transp-IR towers. These VWI values corresponded to canopy conductance (g_c) values of between 120-140 mmol $H_2O/m^2/s$. This threshold range was established from a preliminary study at the trial site during the 2017-2018 season targeted at achieving 80-85% of maximum photosynthesis of each cultivar.

4.2.3.3 Crop evapotranspiration

The crop evapotranspiration method aimed to replace the water loss from the vineyard via the evaporation and transpiration. Based on the measurement of the plant crop coefficient (K_c) and meteorological data (ET_0), the ET_c was computed weekly. This computation was the basis of the irrigation decision for each irrigation cycle. Following deficit irrigation strategies in literature and experience from the region and specific vineyard where 40-50% ET_c was used for the CONV treatment, we maintained the deficit irrigation for the ET treatment at 15% ET_c from fruit set to véraison, and 25% ET_c from véraison to harvest.

4.2.3.4 Soil water status

The SWS treatment aimed to maintain the soil volumetric water content throughout the season. This threshold was determined from the capacitance probe historical data. The threshold was set at 30% below the historical volumetric water content of the vineyards, which was around 33% VWC. The resulting volumetric water content threshold to trigger the irrigation in the SWS treatment was 21% in both vineyards, CAS and SHI.

4.3 Data collection time points

We aimed to acquire direct, proximal and remote sensing field data at key phenological stages of vine development. The purpose of the data was two-fold: a) to decide on the irrigation of the particular treatments, and b) to monitor the performance of the vine as a result of the different irrigation practices. Table 2 shows the data collection time points corresponding to different phenological stages at each season for CAS and SHI.

Table 2: Data collection time points at different phenological stages at each season.

Phenological stage of growth	2018 – 2019	2019 – 2020	2020 – 2021	2021-2022
Winter rainfall May-August, mm	334.2	272.6	272.5	256.6
	Cabernet Sauvignon			
EL stage Budburst (BB) – 4 Flowering (F)– 19 Fruit set (FS)– 27 Pea sized (P)– 31 Veraison (V)– 35 Preharvest (PH)– 37 Harvest (H)– 38	BB – 2nd Oct 2018 F – 20th Nov 2018 FS– 12th Dec 2018 P– 16th Jan 2019 V – 12th Feb 2019 PH – 7th Mar 2019 H – 11th Apr 2019	BB – 24th Sept 2019 F – 18th Nov 2019 FS – 17th Dec 2019 P – 13th Jan 2020 V – 5th Feb 2020 PH – 10th Mar 2020 H – 8th Apr 2020	BB – 21st Sept 2020 F – 20th Nov 2020 FS – 7th Dec 2020 P – 4th Jan 2021 V – 9th Feb 2021 PH – 18th Mar 2021 H – 14th Apr 2021	
	Shiraz			
	BB – 30th Sept 2018 F – 5th Dec 2018 FS – 12th Dec 2018 P – 27th Dec 2019 V – 5th Feb 2019 PH – 7th Mar 2019 H – 21st Mar 2019	BB – 30th Sept 2019 F – 7th Dec 2019 FS – 19th Dec 2019 P – 30th Dec 2020 V – 10th Feb 2020 PH – 9th Mar 2020 H – 17th Apr 2020	BB – 17th Sept 2020 F – 20th Nov 2020 FS – 7th Dec 2020 P – 14th Dec 2021 V – 2nd Feb 2021 PH– 1st Mar 2021 H – 31st Mar 2021	F- 30th Nov 2021 P- 30th Jan 2022 V- 22nd Feb 2022 PH- 18th Mar 2022 H- 06th Apr 2022

4.4 Methodology and processing

4.4.1 Ground data methodology and processing

All the ground data was sorted by date, treatment, block and vine number. A pre-established empirical equation was used for the computation of crop coefficient. Data was statistically analysed by two-way ANOVA using GraphPad Prism 8 Prism software.

4.4.2 Harvest, yield components, and pruning

At harvest, yield parameters such as weight of fifty berries, number of clusters per vine, total bunch weight and cordon length were measured on eight vines per treatment. Vines were pruned later in the season and pruning weight was measured in each vine.

4.4.3 Winemaking

After harvesting, clusters were randomly selected from eight different vines per treatment and they were mixed for winemaking. Twelve small-scale ferments (one 5 L ferment per treatment per vineyard) were prepared according to the following procedure developed by the University of Adelaide. Fruits were crushed using a mechanical crusher de-stemmer and 20 ml of a 2% SO_2 solution was added. Diammonium phosphate was added at 100 ppm to each must before inoculating with the yeast (Lalvin EC-1118 *Saccharomyces cerevisiae bayanus*, Lallemand, Denmark) at 300 mg/L. All ferments were incubated in a temperature-controlled room at 22 °C and skins were hand-plunged twice a day. After two weeks juice was extracted using a basket press and wines were racked after a week. Malolactic fermentation was initiated by inoculating the wine with lactic acid bacteria (strain). Wines were bottled after adding sulphur dioxide (30 ppm) and they were stored at 15 °C until chemical composition analyses was performed.

4.4.4 Berry, juice and wine chemical analyses

All fruit chemical analyses were done on per vine basis. The following chemical parameters were determined as described below.

4.4.4.1 pH/titratable acidity (TA) and total soluble solids (TSS)

TSS was measured using a refractometer. pH and TA were simultaneously assessed using an autotitrator (Mettler Toledo T50).

4.4.4.2 Colour/hue analysis

In order to identify colour and hue of grape juice and wine, absorbance at 420 and 520 nm wavelengths were measured against a blank using a UV/Vis spectrophotometer. A glucose solution (20%) with 1 g tartaric acid was used as a blank for grape juice, whereas 10% ethanol was used for wine. Colour density and hue/tint were calculated using the following formulae:

$$\text{Colour density} = A_{520} + A_{420}$$

$$\text{Hue/Tint} = A_{420}/A_{520}$$

4.4.4.3 Total anthocyanin

Anthocyanin content was determined by measuring the differential absorbance at 520 nm between wines at pH 1.0 and pH 4.5. Ten-fold diluted samples were prepared using pH 1.0 and pH 4.5 buffers and absorbance at 420 and 520 nm were measured following a 1 hr of dark incubation. Total anthocyanin concentration was calculated as malvidin chloride 3, 5-diglucoside (equivalents) using the following formula.

$$\text{Total anthocyanins (mg/L)} = (A^{520}_{pH\ 1.0} - A^{520}_{pH\ 4.5}) \text{ X } 255.75$$

4.4.4.4 Total phenolics

Two microliters of the sample (or 20 µl of the 10:1 diluted sample), 1.58 ml of distilled water and 100 µl of Folin & Ciocalteu's phenol reagent were added to a glass cuvette and after 1 min incubation at room temperature, 300 µl of sodium carbonate solution was added. The solution was incubated at 40 ^{0}C for 30 min under dark and absorbance was measured at 765 nm against a blank. Total phenolics were then quantified using a Gallic acid standard curve and expressed in mg/L of gallic acid equivalents (GAE).

4.4.5 Remote sensing data methodology and processing

4.4.5.1 Mosaicking

Three cameras (multispectral, thermal, and RGB) were used to co-acquire aerial imagery of the vineyards at four phenological stages (Flowering (EL-19), PeaSize (EL-31), Veraison (EL-35), and Pre-harvest (EL-37)). Initially, the photogrammetric software, Agisoft Metashape, was used to mosaic the series of images to create a map.

The RGB images were mosaicked using a standard workflow of image alignment followed by camera calibration, dense point cloud generation, 3D model generation, and orthomosaic generation. The output from the RGB images include orthomosaic and report for each orthomosaic. Since the bands presented in the RGB are a subset of the multispectral camera, the multispectral products sufficed our necessity and hence the RGB products were not used in further processing.

The Multispectral images were mosaicked using the workflow recommended by the Agisoft Metashape. The workflow includes in following order: a) creating multi-spectral images, b) image alignment, c) camera calibration, d) dense point cloud, e) classification of pointcloud, f) DEM generation, g) DSM generation, and h) orthomosaic generation. The multispectral camera generated most of the basic products for this project. The output from a multispectral camera included 12 sets of the following products: a) georeferenced orthomosaic, b) digital elevation model, c) digital surface model, d) 3D pointcloud, e) processing report.

The thermal camera was new to the processing chain requiring a unique workflow. Firstly, the thermal camera in *.TMZ format was converted to raw image files. Using a batch processing script the *.TMZ file captured by the camera were converted to raw *.TIFF file along with the metadata encoded in a *.CSV file. The image files were then processed in Agisoft Metashape to generate thermal maps. The thermal images contained value of temperature data encoded in 14-bit format. As the variation in temperature between the scenes was not minimal, thermal images appeared completely dark when viewed in raw. This resulted in minimum, at best, match points between the consecutive images, failing image alignment. As a solution, raster transformation was applied before processing the images in Agisoft Metashape and reverted before exporting products out of Metashape. The processing workflow of the thermal images in Agisoft Metahshape included: a) raster transformation, b) image alignment, c) camera calibration, d) dense point cloud generation, e) 3D model generation, f) orthomosaic generation, g) reset of raster transformation, h) exporting of products. The products from the thermal images included the orthomosaic and processing report.

The orthomosaic, DEM, and DSM from the multispectral camera and the thermal orthomosaic were processed further within the scope of this project. Whereas, the processing of the RGB orthomosaic and multispectral 3D pointcloud were considered of low priority.

4.4.5.2 Georeferencing

The multispectral camera had a functional GPS antenna encoding a navigation-grade position to each of the images. This information is exploited to georeference the multispectral images within the Agisoft Metashape via direct georeferencing, whereby, all the products from the multispectral camera were in projected MGA 54 projected coordinate frame.

The thermal orthomosaics were not georeferenced to any coordinate frame, due to the lack of functional GPS antenna. In this process of georeferencing, the thermal orthomosaic were georeferenced on top of the multispectral orthomosaic. For this, the GCPs spread across the scene were used as the common tie-points between two orthomosaics. Using a polynomial fit, the thermal orthomosaics were fitted to the multispectral orthomosaics in ArcGIS software.

4.4.5.3 Atmospheric radiometric correction

The thermal and multispectral images were captured at various time point throughout the season. As each time point was environmentally different, we required a calibration to account for changing environmental conditions between different days and times of the day. This calibration corrects for environmental factors such as high/low solar illumination and VPD, and highlights the plants spectral/thermal signal. For this, four shaded standard calibration panels were used in the field for each of the flight. The calibration panels were sized (45 x 45 cm) such that they are visible and had sufficient pixels (over 50) representing a single panel. The calibration panels were manufactured using black enamel paint and white $BaSO_4$ following a prescribed mixing ratio, coating thickness, and number of coats. The panels were expected to have a uniform reflectance profile sustained throughout the season. The manufactured panels were four shade of grey: a white (90% white and 10% black), light grey (70% white and 30% black), dark grey (30% white and 70% black) and black (10% white and 90% black) (see Figure 5). For spectral calibration, the panel reference spectra were measured, at the start and the end of the season, on the ground using an ASD Handheld2 spectroradiometer. On each flight, the multispectral camera captured few snaps of the panels. Using the reference spectral profile (measured on the ground), the calibration was applied to the raw spectral profile (acquired during flight).

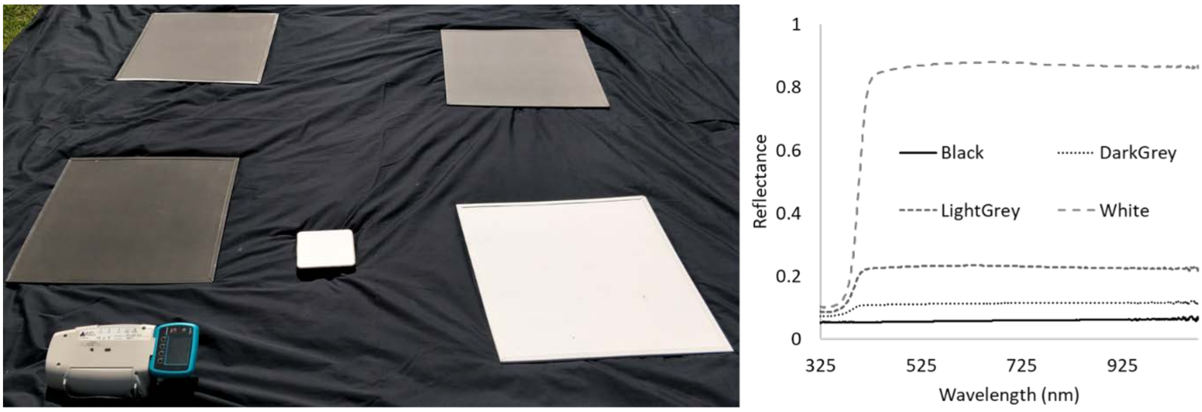

Figure 6: The four calibration panels: White (90% white, 10% black), Light Grey (70% white, 30% black), Dark Grey (30% white, 70% black), Black (10% white, 90% black) along with the Spectralon panels (calibrated and non-calibrated), and the ASD handheld2 spectroradiometer used to acquire the spectral calibration data. The reflectance profile of the four calibration panels is displayed in the right pane.

The shaded panel also develops unique temperature when placed under the sun. This was exploited to calibrate the thermal camera using the same calibration panels prepared for the multispectral. The panels were placed in the field, under full sun, at least 45 minutes before the flight. By about 45 minutes, each panel reached a unique and stable temperature. For a typical day, the observed difference between the white and black panel was in the order of 30^{o} C. During the flight, the thermal camera captured several images of the panels whenever the panels were in the field of view. Concurrently, on the ground, the panel temperature was measured continuously using a high accuracy Fluke IR temperature gun. Using the known panel temperature (measured on the ground), the calibration was applied to the raw thermal data (acquire during flight).

4.4.5.4 Single canopy data extraction

Following the radiometric/atmospheric calibration of the georeferenced orthomosaics, single canopy level data was extracted. For this, a global mask was applied to the orthomosaics. The mask incorporated the normalised difference vegetation index (NDVI) and the canopy height thresholds to remove any non-canopy pixels from the orthomosaic (see Figure).

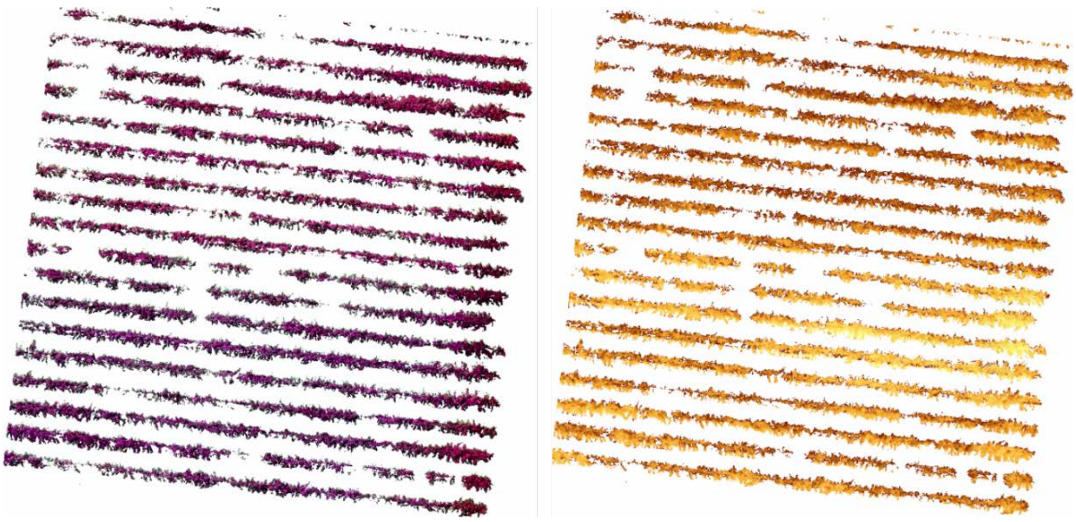

Figure 13: The masked multispectral (left pane) and thermal (right pane) orthomosaics from Alex88-east at EL-35. Note the masking is performed using the NDVI threshold (0.4) and the canopy height threshold (1 m).

From the masked multispectral and thermal orthomosaic, single canopy (vine-level) data was extracted by using the ArcGIS/QGIS Zonal Statistics tool. For zonal statistics to be applied, the vines within the scene were digitised using a grid (in Q-GIS) where one polygon represented the vine space (row x vine spacing) for a single canopy (see Figure).

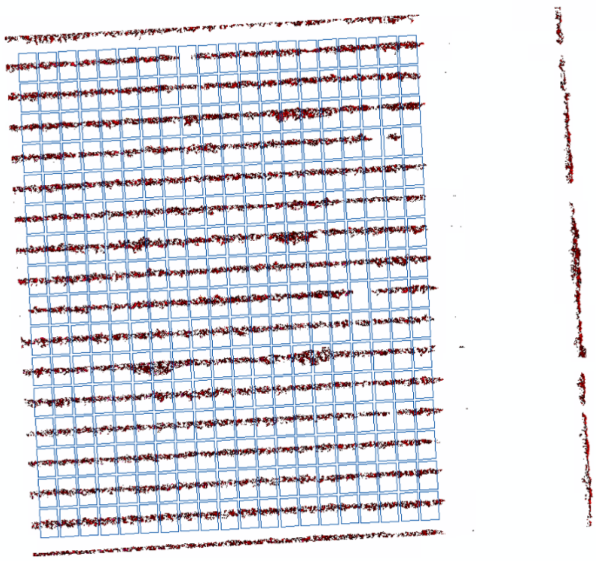

Figure 14: The digitised canopy space for the Katnook Homestead block at EL-31. Note each of the rectangular polygons represents the vine space for a single canopy. The gap between two polygons is used as inter-canopy 20 cm buffer.

4.4.5.5 Identification of key indices

Numerous structural, spectral, thermal, and composite indices were computed from the remote sensing data. These indices were, at a later stage, used for spatial prediction of grapevine ecophysiology including stomatal conductance, net photosynthesis, predawn and stem water potentials, crop coefficient, and LAI.

4.4.5.5.1 Structural indices

From the single vine data, the following structural properties of each canopy were extracted and structural indices computed (see Table):

Table 3: Structural properties and indices computed using remote sensing

SN	Name	Description	Formula
1	p_height	Mean height of the canopy	n/a
2	area	The top surface area of the canopy	n/a
3	width	Width of the canopy	n/a
	P_fraction	Fractional cover of the canopy within the vine space	area/(rowSpacing*vineSpacing)

4.4.5.5.2 Spectral indices

Various spectral indices were computed using the five bands of the multispectral images (see Table 4).

Table 4: The spectral indices computed using the MicaSense RedEdge-M. Note b = Blue, g = Green, r = Red, nir = near-infrared, re = RedEdge.

SN	Name	Description	Formula
1	CAR	Chlorophyll absorption ratio	((re-b)*r+r+(g-((re-b)*r)*g))/np.sqrt(((re-b)*r)**2)
2	CAR1	Chlorophyll absorption ration#1	CAR*re/r
3	GI	Greenness index	g/r

4	GNDVI	Green normalised difference vegetation index	(nir-g)/(nir+g)
5	NDVI	Normalised difference vegetation index	(nir-r)/(nir+r)
6	MCARI	Modified chlorophyll absorption in reflectance	((re-r)-0.2*(re-g))*(re/r)
7	MCARI1	Modified chlorophyll absorption in reflectance#1	1.2*(2.5*(nir-r)-1.3*(nir-g))
8	MCARI2	Modified chlorophyll absorption in reflectance#2	MCARI1/np.sqrt((2*nir+1)**2-6*(nir-5*r)-0.5)
9	MSAVI	Modified soil adjusted vegetation index	(1/2)*(2*nir+1-np.sqrt((2*nir+1)**2-8*(nir-r)))
10	OSAVI	Optimised soil adjusted vegetation index	(1+0.16)*(nir-r)/(nir+r+0.16)
11	SRI	Simple ratio index	nir/g
12	MSR	Modified simple ratio	((nir/r)-1)/(np.sqrt((nir/r)+1))
13	MTVI	Modified triangular vegetation index	1.2*(1.2*(nir-g)-2.5*(r-g))
14	PCD	Plant canopy density	nir/r
15	PRI	Photo-chemical reflective index	(g-b)/(g+b)
16	RDVI	Renormalised difference vegetation index	(nir-r)/np.sqrt(nir+r)
17	TCARI	Transformed chlorophyll absorption reflectance index	3*((re-r)-0.2*(re-g)*(re/r))
18	TCARI/OSAVI		TCARI/OSAVI
19	VDVI	Visible-band difference vegetation index	(2*g - r - b)/(2*g + r + b)
20	ENDVI#1	Enhanced normalised difference vegetation index#1	((nir+g)-2*b)/(nir+g+2*b)
21	ENDVI#2	Enhanced normalised difference vegetation index#2	((nir+g)-2*r)/(nir+g+2*r)
22	ENDVI#3	Enhanced normalised difference vegetation index#3	((nir+g)-r-b)/(nir+g+r+b)

4.4.5.5.3 Thermal indices

Various thermal indices were computed using the five bands of the multispectral images (see Table).

Table 5: The indices computed using the thermal data.

SN	Name	Description	Formula
1	Tc	Mean temperature of the canopy	n/a
2	Tc/Ta	Canopy to atmospheric temperature ratio	Tc/Ta

3	Tc-Ta	Canopy to the atmosphere temperature difference	Tc-Ta
4	CWSI	Crop water stress index	(Tc-Twet)/(Tdry-Twet)
5	ig	Crop water stress index	(Tdry-Tc)/(Tc-Twet)
6	i3	Crop water stress index	(Tc-Twet)/(Tdry-Tc)

4.4.5.5.4 Composite indices

Various thermal indices were computed using the five bands of the multispectral images (see Table 6).

Table 6: The composite indices computed using the thermal, spectral, and structural indices.

SN	Name	Description	Formula
1	cum_ndvi	Cumulative NDVI for entire canopy	NDVI*area
2	TVDI	Temperature vegetation dryness index	Tc/NDVI
3	TVDI#1	Temperature vegetation dryness index#1	(Tc-Ta)/NDVI
4	TVDI#2	Temperature vegetation dryness index#2	CWSI/NDVI
5	TVDI#3	Temperature vegetation dryness index#3	ig/NDVI
6	TVDI#4	Temperature vegetation dryness index#4	i3/NDVI

4.4.6 Financial Analysis

The following economic parameters were calculated for the last 3 seasons (2018-2021): Economic Productivity (EP), Economic Water Productivity (EWP), unit production cost, total operational cost, income, cash flow, Net Present Value (NPV), Internal Rate of Return (IRR), Pay-back Period (PB) and total margin.

$$\boldsymbol{EP} = \frac{\boldsymbol{Gross\ margin}\ (\$)}{\boldsymbol{Total\ yield}\ (\boldsymbol{t})}$$

$$\boldsymbol{EWP} = \frac{\boldsymbol{Gross\ margin}\ (\$)}{\boldsymbol{Total\ irrigation\ water}\ (\boldsymbol{ML})}$$

$$\boldsymbol{BP} = \frac{\boldsymbol{Total\ operational\ costs}\ (\$)}{\boldsymbol{Total\ yield}\ (\boldsymbol{t})}$$

Discounted cash flow analysis (DCFA) was undertaken in order to investigate each irrigation strategy based on estimated future farm returns to calculated the net present value (NPV):

$$\boldsymbol{NPV} = -\boldsymbol{k} + \sum_{\boldsymbol{t}=1}^{\boldsymbol{n}} \frac{\boldsymbol{CF_n}}{(\boldsymbol{1}+\boldsymbol{i})^{\boldsymbol{n}}}$$

See the attached paper in the Appendix for details on these financial parameters as well as model assumptions.

4.4.7 Vineyard Irrigation Survey

A survey was conducted to understand the irrigation practices of grapevine growers in the Limestone Coast viticultural regions. This survey was launched on the 14th of June, 2021 and closed on the 23rd of August, 2021. Growers were asked about their current operation, irrigation practices, use of data to inform irrigation scheduling, and awareness of water status sensors and their value.

5 Results and discussion

5.1 Seasonal irrigation

Table 7 shows the total irrigation, in ML/ha, supplied to all irrigation treatments across the three vineyards.

Table 7: Total irrigation (ML/ha) supplied across the three vineyards during each season.

	AX88-E			AX88-W			Katnook			
Season	S1	S2	S3	S1	S2	S3	S1	S2	S3	S4
CONV	0.6	0.55	0.55	0.45	0.46	0.35	-	0.936	1.2	0.72
CONV+	-	-	1.01	-	-	0.7	-	-	2.39	1.43
ET	0.3	0.4	0.21	0.14	0.34	0.21	-	0.672	0.5	0.57
PWS1	0.3	0.44	0.37	0.14	0.31	0.25	-	0.672	0.54	0.42
PWS2	-	-	-	-	-	-	-	-	-	0.62
SWS	0.6	0.34	0.34	0.45	0.37	0.25	-	0.552	0.53	0.59

As shown in Table 8, the evidence-based strategies reduced the amount of irrigation applied significantly relative to conventional treatment.

Table 8: Irrigation supplied as a percentage of CONV treatment across the three vineyards during each season.

	AX88-E			AX88-W			Katnook			
Season	**S1**	**S2**	**S3**	**S1**	**S2**	**S3**	**S1**	**S2**	**S3**	**S4**
ET	50	73	38	31	74	60	-	72	42	79
PWS1	50	80	67	31	67	71	-	72	45	58
PWS2	-	-	-	-	-	-	-	-	-	86
SWS	-	62	62	100	80	71	-	59	44	82

5.2 Soil moisture and vine performance measured via proximal sensing

5.2.1 Seasonal soil moisture

Soil moisture content significantly varied across three different vineyards and between vines irrigated according to different sensor-driven schedules.

2018/2019 season

In both Alex88-East and Alex88-West, no statistically significant differences were observed in Ψ_{pd} between irrigation treatments at the pre-veraison stage. However, during post-veraison stage, Ψ_{pd} was significantly lower in both ET and PWS vines relative to CONV (Figure 19). In Alex88-east, percentage of volumetric water content (%VWC) of ET vines were slightly higher that CONV vines throughout the season, whereas PWS vines exhibited lower VWC relative to CONV. In contrast, both ET and PWS vines exhibited lower VWC compared to CONV vines. The SHI vines in Prodigy vineyard had consistently higher soil moisture levels compared to the treatment block (Fig 19e).

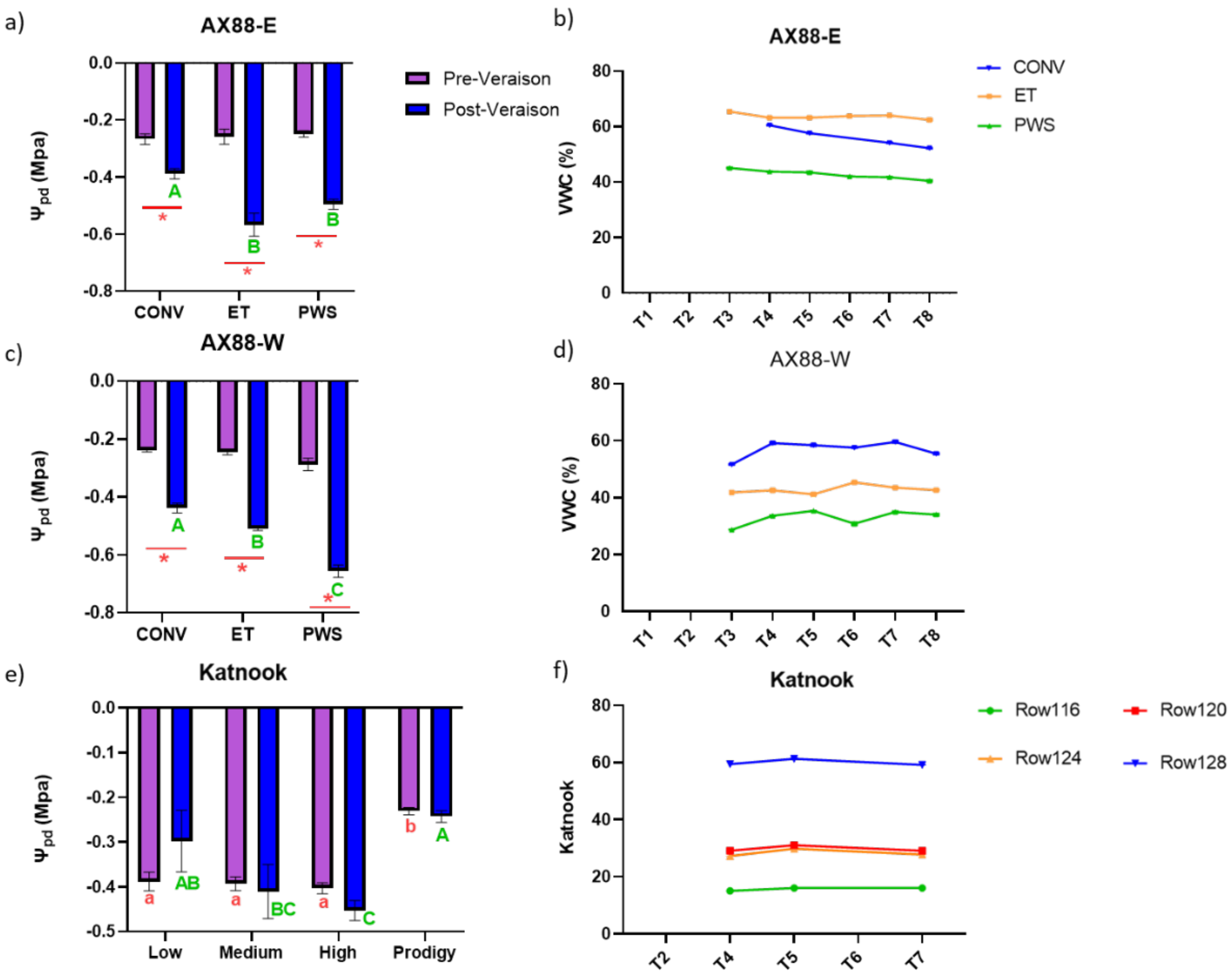

Figure 19: Variations in predawn water potential (Ψ_{pd}) (a, c, e) and percentage of volumetric water content (%VWC) (b, d, f) in CAS and SHI in response to different irrigation treatments. Values are means ± SEM of 4 biological replicates. Statistical analysis was conducted using two-way ANOVA. Asterisks indicate statistically significant differences (P<0.05) between pre- and post-veraison stages. Lowercase letters indicate statistically significant differences (P<0.05) between irrigation treatments at pre-veraison stage. Uppercase letters indicate statistically significant differences (P<0.05) between irrigation treatments at post-veraison stage.

2019/2020 season

Similar to the previous season, no statistically significant differences were observed in Ψ_{pd} between irrigation treatments in both Alex88-east and Katnook vines before veraison. After veraison, Ψ_{pd} was significantly higher in ET, PWS and SWS vines in Alex88-east relative to CONV vines. However, any irrigation treatment in Katnook, did not cause any differences in Ψ_{pd} after veraison. Even though, PWS and SWS vines in Alex88-west exhibited similar Ψ_{pd} to CONV vines before and after veraison, their Ψ_{pd} was significantly lower throughout the season relative to ET vines (Figure 20). The soil moisture levels in the Prodigy block were similar to the treatment block.

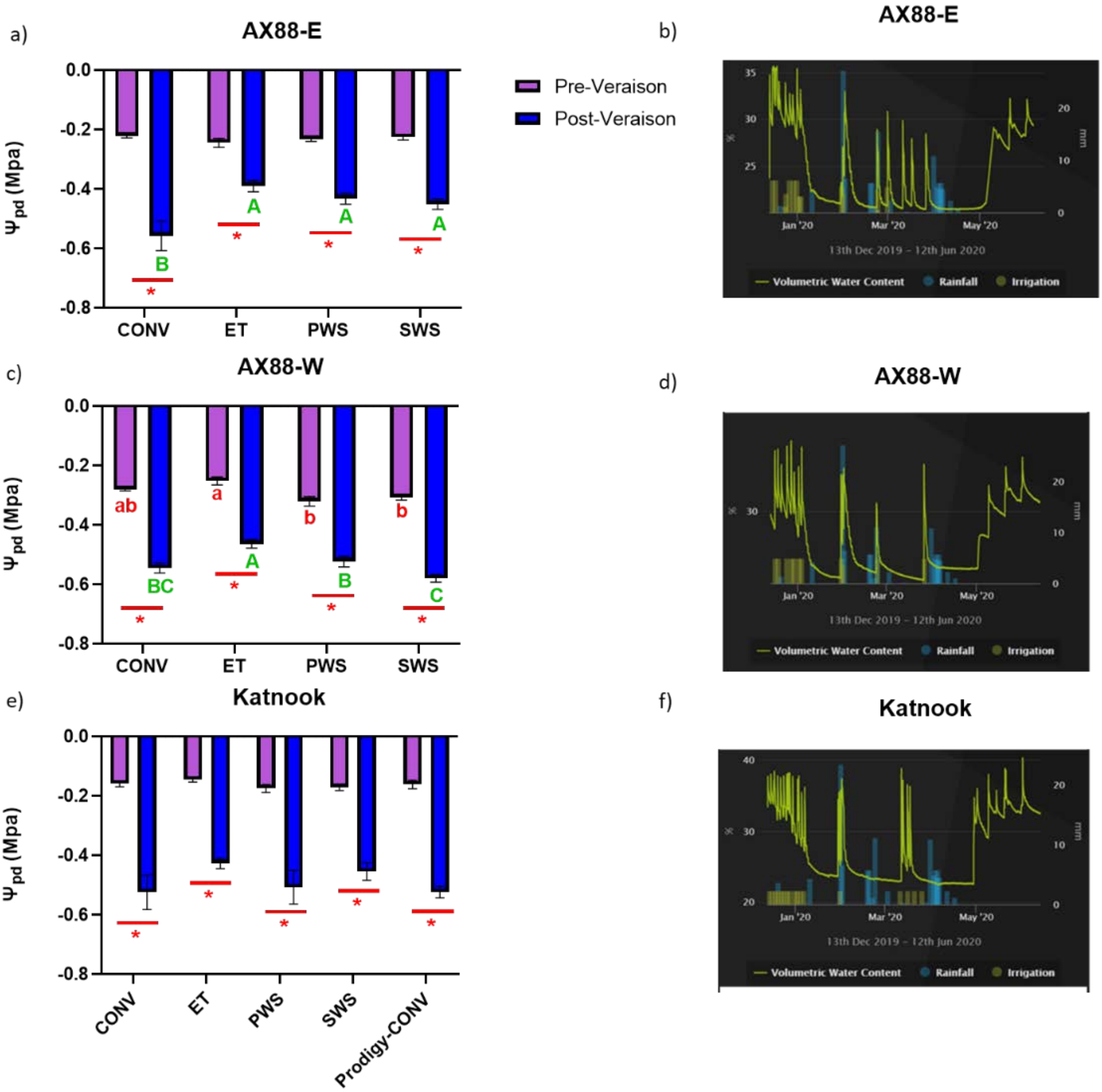

Figure 20: Variations in predawn water potential (Ψ_{pd}) (a, c, e) and percentage of volumetric water content (%VWC) (b, d, f) in CAS and SHI in response to different irrigation treatments. Values are means ± SEM of 8 biological replicates. Statistical analysis was conducted using two-way ANOVA. Asterisks indicate statistically significant differences (P<0.05) between pre- and post-veraison stages. Lowercase letters indicate statistically significant differences (P<0.05) between irrigation treatments at pre-veraison stage. Uppercase letters indicate statistically significant differences (P<0.05) between irrigation treatments at post-veraison stage.

2020/2021 Season

In Alex88-east, Ψ_{pd} was similar in ET and SWS vines relative to CONV vines before the veraison, whereas PWS vines showed significantly lower Ψ_{pd}. The post-veraison Ψ_{pd} in PWS and SWS was similar to CONV, but ET vines displayed significantly lower Ψ_{pd} compared to CONV. In Alex88-west, PWS and SWS vines had significantly lower pre-verasion Ψ_{pd} values relative to CONV, but after veraison, Ψ_{pd} was significantly lower in ET and sws treatments compared to CONV. In SHI in Katnook, pre-veraison Ψ_{pd} did not change in response to different irrigation treatments, however, Ψ_{pd} in ET, PWS and SWS vines after veraison were markedly lower relative to CONV (Figure 21).

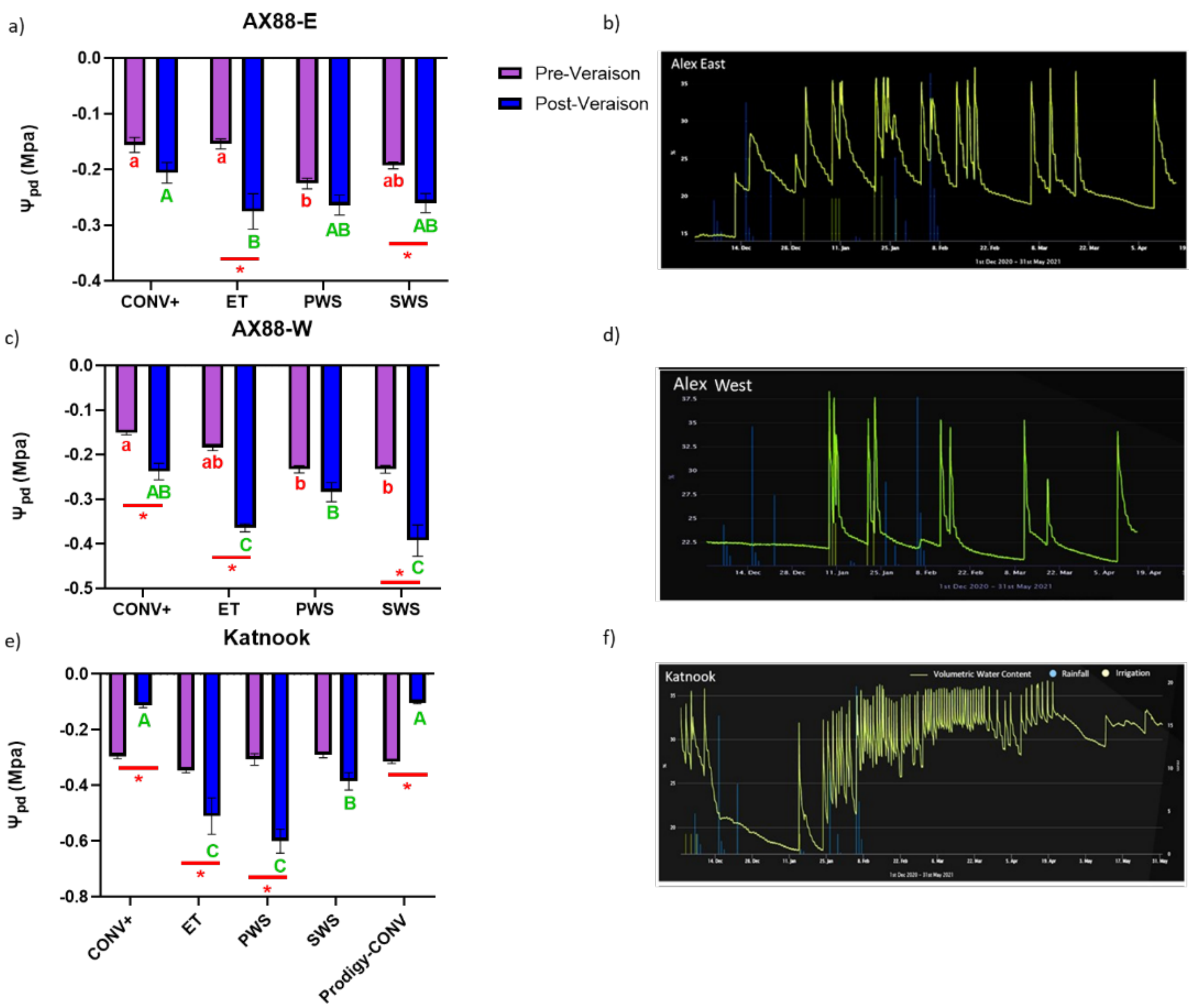

Figure 21: Variations in predawn water potential (Ψ_{pd}) (a, c, e) and percentage of volumetric water content (%VWC) (b, d, f) in CAS and SHI in response to different irrigation treatments. Values are means ± SEM of 8 biological replicates. Statistical analysis was conducted using two-way ANOVA. Asterisks indicate statistically significant differences (P<0.05) between pre- and post-veraison stages. Lowercase letters indicate statistically significant differences (P<0.05) between irrigation treatments at pre-veraison stage. Uppercase letters indicate statistically significant differences (P<0.05) between irrigation treatments at post-veraison stage.

2021/2022 Season

Unlike previous seasons, different irrigation treatments caused significant variations in Ψ_{pd} in SHI. For instance, before and after veraison, Ψ_{pd} was significantly lower in ET, PWS1, PWS2 and SWS vines relative to CONV, CONV+ and Prodigy vines (Figure 22). The Prodigy block had consistently higher soil moisture levels compared to the treatment block.

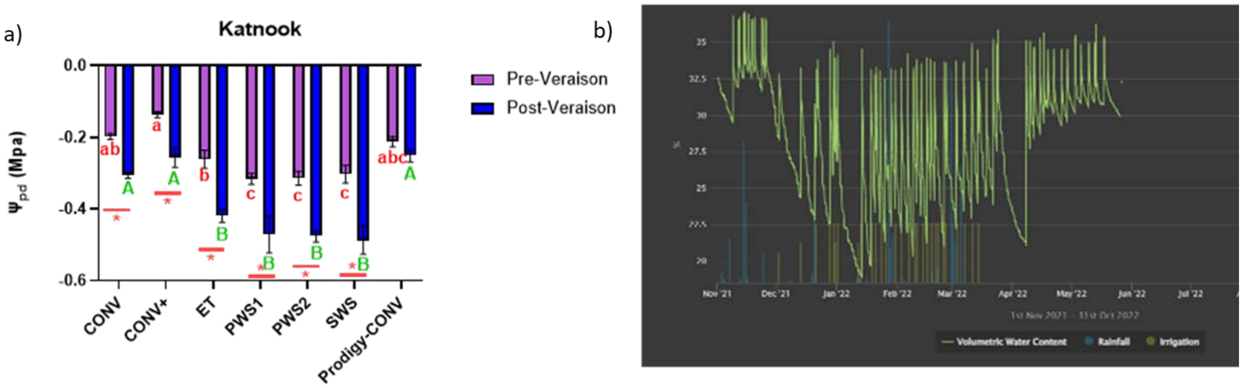

Figure 22: Variations in predawn water potential (Ψ_{pd}) (a, c, e) and percentage of volumetric water content (%VWC) (b, d, f) in SHI in response to different irrigation treatments. Values are means ± SEM of 8 biological replicates. Statistical analysis was conducted using two-way ANOVA. Asterisks indicate statistically significant differences (P<0.05) between pre- and post-veraison stages. Lowercase letters indicate statistically significant differences (P<0.05) between irrigation treatments at pre-veraison stage. Uppercase letters indicate statistically significant differences (P<0.05) between irrigation treatments at post-veraison stage.

5.2.2 Seasonal light interception and vine vigour (Leaf area index and porosity)

In Alex88-East and Alex88-West, no statistically significant differences in LAI and porosity were observed between irrigation treatments both at pre- and post-veraison stages across three seasons (2018/2019, 2019/2020 and 2020/2021). Even though it was consistently observed across three seasons that the LAI and porosity in SHI at Katnook were similar between irrigation treatments both before and after veraison (except in 2020/2021 season), Prodigy vines always produced relatively smaller canopy sizes and higher porosity levels (Figure 23, 24, 25 and 26). The high porosity in Prodigy may have been a contributing factor to the high grape composition and quality in that block.

2018/2019 season

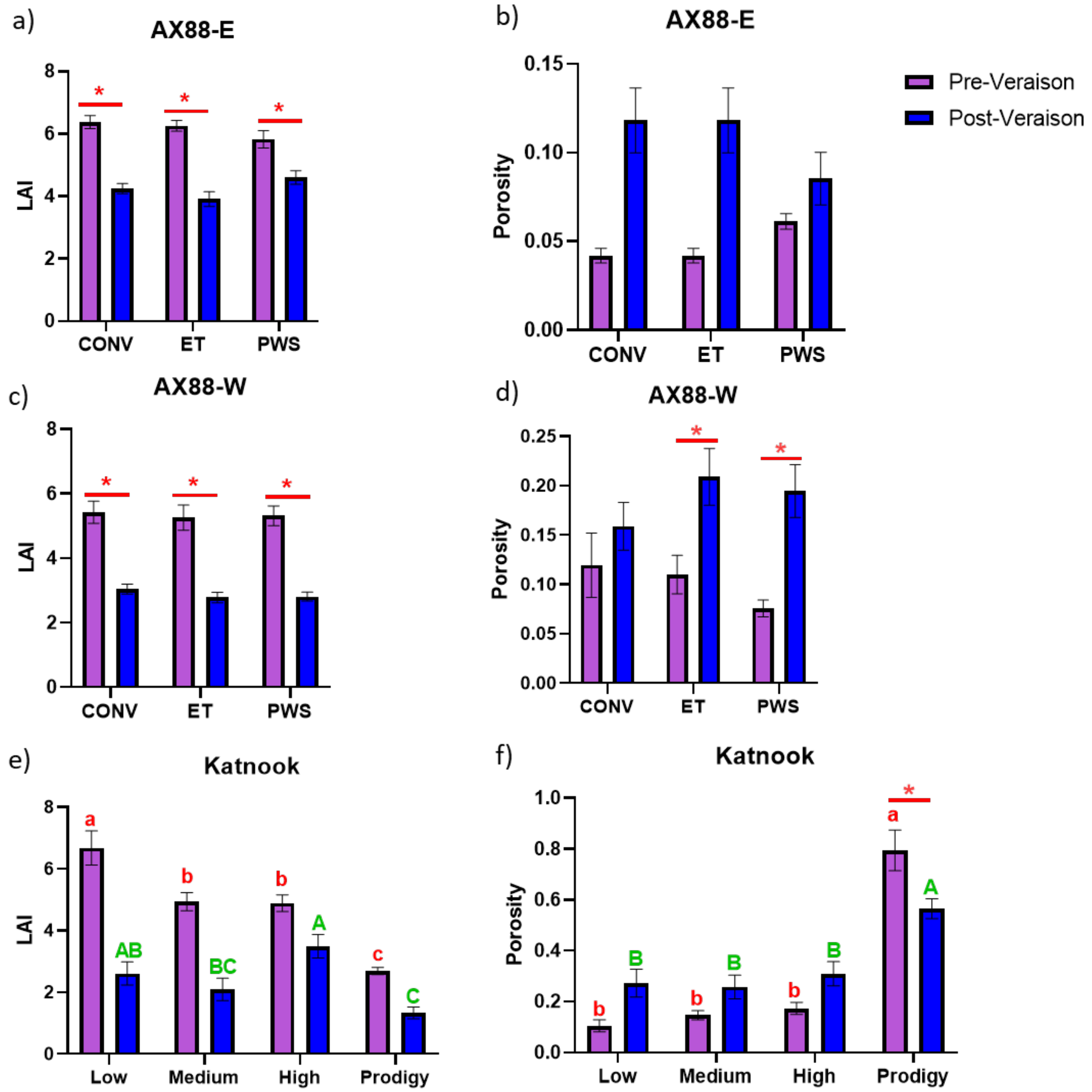

Figure 23: Changes in Leaf Area Index (LAI) (a, c, e) and porosity (b, d, f) in CAS and SHI in response to different irrigation treatments. Values are means ± SEM of 8 biological replicates. Statistical analysis was conducted using two-way ANOVA. Asterisks indicate statistically significant differences (P<0.05) between pre- and post-veraison stages. Lowercase letters indicate statistically significant differences (P<0.05) between irrigation treatments at pre-veraison stage. Uppercase letters indicate statistically significant differences (P<0.05) between irrigation treatments at post-veraison stage.

2019/2020 season

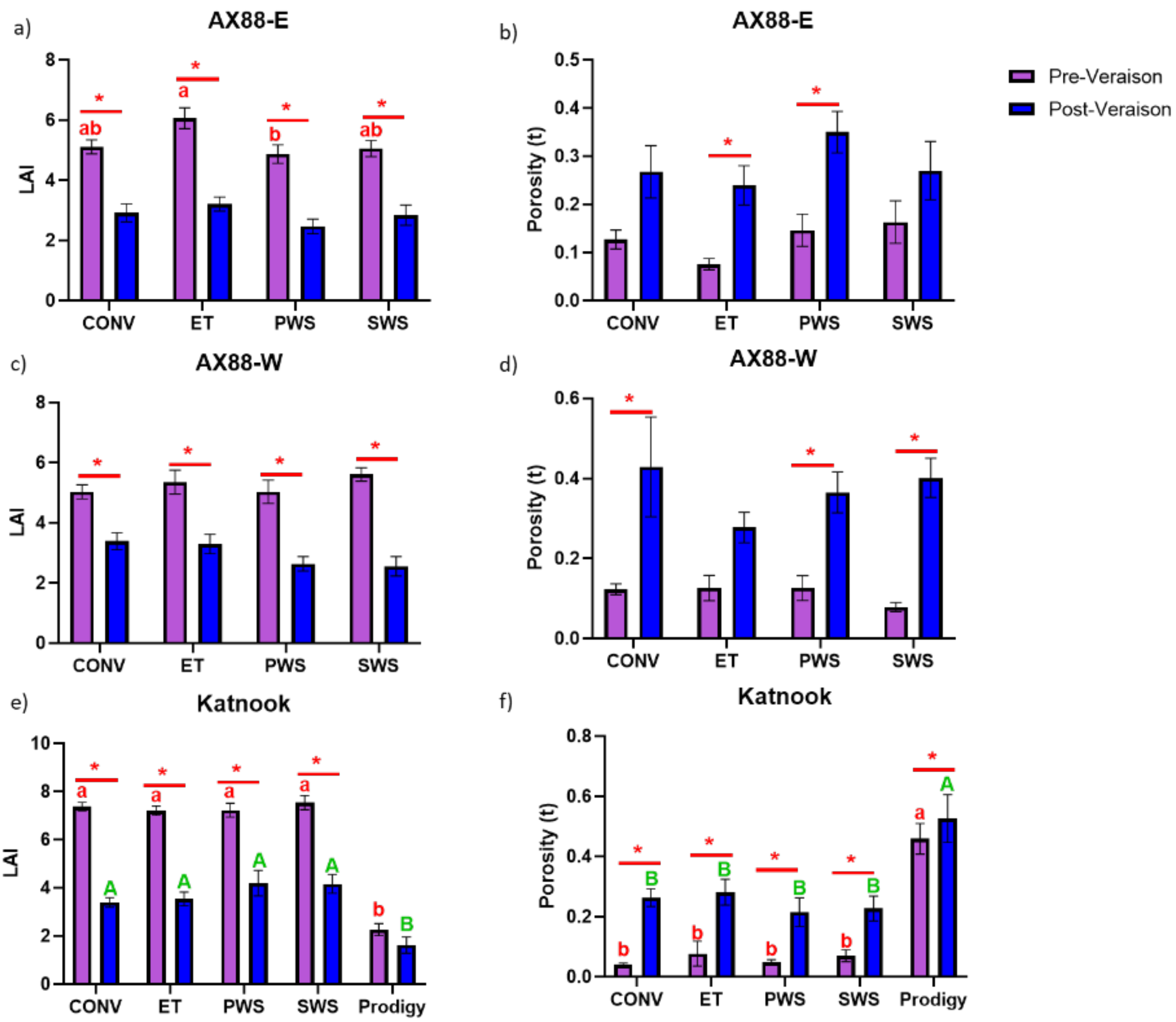

Figure 24: Changes in Leaf Area Index (LAI) (a, c, e) and porosity (b, d, f) in CAS and SHI in response to different irrigation treatments. Values are means ± SEM of 8 biological replicates. Statistical analysis was conducted using two-way ANOVA. Asterisks indicate statistically significant differences (P<0.05) between pre- and post-veraison stages. Lowercase letters indicate statistically significant differences (P<0.05) between irrigation treatments at pre-veraison stage. Uppercase letters indicate statistically significant differences (P<0.05) between irrigation treatments at post-veraison stage.

2020/2021 season

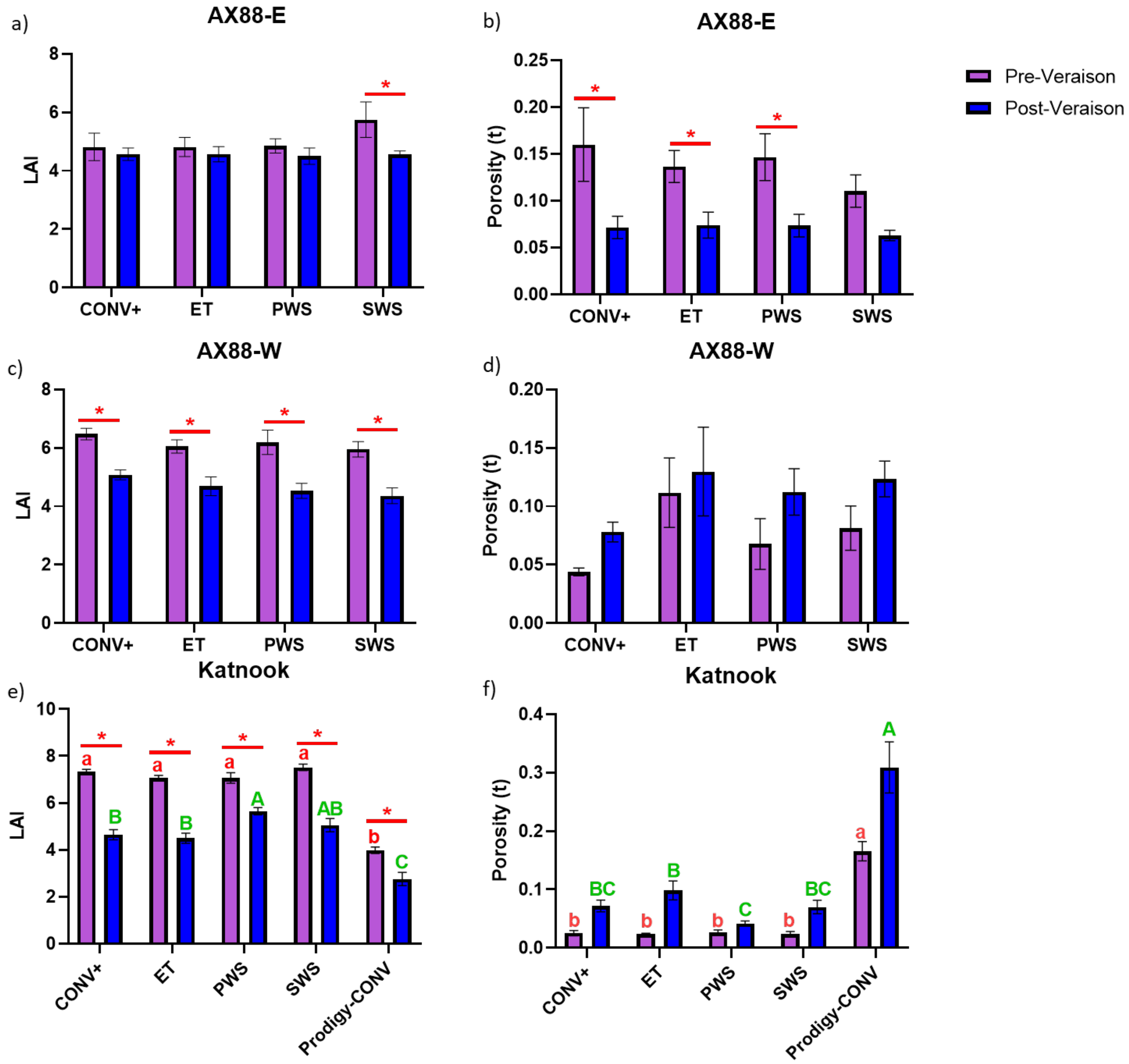

Figure 25: Changes in Leaf Area Index (LAI) (a, c, e) and porosity (b, d, f) in CAS and SHI in response to different irrigation treatments. Values are means ± SEM of 8 biological replicates. Statistical analysis was conducted using two-way ANOVA. Asterisks indicate statistically significant differences (P<0.05) between pre- and post-veraison stages. Lowercase letters indicate statistically significant differences (P<0.05) between irrigation treatments at pre-veraison stage. Uppercase letters indicate statistically significant differences (P<0.05) between irrigation treatments at post-veraison stage.

2021/2022 season

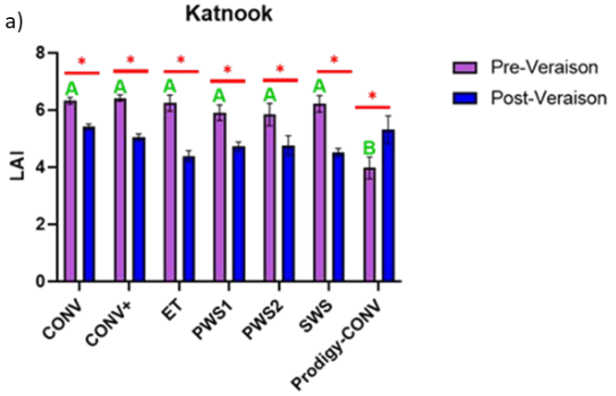

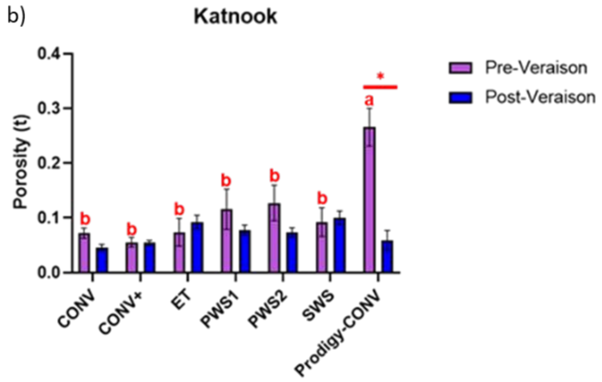

Figure 26: Changes in Leaf Area Index (LAI) (a, c, e) and porosity (b, d, f) in SHI in response to different irrigation treatments. Values are means ± SEM of 8 biological replicates. Statistical analysis was conducted using two-way ANOVA. Asterisks indicate statistically significant differences (P<0.05) between pre- and post-veraison stages. Lowercase letters indicate statistically significant differences (P<0.05) between irrigation treatments at pre-veraison stage. Uppercase letters indicate statistically significant differences (P<0.05) between irrigation treatments at post-veraison stage.

5.2.3 Seasonal evapotranspiration (ET_0) and crop coefficient (K_c)

Variation in rainfall, evapotranspiration and crop coefficient during each season are shown in Figures 27-30.

2018/2019 season

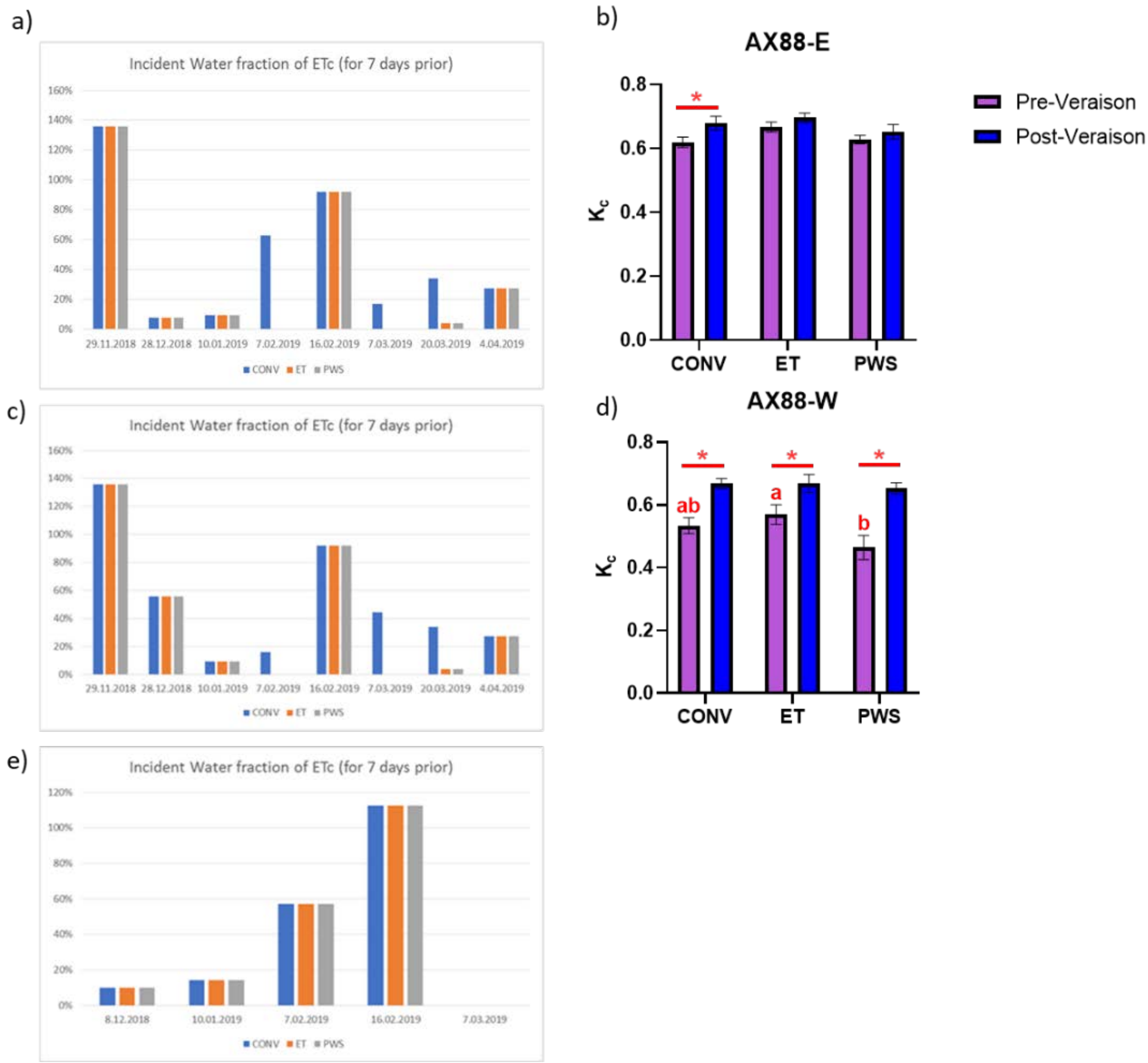

Figure 27: Seasonal Crop Evapotranspiration (ETc) (a, c, e) and crop factor (Kc) (b, d) in CAS (a-d) and SHI (e) in response to different irrigation treatments. Values are means ± SEM of 8 biological replicates. Statistical analysis was conducted using two-way ANOVA. Asterisks indicate statistically significant differences (P<0.05) between pre- and post-veraison stages. Lowercase letters indicate statistically significant differences (P<0.05) between irrigation treatments at pre-veraison stage.

2019/2020 season

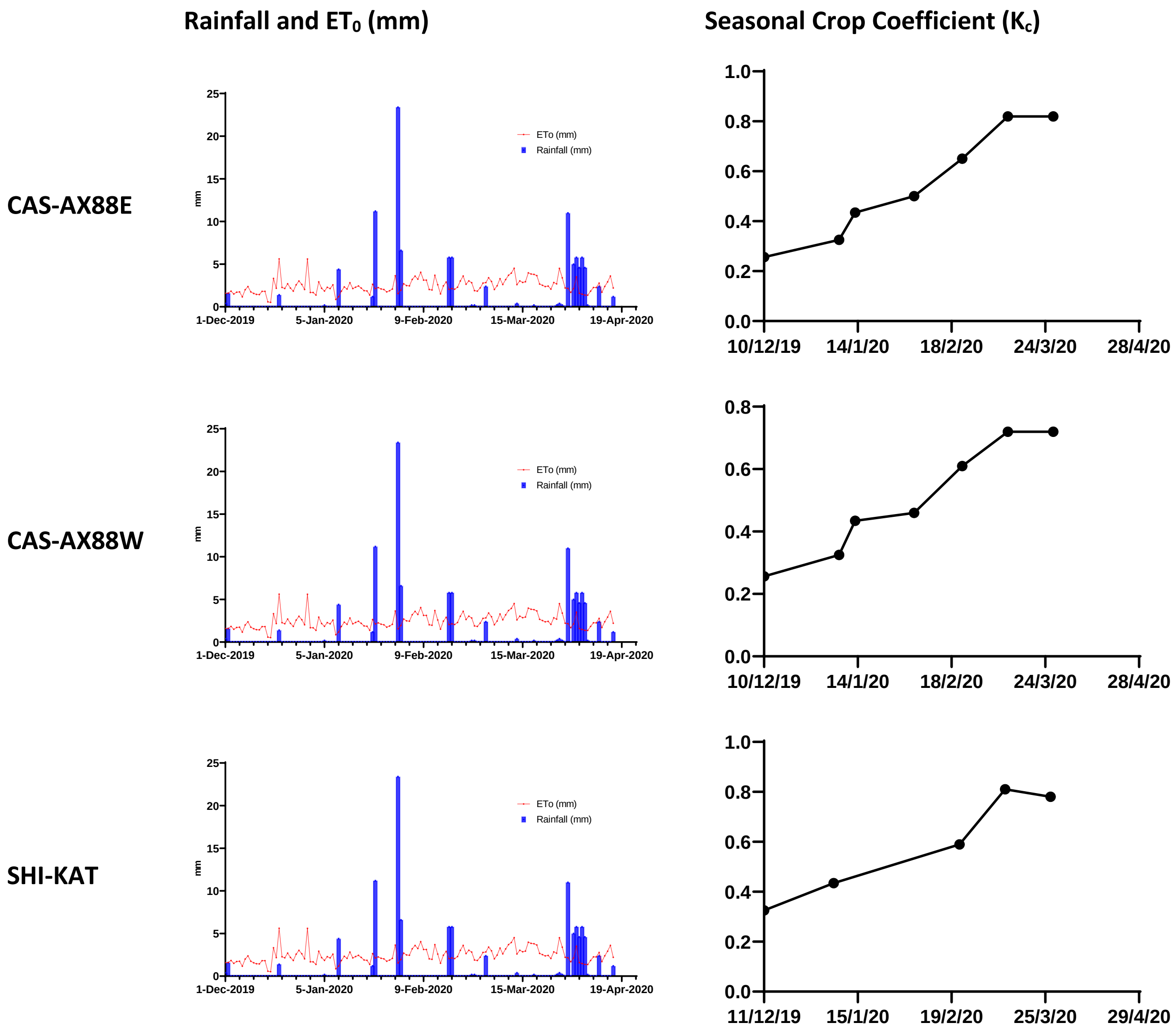

Figure 28: Seasonal Crop Evapotranspiration (ETc) (a, c, e) and crop factor (Kc) (b, d) in CAS and SHI in response to different irrigation treatments.

2020/2021 season

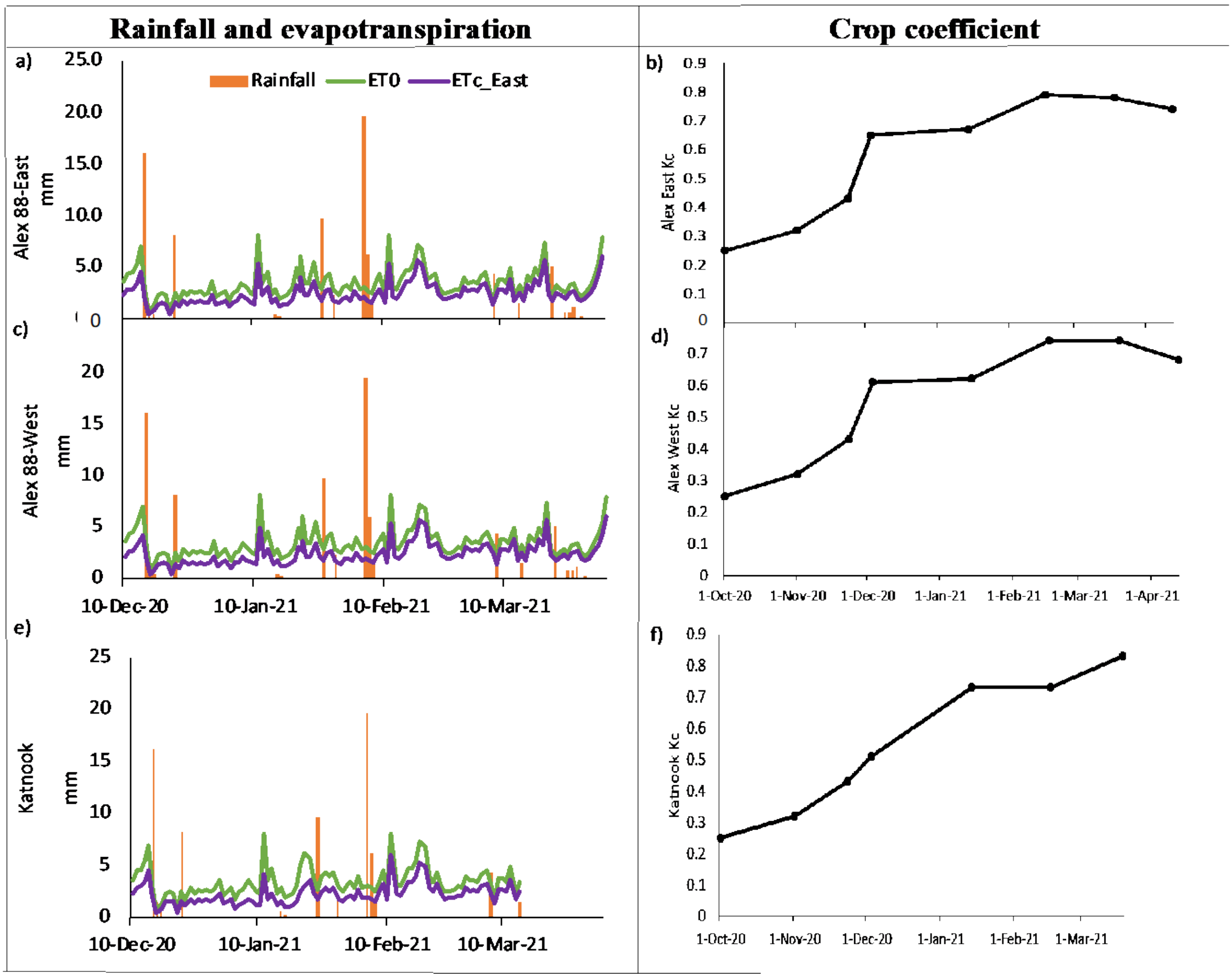

Figure 29: Seasonal Crop Evapotranspiration (ETc) (a, c, e) and crop factor (Kc) (b, d) in CAS and SHI in response to different irrigation treatments.

2021/2022 season

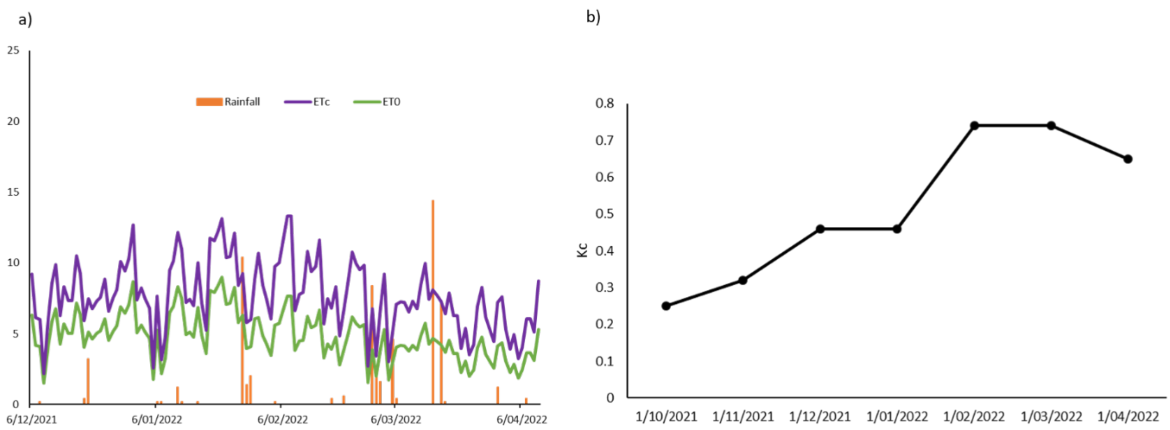

Figure 30: Seasonal Crop Evapotranspiration (ETc) (a, c, e) and crop factor (Kc) (b, d) in SHI in response to different irrigation treatments.

5.2.4 Seasonal plant water status and stomatal conductance

In both Alex88-East and Alex88-west, plant water status did not significantly change at the pre-verasion stage, across three seasons from 2018 to 2021, except in 2020/2021 season where PWS and SWS vines showed significantly lower Ψ_{stem} relative to ET vines. However, after veraison, ET and PWS vines exhibited significantly lower Ψ_{stem} relative to CONV in the 2018/2019 season. Similar reduction of Ψ_{stem} was also observed in ET, PWS and SWS vines in the 2020/2021 season in Alex88-east. In the same season, in Alex88-west, Ψ_{stem} in ET and SWS was also significantly lower relative to CONV. In the 2019/2020 season, no statistically significant differences in Ψ_{stem} was detected between irrigation treatments post-veraison in SHI. In the 2020/2021 season, Ψ_{stem} was similar between CONV, PWS and SWS, whereas ET vines displayed significantly lower Ψ_{stem} relative to the Prodigy vines. Interestingly, in the 2021/2022 season, pre-veraison Ψ_{stem} did not change in response to sensor-driven irrigation treatments relative to CONV. However, post-veraison Ψ_{stem} was significantly higher in CONV+ and lower in PWS1, PWS2 and SWS compared to CONV.

In the 2018/2019 growing season, PWS-based irrigation scheduling did not change pre-veraison stomatal conductance (g_s) in Alex88-East, however, it was significantly increased in response to ET treatment. After veraison, g_s was markedly declined in both ET and PWS vines relative to CONV. Pre-veraison g_s remained unchanged in all the treated vines in Alex88-east and Alex88-west across the rest of the seasons. However, after veraison, statistically significant variations were observed in g_s in response to different irrigation treatments. In both 2019/2020 and 2020/2021 seasons, post-veraison g_s remained unchanged in response to different irrigation scheduling in Katnook. However, the Prodigy vines displayed significantly lower g_s relative to SHI in Katnook in the 2019/2020 growing season. In the 2021/2022 season, CONV+ and Prodigy vines exhibited significantly higher pre-veraison g_s relative to other treatments. Among all the irrigation treatments, only PWS1 caused significant reduction in g_s relative to CONV (Figure 31, 32, 33 and 34).

2018/2019 season

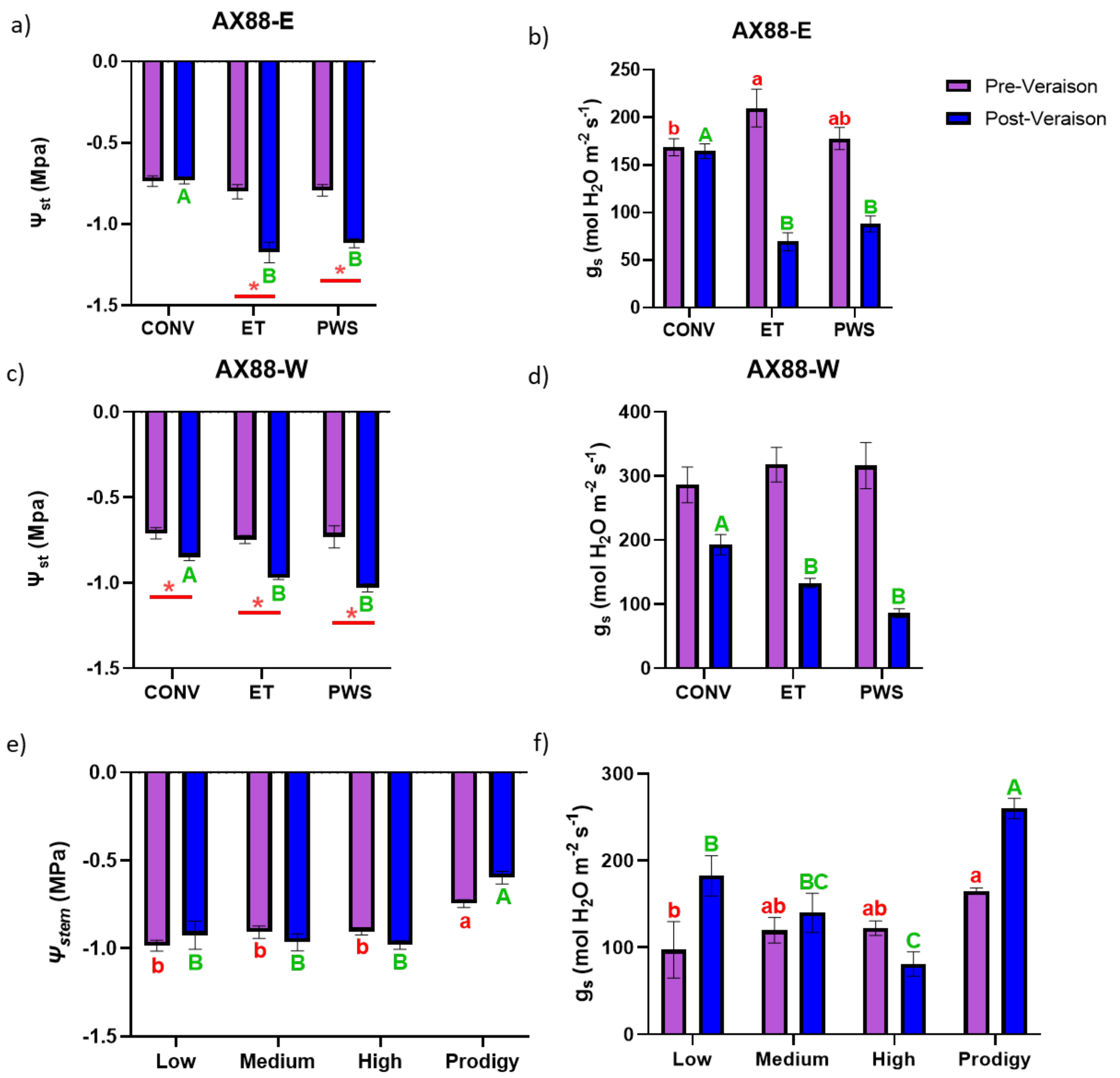

Figure 31: Changes in Mid-day stem water potential (Ψ_{stem}) (a, c, e) and stomatal conductance (g_s) (b, d, f) in CAS and SHI in response to different irrigation treatments. Values are means ± SEM of 4 biological replicates. Statistical analysis was conducted using two-way ANOVA. Asterisks indicate statistically significant differences (P<0.05) between pre- and post-veraison stages. Lowercase letters indicate statistically significant differences (P<0.05) between irrigation treatments at pre-veraison stage. Uppercase letters indicate statistically significant differences (P<0.05) between irrigation treatments at post-veraison stage.

2019/2020 season

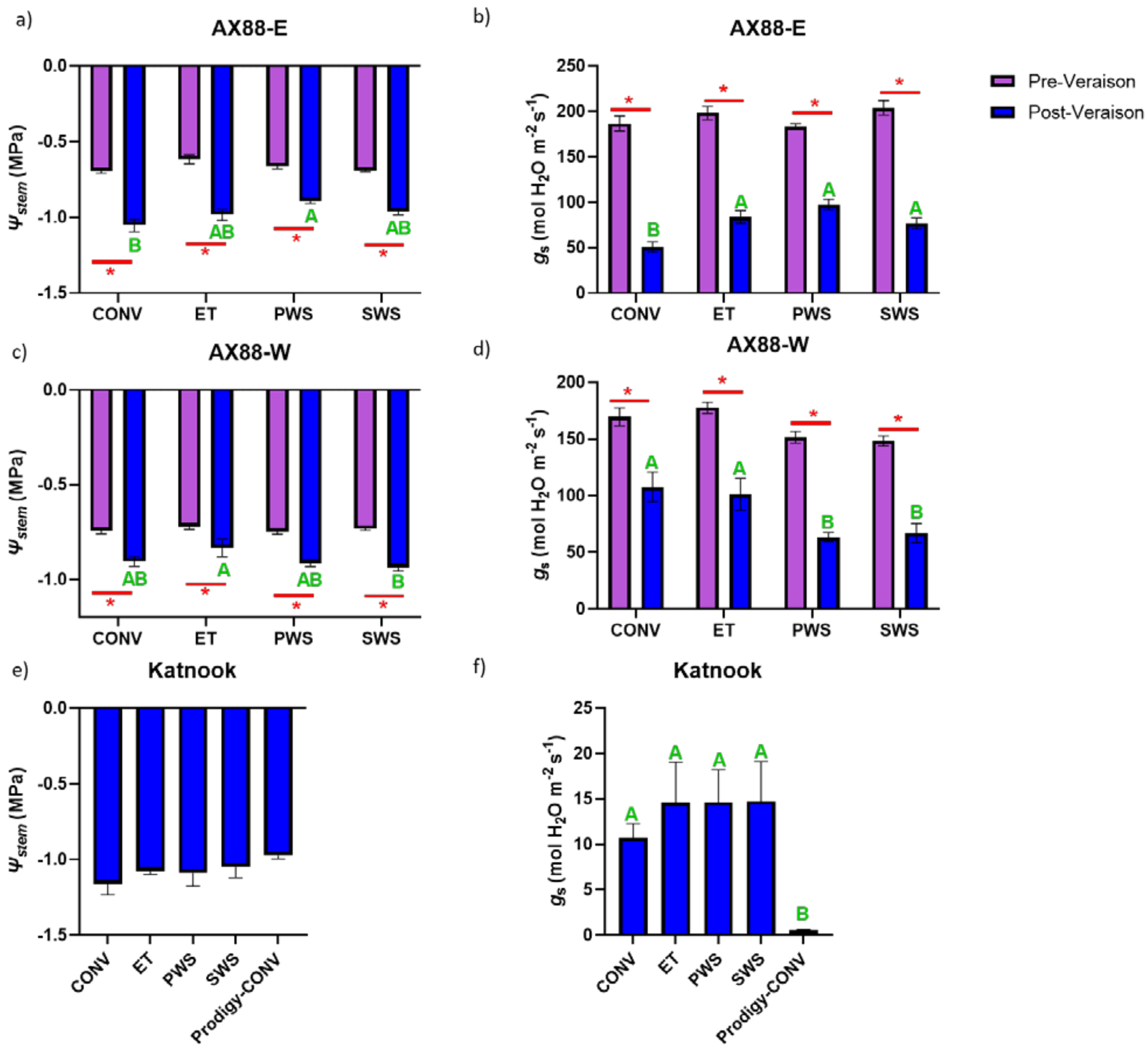

Figure 32: Changes in Mid-day stem water potential (Ψ_{stem}) (a, c, e) and stomatal conductance (g_s) (b, d, f) in CAS and SHI in response to different irrigation treatments. Values are means ± SEM of 8 biological replicates. Statistical analysis was conducted using two-way ANOVA. Asterisks indicate statistically significant differences (P<0.05) between pre- and post-veraison stages. Lowercase letters indicate statistically significant differences (P<0.05) between irrigation treatments at pre-veraison stage. Uppercase letters indicate statistically significant differences (P<0.05) between irrigation treatments at post-veraison stage.

2020/2021 season

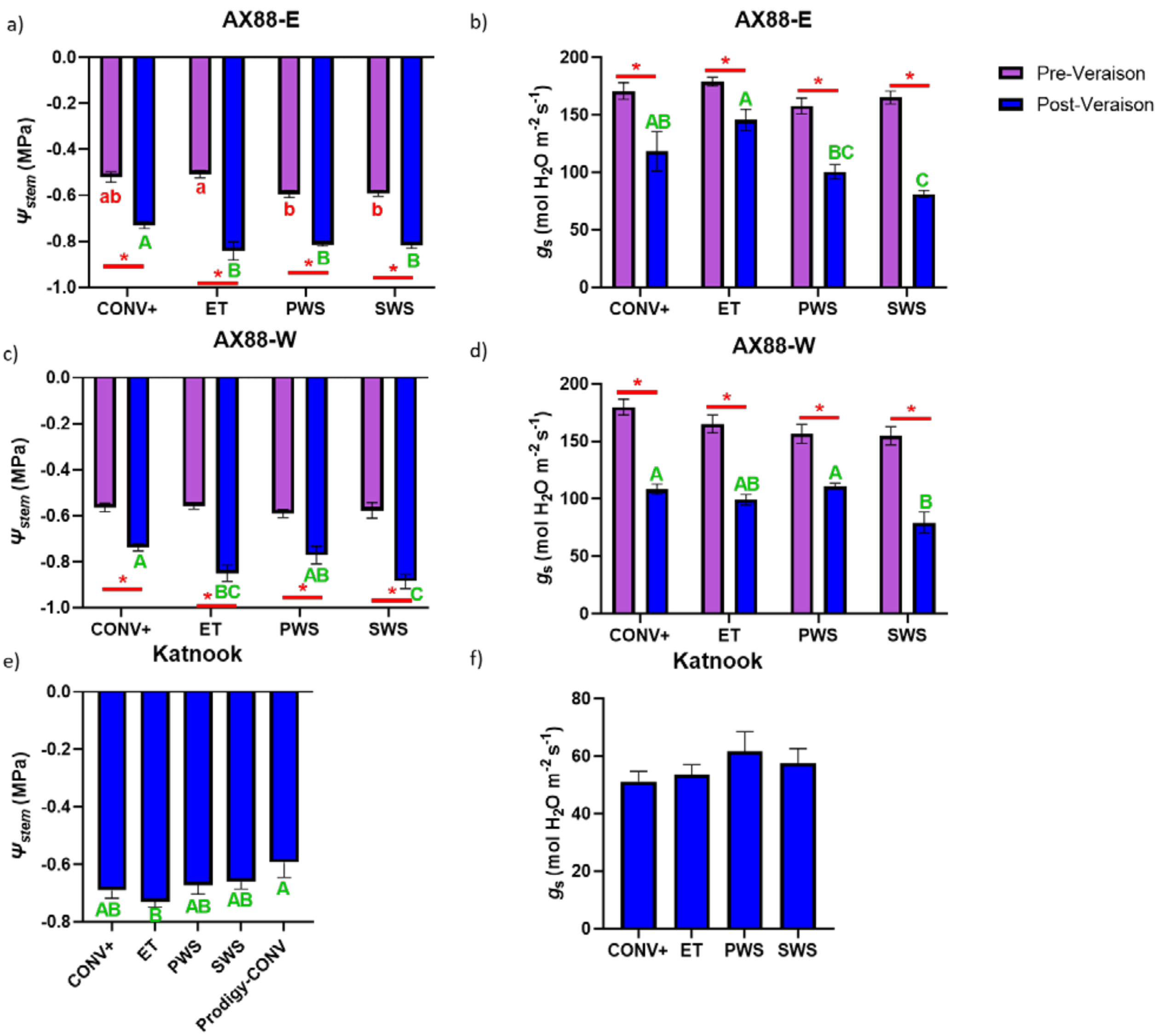

Figure 33: Changes in Mid-day stem water potential (Ψ_{stem}) (a, c, e) and stomatal conductance (g_s) (b, d, f) in CAS and SHI in response to different irrigation treatments. Values are means ± SEM of 8 biological replicates. Statistical analysis was conducted using two-way ANOVA. Asterisks indicate statistically significant differences (P<0.05) between pre- and post-veraison stages. Lowercase letters indicate statistically significant differences (P<0.05) between irrigation treatments at pre-veraison stage. Uppercase letters indicate statistically significant differences (P<0.05) between irrigation treatments at post-veraison stage.

2021/2022 season

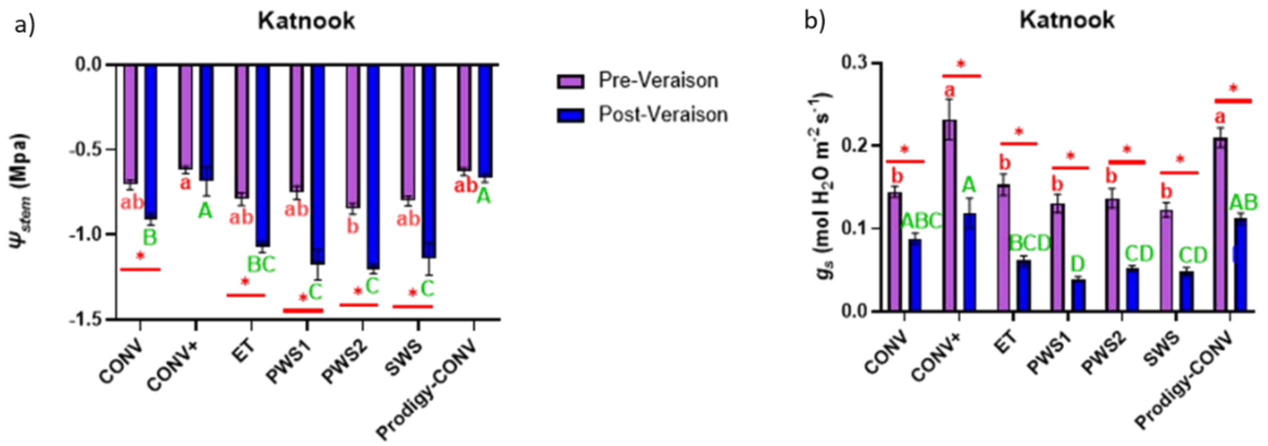

Figure 34: Variations in mid-day stem water potential (Ψ_{stem}) and stomatal conductance (g_s) in response to different irrigation treatments. Values are the means ± SEM of 8 biological replicates. Asterisk represents the statistically significant differences ($p<0.05$) between pre- and post-veraison stages. The lowercase letters on the graph represents the statistically significant differences between irrigation treatments at pre-veraison stage. The uppercase letters represent the statistically significant differences between irrigation treatments at post-veraison stage.

5.2.5 Seasonal net photosynthesis and intrinsic water use efficiency

In both Alex88-East and Alex88-West, pre-veraison A_N did not change in response to different irrigation treatments across four seasons. However, sensor-drive irrigation scheduling considerably changed post-veraison A_N over different season. For instance, in the 2018/2019 season, CAS vine in the Alex88-east, significantly reduced post-veraison A_N in response to both ET and PWS treatments. However, in the Alex88-west, significantly lower post-veraison A_N was observed only with PWs vines. In the 2019/2020 season, post-veraison A_N was significantly higher in Alex88-east ET, PWS and SWS vines relative to CONV vines. However, amoung Alex88-west vines, statistically significant differences were observed only between PWS, SWS and CONV. Intriguingly, in the 2020/2021 season, only SWS vines in both Alex88-east and Alex88-west vineyards exhibited significantly lower A_N relative to other irrigation treatments.

In 2019/2020 and 2020/2021 seasons, no statistically significant differences were observed in post-veraison A_N between different irrigation treatments of SHI vines. However, in the 2019/2020 season, prodigy vines displayed significantly lower post-veraison A_N relative to all the other treated SHI vines in the Katnook vineyard. In contrast, in the 2021/2022 growing season, ET, PWS1, PWS2 and SWS vines exhibited significantly lower post-veraison A_N relative to both CONV and CONV+. However, their pre-veraison A_N did not change dramatically in response to different irrigation scheduling.

Pre-veraison WUE_i remained unchanged in CAS across all seasons in both Alex88-east and Alex88-west. In the 2018/2019 season, post-veraison WUE_i also did not change in the Alex88-east vineyard. However, in both 2018/2019 and 2019/2020 seasons, Alex88-west, post-veraison WUE_i was significantly higher in PWS vines relative to CONV vines. In contrast, in 2019/2020 season, Alex88-east PWS vines displayed dramatic reduction of WUE_i relative to CONV.

In both 2019/2020 and 2020/2021 seasons, different irrigation scheduling strategies did not affect post-veraison WUE_i in SHI vines in Katnook. However, in the 2019/2020 season, all SHI vines displayed significantly higher WUE_i relative to prodigy vines. Interestingly, during 2021/2022 season, both PWS1 and PWS2 treatments significantly up-regulated post-veraison WUE_i relative to all the other irrigation treatments (Figure 35, 36, 37 and 38).

2018/2019 season

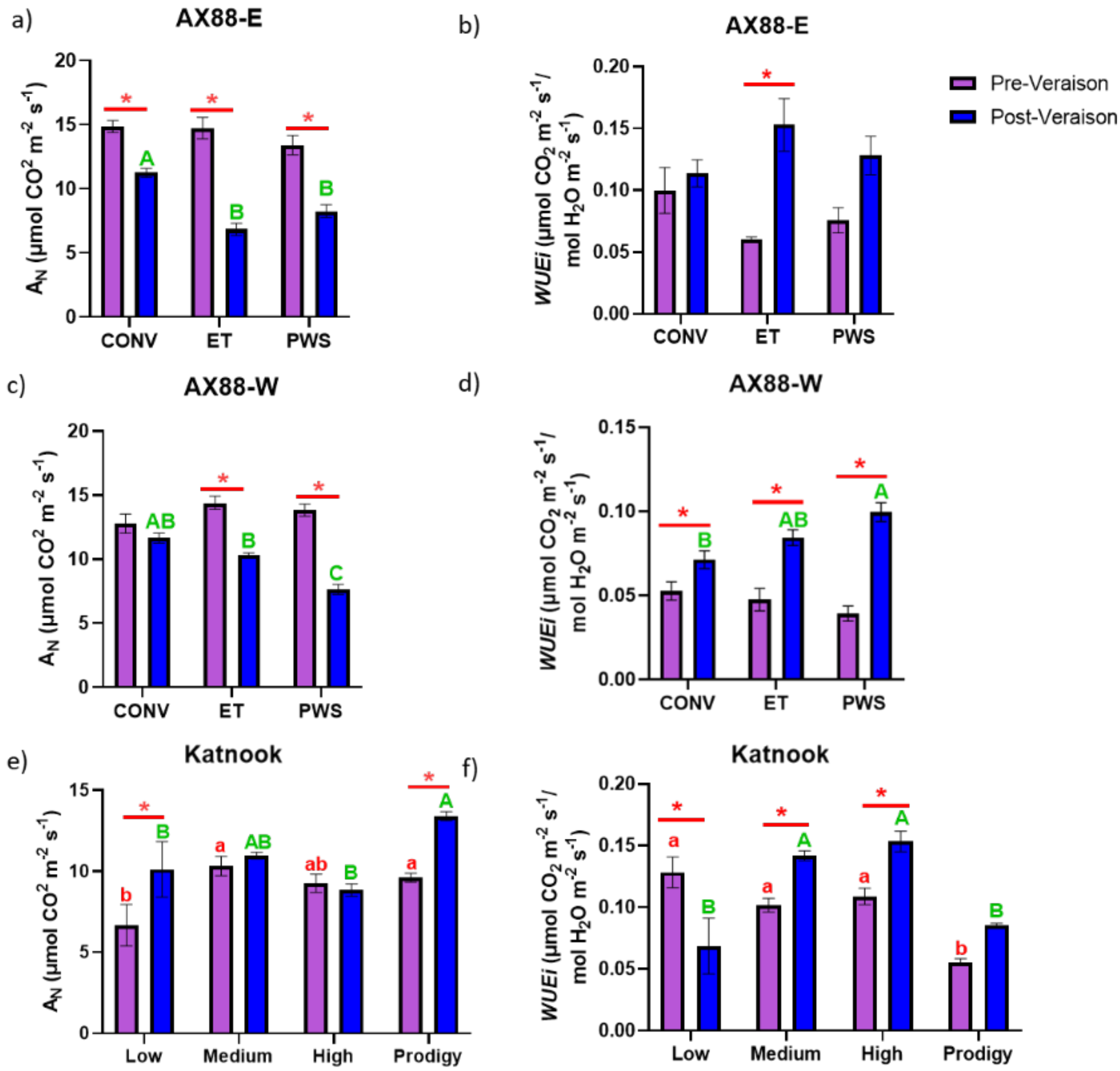

Figure 35: Variations in net carbon assimilation (A_N) (a, c, e) and intrinsic water use efficiency (WUE_i) (b, d, f) in CAS and SHI in response to different irrigation treatments. Values are means ± SEM of 4 biological replicates. Statistical analysis was conducted using two-way ANOVA. Asterisks indicate statistically significant differences (P<0.05) between pre- and post-veraison stages. Lowercase letters indicate statistically significant differences (P<0.05) between irrigation treatments at pre-veraison stage. Uppercase letters indicate statistically significant differences (P<0.05) between irrigation treatments at post-veraison stage.

2019/2020 season

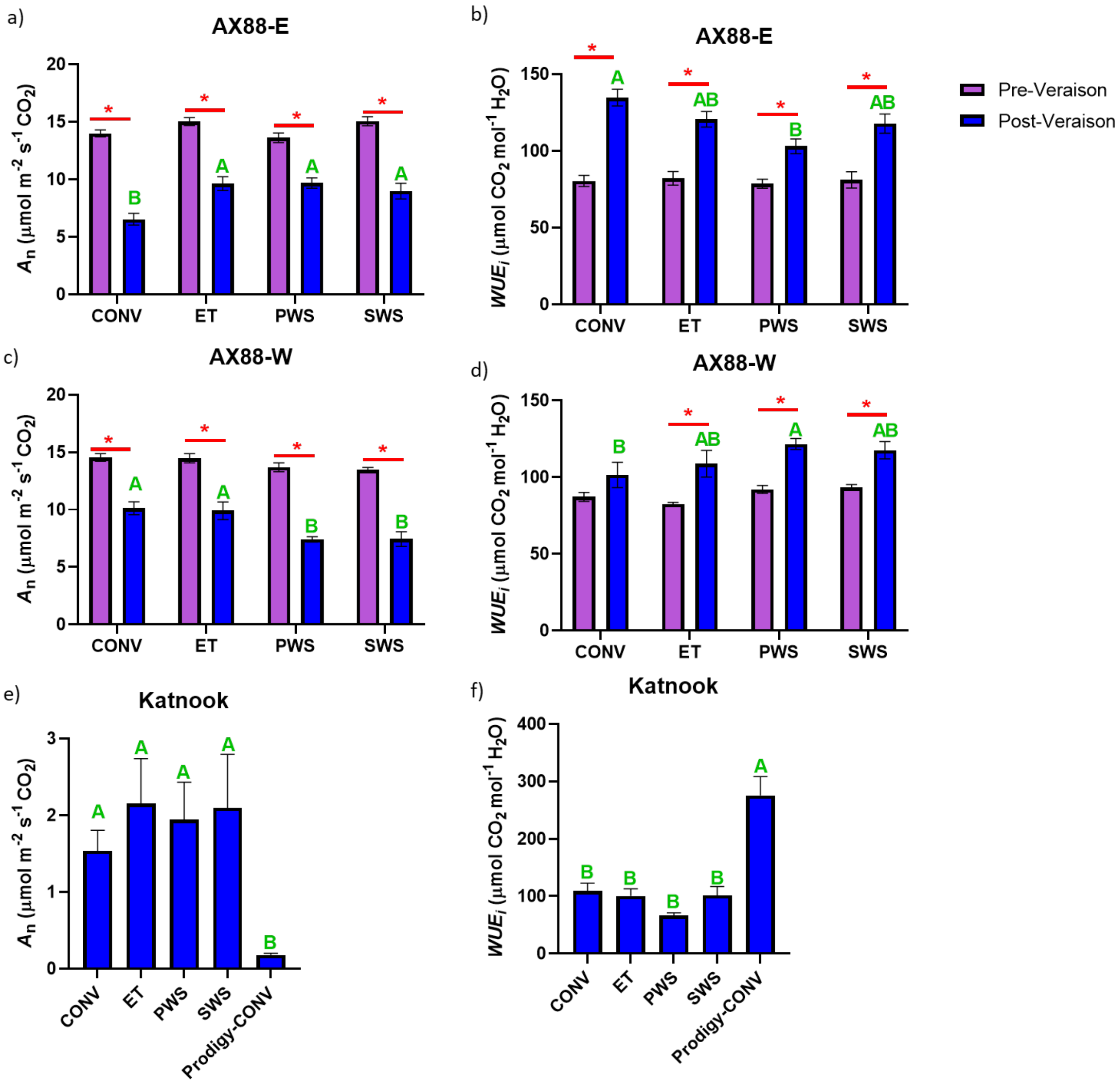

Figure 36: Variations in net carbon assimilation (A_N) (a, c, e) and intrinsic water use efficiency (WUE_i) (b, d, f) in CAS and SHI in response to different irrigation treatments. Values are means ± SEM of 4 biological replicates. Statistical analysis was conducted using two-way ANOVA. Asterisks indicate statistically significant differences (P<0.05) between pre- and post-veraison stages. Lowercase letters indicate statistically significant differences (P<0.05) between irrigation treatments at pre-veraison stage. Uppercase letters indicate statistically significant differences (P<0.05) between irrigation treatments at post-veraison stage.

2020/2021 season

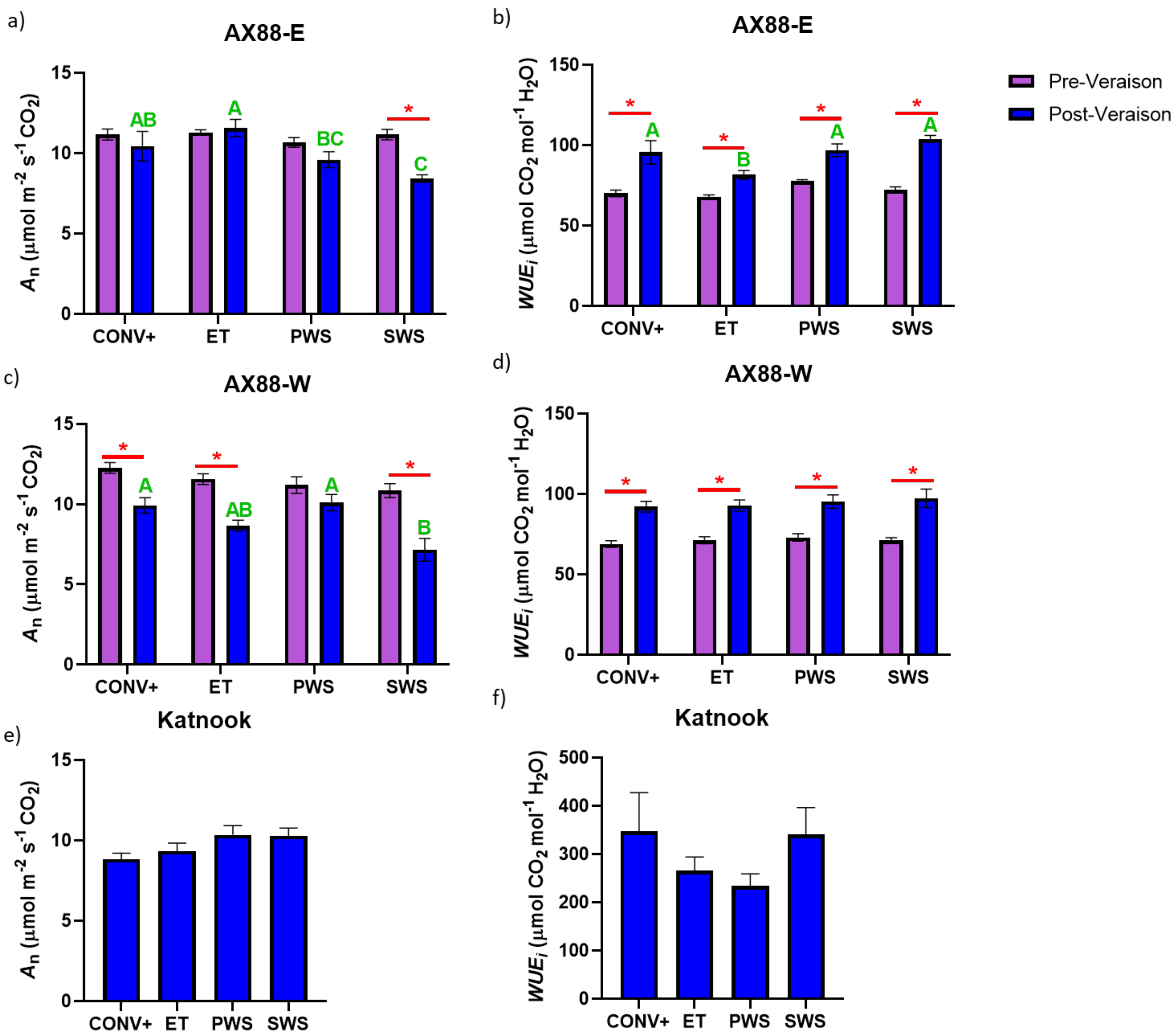

Figure 37: Variations in net carbon assimilation (A_N) (a, c, e) and intrinsic water use efficiency (WUE_i) (b, d, f) in CAS and SHI in response to different irrigation treatments. Values are means ± SEM of 4 biological replicates. Statistical analysis was conducted using two-way ANOVA. Asterisks indicate statistically significant differences (P<0.05) between pre- and post-veraison stages. Lowercase letters indicate statistically significant differences (P<0.05) between irrigation treatments at pre-veraison stage. Uppercase letters indicate statistically significant differences (P<0.05) between irrigation treatments at post-veraison stage.

2021/2022 season

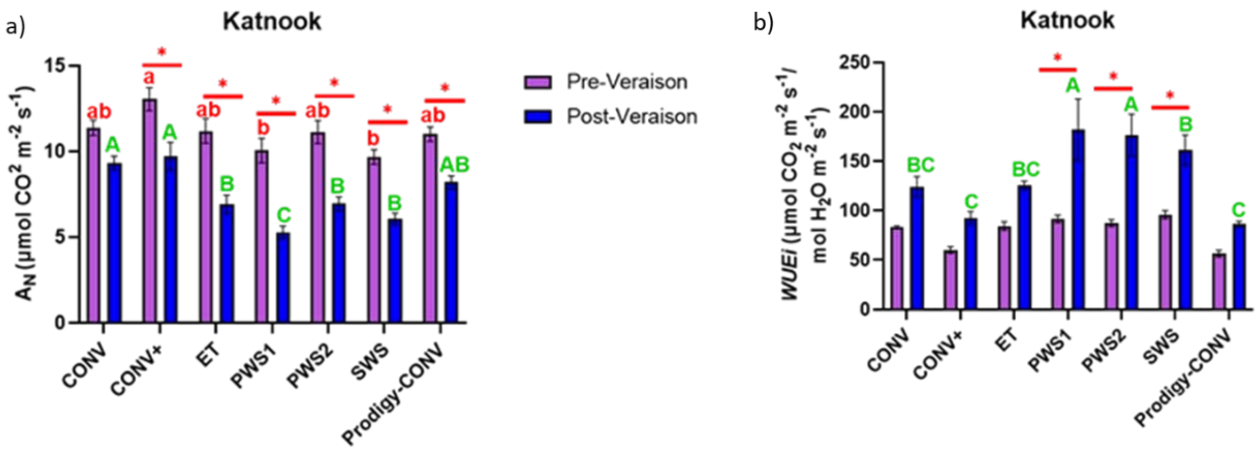

Figure 38: The photosynthetic rate ($A_{N;}$ a) and intrinsic water use efficiency (WUE_i, b) of SHI under different irrigation treatments. Values are the means ± SEM of 8 biological replicates. Asterisk represents the statistically significant differences (p<0.05) between pre- and post-veraison stages. The uppercase letters represent the statistically significant differences between irrigation treatments at post-veraison stage.

5.3 Continuous sensor-based data

Soil moisture

Volumetric water content of the soil, rainfall and irrigation applied during the 2019/2020 and 2020/2021 seasons are shown in the figure below.

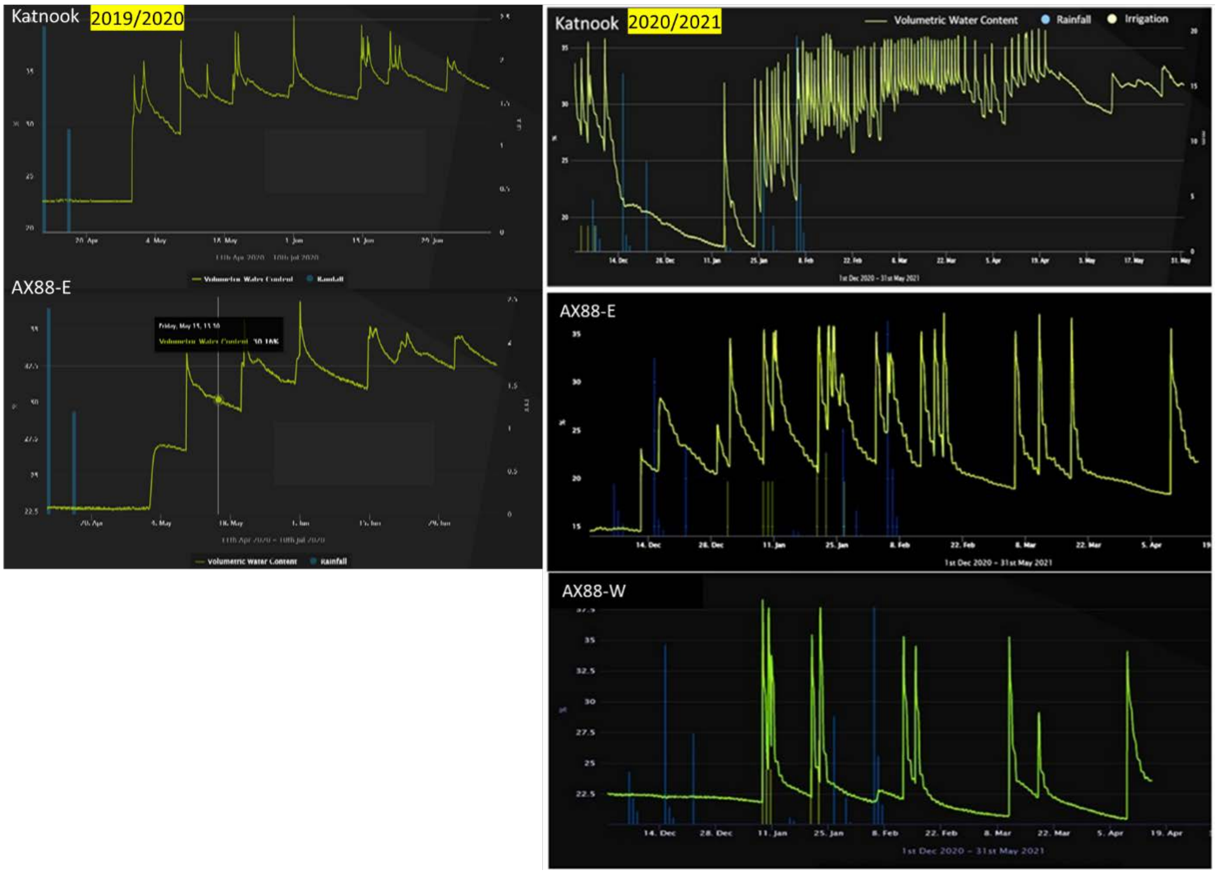

Figure 39: Sample soil moisture data from Katnook, Alex88E and Alex88W during 2019/2020 and 2020/2021 seasons on the GreenBrain dashboard

Soil moisture levels in both vineyards were maintained between 22% (pre-irrigation) and 35% (post-irrigation), where the lower end of the range represented an approx. 30% reduction in historical seasonal soil moisture of the AX88 block. Due to the similarity in soil type between the CAS and SHI blocks, the same threshold of 22% VWC was applied to both as the minimum VWC to trigger an irrigation, done on a weekly basis. In AX88 (CAS), approx. 4 hours per week of irrigation were applied during the peak summer period starting in late-December through to harvest around early- to mid-April. This time equated to approx 21 L/vine/week or ~5 mm/week. In SHI, during the same peak period, 3 weekly irrigations of 3 h each were applied for a total of 9 h of irrigation. This translated to a water application of 7.2 mm/week or ~35 L/vine/week. The SHI irrigation season would typically commence earlier than the CAS season owing to differences in phenology, production targets (yield vs quality), and vine size and age.

Vine Water Index (VWI)

Transp-IR thermal sensors were used to continuously measure canopy temperature, and ambient temperature and relative humidity to calculate a daily index of plant water stress termed 'Vine Water Index' (VWI). This index utilises several timepoints of the day to determine the relevant values for the VWI number that vary based on environmental conditions (e.g. hot vs cool day), cultivar isohydricity, and soil moisture. A snapshot of the Transp-IR dashboard is shown in the figure below.

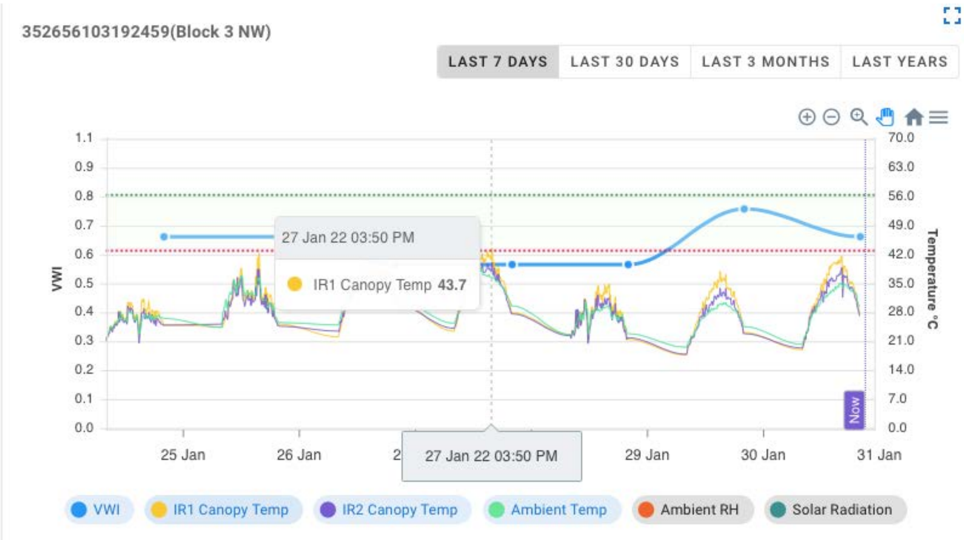

Figure 39: Transp-IR dashboard during the 2020-21 season in Shiraz grapevines showing the daily VWI value, and 10-min data of canopy temperatures, ambient temperature, and relative humidity. The dashboard also provides an option to visualise incident solar radiation.

A key benefit of using the Transp-IR solution is the provision of an 'optimum' VWI range, indicated on the dashboard as a horizontal green band. This region of VWI values corresponds to a stomatal conductance (g_s) value that in turn corresponds to 80-85% of the maximum net photosynthesis (P_n) of the leaves thereby achieving high water use efficiencies. The optimum range and VWI values vary per crop species and cultivar. This strategy was used to schedule irrigation in the PWS or PWS1 treatment.

Trunk Water Potential (Ψ_{trunk})

Microtensiometers were used to continuously measure trunk water potential in CAS and SHI during the 2020/2021, shown in the figure below (sub-figure (c)).

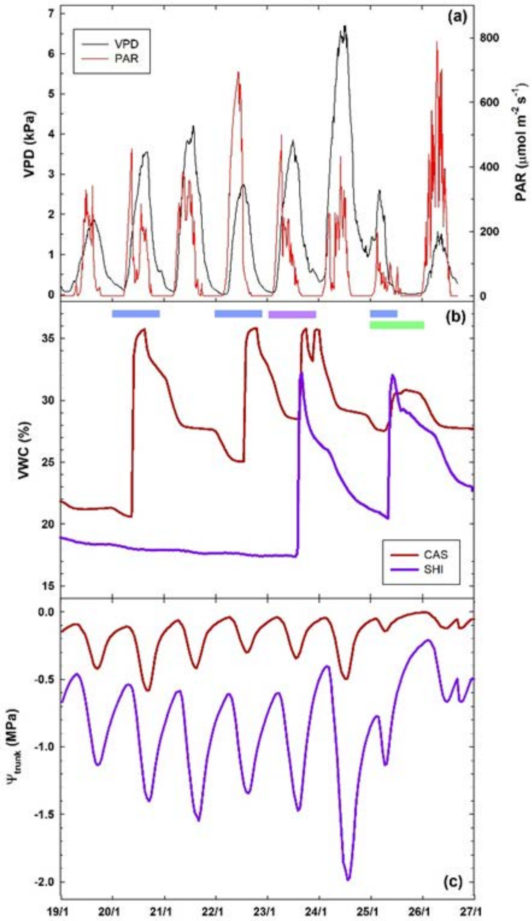

Figure 40: Trunk water potential of CAS and SHI during the 2020-21 season (c) in response to VPD (a) and volumetric water content (b)

Due to the nature of their continuous measurements of plant (trunk) water potential, microtensiometers can be used to effectively measure both soil moisture – through the highest Ψ_{trunk} value at pre-dawn – as well as vine water status at maximum transpiration rate – the lowest value of Ψ_{trunk} on a diurnal basis. As seen above and reported in detail in Pagay (2022), Ψ_{trunk} corresponded to both soil moisture availability (VWC) as well as environmental demand (VPD). Higher VPD days and/or low soil moisture tended to decrease Ψ_{trunk} and vice-versa. It should be noted that use of Ψ_{trunk} for irrigation scheduling needs to develop new thresholds for this metric rather than using the values reported in the literature for stem or leaf water potentials.

5.4 Remotely-sensed canopy performance

High resolution remote sensing using unmanned aerial vehicles (UAVs) allowed for the capture of sub-vine level spectral reflectance data over the growing season. These datasets were used, in conjunction with ground-based physiological measurements, to model the same physiological measurements across space and time. We predicted select physiological parameters at key phenological stages; maps were generated for the pre-harvest period as an example of what predictions are possible with these models.

5.4.1 Correlation analysis

Initial steps in the modelling involved assessing which of the spectral bands were highly correlated with the ground-based physiological data. Select spectral bands (horizontal axis of matrix below) and physiological indicators (left vertical column) for CAS indicate high degree of correlation between canopy leaf area as observed from the UAV and soil and vine water status, and canopy conductance. The thermal wavelengths were also significantly correlated with the same parameters, as might be expected.

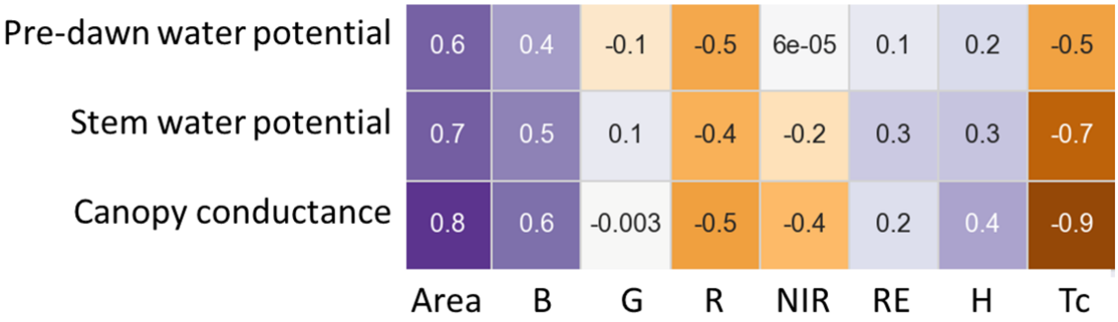

Figure 7: Correlation analysis of soil and vine water status metrics with UAV-derived thermal, structural, and spectral responses of CAS grapevines.

5.4.2 High resolution prediction of soil and vine water status

Cabernet Sauvignon

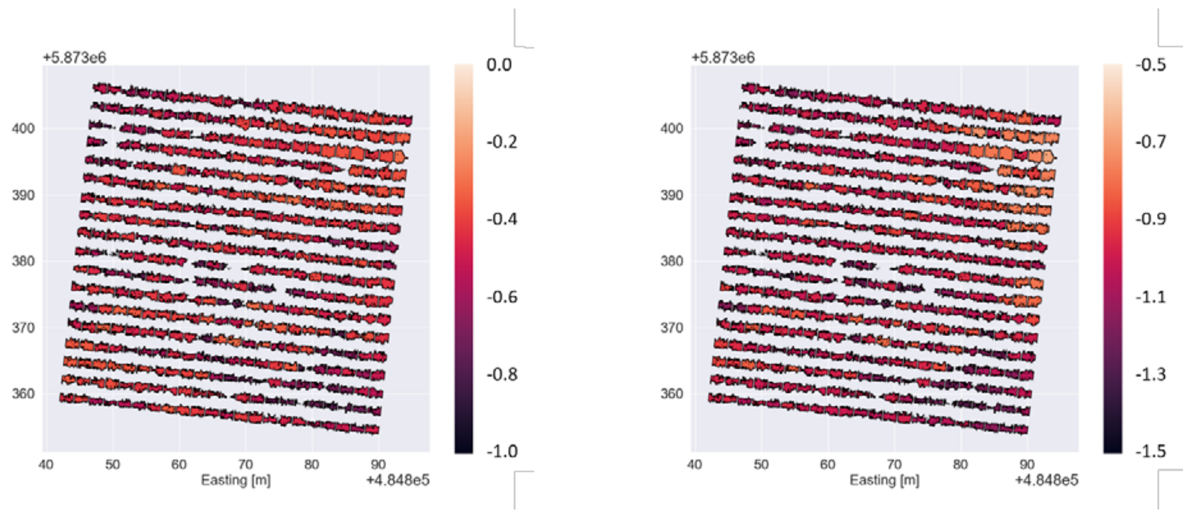

(a) **(b)**

Figure 42: Spatial and temporal prediction of pre-dawn leaf water potential, an indicator of soil moisture (a), and stem water potential at midday (b). Single vine level data is presented for the entire mapping area of the AX88E (CAS) vineyard beyond the sentinel vines at EL-37 (pre-harvest).

Using a model developed through statistical and machine learning methods with high resolution multispectral and thermal imagery from a low-altitude UAV, we were able to obtain predictions of soil and vine water status at the single vine level (Fig. 42). This method is an alternative to spatial interpolation methods such as kriging that are based on sparse spatial data. The variations in soil moisture across the AX88E block (Fig 42a) were captured with low MAE (Table 9), particularly with the random forest model, which is an ensemble of models based on decision trees. From the map, it was obvious that the south end of the block had lower soil moisture availability, which translated into higher vine water stress (Fig. 42b). This knowledge can help growers implement precision irrigation whereby that (more stressed) section of the block is zoned via a valve, and irrigated at a higher level or rate.

Table 9: Accuracy of various linear and non-linear statistical models and machine learning models for the prediction of various CAS vine components at EL-37 (pre-harvest). RMSE = root mean square error; R^2 = correlation coefficient; MAE = mean absolute error. Models: Linear, GLM = Generalised Linear Model, RF = Random Forest.

	Pre-dawn leaf water potential (Ψ_{pd}, MPa)			**Midday stem water potential (Ψ_s, MPa)**		
Model	RMSE	R^2	MAE	RMSE	R^2	MAE
Linear	0.150	0.371	0.127	0.265	0.293	0.181
GLM	0.138	0.505	0.102	0.130	0.726	0.108
RF	0.096	0.068	0.068	0.117	0.087	0.087

Shiraz

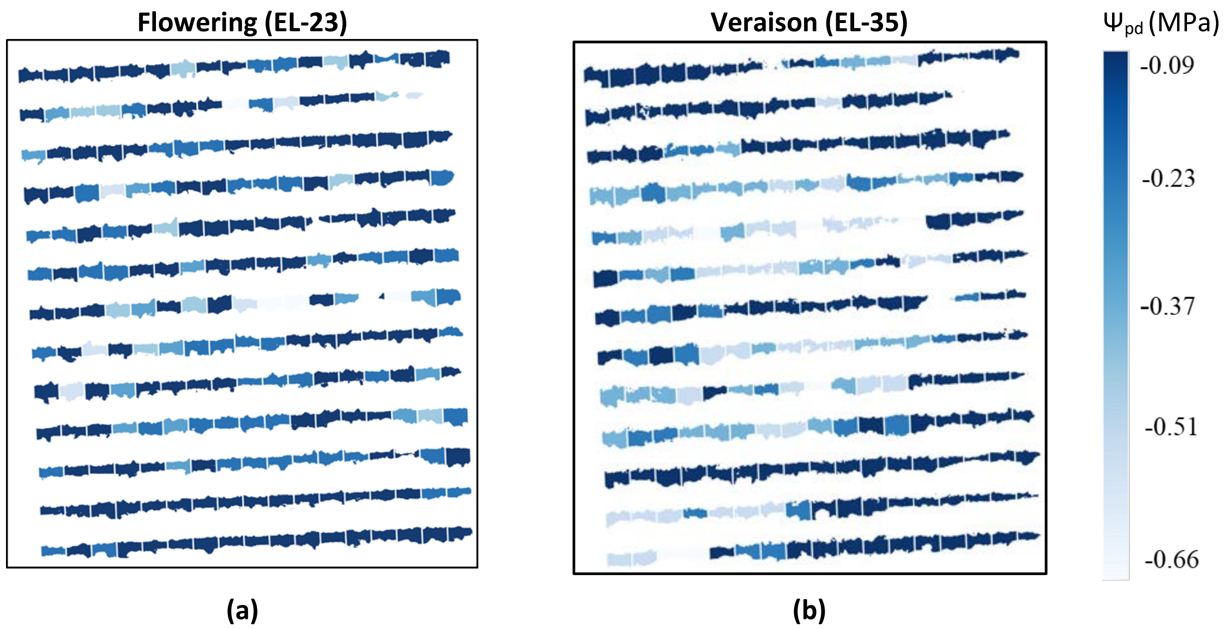

Figure 43: Spatial and temporal prediction of pre-dawn leaf water potential, an indicator of soil moisture. Single vine level data is presented for the entire mapping area of the KAT (SHI) vineyard beyond the sentinel vines at EL-23 (flowering) and EL-35 (véraison).

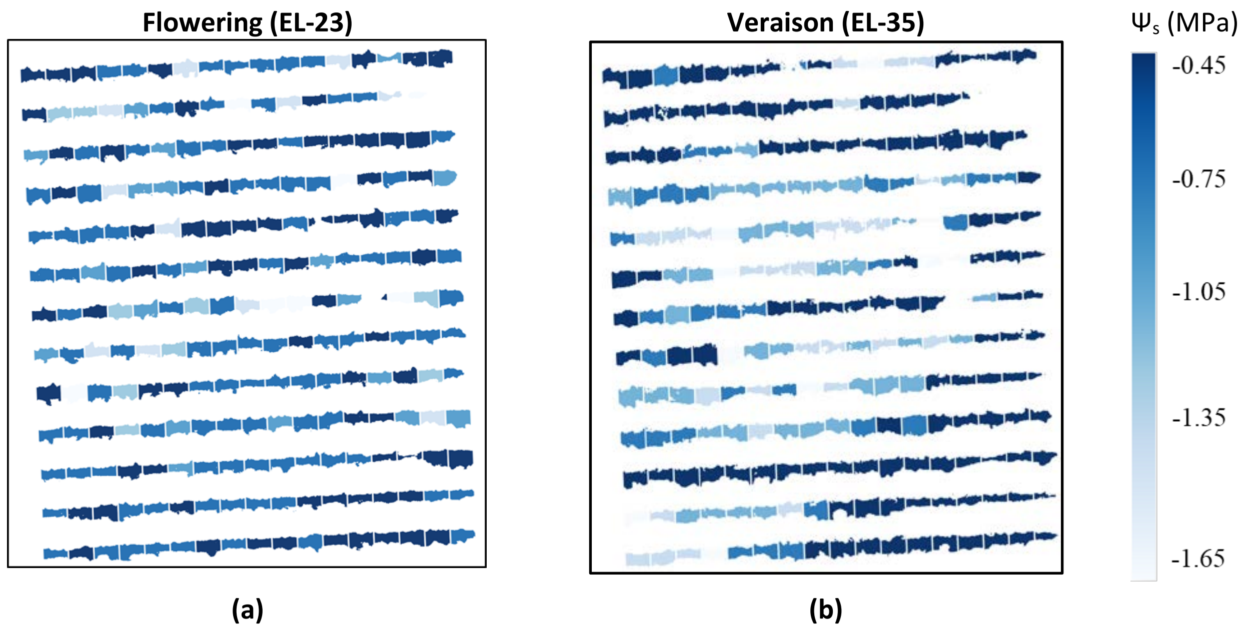

Figure 44: Spatial and temporal prediction of midday stem water potential. Single vine level data is presented for the entire mapping area of the KAT (SHI) vineyard beyond the sentinel vines at EL-23 (flowering) and EL-35 (véraison).

In the Katnook Shiraz block, both predawn leaf and midday stem water potentials were modelled to provide a spatial (single vine resolution) and temporal (two important phenological stages, flowering and véraison) prediction of soil and vine water status, respectively. Predawn leaf water potentials (Ψ_{pd}), which reflect the available soil moisture to the vines, ranged from -0.1 to -0.4 MPa at flowering, and -0.1 to -0.7 MPa by véraison (Fig. 43). The extent of spatial variation of soil moisture across the block was not significant as indicated by the narrow range of Ψ_{pd} values. By véraison, a significantly higher proportion of vines had access to less soil moisture, as expected, due to deficit irrigation and greater vine size that use more water.

With regards to midday stem water potentials (Ψ_s), reflecting the vine's water status, values ranged from -0.5 to -1.3 MPa at flowering, and -0.5 to -1.7 MPa by véraison. There was clearly a central section of the block that had lower vine water status (more water stress); this region would be a candidate for increased irrigation through zoning. The central section also had lower Ψ_{pd} values at véraison, perhaps due to shallower soils and smaller rootzones.

5.4.3 High resolution prediction of vine crop coefficient

Cabernet Sauvignon

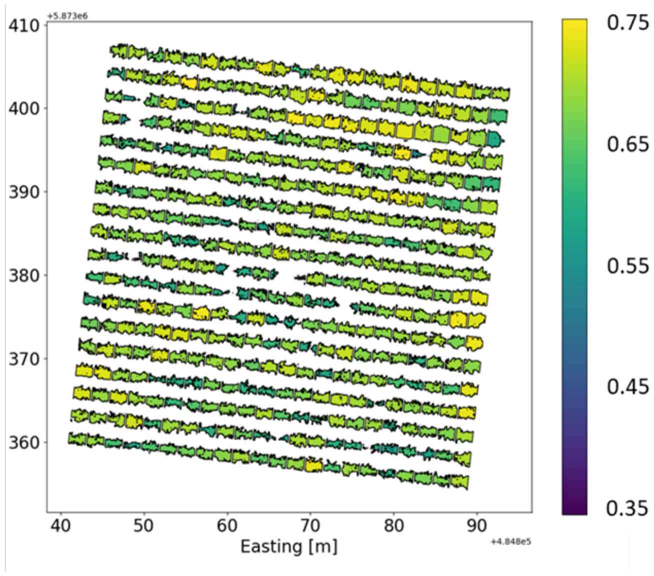

Figure 44: Spatial prediction of crop coefficient (K_c) of AX88E (CAS) at pre-harvest. Single vine level data is presented for the entire mapping area of the vineyard beyond the sentinel vines.

The crop coefficient (K_c) is an important variable for the calculation of crop evapotranspiration (ET_c) for determining irrigation schedules (i.e. timing and volume of irrigation applications). Here, we predicted the spatial variation in K_c across the AX88E block on a per-vine basis such that precision irrigation could be implemented in the future (Fig. 44). The spatial pattern of K_c appears to be highly variable across the mapped region, with values ranging from 0.4 through 0.75 at the EL-37 stage, which is a large variation in vine size (leaf area) and canopy light interception, both of which drive transpiration and vine water use and consequently determine irrigation rates. Such large variability in the K_c suggests that there may be high underlying variation in the rooting depth of the vines (due to considerable spatial variations in the depth to the impermeable limestone layer), and/or high variations in vine health, e.g. due to trunk diseases, which are common in the region.

Table 10: Accuracy of various linear and non-linear statistical models and machine learning models for the prediction of CAS crop coefficient (K_c) at EL-37 (pre-harvest). RMSE = root mean square error; R^2 = correlation coefficient; MAE = mean absolute error. Models: Linear, GLM = Generalised Linear Model, GAM = Generalised Additive Model, CNN = Convolution Neural Network, RF = Random Forest.

	Crop coefficient (K_c)		
Model	RMSE	R^2	MAE
Linear	0.091	0.295	0.076
GLM	0.074	0.528	0.061
GAM	0.069	0.594	0.055
CNN	0.072	0.619	0.060
RF	0.062	0.675	0.047

The various statistical and machine learning models employed compared quite similarly to one another; the best predictions were obtained with the RF model (lowest RMSE and MAE values, highest R^2). Considering the low values of MAE for all models tested, even the linear model did well in predicting K_c. This allows the use of simple tools and spreadsheets for future prediction of K_c.

A manuscript was published in the journal *Remote Sensing* based on this work on K_c and is attached to this report.

Shiraz

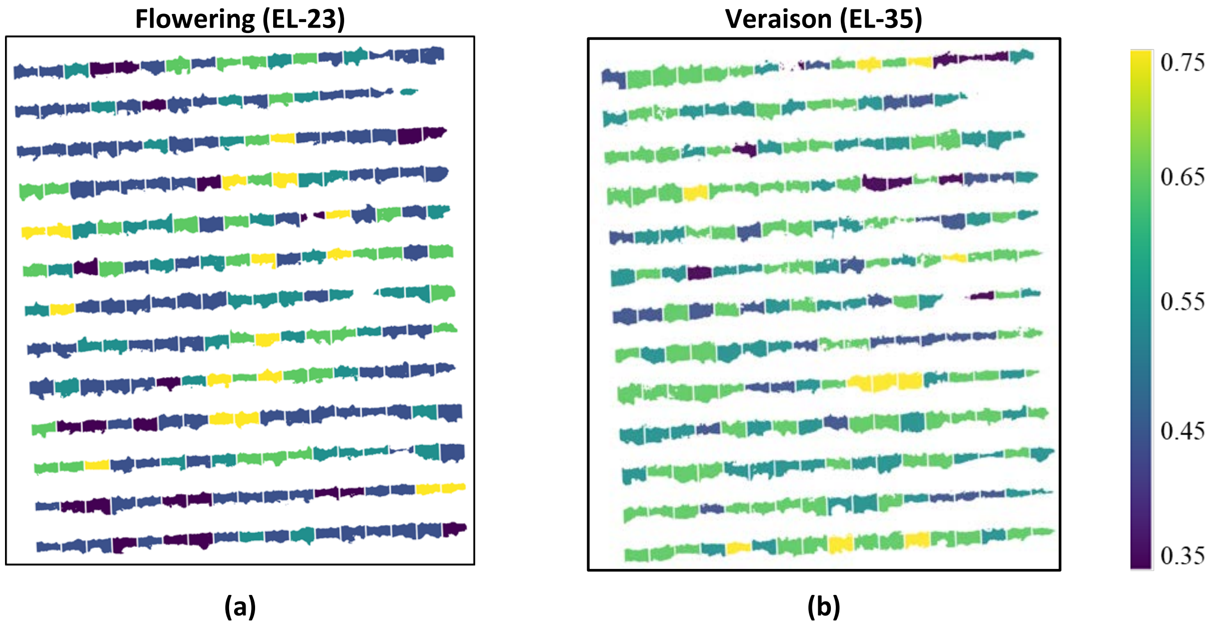

Figure 45: Spatial and temporal prediction of crop coefficient (K_c) for KAT Shiraz grapevines at flowering (a) and véraison (b). Single vine level data is presented for the entire mapping area of the vineyard including and beyond the sentinel vines.

Variations in K_c across the Shiraz block during the early season (flowering, EL-23) ranged from 0.35 to 0.55 with a few vines exceeding 0.7. By véraison, most of the vines had K_c values exceeding 0.6, with only a few vines around 0.75, suggesting that canopies were not overly large in terms of leaf area intercepting light. These single-vine values of K_c allow for the delineation of irrigation zones (if adopting the ET strategy) although the uniformity in this block was relatively high thereby not requiring zoning of irrigation unlike the Alex88 CAS block, which had much higher spatial variation of K_c.

5.4.4 High resolution prediction of canopy gas exchange

Cabernet Sauvignon

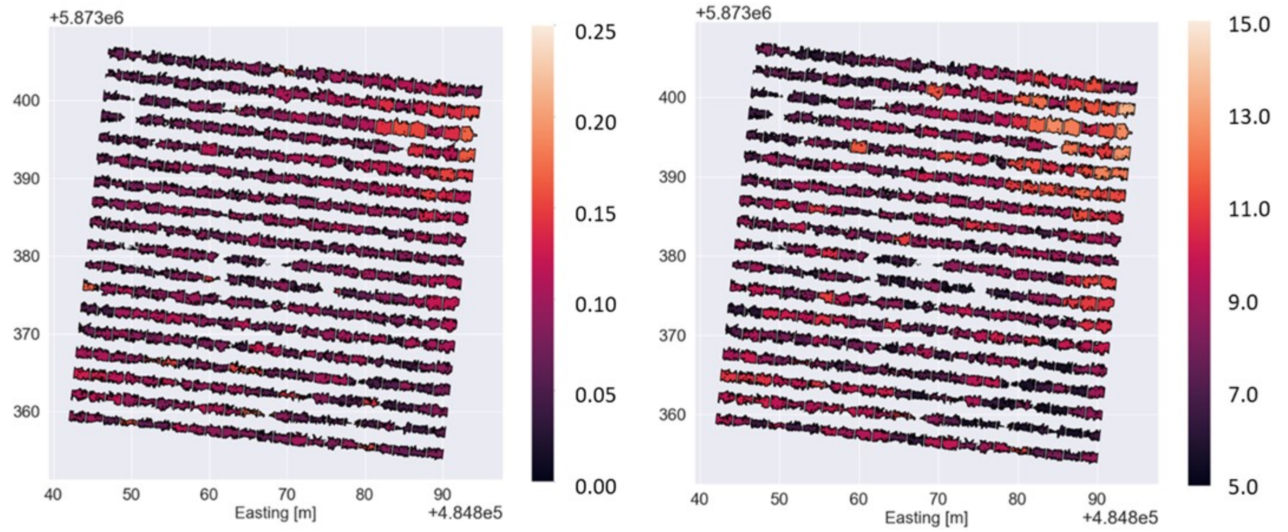

(a) (b)

Figure 46: Spatial prediction of canopy conductance, g_c (a) and net photosynthesis, A_n (b) in AX88E (CAS) at pre-harvest. Values for g_c are shown in mol H_2O m^{-2} s^{-1}; values for A_n are shown in µmol CO_2 m^{-2} s^{-1}. Single vine level data is presented for the entire mapping area of the vineyard beyond the sentinel vines.

High resolution remote sensing using thermal and multispectral cameras allowed for the modelling of canopy gas exchange parameters, canopy conductance (g_c) and net photosynthesis (A_n). Spatial variations in g_c indicate a range of 0.05 – 0.2 mol H_2O m^{-2} s^{-1}, which reflects the consistently high vine-to-vine variability in water status and physiological performance in this block. Net photosynthesis rates are also similarly variable; values range from 5 – 13 µmol CO_2 m^{-2} s^{-1}. These values match the range of values obtained from our ground measurements with an infrared gas analyser.

Table 11: Accuracy of various linear and non-linear statistical models and machine learning models for the prediction of CAS canopy gas exchange at EL-37 (pre-harvest). RMSE = root mean square error; R^2 = correlation coefficient; MAE = mean absolute error. Models: Linear, GLM = Generalised Linear Model, RF = Random Forest.

	Canopy conductance (g_c)			**Canopy net photosynthesis (A_n)**		
Model	RMSE	R^2	MAE	RMSE	R^2	MAE
Linear	0.059	0.149	0.047	1.497	0.371	1.272
GLM	0.055	0.265	0.042	1.379	0.505	1.015
RF	0.039	0.622	0.030	0.962	0.751	0.681

Comparing the performance of the various models, the Random Forest model again was superior to the other two evaluated in this study. Values of RMSE and MAE were the lowest for both parameters, g_c and A_n.

Further work on this dataset would include predictions of spatial and temporal patterns of leaf and crop water use efficiencies, as well as extending these predictions to other neighbouring vineyards with the same cultivar based on limited ground-based measurements in those blocks to fine-tune the models developed here.

Shiraz

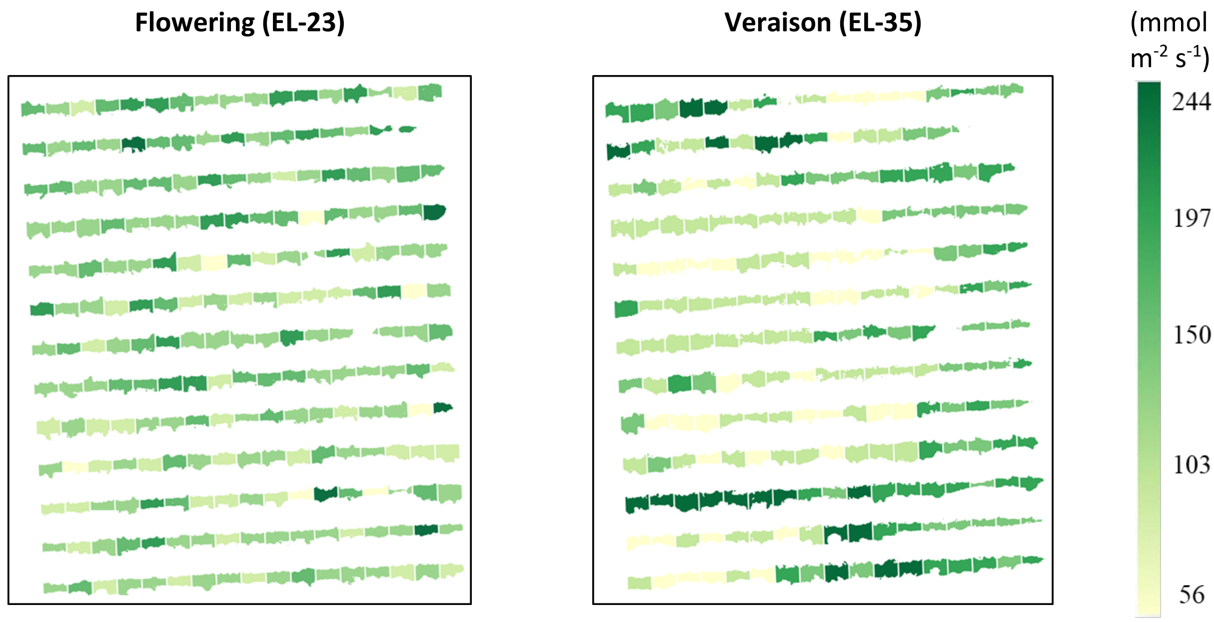

(a) **(b)**

Figure 47: Spatial and temporal prediction of canopy conductance, g_c, in KAT-SHI during flowering (a) and véraison (b). Values for g_c are shown in mmol H_2O m^{-2} s^{-1}. Single vine level data is presented for the entire mapping area of the vineyard beyond the sentinel vines.

Remote sensing-based model predictions of spatial canopy conductance through multispectral and thermal high-resolution imagery, indicated that, at flowering, g_c ranged from 56 to ~200 mmol H_2O m^{-2} s^{-1}, with no clear spatial structure in the data (lack of defined zones). By véraison, these values ranged from 56 to 244 mmol H_2O m^{-2} s^{-1}, with significantly more vines at the higher g_c values compared to at flowering. At this later stage, there appeared to be a separation between the central rows (with lower g_c) and the sides of the block (with higher gc), which provide guidance on where to implement precision irrigation through irrigation zoning. This pattern was consistent with the spatiotemporal trends of both predawn and stem water potentials (Figs. 43, 44), but not K_c (Fig. 45).

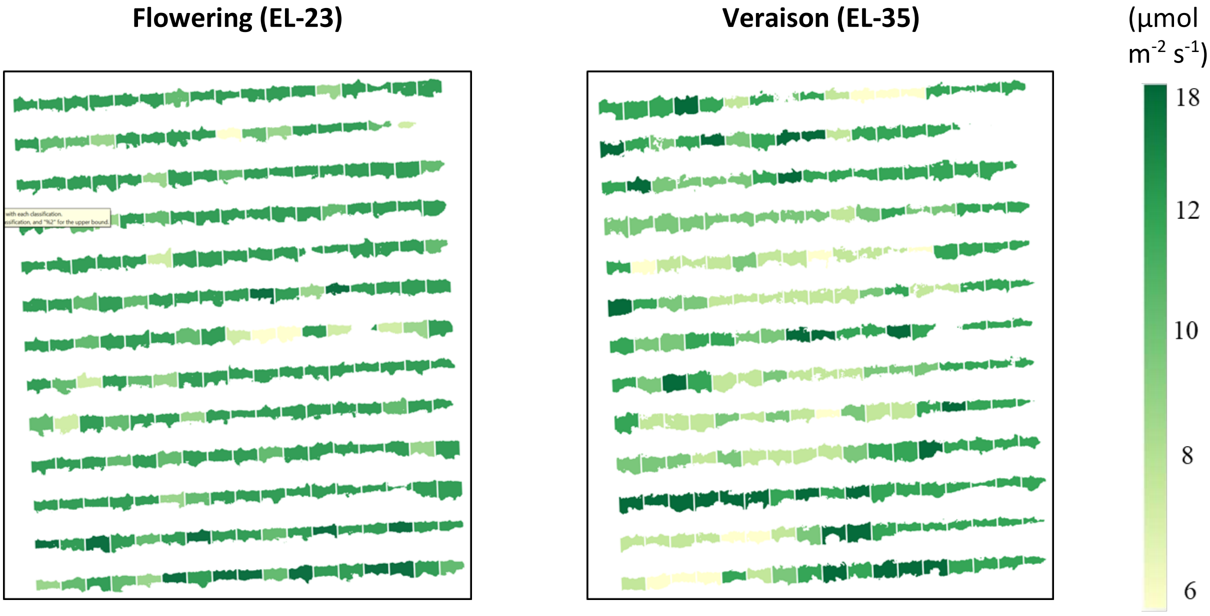

(a) (b)

Figure 48: Spatial and temporal prediction of canopy net photosynthesis, A_n, in KAT-SHI during flowering (a) and véraison (b). Values for A_n are shown in µmol CO_2 m^{-2} s^{-1}. Single vine level data is presented for the entire mapping area of the vineyard beyond the sentinel vines.

Canopy net photosynthesis rates predicted at the single vine level via HR-RS indicated a range of 8-12 µmol CO_2 m^{-2} s^{-1} during flowering, rising to 10-18 µmol CO_2 m^{-2} s^{-1} by véraison. The Shiraz block showed spatial structure between these two phenological stages; the upper and lower portions of the block had higher values of P_n, consistent with g_c, and soil and vine water status spatial trends.

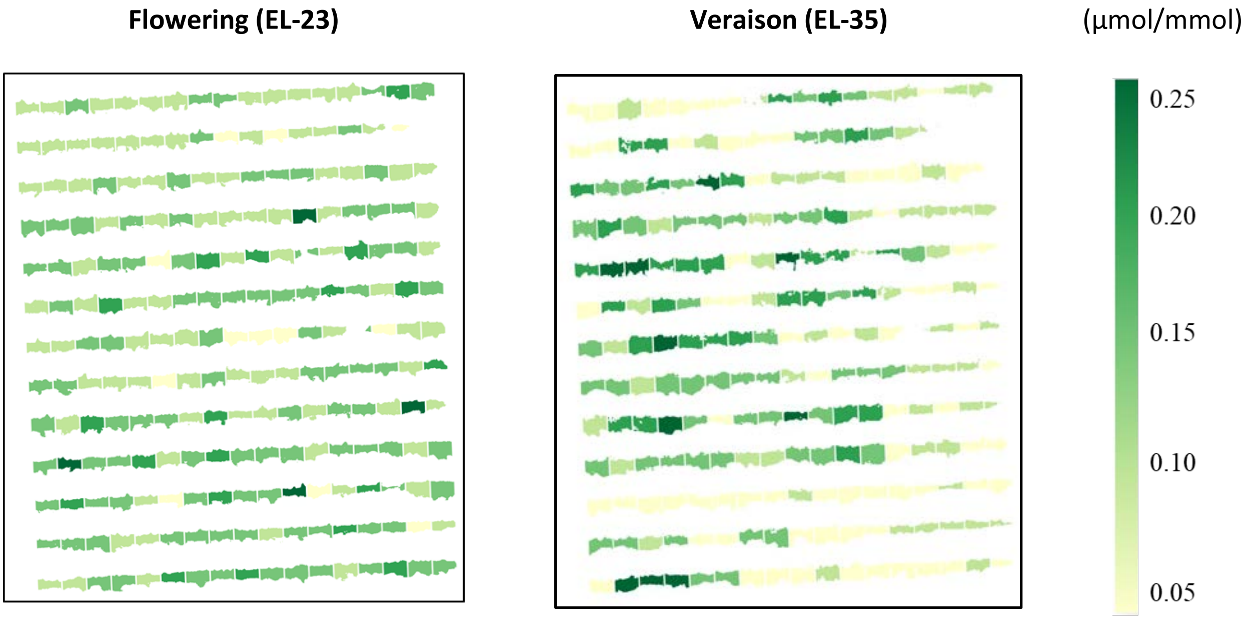

(a) (b)

Figure 49: Spatial and temporal prediction of leaf intrinsic water use efficiency ($WUE_i = A_n/g_s$) in KAT-SHI during flowering (a) and véraison (b). Values for WUE_i are shown in µmol CO_2 $mmol^{-1}$ H_2O. Single vine level data is presented for the entire mapping area of the vineyard beyond the sentinel vines.

Using the spatial and temporal A_n and g_s information in Figs. 47-48, the spatial and temporal patterns of leaf intrinsic water use efficiency (WUE_i) were obtained for the Shiraz vineyard during the 2021-22 season (Fig. 49). During the early season, around flowering, WUE_i values ranged from 0.05 to 0.2 across the block, wbile later in the season, around véraison, those value shifted higher in the center of the block to around 0.2-0.25. The two north-south edges of the block clearly had low *WUE_i*; this could be attributed to the larger canopies in those regions (high Kc values, Fig. 45) using more water due to their relatively higher g_s values (Fig. 47) that was not matched by the increase in A_n (Fig. 48). This is another opportunity to implement precision irrigation by zoning the two ends of the vineyard and applying water at lower rates to decrease the g_s relative to A_n. The central rows are clearly quite efficient in their water use patterns, showing high *WUE_i*.

5.5 Yield components and pruning weights

As shown in the table 9, total yield per vine did not change dramatically with different irrigation treatments in both Alex88-east and Alex88-west during 2018/2019 (S1) and 2019/2020 (S2) seasons. However, in the 2020/2021 season, total yield of CONV+ vines was significantly higher relative to SWS vines due to increased average berry weight. Even though yield per unit length (kg m^{-1}) seemed to be constant in Alex88-east during all three seasons despite of different irrigation scheduling strategy, in Alex88-west CONV vines displayed significantly higher yield per meter relative to PWS vines in S2.

Table 9: Yield components for all irrigation treatments in Alex88-east and Alex88-west and experimental season (2018/2019, 2019/2020 and 2020/2021). Means (n = 4 – 8) are presented. Interactions between irrigation treatments are reported both within a soil type and between soil types.

	Season	S1		S2		S3		ANOVA				
	Treatment	AX88-E	AX88-W	AX88-E	AX88-W	AX88-E	AX88-W	T	ST	S	T×ST	S×ST
Yield (kg $vine^{-1}$)	CONV	7.33	7.12	3.85	4.20	-	-	**	***	***	ns	ns
	PWS	7.19	5.24	4.59	3.04	6.53 ab	5.30					
	ET	-	-	5.80	3.33	7.02 ab	6.67					
	SWS	-	-	4.97	3.10	4.88 b	4.73					
	CONV+	-	-	-	-	8.71 a	7.48					
Yield (kg m^{-1})	CONV	2.22	2.28	1.14	1.35 a	-	-	*	**	***	**	*
	PWS	2.16	1.38	1.36	0.81 b	1.94	1.60					
	ET	-	-	1.56	0.96 ab	1.80	1.92					
	SWS	-	-	1.51	0.89 ab	1.47	1.37					
	CONV+	-	-	-	-	1.91	2.12					
Bunch count (bunches m^{-1})	CONV	43.4	51.2 a	29.6	32.7	-	-	*	*	***	ns	ns
	PWS	41.3	34.4 b	30.8	25.3	42.2	34.8					
	ET	-	-	36.5	22.8	39.6	39.8					
	SWS	-	-	39.2	24.7	36.2	35.8					
	CONV+	-	-	-	-	49.2	52.1					
Berries per bunch	CONV	55.8	54.0	40.5	51.3	-	-	ns	*	***	ns	**
	PWS	60.1	47.8	46.1	43.3	53.3	44.1 ab					
	ET	-	-	44.9	46.9	51.9	49.6 a					
	SWS	-	-	41.2	45.1	49.0	41.0 b					

	CONV +	-	-	-	-	54.2	45.4 ab					
Average berry weight (g)	CONV	0.92	0.83	0.95	0.84	-	-	**	***	ns	ns	***
	PWS	0.86	0.85	1.00	0.78	0.88 b	0.97					
	ET	-	-	0.98	0.90	0.85 b	0.98					
	SWS	-	-	0.96	0.82	0.85 b	0.92					
	CONV +	-	-	-	-	0.98 a	1.02					
Average bunch weight (g)	CONV	51.1	44.6	38.3	41.6	-	-	*	***	***	*	ns
	PWS	51.9	40.7	46.3	32.6	46.8	42.6 ab					
	ET	-	-	44.3	42.0	44.5	48.5 a					
	SWS	-	-	39.2	36.2	41.5	37.4 b					
	CONV +	-	-	-	-	53.2	44.3 ab					
Pruning weight (kg m^{-1})	CONV	0.66	0.57	0.73	0.45	-	-	ns	***	**	ns	***
	PWS	0.67	0.46	0.84	0.56	0.51	0.42					
	ET	-	-	0.83	0.49	0.53	0.52					
	SWS	-	-	0.86	0.42	0.53	0.52					
	CONV +	-	-	-	-	0.44	0.64					
Ravaz Index (kg kg^{-1})	CONV	3.62	4.44	1.66	3.11 a	-	-	ns	ns	***	ns	ns
	PWS	3.26	3.74	1.73	1.57 b	3.77	3.52					
	ET	-	-	2.08	2.31 ab	3.52	3.92					
	SWS	-	-	1.90	2.18 ab	2.84	2.77					
	CONV +	-	-	-	-	4.62	3.65					

It was consistently observed across three seasons that the total yield of SHI in the Prodigy block, was significantly lower relative to all trial SHI vines at Katnook. For instance, in S1 and S3, PWS1 and SWS vines showed significantly higher yield relative to Prodigy vines, whereas in the 2021/2022 season, all irrigation treatments produced significantly higher yield compared to prodigy vines. Yield reduction in Prodigy can be attributed to significantly lower berries per bunch as well as average bunch weight.

Table 10: Yield components for all irrigation treatments in Katnook during four experimental seasons (2018/2019, 2019/2020, 2020/2021 and 2021/2022). Means (n = 4 – 8) are presented. Prod=Prodigy block. Interactions between irrigation treatments are reported.

	Season	S1	S2	S3	S4	T	S	T× S
Yield (kg vine^{-1})	CONV	5.3 ab	1.9 ns	-	7.5 a	**	***	ns
	CONV +	-	-	9.9 a	8.4 a			
	ET	5.2 ab	1.3	8.7 ab	6.2 a			
	PWS1	5.9 a	2.1	10.4 a	6.2 a			
	PWS2	-	-	-	6.4 a			
	SWS	6.0 a	1.6	9.7 a	5.9 a			
	Prod-CONV	3.5 b	-	4.8 b	3.0 b			
Yield (kg vine^{-1})	CONV	3.0 ns	1.1 ns	-	4.6 ns	ns	ns	ns
	CONV +	-	-	5.7 ns	4.2			
	ET	3.0	0.74	5.0	3.5			
	PWS1	3.4	1.2	5.9	3.5			
	PWS2	-	-	-	3.6			
	SWS	3.4	0.94	5.6	3.3			
	Prod-CONV	-	-	-	3.4			
Bunch count (bunches m^{-1})	CONV	18.14 a	17.1 ns	-	26.1 b	*	***	*
	CONV +	-	-	32.8 ns	25 b			
	ET	5.0 b	11.4	36.7	24 b			
	PWS1	5.9 b	17.9	42.4	22.1 b			
	PWS2	-	-	-	24.1 b			
	SWS	5.6 b	14.3	38.1	23.5 b			
	Prod-CONV	-	-	-	42.2 a			
Berries per bunch	CONV	131.4 b	44.2 ns	-	121 a	**	***	*
	CONV +	-	-	113.6 a	102 a			
	ET	126 b	49.2	113.6 a	109 a			
	PWS1	124 b	50.1	104.4 a	111 a			
	PWS2	-	-	-	115 a			
	SWS	128 b	49.4	125.7 a	120 a			
	Prod-CONV	194 a	-	70.0 b	41 b			
Average berry	CONV	1.13 ns	1.36 ns		1.5 ab	**	**	*
	CONV +	-	-	1.54 a	1.6 a			
	ET	1.15	1.35	1.20 b	1.3 bc			

	PWS1	1.20	1.37	1.31 b	1.4 bc			
	PWS2	-	-	-	1.4 bc			
	SWS	1.16	1.33	1.15 b	1.3 c			
	Prod-CONV	1.1	-	-	1.3 bc			
Average bunch weight (g)	CONV	148.0 b	59.8 ns	-	178 a			
	CONV +	-	-	174 a	168 ab			
	ET	145.3 b	64.5	134.6 b	145 b	*	***	*
	PWS1	148.0 b	66.4	136.2 b	150 ab			
	PWS2	-	-	-	155 ab			
	SWS	147.8 b	65.7	143.9 b	151 ab			
	Prod-CONV	203.4 a	-	86.2 c	53 c			
Pruning weight (kg m−1)	CONV	0.80 ns	-	1.0 ns				
	CONV +	-	-	-				
	ET	0.91	-	0.84		ns	ns	ns
	PWS1	0.95	-	1.10				
	PWS2	-	-	-				
	SWS	0.81	-	1.00				
	Prod-CONV	-	-	-				
Ravaz Index (kg kg^{-1})	CONV	3.9 ns	-	5.6 ns				
	CONV +	-	-	-				
	ET	3.5	-	6.0		ns	ns	ns
	PWS1	4.5	-	5.9				
	PWS2	-	-	-				
	SWS	4.2	-	5.7				
	Prod-CONV	5.2	-	-				

5.6 Water use efficiency

5.6.1 Crop water use efficiency

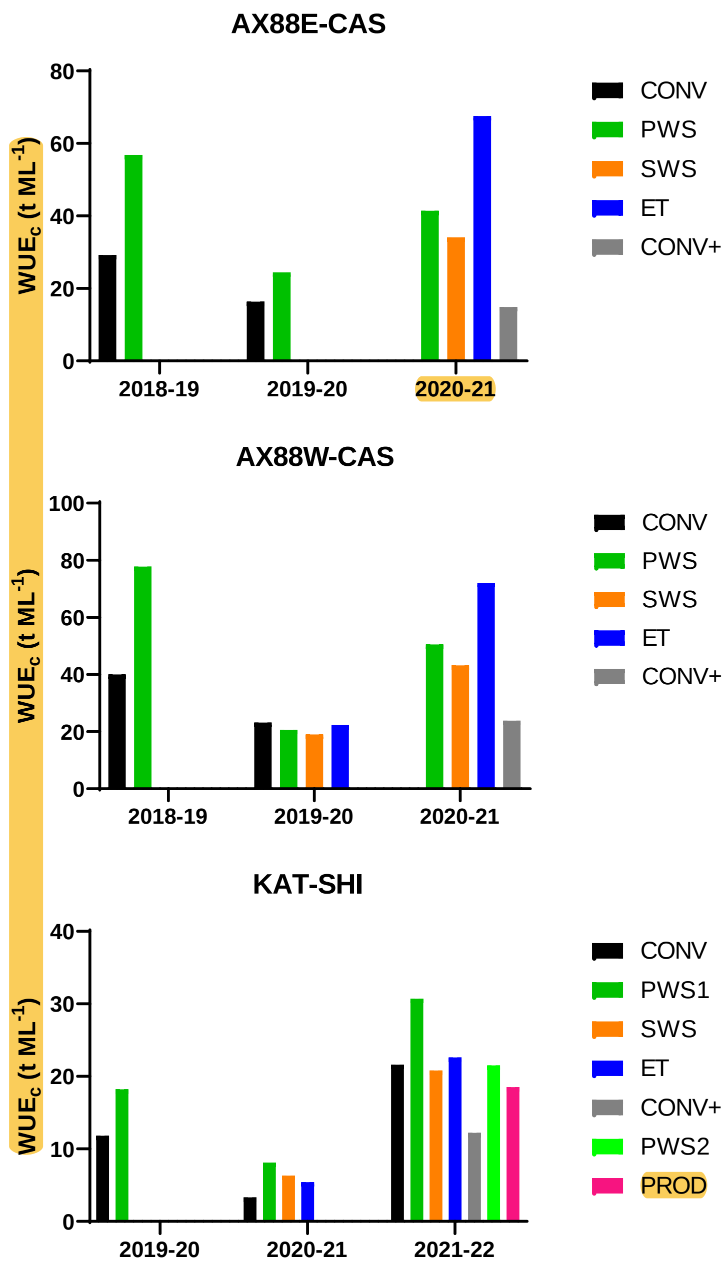

Figure 50: Crop water use efficiency (WUEc, t/ML) for the AX88E (CAS), AX88W (CAS) and KAT (SHI) vineyards during the three seasons. Water application volumes do not include rainfall during the growing season.

Crop water use efficiency (WUE_c) metrics derived from yield and irrigation data, also known as Irrigation Water Productivity, were calculated for each of the three seasons of the trial in the CAS and SHI vineyards. The 2019-20 season notwithstanding, WUE_c values in CAS were highest in the PWS and ET treatments, followed by the SWS treatment. These data-driven treatments were significantly higher than the CONV, by 3-6 fold (300-600%) in the final season. This is strong evidence that using data to drive irrigation decisions, regardless of the approach, is beneficial to improve WUE, even in premium vineyards that are routinely deficit irrigated to increase grape/wine quality. In SHI, similar trends were observed; while there was only a slight increase in WUE_c in the first season using the PWS treatment, by the second season, all data-driven approaches were over double the WUE_c of the CONV group. In the final season, 2021-22, the PWS1 treatment based on the proximal IR sensors appeared to have the highest WUE_c of the group, which were not different from each other or versus CONV or the Prodigy block (PROD). The only outlier in this group was the CONV+ treatment, which received double the CONV irrigation volume, and clearly this did not translate to a proportional yield increase and thereby decreasing its WUE_c (relative to CONV).

Unlike many warm climate vineyards, it seems that in a cooler region with smaller vines, higher irrigation volumes may not benefit growers seeking to increase yields in mid-grade SHI blocks that are already yielding upwards of 13 t/ha as in the case of KAT. A similar observation was made in AX88E-CAS on Terrarossa; in the final season, 2020-21, increased irrigation from 0.4 ML/ha (PWS) to 1 ML/ha (CONV+) did not alter yield; both groups had yields of ~15 t/ha. The heavier Rendzina vineyard, AX88W, did, however, benefit from increased irrigation in the CONV+ group; yield in this group was ~33% higher than the data-driven groups receiving less irrigation, but this yield increase (in CONV+) required an irrigation increase from 0.25 ML/ha to 0.7 ML/ha, i.e. approx. 80% higher than the data-driven groups, PWS and ET. The marginal yield benefit (increased yield per unit increase of water application) is therefore quite low and not favouring high irrigation rates.

5.6.2 Berry carbon isotopes

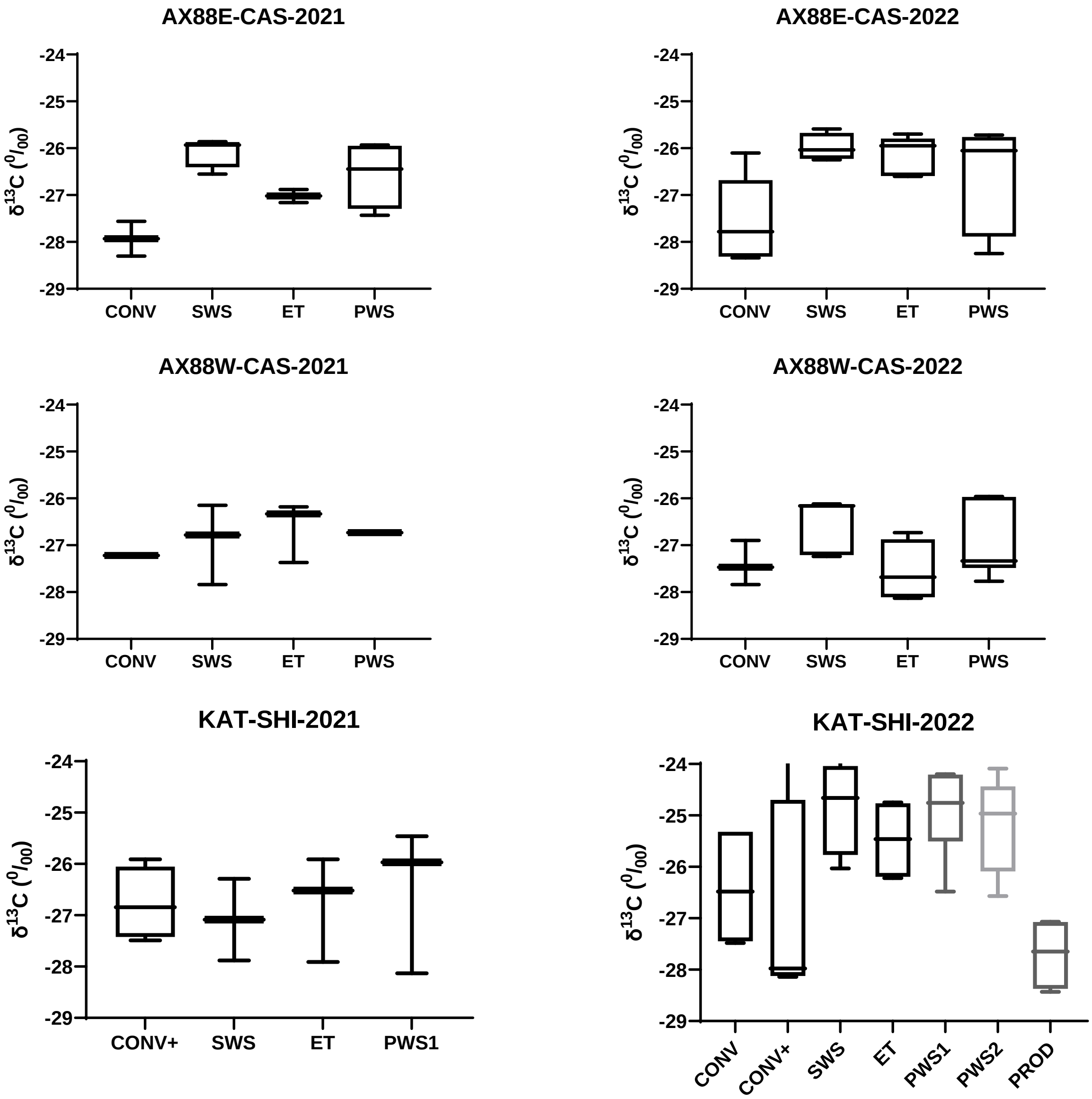

Figure 51: Carbon isotope ($\delta^{13}C$) analysis of SHI and CAS grape berries. Boxplots show median value (horizontal line inside the box), minimum and maximum values (lower and upper edges of box), and SE (whiskers).

Carbon isotope analysis was used as an estimate of the seasonal water use efficiency (WUE) of the vines as there is a high correlation between the $\delta^{13}C$ value and leaf-level instantaneous WUE (or Transpiration Efficiency, TE) as reported in several published studies. In AX88E-CAS (on Terrarossa), the highest (least negative) $\delta^{13}C$ values were found in the data-driven treatments, indicating higher WUE than the CONV in both seasons. The CAS vines on Rendzina soils (at AX88W) had fewer differences even though the same trend held in 2021. Amongst the data-driven treatments in CAS-Terrarossa, the PWS and SWS treatments had the highest $\delta^{13}C$ values in the first season.

For SHI grapevines on Terrarossa, ET and PWS had the highest $\delta^{13}C$ values in the first season, with no differences between the CONV+ and SWS treatments. In the second season, 2021-2022, all the data driven treatments were significantly higher than the CONV, CONV+ and PROD vines, indicative of their high WUE. Comparing these data-driven groups, the highest $\delta^{13}C$ values were observed in the SWS, PWS1 and PWS2 treatments, consistent with the WUE_i values obtained from leaf gas exchange (Figure 38b).

5.7 Berry and juice composition

It was consistently observed that juice quality of CAS in both Alex88-east and Alex88-west vineyards, did not significantly vary in response to different irrigation treatments across the first two seasons. However, berry quality attributes (colour, total phenolics and tannin concentrations) were significantly lower in SWS vines in the S1 relative to CONV vines.

In the 2020/2021 season in both Alex88-east and Alex88-west, berry quality and most of the juice quality parameters remained unchanged. However, in Alex88-east, both PWS and SWS vines showed significantly lower pH and TA relative to CONV+ (Table 11).

Table 11: Variations in berry and juice composition in Alex88-east and Alex88-west during three experimental seasons (2018/2019, 2019/2020 and 2020/2021) in response to different irrigation treatments. Means (n = 4 – 8) are presented. Interactions between irrigation treatments are reported.

	Season	S1		S2		S3	
		Alex88-E	**Alex88-W**	**Alex88-E**	**Alex88-W**	**Alex88-E**	**Alex88-W**
pH	CONV	-	-	4.2 ns	3.6 ns	-	-
	CONV+	-	-	-	-	6.3 a	4.1 ab
	ET	-	-	4.2	3.7	5.9 ab	4.1 ab
	PWS	-	-	4.2	3.5	5.3 bc	5.0 a
	SWS	-	-	4.2	3.1	5.1 c	3.8 b
TA	CONV	-		3.0 ns	3.6 ns	-	-
	CONV+	-	-	-	-	6.3 a	4.1 ab
	ET	-	-	3.2	3.7	5.9 ab	4.4 ab
	PWS	-	-	3.3	3.5	5.3 bc	5.0 a
	SWS	-	-	2.9	3.1	5.1 c	3.8 b
TSS	CONV	-	-	25.2 ns	26.3 a	-	-
	CONV+	-	-	-	-	26.2 ab	26.8 ns
	ET	-	-	25.5	25.2 b	26.0 b	26.9
	PWS	-	-	25.7	25.7 ab	27.4 a	26.7
	SWS	-	-	25.7	25.7 ab	27.2 a	26.9
Colour per berry (mg anthocyanins per berry)	CONV	3.5 ns	3.5 ns	1.8 ab	1.5 ns	-	-
	CONV+	-	-	-	-	2.2 ns	2.6 ns
	ET	3.5	3.4	2.2 a	1.6	2.3	2.6
	PWS	3.4	3.7	1.8 ab	1.6	2.3	2.6
	SWS	3.0	3.7	1.7 b	1.6	2.2	2.5
Colour per gram berry weight (mg anthocyanins per	CONV	4.2 a	4.2 ns	1.9 ns	1.8 ns	-	-
	CONV+	-	-	-	-	2.4 ns	2.7 ns
	ET	3.8 ab	3.8	2.3	1.8	2.4	2.6
	PWS	3.9 ab	4.3	1.8	1.9	2.6	2.7
	SWS	3.2 b	4.2	1.9	1.9	2.6	2.8

	Season	S1	S2	S3			
		Alex88-E	Alex88-W	Alex88-E	Alex88-W	Alex88-E	Alex88-W
Total phenolics per berry (absorbance units (au) per	CONV	2.5 ns	2.5 ns	1.8 ns	1.5 ns	-	-
	CONV+	-	-	-	-	2.0ns	2.2 ns
	ET	2.5	2.4	1.8	1.7	2.1	2.3
	PWS	2.4	2.5	1.8	1.6	2.0	2.3
	SWS	2.2	2.6	1.7	1.6	1.9	2.2
Total phenolics per gram berry weight (absorbance units (au) per gram berry	CONV	3.0 a	3.0 ns	1.9 ns	1.8 ns	-	-
	CONV+	-	-	-	-	2.2 ns	2.3 ns
	ET	2.7 ab	2.7	1.9	1.8	2.2	2.3
	PWS	2.8 ab	3.0	1.8	1.9	2.3	2.4
	SWS	2.4 b	2.9	1.9	2.0	2.5	2.4
Tannin concentration in homogenate (mg/g)	CONV	8.2 ab	7.0 ns	5.3 ns	5.2 ns	-	-
	CONV+	-	-	-	-	5.9 ns	5.4 ns
	ET	9.4 a	7.2	4.9	5.4	5.2	5.1
	PWS	8.7 ab	8.6	4.7	5.3	5.4	5.6
	SWS	4.9 b	4.4	4.6	5.5	5.7	5.3
Colour density	CONV	-	-	3.9 ns	4.4 ns	-	-
	CONV+	-	-	-	-	4.7 ns	4.5 ns
	ET	-	-	3.9	4.4	4.7	4.5
	PWS	-	-	3.8	4.4	4.7	4.7
	SWS	-	-	4.2	4.3	4.8	4.6
Hue	CONV	-	-	1.1 ns	1.0 ns	-	-
	CONV+	-	-	-	-	1.0 ns	1.0 ns
	ET	-	-	1.1	1.0	1.0	1.0
	PWS	-	-	1.1	1.0	1.0	1.0
	SWS	-	-	1.1	1.0	1.0	1.0
Total anthocyanins (mg/L)	CONV	-	-	176 ab	220 ns	-	-
	CONV+	-	-	-	-	400 ns	327 ns
	ET	-	-	162 b	203	382	310
	PWS	-	-	170 ab	234	409	307
	SWS	-	-	203 a	215	425	310
Total phenolics	CONV	-	-	2.2 ns	1.7 ns	3.2 ns	1.7 ns
	CONV+	-	-	-	-	-	-
	ET	-	-	1.7	1.8	2.9	2.4
	PWS	-	-	2.0	1.7	3.2	1.9
	SWS	-	-	1.7	1.7	3.8	2.5

In 2018/2019 season, irrigation scheduling did not significantly affect berry anthocyanin, phenolic and tannin concentrations in SHI in Katnook (Table 12). In the 2019/2020, 2020/2021 and 2021/2022 seasons, juice quality parameters such as pH, TA, TSS, hue and total phenolics were also did not change in response to different irrigation treatments in SHI in Katnook. However, statistically significant differences were observed between prodigy vines and SHI in Katnook. For instance, in the S4, prodigy vines showed significantly lower juice quality parameters (pH and TSS) and higher TA and total phenolics relative to SHI vines in Katnook.

Table 12: Variations in berry and juice composition in Katnook during four experimental seasons (2018/2019, 2019/2020, 2020/2021 and 2021/2022) in response to different irrigation treatments. Means (n = 4 – 8) are presented. Interactions between irrigation treatments are reported.

	Season	**S1**	**S2**	**S3**	**S4**	**T**	**S**	**T×S**
pH	CONV	-	4.3 ns	-	3.6 a	**	***	*
	CONV+	-	-	3.4 ns	3.6 a			
	ET	-	4.3	3.3	3.7 a			
	PWS1	-	4.3	3.4	3.7 a			
	PWS2	-	-	-	3.6 a			
	SWS	-	4.3	3.3	3.6 a			
	Prod-CONV	-	-	3.3	3.0 b			
TA	CONV	-	5.5 ns	7.0 ns	5.3 bcd	*	***	**
	CONV+	-	-	-	5.9 b			
	ET	-	5.6	7.0	5.1 d			
	PWS1	-	5.6	6.7	5.1 d			
	PWS2	-	-	-	5.1 d			
	SWS	-	5.2	7.0	5.1 d			
	Prod-CONV	-	-	7.4	8.6 a			
TSS	CONV	-	27.8 ns	-	25.5 a	*	***	*
	CONV+	-	-	22.9 a	25.8 a			
	ET	-	29.6	20.5 b	26.5 a			
	PWS1	-	28.7	20.6 b	26.7 a			
	PWS2	-	-	-	26.7 a			
	SWS	-	28.2	20.8 ab	25.9 a			
	Prod-CONV	-	-	22.5 ab	22.5 b			

	Season	S1	S2	S3	S4	T	S	T×S
Colour per berry (mg anthocyanins per berry)	CONV	4.4 ns	2.3 ns	-	3.0 ab			
	CONV+	-	-	2.9 a	3.5 a			
	ET	4.9	2.4	2.3 ab	2.9 b	*	***	*
	PWS1	4.8	2.7	2.5 ab	3.0 ab			
	PWS2	-	-	-	3.0 ab			
	SWS	4.3	2.1	2.0 bcd	3.0 ab			
	Prod-CONV	-	-	1.5 d	-			
Color per gram berry weight (mg anthocyanins per gram berry weight)	CONV	3.6 ns	2.0 ns	-	2.1 ns			
	CONV+	-	-	1.8 a	2.1			
	ET	4.2	2.1	2.0 a	2.2	**	*	**
	PWS1	4.0	2.1	1.9 a	2.2			
	PWS2	-	-	-	2.2			
	SWS	3.6	1.7	1.8 a	2.4			
	Prod-CONV	-	-	1.2 b	-			
Total phenolics per berry (absorbance units (au) per berry)	CONV	3.2 ns	2.1 ns	-	2.8 ab			
	CONV+	-	-	2.7 a	3.0 a			
	ET	3.4	2.3	2.4 abc	2.6 b	*	***	*
	PWS1	3.3	2.3	2.6 ab	2.7 ab			
	PWS2	-	-	-	2.7 ab			
	SWS	2.9	2.0	2.1 bc	2.6 b			
	Prod-CONV	-	-	2.0 c	-			
Total phenolics per gram berry weight (absorbance units (au) per gram berry weight)	CONV	2.7 ns	1.9 ab	-	1.9 ns			
	CONV+	-	-	1.4 ab	1.9			
	ET	2.9	2.0 a	2.0 a	1.9	*	**	**
	PWS1	2.8	1.9 ab	2.0 a	2.0			
	PWS2	-	-	-	2.0			
	SWS	2.4	1.6 b	1.9 ab	2.0			
	Prod-CONV	-	-	1.6 b	-			

	Season	S1	S2	S3	S4	T	S	T×S
Tannin concentration in homogenate (mg/g)	CONV	9.3 ns	-	-	517 ns			
	CONV+	-	-	2.0 ns	530			
	ET	9.2	-	3.2	517	*	***	*
	PWS1	10.4	-	3.2	582			
	PWS2	-	-	-	568			
	SWS	10.6	-	2.9	685			
	Prod-CONV	-	-	3.2	-			
Colour density	CONV	-	4.7 ns	-	3.3 bc			
	CONV+	-	-	3.7 ab	3.0 c			
	ET	-	4.8	4.3 a	4.0 ab	*	***	*
	PWS1	-	4.8	4.2 a	4.0 ab			
	PWS2	-	-	-	4.2 a			
	SWS	-	4.6	4.1 a	3.7 bc			
	Prod-CONV	-	-	3.2 b	3.8 abc			
Hue	CONV	-	1.0 ns	-	0.82 ns			
	CONV+	-	-	1.0 ns	0.75			
	ET	-	1.0	0.96	0.82	*	***	*
	PWS1	-	1.0	0.97	0.82			
	PWS2	-	-	-	0.86			
	SWS	-	1.0	0.92	0.70			
	Prod-CONV	-	-	0.95	0.77			
Total anthocyanins (mg/L)	CONV	-	254.2 ns	-	100.9 ns			
	CONV+	-	-	162.3 ab	78.82			
	ET	-	237	234 a	105.5			
	PWS1	-	230	230 a	89.41	*	***	*
	PWS2	-	-	-	76.81			
	SWS	-	222	207 a	83			
	Prod-CONV	-	-	114 b	69.21			

	Season	S1	S2	S3	S4	T	S	T×S
Total phenolics (g/L)	CONV	-	2.5 ns	-	1.6 b			
	CONV+	-	-	0.9 ns	1.6 b			
	ET	-	2.5	1.2	1.6 b			
	PWS1	-	2.4	1.1	1.6 b	*	***	*
	PWS2	-	-	-	1.6 b			
	SWS	-	2.2	0.9	1.6 b			
	Prod-CONV	-	-	1.1	2.0 a			

5.8 Wine composition

Table 13: Wine composition of Coonawarra Cabernet Sauvignon from AX88 East and West vineyards under different irrigation regimes.

	Season	Treatment	pH	TA	Colour	Hue	Total Anthocyanins (mg/L)	Total Phenolics (g/L)
Alex East	2018/2019	CONV	4.11	5.35	4.77	1.05	365.47	4.05
		ET	4.14	5.60	4.80	1.05	326.21	3.50
		PWS	4.07	5.43	4.78	1.05	329.02	2.98
		SWS	4.12	5.27	4.79	1.05	279.02	2.77
	2019/2020	CONV	3.98	6.32	4.94	1.04	378.19	2.31
		ET	3.94	6.90	4.93	1.04	393.54	2.47
		PWS	3.98	6.60	4.89	1.04	392.45	2.99
		SWS	3.99	6.52	4.91	1.04	396.28	3.16
	2020/2021	CONV+	4.16	5.70	4.81	1.04	308.05	3.54
		ET	4.24	5.53	4.81	1.04	291.56	3.84
		PWS	4.20	5.56	4.75	1.05	295.90	3.59
		SWS	4.30	5.11	4.80	1.04	296.47	4.25
Alex West	2018/2019	CONV	4.05	5.31	4.77	1.05	335.54	4.94
		ET	4.06	5.10	4.82	1.05	309.84	4.02
		PWS	4.03	5.33	4.80	1.05	337.97	4.63
		SWS	4.06	5.22	4.82	1.05	309.59	4.13
	2019/2020	CONV	3.95	6.48	4.86	1.04	374.35	3.29
		ET	3.95	6.67	4.95	1.04	382.77	3.16
		PWS	3.92	6.37	4.81	1.04	376.78	3.33
		SWS	3.94	6.51	4.77	1.04	397.09	3.34
	2020/2021	CONV+	4.21	5.29	4.83	1.04	322.09	3.75
		ET	4.21	5.43	4.74	1.04	283.29	3.76
		PWS	4.13	5.34	4.81	1.04	312.91	3.43
		SWS	4.21	5.23	4.84	1.04	314.93	4.26

Irrigation scheduling methods did not have a significant effect on basic wine composition parameter, pH and TA, colour and hue in most years. The total anthocyanins in the wine were lower in the ET treatment in most years except 2019/20, with no differences between the other groups. Total phenolics were often higher in the data-driven treatments except in the first season, 2018/19. The higher polyphenolic concentrations were generally related to the extent of vine water stress in the post-veraison period.

Table 14: Wine composition of Coonawarra Shiraz from Katnook Estate under different irrigation regimes. In 2018/19 and 2019/20, the wines were made categorised by three vine water stress levels, LOW, MEDIUM, HIGH.

	Season	Treatment	pH	TA	Colour	Hue	Total Anthocyanins (mg/L)	Total Phenolics (g/L)
Katnook	**2018/2019**	LOW	4.21	4.70	4.78	1.05	354.34	4.13
		MEDIUM	4.13	4.79	4.79	1.05	350.51	3.46
		HIGH	4.14	4.78	4.77	1.05	339.76	4.63
	2019/2020	LOW	4.34	7.15	4.84	1.04	367.51	2.40
		MEDIUM	4.34	7.04	4.94	1.04	299.74	2.15
		HIGH	4.32	6.94	4.88	1.04	372.50	2.44
	2020/2021	CONV+	4.17	5.24	4.74	1.05	265.52	1.99
		ET	3.90	5.47	4.64	1.02	258.54	2.53
		PWS	4.08	5.13	4.72	1.03	260.71	1.86
		SWS	4.00	5.45	4.69	1.03	256.11	2.18
	2021/2022	CONV	4.09	6.30	4.88	1.03	226.90	1.39
		ET	4.05	6.08	4.84	1.04	293.15	1.78
		PWS	4.08	6.19	4.94	1.04	252.56	1.55
		SWS	4.07	6.05	4.87	1.04	308.22	1.65

In Shiraz grapevines, TA, pH, colour and hue were in a narrow range between treatments and did not differ significantly in any of the seasons. When the wines were grouped based on vine water stress levels in the first two seasons, the highest anthocyanin levels were observed in the low and high water stress levels, particularly in the 2019/20 season when the differences were significant. Phenolics followed a similar pattern in those years. When the different irrigation treatments were applied starting in 2020/21 season, the ET treatment had higher phenolics in both seasons, but there were few differences in anthocyanins (except for SWS in the 2021/22 season).

5.9 Financial analysis

Investment and operational costs for each irrigation treatment are shown in Table 15.

Table 15: Approximate investment and operational costs for each irrigation scheduling strategy investigated in this study. Operational costs for the GROW and ET treatments were calculated on a per season basis, whereas PWS and SWS operational costs were considered over a year as data subscription plans occur in 12-month cycles. Costs were considered for a 15-ha vineyard considering an 18-week irrigation period.

	Investment concept	**Initial cost ($)**	**Lifespan (years)**	**Operational concept**	**Yearly operational cost ($)**	**Benefits**
GROW	Experienced vineyard manager and one soil moisture sensor	3,453	10	Cost of wages involved in making decisions, ongoing maintenance of soil moisture probe	479	Minimal equipment requirements and interpretation of complex data
ET	Paso panel and labour required to establish crop factor values over one season	1,172	10	Cost of wages required to calculate ET_c	440	Ability to numerically calculate irrigation needs
PWS	Thermography towers (thermal camera, gateway, waterproof outdoor boxes, pole, self-installation)	6,000	5	Data subscription each month, ongoing annual maintenance, cost of wages to analyse data	580	Integrates data from the whole canopy with measurements directly related to vine transpiration
SWS	Multiple depth capacitance probe (probes, installation cost and software)	13,577	10	Data subscription each month, ongoing maintenance of soil moisture probe, cost of wages to analyse data	357	Well-established methodology with a high degree of support for troubleshooting equipment and data problems

The primary assumptions for the implementation of various sensors to obtain data relate to sensor density (i.e., number of sensors per ha), sensor prices, and lifespan.

The following financial metrics were calculated for three seasons per cultivar (2018-2021 for CAS; 2019-2022 for SHI):

- Economic Productivity (EP)
- Economic Water Productivity (EWP)
- Unit production cost
- Total operational cost
- Income
- Cash flow
- Net Present Value (NPV)
- Internal Rate of Return (IRR)
- Pay-back Period (PB)
- Total margin

Results are presented in Tables 16-18 in the following pages.

5.9.1 Cabernet Sauvignon – Terrarossa

Table 16: Financial indicators of various non-data and data-driven irrigation scheduling approaches for Cabernet Sauvignon grapevines grown on Terrarossa soil in Coonawarra.

	2018/2019				2019/2020				2020/2021				
	GROW	ET	PWS	SWS	GROW	ET	PWS	SWS	GROW+	GROW	ET	PWS	SWS
Gross margin ($ ha^{-1})	20,001	19,925	18,203	20,221	7,635	14,936	9,893	10,775	23,373 a	18,082 ab	19,040 ab	18,668 ab	10,445 b
Economic water productivity ($ ML^{-1})	32,764 b	61,914 a	60,774 ab	33,310 b	13,032 b	34,613 a	22,311 ab	20,026 ab	18,385 c	29,361 bc	86,353 a	61,549 ab	29,524 bc
Breakeven point ($ t^{-1})	1,305	1,337	1,439	1,309	2,313	1,654	1,970	1,976	1,214 a	1,341 a	1,400 ab	1,451 ab	1,897 b
NPV ($ ha^{-1})	121,171	120,719	102,000	122,077	-4,622	69,987	17,492	26,003	155,499	101,603	111,708	106,735	22,630

One-way ANOVA and Tukey's multiple comparison test ($\alpha = 0.05$) was used to compare treatments

In Terrarossa soils, the gross margin of CAS varied quite significantly from season to season; the anomalous year was 2019-20 where the margin was half or less of the other two seasons. The highest margins were found for the GROW treatment (GROW+ in the last year), whereas the lowest values were in the PWS. The EWP was highest in the data-driven treatments, particularly ET and PWS, which was consistent across seasons. These numbers were high due to the low price (or no cost) of water in Coonawarra; in areas where water prices have to be factored into the model, the EWP numbers would be considerably lower, particularly in dry years. This numbers are consistent with the NPV – the highest NPVs are associated with the ET and PWS treatments. In the case where excess irrigation was applied, GROW+, there was a strong yield response translating to the highest NPV values of the group. To evaluate which of the irrigation strategies were economically feasible, the breakeven point was determined. The BP values were around $1300-$1500 per tonne of grapes, which reflects the minimum price that has to be received by growers if selling their crop. Lower BP values were observed in GROW treatment (except in 2019-20) likely due to the low investment costs associated with the sensor infrastructure. However, this is a scenario specific to Coonawarra where water prices are not a factor, and could be quite different in areas like the inland regions along the Murray River, where water is a real cost to production and yields are substantially higher for a given amount of water applied, i.e. higher gains in water use efficiency are expected to decrease the BP relative to GROW/GROW+. These strategies may then have very different feasibilities.

5.9.2 Cabernet Sauvignon – Rendzina

Table 17: Financial indicators of various non-data and data-driven irrigation scheduling approaches for Cabernet Sauvignon grapevines grown on Rendzina soil in Coonawarra.

	2018/2019				2019/2020				2020/2021				
	GROW	ET	PWS	SWS	GROW	ET	PWS	SWS	GROW+	GROW	ET	PWS	SWS
Gross margin ($ ha^{-1})	19,401	18,922	11,889	22,900	7,705	4,995	4,485	3,542	20,802	18,118	17,645	13,234	9,841
Economic water productivity ($ ML^{-1})	43,110 b	119,149 a	70,049 ab	48,511 b	16,452	14,934	13,846	9,539	29,387 b	51,108 ab	81,666 a	58,935 ab	39,004 b
Breakeven point ($ t^{-1})	1,375	1,629	1,954	1,200	2,346	3,334	3,483	3,168	1,380	1,336	1,406	2,416	2,176
NPV ($ ha^{-1})	115,053	110,508	37,774	149,318	-3,884	-38,553	-51,700	-49,992	122,641	101,940	97,522	40,365	16,484

One-way ANOVA and Tukey's multiple comparison test ($\alpha = 0.05$) was used to compare treatments

In the heavier Rendzina soils of Coonawarra, CAS gross margins followed a similar trend to the lighter Terrarossa soils – GROW had higher margins due to the low investment in infrastructure, but this was not linked to EWP or NPV. The returns per unit application of water (EWP) was highest in the ET treatment, primarily due to the low investment cost associated with obtaining crop coefficients and calculating ET_c. The EWP values were generally higher in Rendzina compared with Terrarossa (except 2019-20), reflecting the marginal benefit of using sensor technology in vineyards with heavier soils, possibly due to the greater disconnect between water content in the soil and vine water status that drives yield. The BP values were higher also compared to Terrarossa by nearly $500 per tonne reflecting how critical it is to manage irrigation prudently in heavier soils that have a higher clay content. While NPV values were generally highest in the GROW/GROW+ treatments, the data-driven treatments were only slightly lower due to the investment costs associated with the infrastructure as well as slightly lower yields. With water prices factored in (in other regions), these numbers are likely to tip in favour of the data-driven treatments.

5.9.3 Shiraz – Terrarossa

Table 18: Financial indicators of various non-data and data-driven irrigation scheduling approaches for Shiraz grapevines grown on Terrarossa soil in Coonawarra.

	2019/2020				2020/2021					2021/2022					
	GROW	ET	PWS	SWS	GROW+	GROW	ET	PWS	SWS	GROW+	GROW	ET	PWS1	PWS2	SWS
Gross margin ($ ha^{-1})	5,271	2,610	4,047	2,425	42,154 a	15,827 b	36,116 ab	44,777 a	41,522 a	29,588 ab	31,168 a	23,228 ab	19,779 b	24,265 ab	22,887 ab
Economic water productivity ($ ML^{-1})	5,632	3,885	6,022	4,393	21,077 b	15,827 b	83,992 a	81,412 a	86,505 a	15,096 b	25,136 a	21,310 ab	17,199 ab	21,665 ab	24,092 a
Breakeven point ($ t^{-1})	3,310	5,026	2,686	2,893	471 a	917 b	561 b	492 b	490 b	616 ab	576 a	753 ab	842 b	699 ab	749 ab
NPV ($ ha^{-1})	-72,524	-105,041	-62,701	-87,233	359,906	85,220	297,118	386,263	351,842	228,841	226,375	162,756	125,594	129,137	157,521

One-way ANOVA and Tukey's multiple comparison test ($\alpha = 0.05$) was used to compare treatments

The Shiraz grapevines on Terrarossa soils had similar financial trends to the CAS. The highest gross margins were attained in the GROW treatment while the lowest were in the data-driven treatments. The benefit of using sensor driven technology was apparent when looking at the EWP: the PWS and ET treatments were amongst the highest in the group while the GROW/GROW+ were the lowest. The breakeven points for SHI were considerably lower than for CAS although the trends were the same; the lowest BPs were in the GROW treatment due to the low investment required, while the ET treatment was amongst the lowest in the data-driven group for the same reasons. The plant sensor-based treatments had the lowest BP and highest NPV of the group, so, in the long term, this strategy represents a prudent financial decision for SHI.

5.10 Irrigation Practices Survey

The Limestone Coast irrigation survey was launched on the 14th of July, 2021 and it was closed on the 23rd of August, 2021. Thirty-five grapevine growers were participated in the survey. The irrigation survey and responses are in the Appendix. The survey results were disseminated to the industry in September 2021 and one random respondent to Part 3 of the survey was selected to win a $100 gift card. The number of survey respondents was 32.

Aggregated results of the irrigation practices survey data are provided in the Appendix. The highlights of the survey responses include:

- Most organisations surveyed had total vineyard area between 20-500 ha with average yields between 3-9 t/ha.
- Majority (~90%) of vineyards were irrigated using above-ground drip irrigation.
- Most (72%) irrigation decisions were made based on historical experience of the block(s).
- Most irrigators used weather forecasts to make irrigation decisions; less than 30% of the respondents used ET to schedule irrigation using historical or published crop coefficients.
- Two-thirds of the respondents used soil moisture monitoring; only two growers used plant-based sensors (sap flow, canopy temperature)
- The greatest barriers to adoption of new technology (for irrigation scheduling) was a lack of understanding of the technology, uncertainty of its value, and high cost.
- Approx. half the respondents plan to invest in new or additional irrigation technology within three years.

6 Other related outputs

Three scientific (peer-reviewed) manuscripts have been published as a part of this project:

- Gautam et al. (2021) Estimation of grapevine crop coefficient using a multispectral camera on an unmanned aerial vehicle. *Remote Sensing* 13: 2639.
- Gautam et al. (2020) A review of current and potential applications of remote sensing to study the water status of horticultural crops. *Agronomy* 10: 140.
- Pagay, V. (2021) Evaluating a novel microtensiometer for continuous trunk water potential measurements in field-grown irrigated grapevines. *Irrigation Science* 40: 45-54.

Two additional papers are in preparation:

- Schlank, R. et al. Evaluating different irrigation scheduling strategies in Cabernet Sauvignon grapevines according to soil type and water use efficiency metrics in a Mediterranean climate.
- Schlank, R. et al. Financial analysis of implementing different irrigation scheduling strategies in premium Cabernet Sauvignon grapevine in a cool climate Australian vineyard.

The findings of this research project were presented or will be presented at the following events.

- Pagay, V. (invited) Innovative technologies for precision irrigation in vineyards. 2021. American Society for Enology and Viticulture (ASEV) Precision Viticulture Symposium. (22nd June, 2021)
- Schlank, R. Evaluating different irrigation scheduling strategies in Cabernet Sauvignon grapevines according to soil type and water use efficiency metrics in a Mediterranean climate. Crush 2021- the grape and wine science symposium. Adelaide. 16th June 2021
- Presentations to industry collaborators
    - WA bilateral project updates. Treasury Wine Estates. (27th August 2021)
    - WA bilateral project updates. Katnook Estate. (1st September 2021)
- ASVO podcast on irrigation strategies in vineyards (31st August, 2021)
- AWRI webinar on optimising irrigation in vineyards (November 2021)
- AWRI Irrigation Roadshows (several in 2022)
- AWITC 2022 Workshop on Water Use Efficiency (oral presentation, 26/06/2022)
- Abstract submitted to the ISHS 10th International Symposium on Irrigation of Horticultural Crops, Stellenbosch, South Africa (January-February 2023).

7 Concluding remarks

Irrigation strategies based on data-driven techniques enabled the saving of water whilst not penalising vine physiological performance, yield, or grape composition. A key finding of this trial was that, in premium vineyards under deficit irrigation, seasonal irrigation volumes only partly account for variable yields; irrigation schedules play a vitally important role in this regard, and managing irrigation based on data, whether soil moisture, plant water status or ET_c, can greatly benefit water use efficiency and, importantly, without sacrificing grape/wine quality. We validated two new commercial crop water status sensors – microtensiometers (Florapulse) and TranspIR (Athena IR-Tech) – as part of the trial; both were found to strongly correlate with conventional vine water status metrics such as stem water potential and stomatal conductance. High resolution remote sensing from UAVs was shown to be valuable for (i) assessing spatial variations in water status and canopy performance; and (ii) developing predictive models of these parameters over space and time. Together, these are essential for precision irrigation, informing the placement of crop based sensors as well as zoning of irrigation blocks into sub-blocks. Together, these techniques have the potential to increase water use efficiency in grapevine and other crops that are similarly irrigated. Our choice of the two vineyards for Shiraz and Cabernet Sauvignon that were contrasting in their variability highlighted the importance of understanding spatial variability to improve management practices, including irrigation scheduling. The use of continuous crop water status sensors provided near real-time (or daily) data to inform the temporal management of irrigation to achieve greater efficiencies in water management in Australian vineyards.

8 Acknowledgements

The authors and the PIs would like to acknowledge all the involved industry, industry personnel, researchers, and many students who were involved over the years. Special thanks to Wynns Coonawarra Estate, Katnook Estate, Dr Catherine Kidman, Chris Brodie, Gavin Blacker, Dr Deepak Gautam, Felipe Canela, Rochelle Schlank, Dr Dilrukshi Nagahatenna, Hans Loder, Zac Han Chow, Do Mai Chi, Ockert Le Roux, Heidi Eldridge (Coonawarra Vignerons), Kerry DeGaris, Ulrich-Grey-Smith (LCGWC) for their involvement and assistance at various stages of the project.

9 References

Australia, W. (2022) *Australian wine sector at a glance*, Available: https://www.wineaustralia.com/market-insights/australian-wine-sector-at-a-glance [Accessed 20/08/2022.

AWRI (2019) *Vineyard and winery practices survey*, Available: https://www.awri.com.au/wp-content/uploads/2019/05/AWRI_Practices_Survey_Final_Report.pdf [Accessed 20/08/2022.

Caravia, L., Pagay, V., Collins, C. and Tyerman, S. (2017) Application of sprinkler cooling within the bunch zone during ripening of Cabernet Sauvignon berries to reduce the impact of high temperature. *Australian Journal of Grape and Wine Research* **23**, 48-57.

Cifre, J., Bota, J., Escalona, J. M., Medrano, H. and Flexas, J. (2005) Physiological tools for irrigation scheduling in grapevine (*Vitis vinifera* L.) An open gate to improve water-use efficiency? *Agriculture Ecosystems & Environment* **106**, 159-170.

Collins, M. and Loveys, B. (2010) Optimising irrigation for different cultivars. *Final report to Grape and Wine Research & Development Corporation. Project Number CSP* **5**.

Dry, P. R., Loveys, B. R., McCarthy, M. G. and Stoll, M. (2001) Strategic irrigation management in Australian vineyards. *OENO One* **35**, 129-139.

Fereres, E. and Soriano, M. A. (2006) Deficit irrigation for reducing agricultural water use. *Journal of Experimental Botany* **58**, 147-159.

Fernandez, J. E. (2017) Plant-based methods for irrigation scheduling of woody crops. *Horticulturae* **3**.

Fraga, H., Malheiro, A. C., Moutinho-Pereira, J. and Santos, J. A. (2012) An overview of climate change impacts on European viticulture. *Food and Energy Security* **1**, 94-110.

Green, G. and Pannell, A. (2020) *Guide to climate projections for risk assessment and planning in South Australia.* Adelaide, SA.

Jones, G. V. and Goodrich, G. B. (2008) Influence of climate variability on wine regions in the western USA and on wine quality in the Napa Valley. *Climate Research* **35**, 241-254.

Jones, G. V. and Webb, L. B. (2010) Climate change, viticulture, and wine: challenges and opportunities. *Journal of Wine Research* **21**, 103-106.

Jones, G. V., White, M. A. and Cooper, O. (2004) Climate change and global wine quality. *Bulletin of the American Meteorological Society* **85**, 504-+.

Jones, G. V., White, M. A., Cooper, O. R. and Storchmann, K. (2005) Climate change and global wine quality. *Climatic Change* **73**, 319-343.

Lebon, E., Dumas, V., Pieri, P. and Schultz, H. R. (2003) Modelling the seasonal dynamics of the soil water balance of vineyards. *Functional Plant Biology* **30**, 699-710.

Marks, J., Lines, T., Penfold, C. and Cavagnaro, T. (2022) Cover crops and carbon stocks: How under-vine management influences SOC inputs and turnover in two vineyards. *Science of The Total Environment* **831**, 154800.

Miras-Avalos, J. M. and Araujo, E. S. (2021) Optimization of vineyard water management: challenges, strategies, and perspectives. *Water* **13**.

Muñoz-Carpena, R. (2004) Field devices for monitoring soil water content: BUL343/AE266, 7/2004. *EDIS* **2004**.

Pagay, V. (2018) *Using in-canopy misters to mitigate the negative effects of heatwaves in grapevines*. Wine Australia Project UA 1502.

Rienth, M. and Scholasch, T. (2019) State-of-the-art of tools and methods to assess vine water status. *OENO One* **53**.

Romero, P., Navarro, J. M. and Ordaz, P. B. (2022) Towards a sustainable viticulture: The combination of deficit irrigation strategies and agroecological practices in Mediterranean vineyards. A review and update. *Agricultural Water Management* **259**, 107216.

Santos, J. A., Fraga, H., Malheiro, A. C., Moutinho-Pereira, J., Dinis, L.-T., Correia, C., Moriondo, M., Leolini, L., Dibari, C., Costafreda-Aumedes, S., Kartschall, T., Menz, C., Molitor, D., Junk, J., Beyer, M. and Schultz, H. R. (2020) A review of the potential climate change impacts and adaptation options for European viticulture. *Applied Sciences* **10**, 3092.

Schultz, H. R. and Stoll, M. (2010) Some critical issues in environmental physiology of grapevines: future challenges and current limitations. *Australian Journal of Grape and Wine Research* **16**, 4-24.

Shackel, K. (2011) A plant-based approach to deficit irrigation in trees and vines. *HortScience* **46**, 173-177.

Webb, L., Whetton, P. and Barlow, E. W. R. (2007) Future climate change impacts on Australian viticulture. In: Paper presented to the Actes du colloque “Réchauffement climatique, quels impacts probables sur les vignobles.

Williams, L. E. (2013) Physiological tools to assess vine water status for use in vineyard irrigation management: review and update. In: Paper presented to the 9th International Symposium on Grapevine Physiology and Biotechnology, La Serena, Chile.

10 Appendix: Limestone Coast Vineyard Irrigation Survey

<u>Industry Experience and Operation</u>

1. What is your age range?
    a. 18 – 25
    b. 26 – 35
    c. 36 – 45
    d. 46 - 55
    e. 55+

2. What is your main occupation in the wine industry? (Please circle all that apply)
    a. Grape grower
    b. Viticulturist
    c. Winemaker (not winery owner)
    d. Winery owner

3. How long have you been involved in the grape and wine sector? ____________

    How many of these have you been growing or managing grapes for? ____________

    Of these years, how many have been in the Limestone Coast region? ____________

4. Which region(s) of the Limestone Coast are you based or operating in?

5. What is the total vineyard size in which you operate? (for all varieties grown in the Limestone Coast region)
    a. <20 ha
    b. 20-49 ha
    c. 50-99 ha
    d. 100 - 500 ha
    e. >500 ha

6. What is a typical annual yield range from your operations? (total tonnes for all <u>red winegrape varieties</u> grown in the Limestone Coast region)

    ____

7. Do you typically dry farm or irrigate your grapevines?
    a. Irrigated
    b. Rainfed/dry grown

8. If you irrigate, how do you deliver irrigation? (circle all relevant)
    a. Above ground drip irrigation
    b. Subsurface drip irrigation
    c. Micro sprinklers
    d. Overhead sprinklers
    e. Other (please describe)

Irrigation Scheduling

1. How much time do you devote towards making irrigation decisions during an average week?
    a. Less than 5 minutes

b. 5 to 20 minutes
c. 20+ minutes

2. How do you carry out irrigation scheduling in established vineyards (mature, > 5 years old)? (Please select options within each of a, b, c, d. More than one can be selected)

   a. Historical irrigation levels

   b. Regular visual assessments of vine canopies for signs of water stress

   c. Weather forecasts

   d. Soil moisture monitoring (sensor-based)
      - Soil water tension (e.g. gypsum blocks, tensiometers)
        - How many do you have across all your red winegrape vineyards? ____________

      - Volumetric water content (e.g. capacitance probes)
        - How many do you have across all your red winegrape vineyards? ____________

   e. Evapotranspiration (ET)-driven
      - How do you obtain your reference ET? ________________________________
      - How do you obtain your crop factors (crop coefficients, K_c)? ________________________________
      - Which weather station do you use? ________________________________

   f. Plant water status

      What type of sensor(s) do you use? (include make and model) ____________________________

      - How many do you have across all your red winegrape vineyards? ____________

   g. Other
      - Remote sensing
        - UAVs/Drones
        - Fixed wing aircraft
        - Satellite

        What specific dataset or indices are you looking at? _________________
      - Not listed (if circled, please describe) _________________________________

3. If you use historical irrigation practices and/or weather forecast data, are there any specific barriers that have prevented you from adopting/considering other sensor-based (e.g. soil or plant sensors) technologies listed? Check one or more boxes from the list below:
   a. High cost
   b. Unsure of value of technology / lack of understanding

4. Why did you choose the specific irrigation scheduling approach you are currently using? What motivated this decision? You can circle more than one:
    a. Familiarity/previous experience
    b. Recommended by colleagues
    c. Availability (e.g. sensor hardware, data access/visualization)
    d. Convenience (or sensors already in place), ease of use
    e. Reliability
    f. Maintenance (if sensors used)
    g. Price
    h. Other: ____________________

5. What are your concerns about your current irrigation practices?
    a. No concerns
    b. High energy cost
    c. Maintenance of irrigation infrastructure
    d. Low irrigation system efficiency
    e. Uncertainty about plant and/or soil moisture levels
    f. Inadequate information to make prudent irrigation decisions
    g. Other: ______________________

6. What are your future plans in terms of investment/adoption of technologies to aid in irrigation scheduling? Please describe according to the criteria mentioned below:
    a. Timeframe for investment: __________________
    b. Infrastructure/sensors(s): ___________________
    c. Budget: ________________________
    d. No current plans to invest in irrigation technology

Thank you for your participation. If you would like to receive a copy of the aggregated survey results of the region, please fill in your contact details.

BOX to allow participants to fill in name, email address, phone number (optional)

You may optionally continue to the next page to provide some cultivar specific information for a chance to win a $50 gift card/voucher. Please remember to enter your contact details above before you proceed to the next page.

Cultivar-specific irrigation

Please fill in all relevant information for the varieties you typically grow focusing on only one specific block per cultivar during growing season (not including frost protection). Please fill in as much as you are comfortable providing information about.

	Size and soil type of plantings (Ha)	Region within Limestone Coast	Vine age (mature, more than 5 years old)	Vine density (vine/ha)	Is this block deficit irrigated, and if so what regime? (RDI* or SDI*, other)	Typical irrigation regime (mm per week)	Number of irrigation applications per week	Total seasonal irrigation ML/ha (typical ranges, max and min)	Yield (t/Ha) (2020 and 2016 vintage)	Average farm gate value for grapes ($/tonne) a. <$500 b. $500 - $1200 c. $1200 - $2000 d. $2000+
Barbera										
Cabernet Franc										
Cabernet Sauvignon										
Malbec										
Merlot										
Nebbiolo										
Petit Verdot										
Pinot Meunier										
Pinot Noir										
Shiraz										
Tempranillo										
Other red:										
Chardonnay										
Gewürztraminer										
Pinot Gris/Grigio										
Riesling										
Sauvignon Blanc										
Semillon										
Other white:										

*RDI: Regulated deficit irrigation *SDI: Sustained deficit irrigation

Vineyard Irrigation Practices Survey
Limestone Coast Region (SA)

- **Date of Survey: July-August 2021**

- **Number of respondents: 32 (17 completed all three sections)**

- **Survey conducted by Dr Vinay Pagay, University of Adelaide (vinay.pagay@adelaide.edu.au)**

Age and occupation

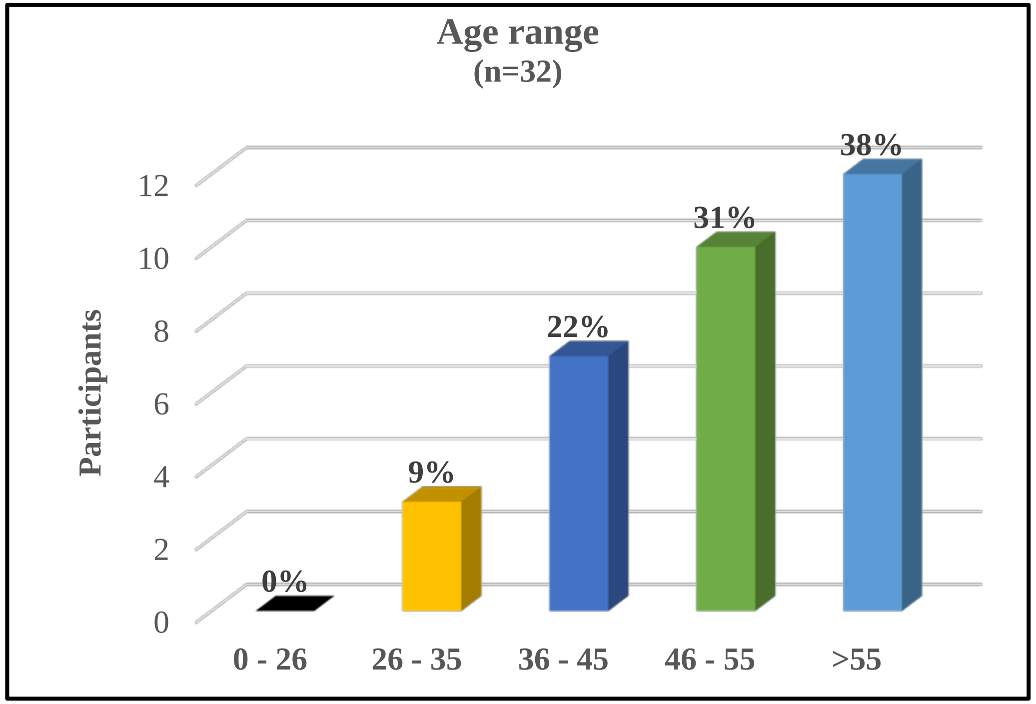

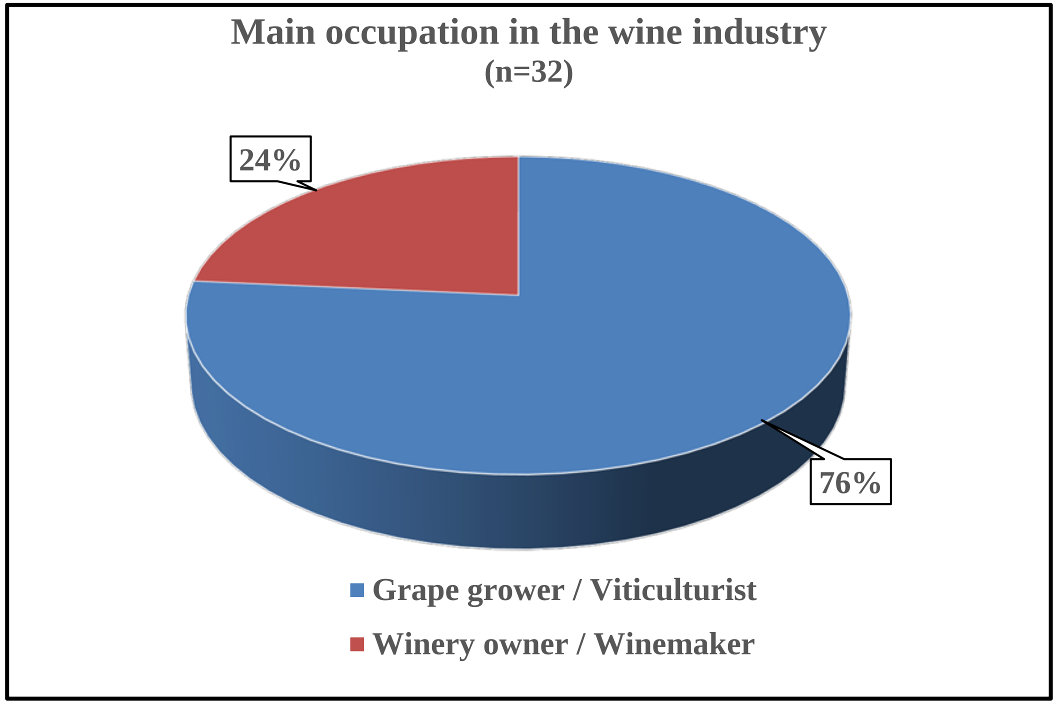

Background/experience

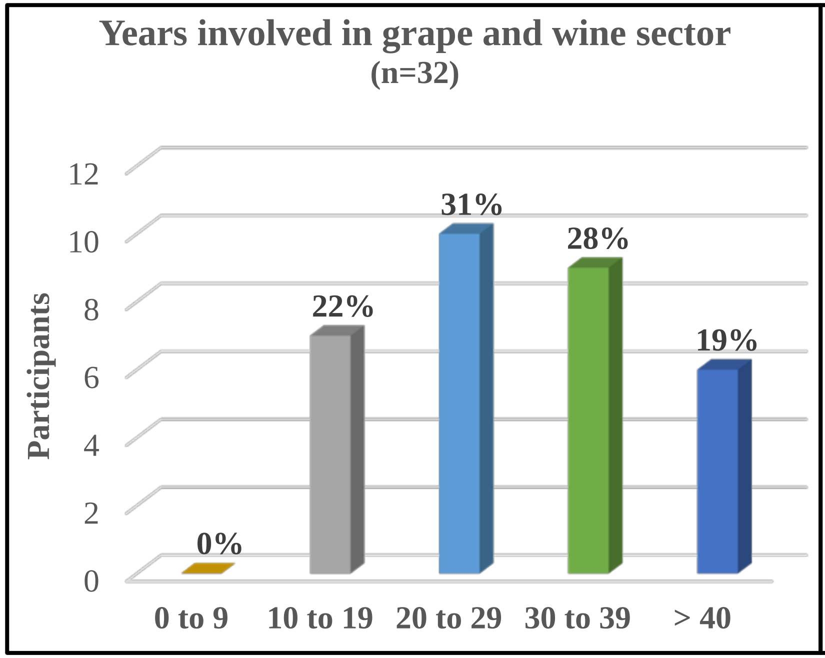

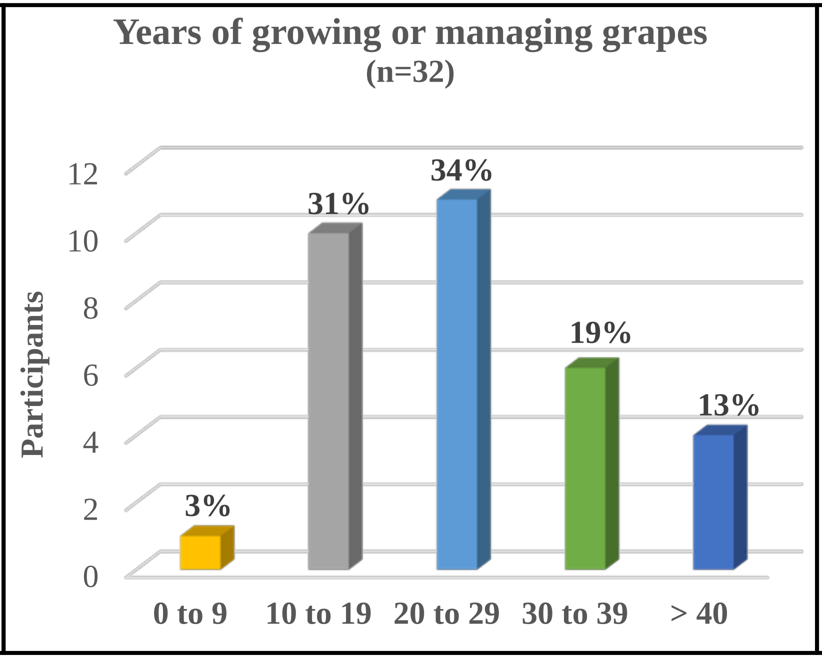

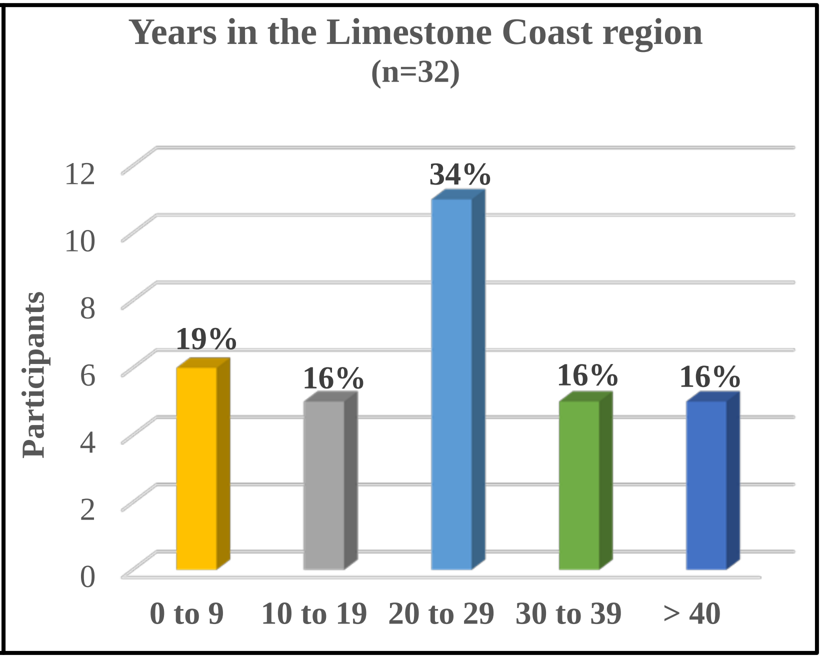

Operation location(s) (sub-regions), Vineyard size

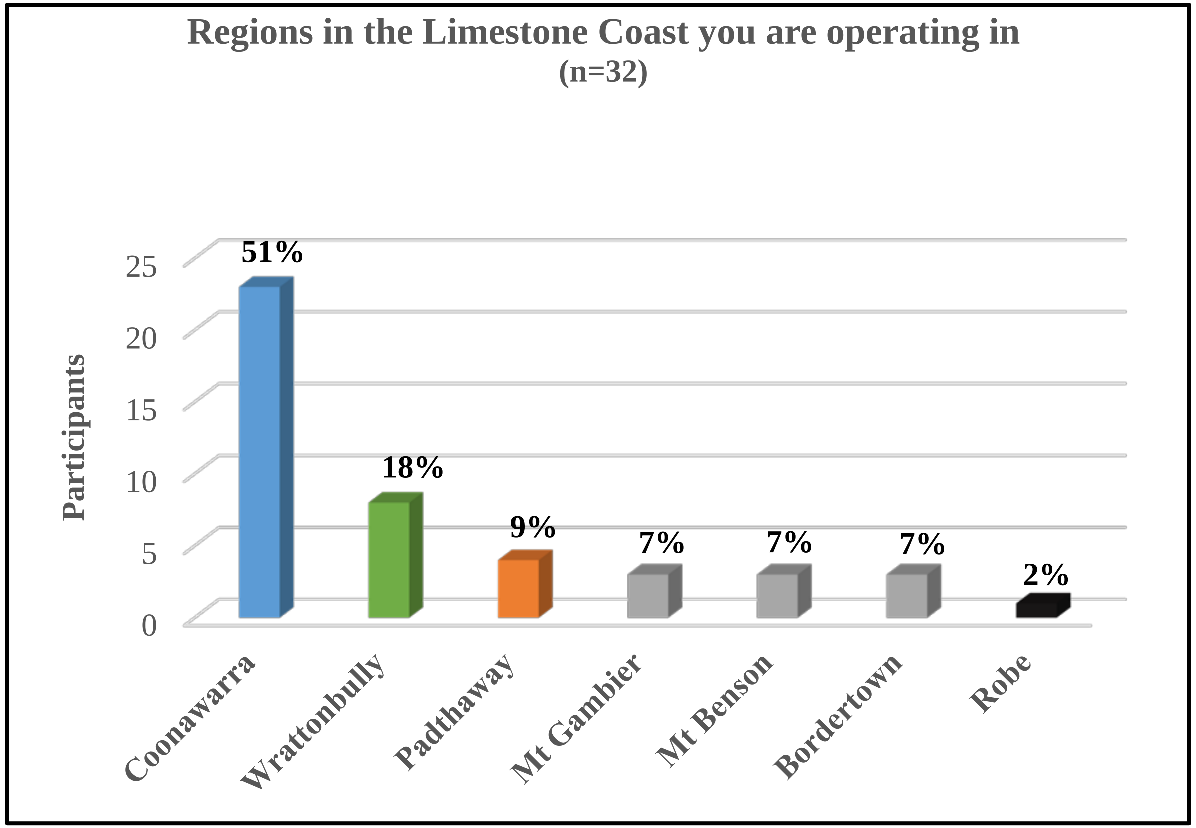

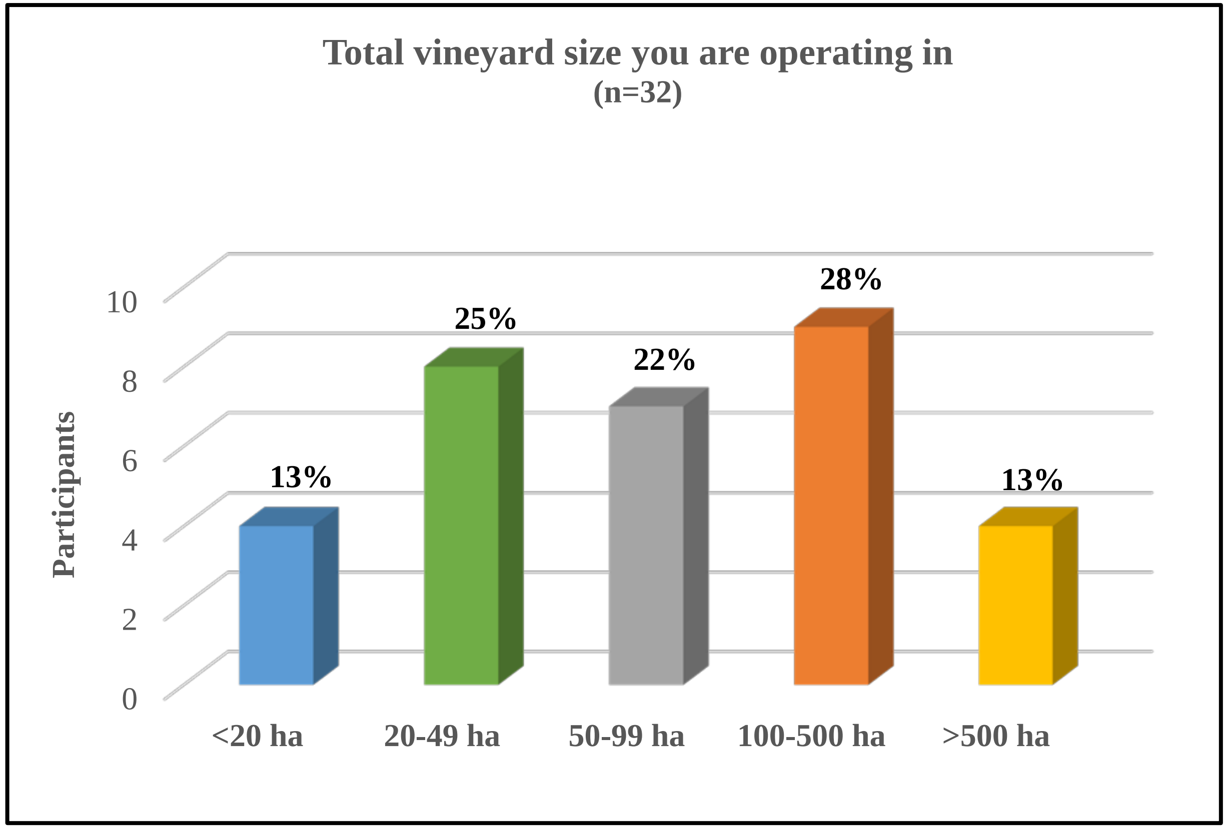

Annual Yields

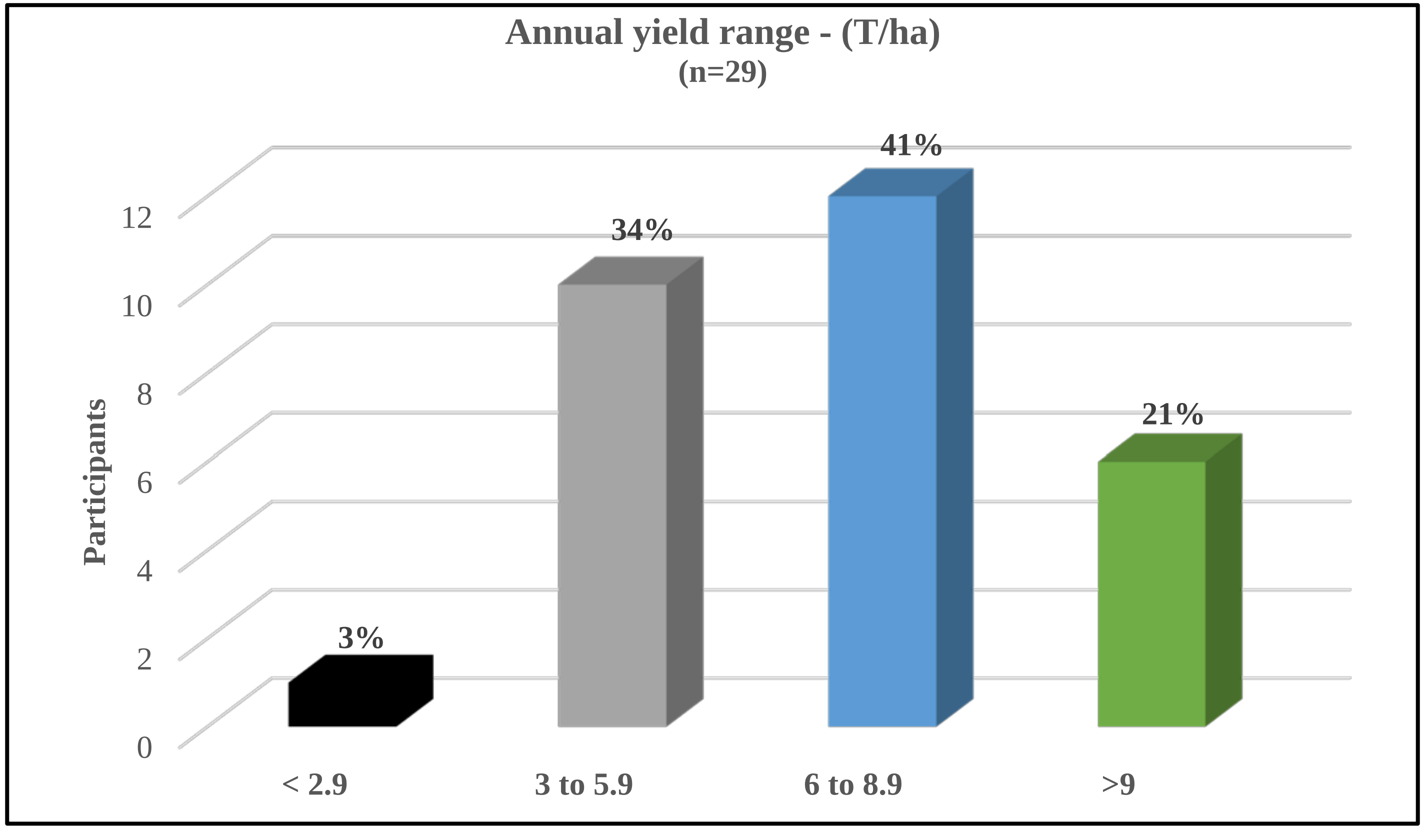

Bordertown and **Padthaway** are **not** included into the graph.
Median: 9 T/ha

Irrigation system type

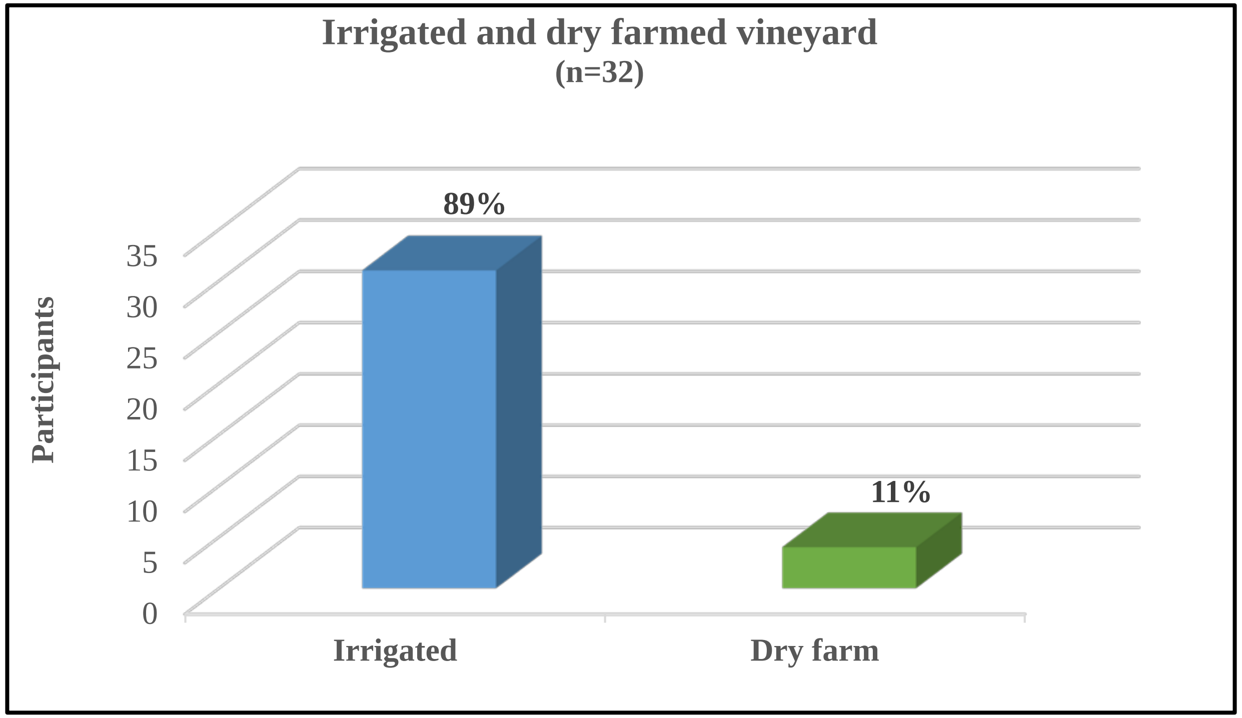

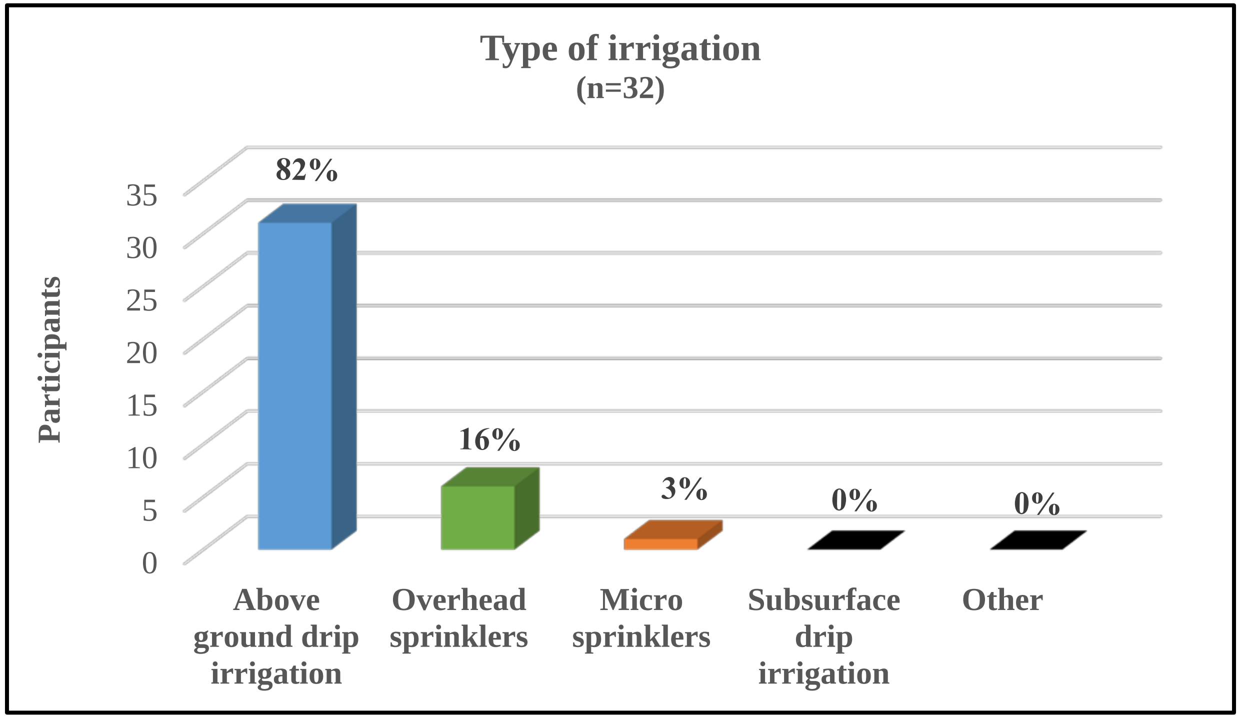

Irrigation Decision-making (time, method)

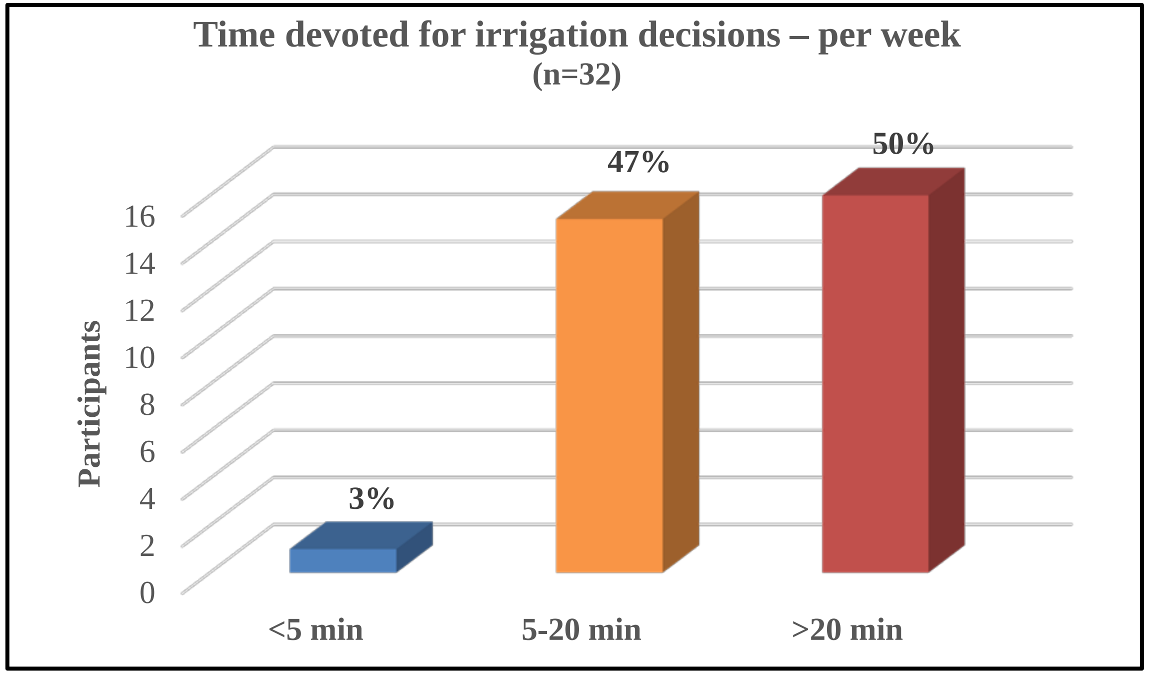

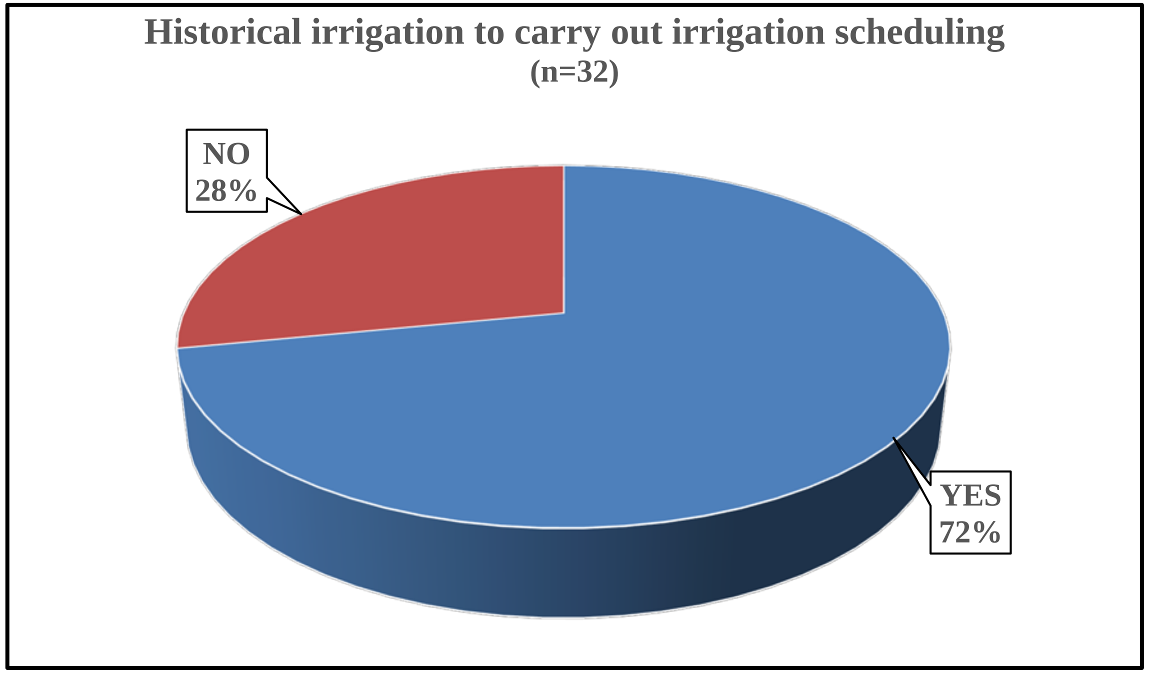

Irrigation Scheduling
Use of Soil moisture and weather forecasts

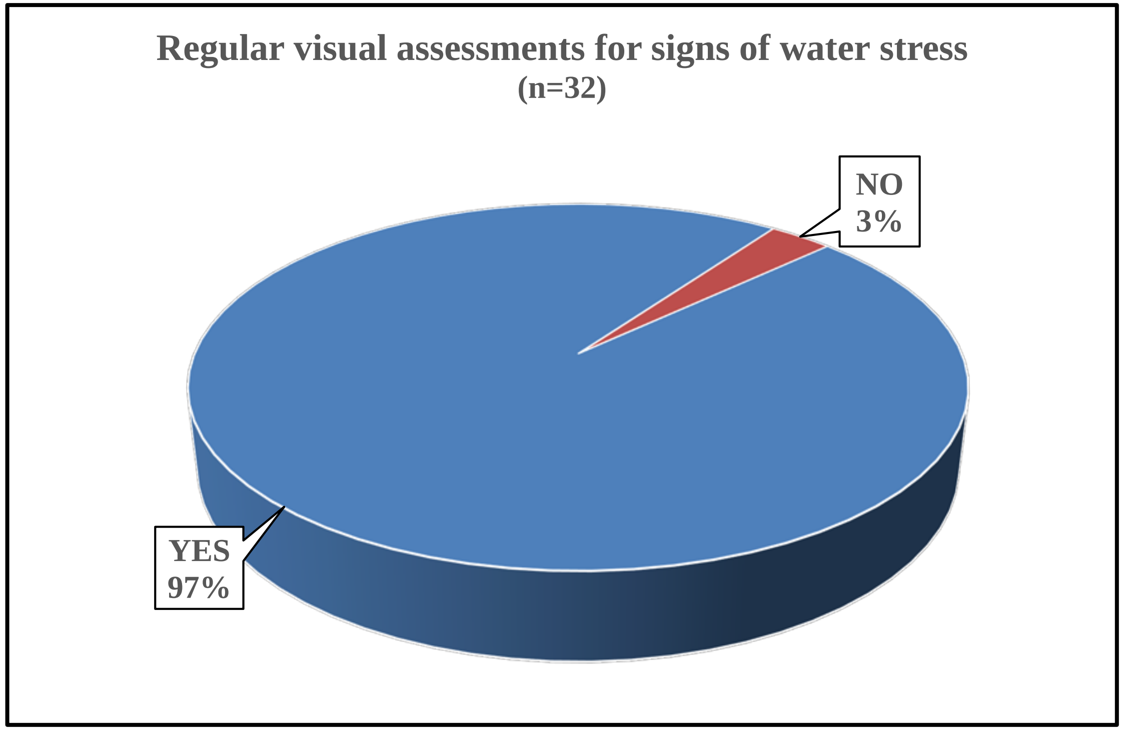

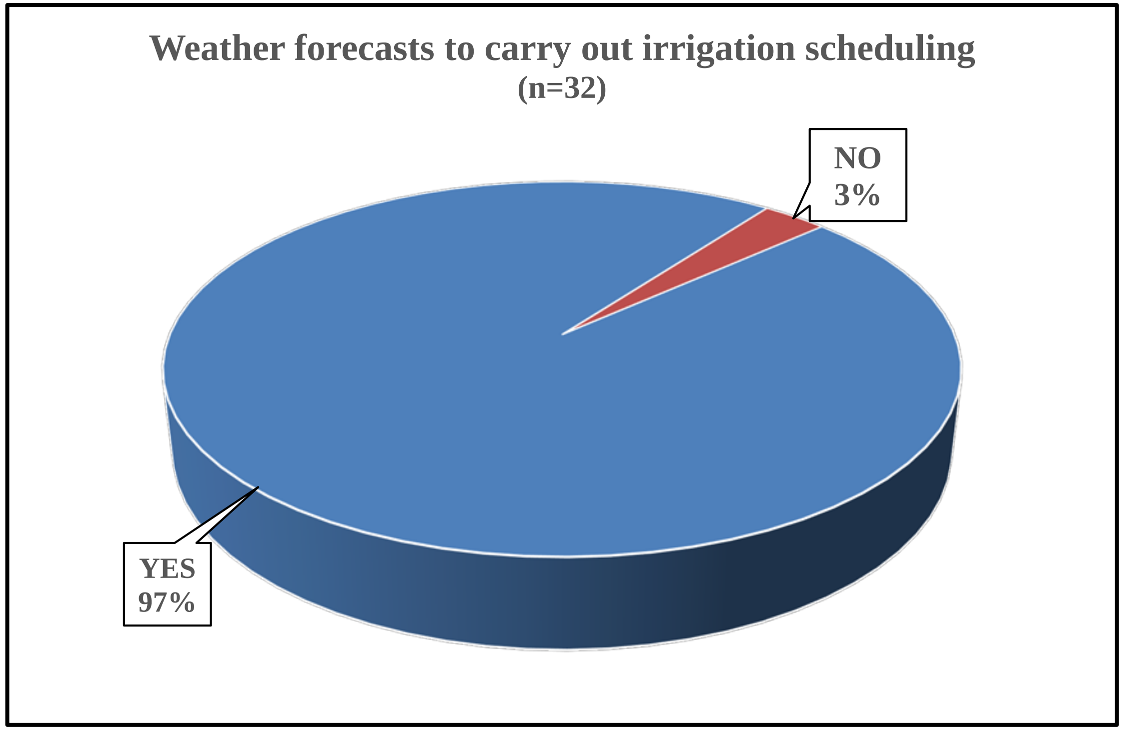

Irrigation Scheduling
Use of Evapotranspiration - ET

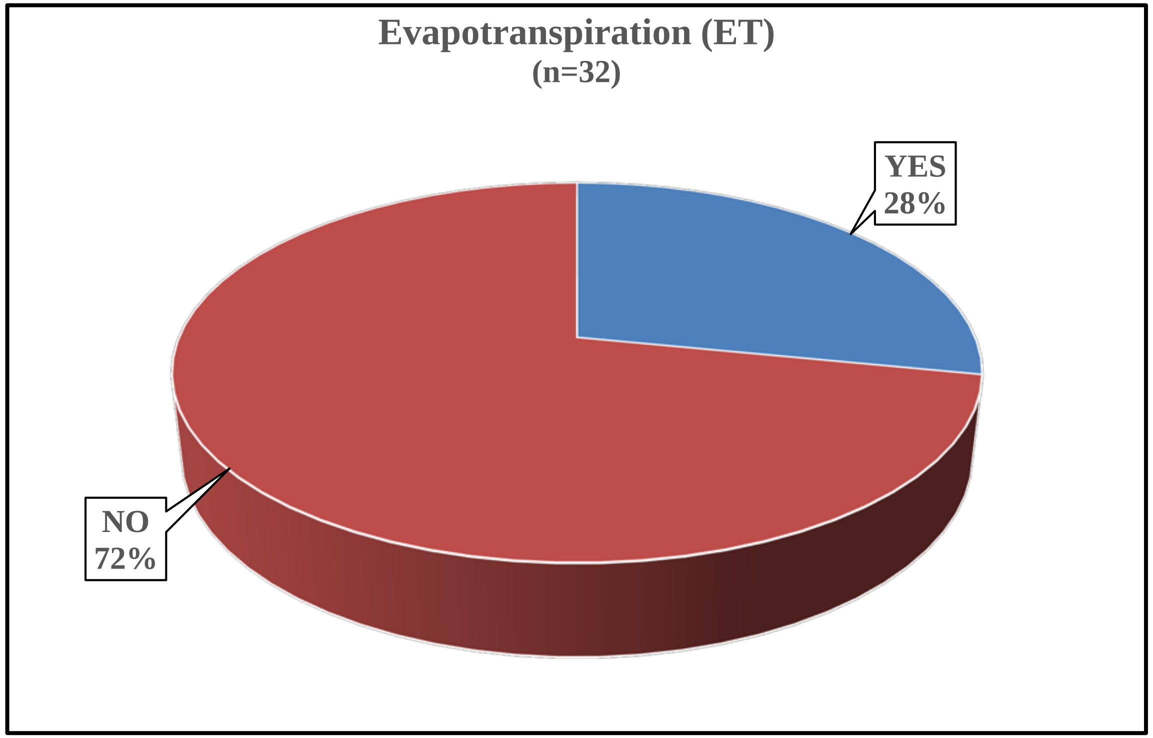

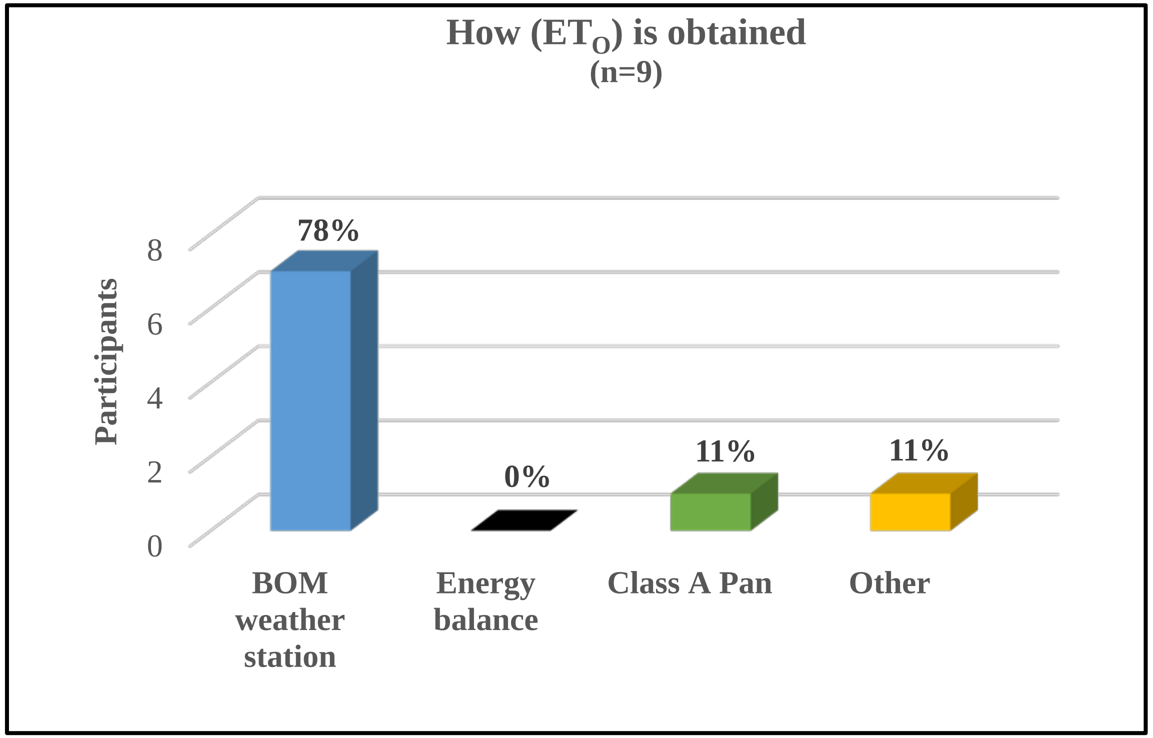

Irrigation Scheduling
Use of Evapotranspiration – ET – Crop Factors

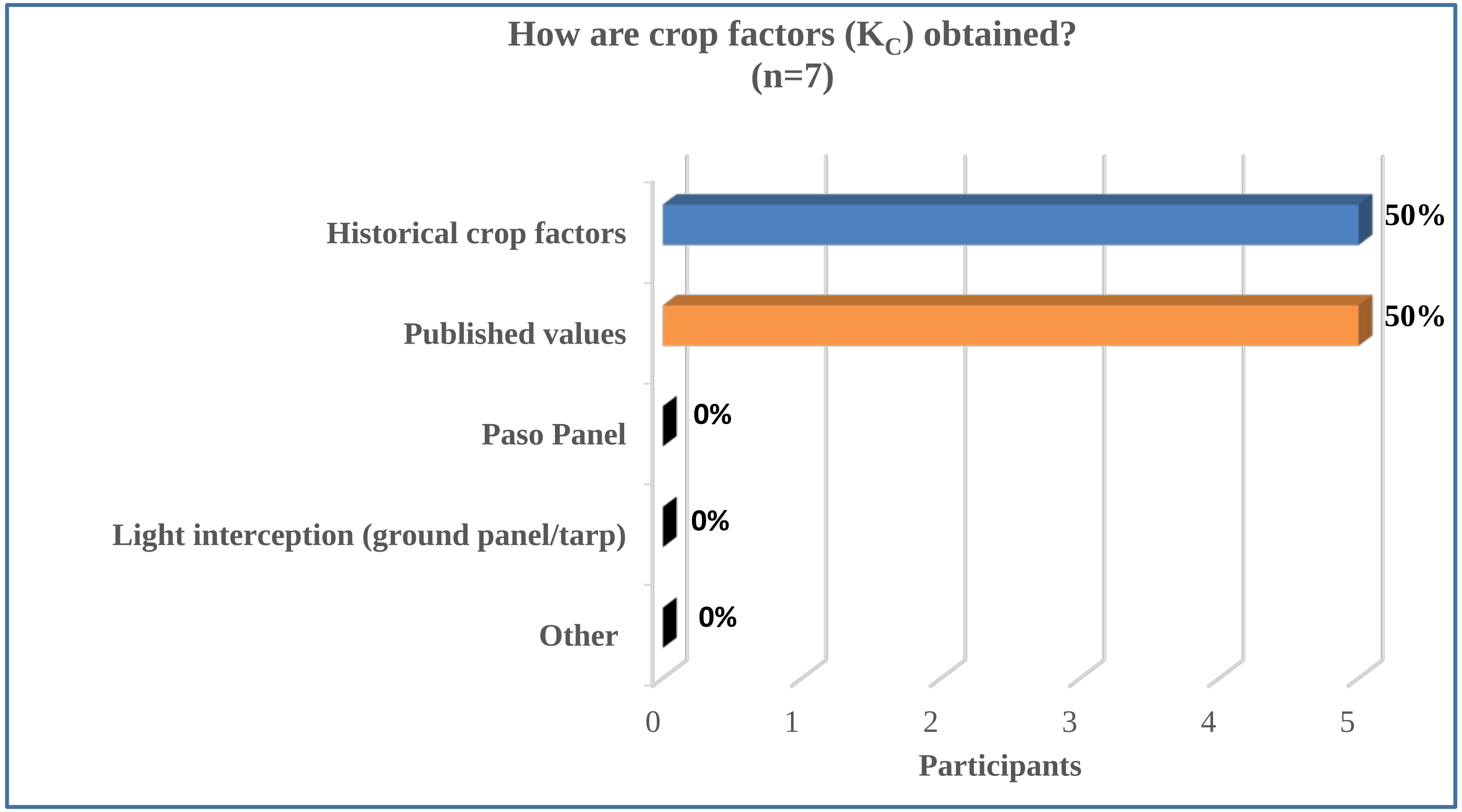

Irrigation Scheduling
Use of Soil moisture sensors

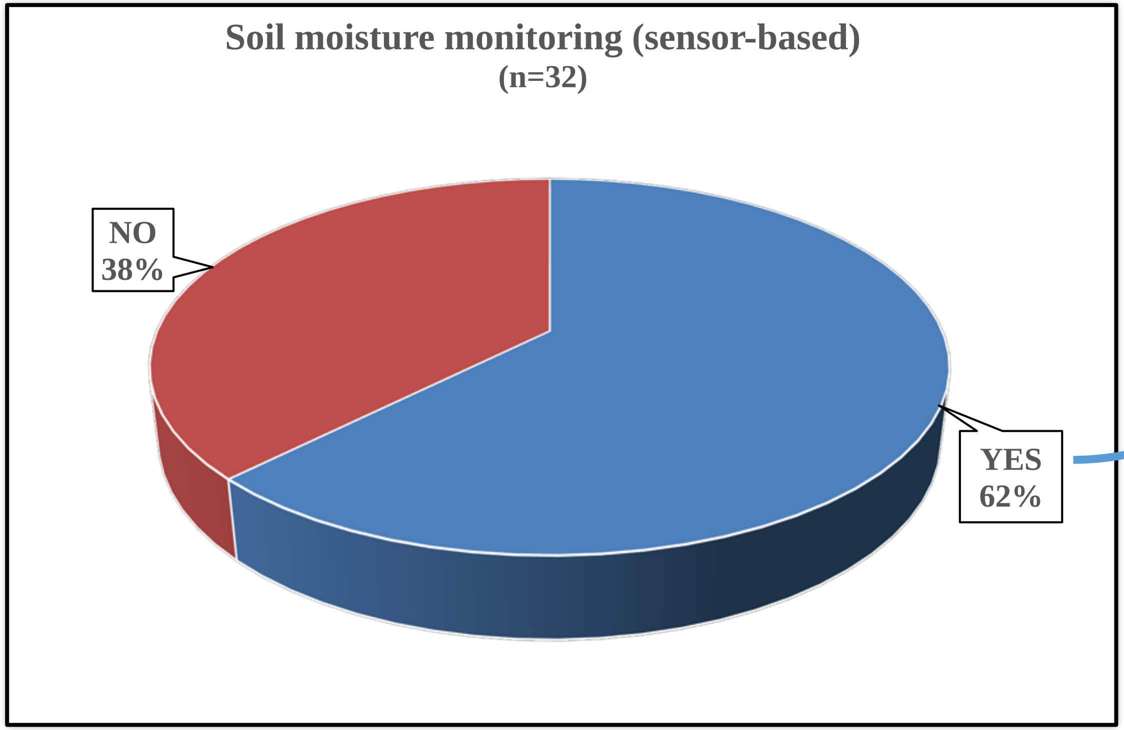

From 62% using soil moisture (n=20);
51 sensors: Soil water tension (e.g. gypsum blocks, tensiometers) **(n=3)**
133 sensors: Volumetric water content (e.g. capacitance probes) **(n=17)**

Irrigation Scheduling
Use of plant-based sensors

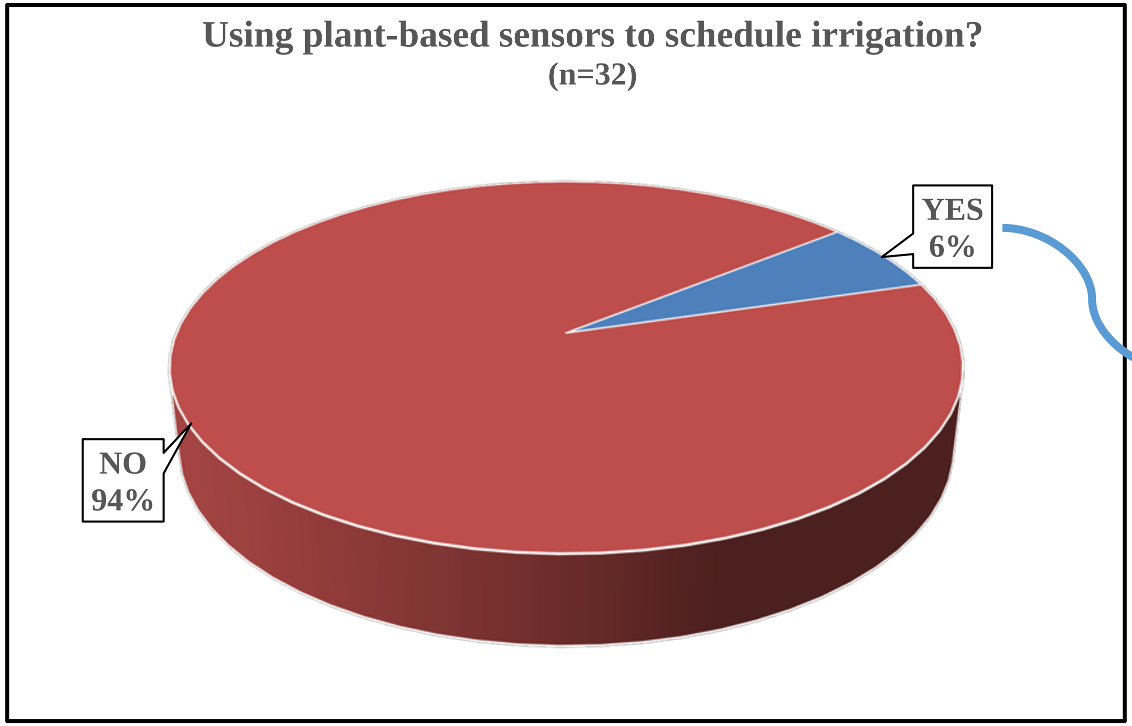

1 grower using leaf/canopy temperature sensor for PWS
1 grower using sapflow sensors for PWS

Irrigation Scheduling
Use of Remote Sensing

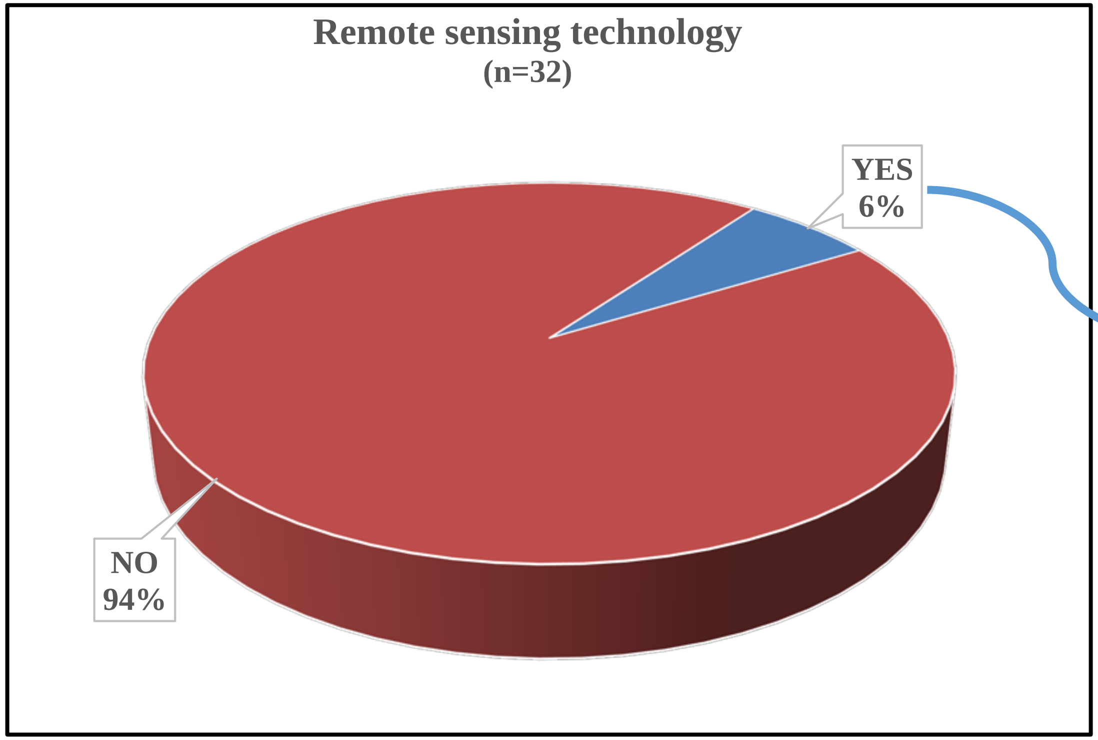

2 growers using satellites

Adoption of AgTech - Barriers

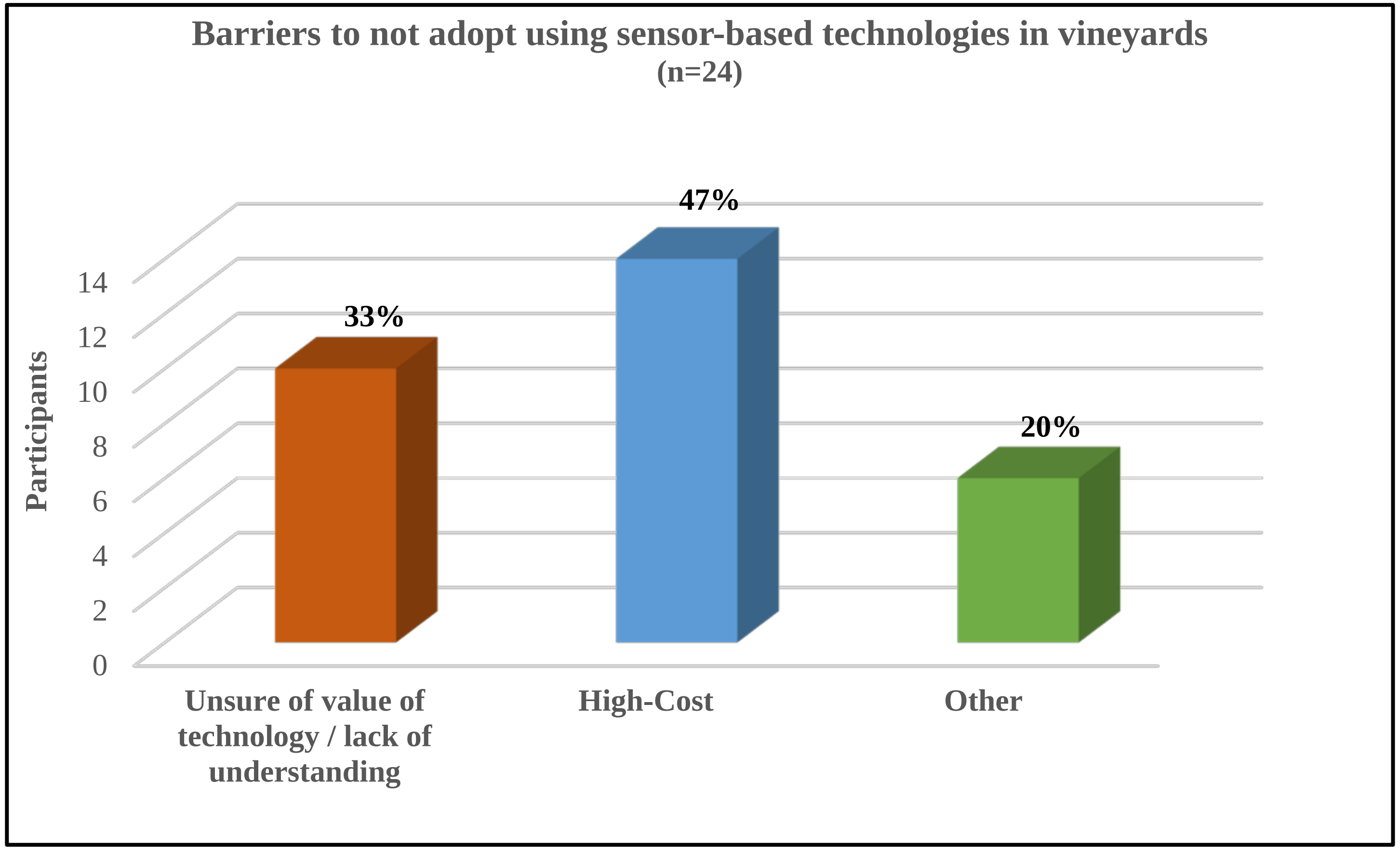

***Other/Comments: "**Use in combination with other devices", "Easy to find information", "Nothing replaces feet in the vineyard", "Use of shovel and boot".

Adoption of AgTech – Investment Plans

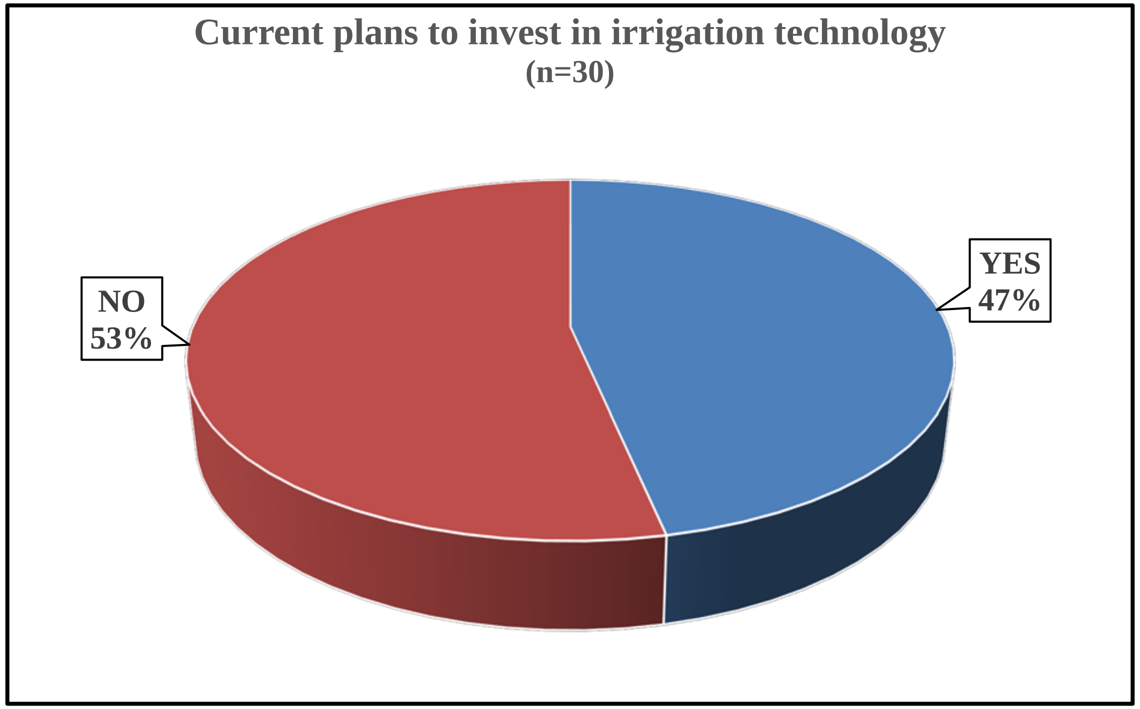

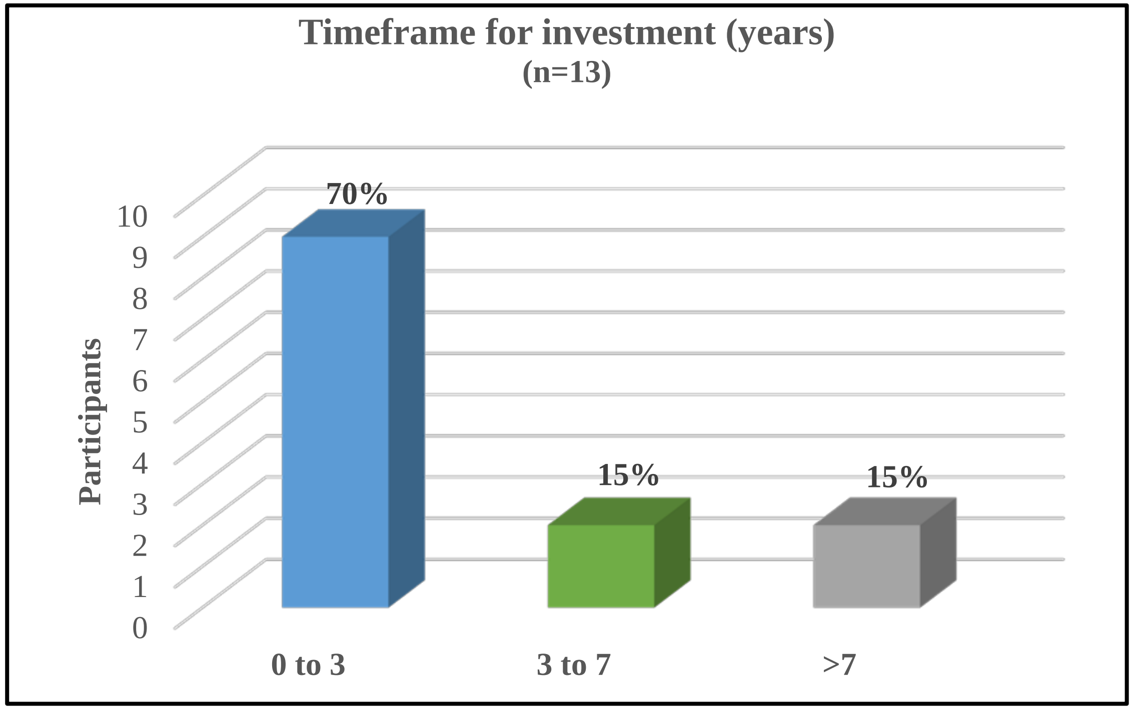

Adoption of AgTech – Future Plans

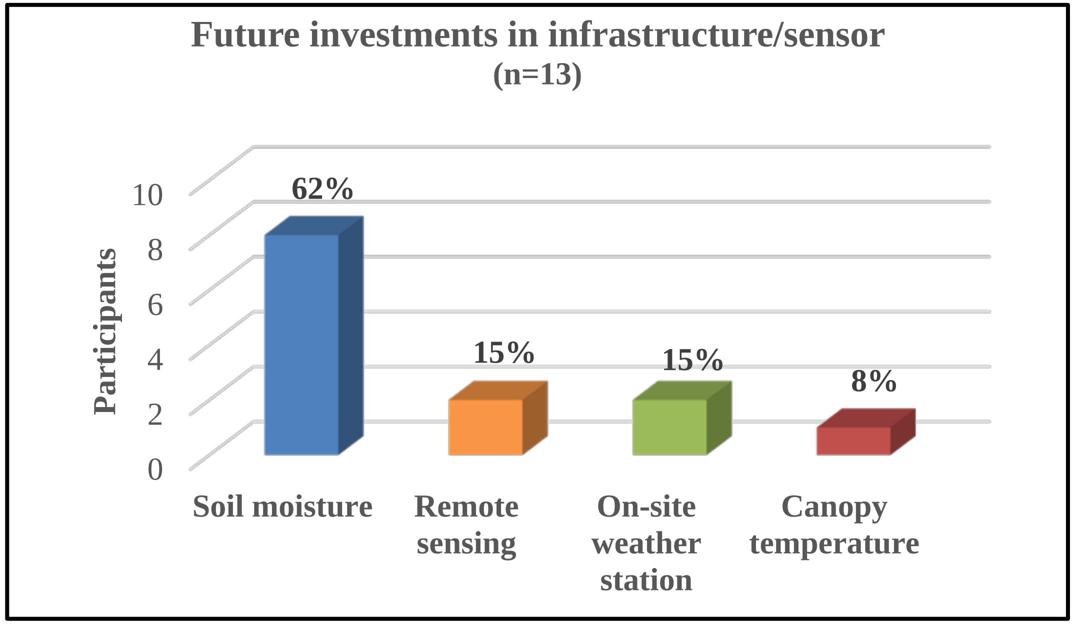

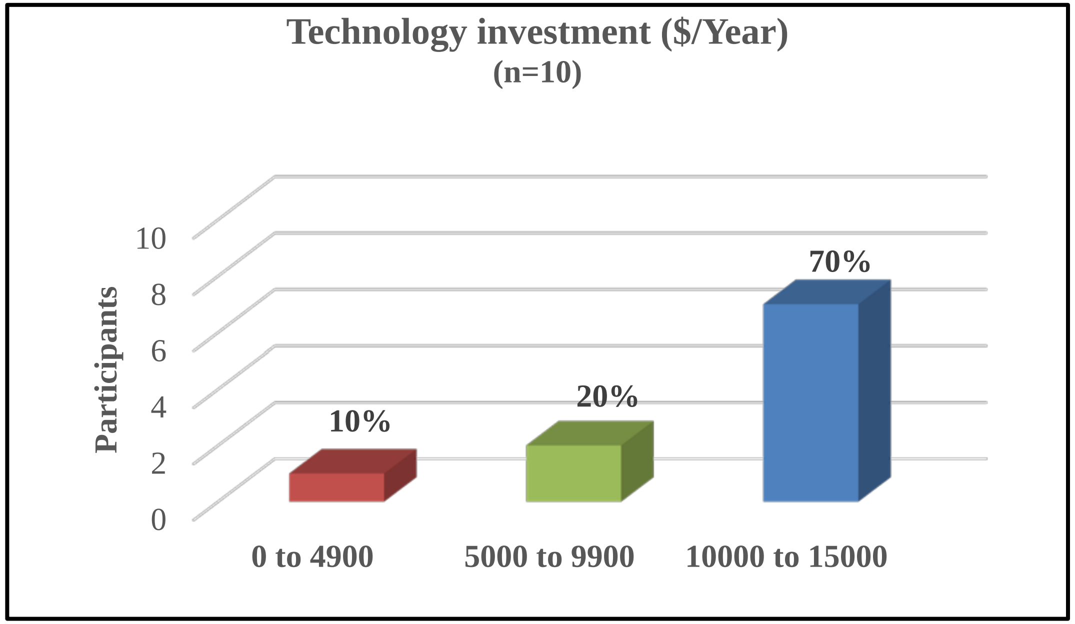

Motivation to continue current irrigation approach

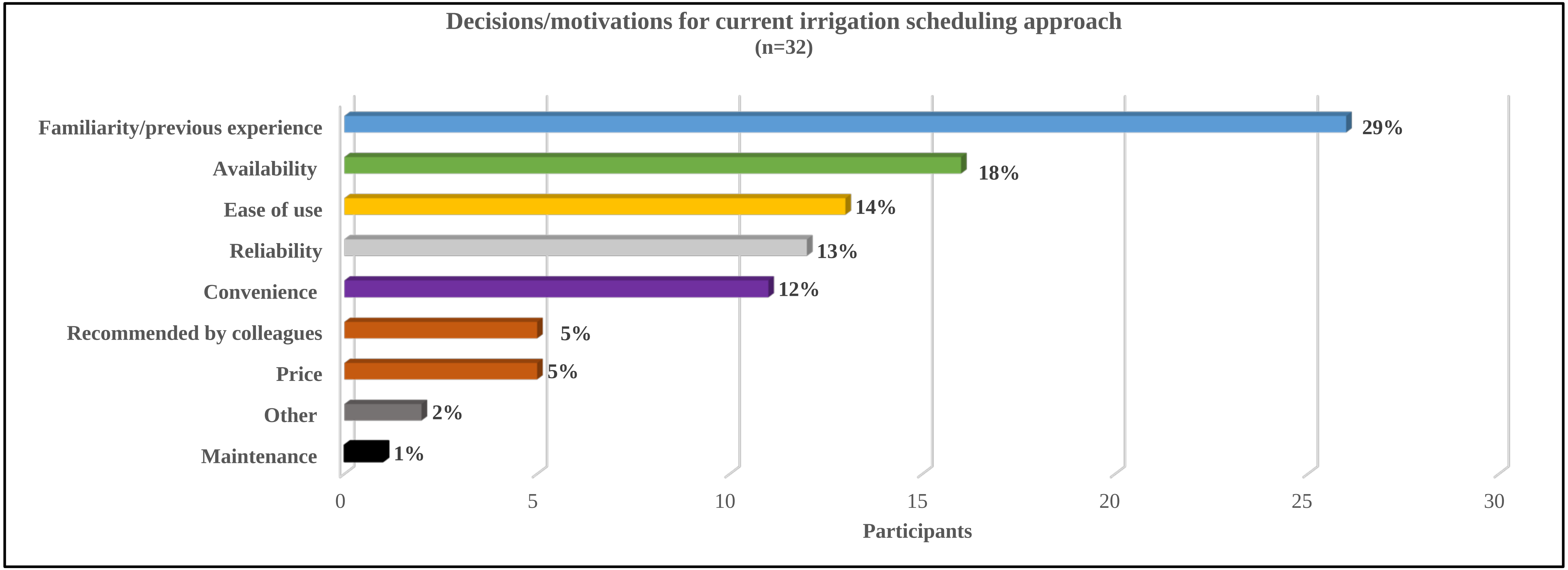

Other/Comments: “It was what was here when we purchased 6 years ago”, “Employ a water monitoring company to do the scheduling recommendations”

Irrigation Scheduling – Concerns

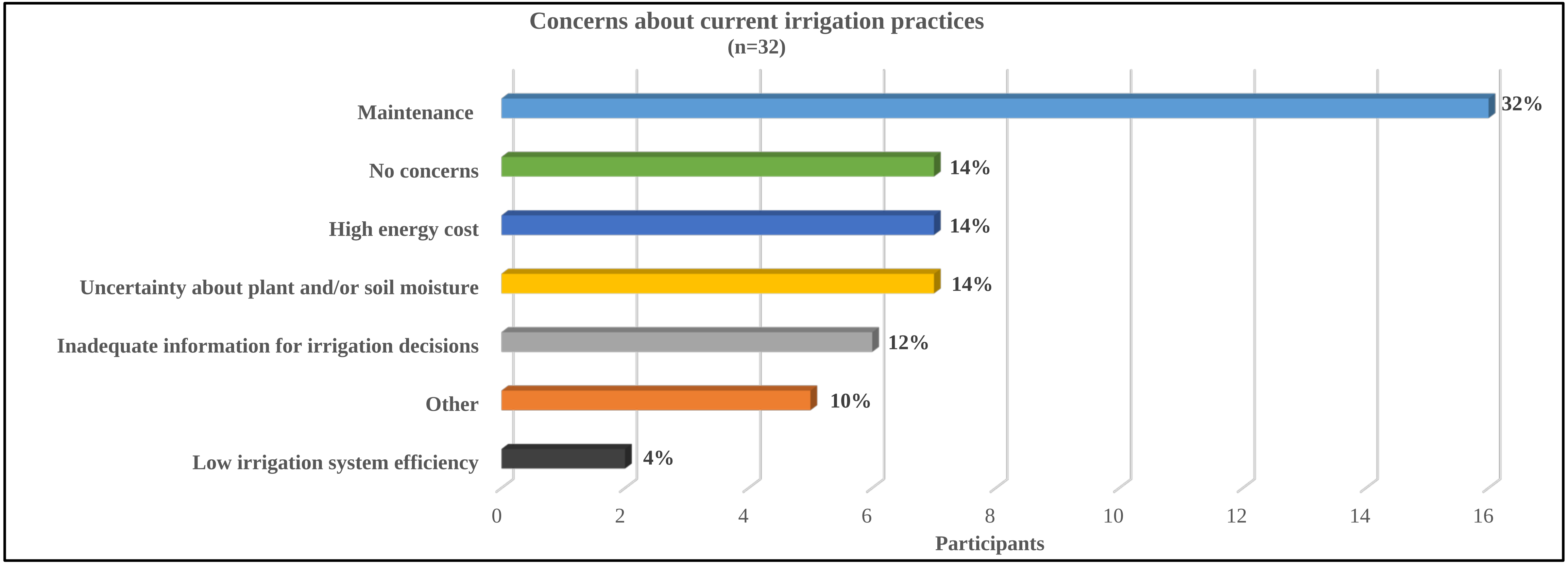

***Other/Comments: "**Sensors often getting damaged or failing", "We feel the monitoring is sometimes giving us information which may be pushed towards the high end of the vine's needs", "Employing a water monitoring company is quite costly", "Looking to maximise water use efficiency while trying to minimise actual volume used", "Salinity & water availability in a changing climate", "We run high stress levels , there is a fine line in running high stress levels if the weather pattern is unstable".

Limestone Coast – Cultivars (from survey responses)

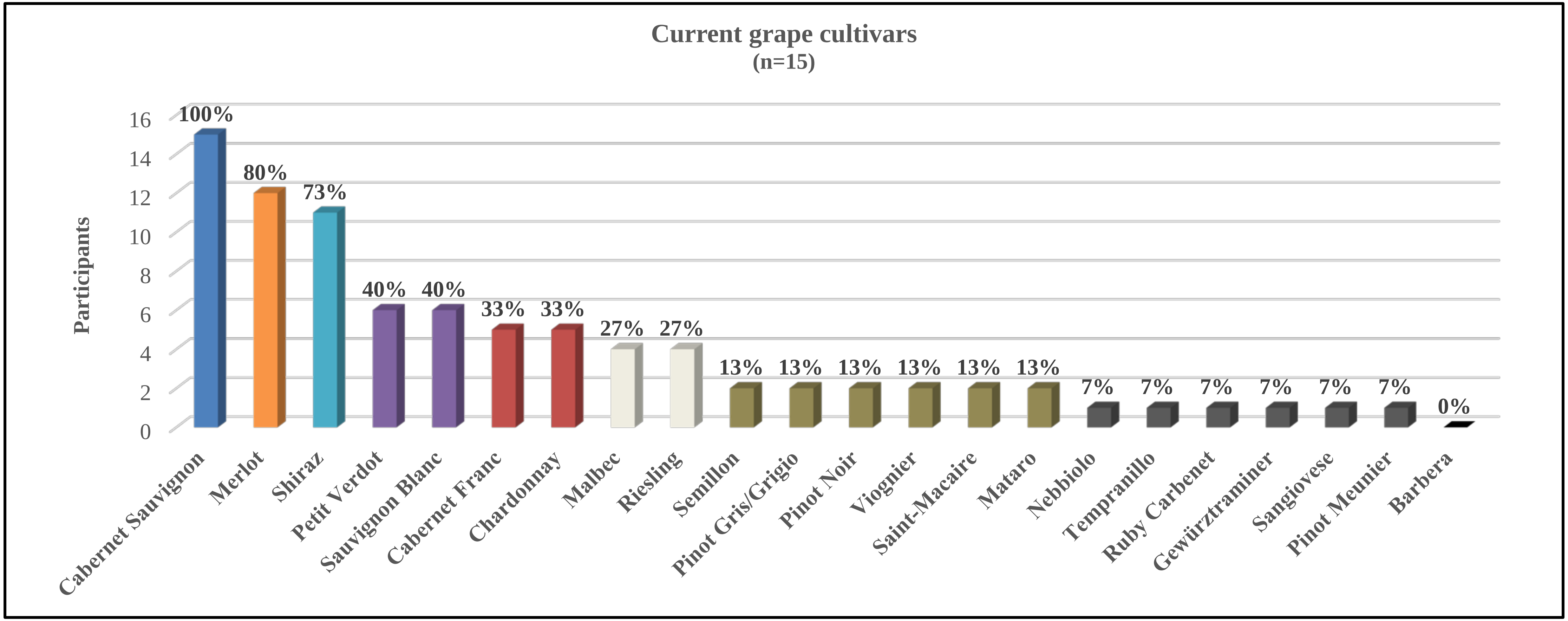

Additional responses received for Coonawarra and Mount Benson

- **Variety:** Cabernet Sauvignon, Merlot, Shiraz and Chardonnay
- **Median size area:** 7.75 ha **Range:** 0.1 to 45 ha
- **Soil type**: Terra Rossa and Rendzina
- **Regions:** Coonawarra and Mount Benson
- **Median vine age:** 24 years **Range:** 7 to 35 years
- **Average vine density:** 1908 vines/ha **Range:** 1580 to 2424 vines/ha
- **82%** do not use deficit irrigation regimes, **18%** using RDI regimes for deficit irrigation **No SDI used**
- **Median irrigation volumes:** 12.5 mm/week **Range**: 6 to 16 mm/week
- **Irrigation frequency:** 1 to 4 per week
- **Seasonal irrigation applied:** 0.2 to 3.0 ML/ha (Mount Benson average 2.75 ML/ha)
- **Annual farmgate value of winegrapes ($/tonne):** approx $2000 **Range:** $1100 to $5000

agronomy

MDPI

Review

A Review of Current and Potential Applications of Remote Sensing to Study the Water Status of Horticultural Crops

Deepak Gautam and Vinay Pagay *

School of Agriculture, Food and Wine, The University of Adelaide, PMB 1, Glen Osmond, SA 5064, Australia; deepak.gautam@adelaide.edu.au

* Correspondence: vinay.pagay@adelaide.edu.au; Tel.: +61-8-83130773

Received: 25 August 2019; Accepted: 9 January 2020; Published: 17 January 2020

Abstract: With increasingly advanced remote sensing systems, more accurate retrievals of crop water status are being made at the individual crop level to aid in precision irrigation. This paper summarises the use of remote sensing for the estimation of water status in horticultural crops. The remote measurements of the water potential, soil moisture, evapotranspiration, canopy 3D structure, and vigour for water status estimation are presented in this comprehensive review. These parameters directly or indirectly provide estimates of crop water status, which is critically important for irrigation management in farms. The review is organised into four main sections: (i) remote sensing platforms; (ii) the remote sensor suite; (iii) techniques adopted for horticultural applications and indicators of water status; and, (iv) case studies of the use of remote sensing in horticultural crops. Finally, the authors' view is presented with regard to future prospects and research gaps in the estimation of the crop water status for precision irrigation.

Keywords: UAS; UAV; drone; unmanned; satellite; water stress; irrigation; vegetation index

1. Introduction

Understanding the water status of crops is important for optimal management and application of water to accommodate for inter and intra-field variability to achieve a specific target, such as maximum water use efficiency, yield, quality, or profitability [1,2]. The importance of optimal water management in agriculture in semi-arid or arid regions has become increasingly important in light of recent water scarcities through reduced allocations, as well as increased demand due to greater areas under production [3,4]. Climate change is expected to further intensify the situation due to the increased frequency of heatwaves and drought episodes [5]. Climate change coupled with the necessity to increase food production due to an increase in global population has placed pressure on horticultural sector to improve efficiencies in resources use, e.g., water, for sustainable farming [6–10]. Horticultural crops will have to produce more 'crop-per-drop' in the face of limited water resources. Informed management of water resources whilst maintaining or increasing crop quality and yield are the primary goals of irrigation scheduling in horticulture. These goals can be achieved by improving our understanding of the water status of the crops at key phenological stages of development.

Traditional decision-making for irrigation of horticultural crops includes using information from a combination of sources such as historical regimes, soil moisture measurements, visual assessments of soil and/or crop, weather data including evapotranspiration (ET), and measurements of crop water status using direct-, proximal- or remote-sensing techniques [11–13]. Some growers undertake routine ground-based measurements, e.g., pressure chamber, for estimation of crop water status to make decisions on irrigation [14–16]. These ground-based measurements are robust; however, destructive, cumbersome, and expensive to acquire a reasonable amount of data [14,16–18]. Consequently, the measured leaf is assumed to represent the average population of leaves of the individual crop, and a few crops are assumed to represent the average population of the entire irrigation block. As a result, over- or under-watering can occur, which can lower yield and fruit quality [19–22]. This is especially evident for non-homogenous blocks where spatial variability of soil and water status is expected [23–25].

To address some of the limitations of ground-based measurements, remote measurement techniques were introduced with capabilities to measure at higher spatial resolution, larger area, and on a regular basis [26–29]. Remote sensing, in particular, unmanned aircraft systems (UAS), presents a flexible platform to deploy on-demand sensors as a tool to efficiently and non-destructively measure crop water status [30]. Using thermal and spectral signatures, remote sensing techniques can be used to characterise a crop's water status. Knowledge of crop water status allows growers to more efficiently schedule irrigation (i.e., when and how much water to apply). In this regard, UAS platforms provide a convenient methodology to monitor the water status across a farm, both spatially and temporally at the canopy level [31–33]. The spectral, spatial, and temporal flexibility offered by UAS-based remote sensing may in future assist growers in irrigation decision-making [34,35].

This review provides an overview of the application of remote sensing to understand the crop's water status (e.g., leaf/stem water potential, leaf/canopy conductance), soil moisture, ET, and physiological attributes, all of which can contribute to understanding the crop's water status to implement precision irrigation. Although the key focus of this review is UAS-based remote sensing, a comparison has been undertaken with other remote sensing platforms, such as earth observation satellites, which are being increasingly used to acquire similar information. In the following sections, we provide an overview of the most common remote sensing platforms in horticulture, various sensors used for remote sensing, and several predictive indices of crop water status. Two case studies of remote sensing in horticultural crops, grapevine and almond, are then presented followed by an overview of the current research gaps and future prospects.

2. Remote Sensing Platforms

Ground-based direct or proximal sensors acquire instantaneous water status measurement from a spatial location. For decision-making purposes, the data is generally collected from multiple locations across a field, which allows geospatial interpolation, such as kriging, to be applied [36–38]. This scale of data collection is, however, cumbersome, inefficient, and error-prone, especially for water status measurements of large areas [17]. Monitoring and observing farms at a larger spatial scale prompted the launch of several earth observation satellite systems that typically operate at an altitude of 180–2000 km [39]. Manned high-altitude aircraft (operating within few km) and, more recently, UAS (operating under 120 m) filled the spatial gap between high-resolution ground measurements and relatively low-resolution satellite measurements [40,41]. In the context of water status estimation for horticultural crops, all the aforementioned remote sensing platforms are utilised depending on the user requirements [23,42,43]. Each remote sensing platform has its own advantage and shortcomings. The decision to obtain remote sensing crop water status data from one or more of these platforms will depend on the spatial and temporal resolution desired. Satellite and manned aircraft can be useful for regional-scale characterisation, whereas UAS can be more useful to map the intra-field variability. Vehicle-based ground systems also possess similar measurement capabilities, like remote sensing, however, at a smaller scale [44,45]. These systems can move within the horticultural rows obtaining water status measurements of adjacent plants while the vehicle is moving, enabling them to cover a relatively larger area as compared to ground-based direct measurements [46–48].

2.1. Satellite Systems

The use of satellite systems for remote sensing started with the launch of Landsat-1 in 1972 [39,49]. The subsequent launch of SPOT-1 in 1986 and Ikonos in 1999 opened the era of commercial satellite systems that resulted in rapid improvement in imaging performance, including spatial and spectral resolution [50]. Continued launch of satellites from the same families, with newer sensor models and improved capability, resulted in the formation of satellite constellations (e.g., Landsat, Sentinel, SPOT, RapidEye, GeoEye/WorldView families). The satellite constellation substantially improved the revisit cycle of the satellite system [51]. Recently, the miniature form of the satellite termed Nanosat or Cubesat has been developed, which can be deployed on the same orbit in a large number (20s–100s), enabling frequent and high-resolution data acquisition (e.g., Dove satellite from Planet Labs) [52].

The earth observation satellite system, such as Landsat, Sentinel, MODIS, RapidEye, and GeoEye, have been used to study horticultural crops (Table 1). These satellite system offer camera systems with spectral bands readily available in visible, near infrared (NIR), short-wave infrared (SWIR), and thermal infrared (TIR). The measurement in these bands provides opportunities to study a crop's water status indirectly via, for example, calculation of the normalised difference vegetation index (NDVI), crop water stress index (CWSI), and ET [8–10] at the field- and regional-scales.

Table 1. Some satellite systems that have been used to study the water status of horticultural crops.

Satellites	Band Numbers: Band Designation	Spatial Resolution (m)	Revisit Cycle
Landsat 7	8: V ^{3}, NIR ^{1}, SWIR ^{2}, TIR ^{1}, Pan ^{1}	15–60	16 days
Landsat 8	11: C ^{1}, V ^{3}, NIR ^{1}, SWIR ^{2}, Pan ^{1}, Ci ^{1}, TIR ^{2}	15–100	16 days
Sentinel-2	13: C ^{1}, V ^{3}, RE ^{3}, NIR ^{2}, WV ^{1}, Ci ^{1}, SWIR ^{2}	10–60	5 days
Spot-6 and-7	5: Pan ^{1}, V ^{3}, NIR ^{1}	1.5	1 day
RapidEye	5: V ^{3}, NIR ^{1}, RE ^{1}	5	5.5 days
GeoEye-1	5: Pan ^{1}, V ^{3}, NIR ^{1}	0.41–2	3 days

Note: Superscript integers $^{1, 2, 3}$ represent the number of bands; V = visible, NIR = near infrared, SWIR = short-wave infrared, TIR = thermal infrared, Pan = panchromatic, C = coastal, Ci = cirrus, RE = red edge, WV = water vapour.

The reflected/emitted electromagnetic energy from the crop reaching the sensor is recorded at a specific wavelength. The width of the observed wavelength expressed in full width at half maximum (FWHM) is called spectral resolution. The number of observed bands and the spectral resolution indicates the ability of the satellite to resolve spectral features on the earth's surface. Commonly used earth observation satellite systems possess between four and 15 bands with approximately 20–200 nm FWHM spectral resolution. The bands are generally designated for the visible and NIR region with extended capabilities in SWIR, TIR, as well as red edge region (Table 1). The most widely used band combinations to study the water status of vegetation are the visible, NIR and TIR bands [23,25,53,54]. With the plethora of satellite systems currently available, user requirements on band combination may be achieved by using multiple satellites. However, acquiring an extra or a narrower band to the existing capabilities is not possible.

The ground distance covered per pixel of the satellite image is called the spatial resolution, whereby, a higher spatial resolution indicates a smaller ground distance. Existing satellite systems, due to their lower spatial resolution and large coverage, are suited to study larger regions [55]. For a smaller observation area, such as a farm block, an irrigation zone, a single row of the horticultural crop, or a single canopy, this spatial resolution is considered sub-optimal. Often, a pixel of the satellite image comprises of multiple rows and multiple canopies of horticultural crops [42,56]. Thus, the spectral response on a single pixel of the satellite image includes a mixed spectral signal from the canopy, inter-row vegetation and/or bare soil. The mixed-pixel is particularly unavoidable in horticultural crops with large inter-row surfaces, introducing errors in satellite-based estimations [42,56]. Improving the spatial resolution from freely available Landsat/Sentinel satellites (spatial resolution 10–15 m) to such as WorldView-3 (spatial resolution 0.3 m), does not necessarily resolve single canopies of many horticultural crops.

Current satellite systems generally offer a temporal resolution of about 1–2 weeks this resolution corresponds to the satellite's revisit interval (Table 1). For example, freely available Landsat-8 and Sentinel-2 offer revisit cycles of 16 and 5 days, respectively. Although the MODIS sensor on NASA's Terra and Aqua satellites offer a greater temporal resolution (1–2 days), its spatial resolution is relatively coarse (250 m–1 km) to be valuable for horticulture [25]. The revisit cycle of satellites does not alone represent the timeframe on which the data can be interpreted. For instance, post-data acquisition, there are often delays in data transfer to the ground station, handling, and delivery to the end user. The end user then needs to process the data before making an interpretation. Such processing can be a combination of atmospheric, radiometric, and geometric corrections, where applicable [57,58]. Furthermore, as the agricultural applications of the satellite imagery are illumination sensitive and weather dependent, conditions have to be optimal on the satellite revisit day to avoid data corruption due to, for example, cloud cover [23,53]. Cloud corrupted data (~55% of the land area is covered by cloud at any one time [59]) will require users to wait for the next revisit to attempt the data acquisition. Time-series image fusion techniques, such as the spatial and temporal adaptive reflectance fusion model, can improve the spatial and temporal resolution of the satellite data [60,61]. These fusion techniques blend the frequent (however low-resolution) with higher-resolution (but infrequent) satellite data [62,63]. The result combines the best aspects of multiple satellite systems to produce frequent and higher-resolution data, which can be useful for timely monitoring of water status.

The clear advantage of the satellite system is the ability to capture data at a large scale and at an affordable cost (e.g., the user can download Landsat and Sentinel data for free). The compromise with the satellite data is in spatial resolution, as well as the relatively long revisit cycle (in the order of days to weeks), making the data less than ideal for specific applications, e.g., irrigation scheduling.

2.2. Manned Aircraft System

Operating within few kilometres above ground level, manned aircraft have been used to remotely acquire agricultural data at higher spatial detail (compared to the satellites) and over a larger region (compared to UAS) [42,64]. Light fixed-wing aircraft and helicopters are the commonly used manned aircraft employed in agricultural remote sensing. The fixed-wing aircraft generally flies higher and faster, enabling the coverage of a larger area, whereas the helicopters are traditionally flown lower and slower, enabling a spatially detailed observation. A significant advantage of the manned aircraft, compared to UAS, lies in their ability to carry heavier high-grade sensors, such as AVIRIS, HyPlant, HySpex SWIR-384, Specim AisaFENIX, and Riegl LMS Q240i-60 [65–67]. The use of manned aircraft is, however, limited by high operational complexity, safety regulations, scheduling inflexibility, costs, and product turnaround time. As a result, these platforms are barely used as compared to the recent surge in the use of UAS, specifically for horticultural crops [68–70].

In horticulture, manned aircraft was used to characterise olive and peach canopy temperature and water stress using specific thermal bands (10.069 μm and 12.347 μm) of a wideband (0.43–12.5 μm) airborne hyperspectral camera system [71,72]. This work found moderate correlations (R^2 = 0.45–0.57) of ground vs. aerial olive canopy temperature measurements [72], and high correlations (R^2 = 0.94) of canopy temperature vs. peach fruit size (diameter) [71]. The advantage of manned aircraft for remote sensing of a large region was highlighted in recent work that characterised regional-scale grapevine (*Vitis vinifera* L.) water stress responses of two cultivars, Shiraz and Cabernet Sauvignon, in Australia [64]. Airborne thermal imaging was able to discriminate between the two cultivars based on their water status responses to soil moisture availability (Figure 1).

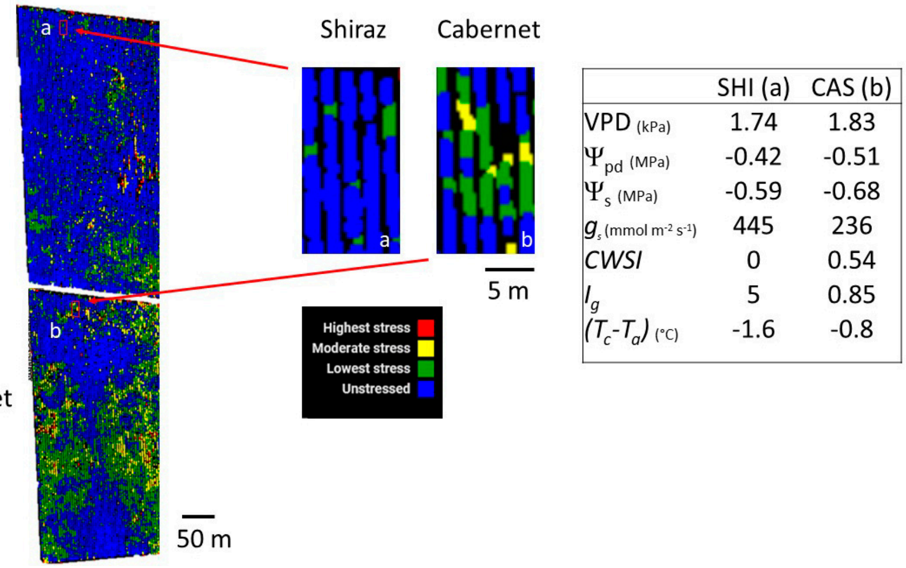

Figure 1. Water status of Shiraz and Cabernet Sauvignon under similar soil moisture as captured from manned aircraft [64].

2.3. Unmanned Aircraft Systems

Both the fixed-wing and the rotary-wing variant of UASs are used in agricultural remote sensing. Each variant has its advantages and shortcomings vis-à-vis sensor payload, flexibility, and coverage. In this regard, the literature provides a list of state-of-the-art UAS [73], their categorisation [74], and overview of structural characteristics, as well as flight parameters [75], in the context of agricultural use. Depending on the number of rotors, a rotary-wing UAS can be a helicopter, a quadcopter, a hexacopter, or an octocopter, among others. Rotary-wing UAS are more agile and can fly with a higher degree of freedom [76], while fixed-wing UAS needs to be moving forward at a certain speed to maintain thrust. As a result, rotary-wing UAS provides flexibility and specific capabilities, such as hovering, vertical take-off and landing, vertical (up and down) motions, or return to the previous location. On the contrary, fixed-wing UAS fly faster, carry heavier payloads, and have greater flying time enabling coverage of larger areas in a single flight [77]. Recently developed fixed-wing UAS with vertical take-off and landing capabilities, such as BirdEyeView FireFly6 PRO, Elipse VTOL-PPK, and Carbonix Volanti, captures the pros of both fixed-wing and rotary-wing, making them a promising platform for agricultural purposes. In the context of precision agriculture, the application of UAS, their future prospects, and knowledge gaps are discussed in [53,78–81]. While many horticultural crops have been studied using UAS technology, the most studied horticultural crops are vineyards [31,82–84], citrus [85,86], peach [32,33], olive [18,87,88], pistachio [89,90], and almond [91–94], among others [95–99]. Some of the UAS types used for water status studies of horticultural crops are shown in Figure 2.

(**a**) (**b**)

(**c**) (**d**)

Figure 2. Examples of unmanned aircraft systems (UAS) used to study water status in horticulture crops: (**a**) hexacopter equipped with RGB, multispectral and thermal camera at The University of Adelaide, Adelaide, Australia (**b**) quadcopter equipped with a thermal and multispectral camera [100], (**c**) fixed-wing aircraft used for GRAPEX project to carry RGB, thermal and monochrome camera with narrowband filters [101], and (**d**) helicopter used for various studies of crop water status [18,92,102].

UAS offers flexibility on spatial resolution, observation scale, spectral bands, and temporal resolution to collect data on any good weather day. However, like satellite and manned aircraft, the UAS is inoperable during precipitation, high winds, and temperatures. By easily altering the flying altitude, the UAS provides higher flexibility to observe a larger area with lower spatial resolution or smaller area with much greater detail [103]. Temporally, the UAS can be scheduled at a user-defined time at short notice, thus accommodating applications that are time-sensitive, such as capturing vital phenological stages of crop growth. Spectrally, UAS offer flexibility to carry on-demand sensors and interchangeability between sensor payloads; thus, any desired combination of sensors and spectral bands can be incorporated to target specific features.

UAS-acquired image data requires post-processing before it can be incorporated into the grower decision-making process. Mosaicking of UAS images currently has a turnaround time of approximately one day to one week, subject to the size of the dataset, computational power, and spectral/spatial quality of the product [104,105]. Spectral quality of the data is of optimal importance, whereas the spatial quality can be of less importance, such as for well-established horticultural crops. Higher spectral quality demands calibration of the spectral sensors and correction of atmospheric effects. Following post-processing of aerial images, the UAS-based spectral data have shown to be highly correlated with ground-based data [82,102,106].

The most common UAS-based sensor types to study the crop water status are the thermal, multispectral and RGB, while hyperspectral and LiDAR (Light detection and ranging) sensors are used less often [23,79,107]. Spectral sensors provide the capability to capture broader physiological properties of the crop, such as greenness (related to leaf chlorophyll content and health) and biomass, that generally correlate with crop water status [82,108]. Narrower band spectral sensors provide direct insight into specific biophysical and biochemical properties of crops, such as via photochemical reflectance index (PRI) and solar-induced chlorophyll fluorescence (SIF), which reflects a plant's photosynthetic efficiency [109,110]. Thermal-based sensors capture the temperature of the crop's surface, which indicates the plant's stress (both biotic and abiotic) [53]. Generally, digital RGB camera and LiDAR can be used to quantify 3D metrics, such as the plant size and shape, via 3D pointclouds with sufficient accuracy for canopy level assessment [111–118].

3. Remote Sensor Types

3.1. Digital Camera

A digital camera typically incorporates an RGB, modified RGB, and a monochrome digital camera. The lens quality of the camera determines the sharpness of the image, while the resolution of the camera determines its spatial resolution and details within an image. The RGB camera uses broad spectral bandwidth within the blue, green and red spectral region to capture energy received at the visible region of the electromagnetic spectrum. The images are used to retrieve dimensional properties of the crop, terrain configuration, macrostructure of the field, and the spatial information. Based on the dimensional properties, such as size, height, perimeter, and area of the crown, the resource need practices can be estimated [119–121]. Generally, a larger crop is expected to more quickly use available water resources, resulting in crop water stress at a later stage of the season if irrigation is not sufficient. The evolution of canopy structure within and between seasons can be useful to understand the spatial variability within the field and corresponding water requirements. The macro-structure of horticultural crops, such as row height, width, spacing, crop count, the fraction of ground cover, and missing plants, can be identified remotely, which can aid in the allocation of resources [113,122]. The terrain configuration in the form of a digital elevation model (DEM) generated from a digital camera can also enable understanding of the water status in relation to the aspect and slope configuration of the terrain.

3.2. Multispectral Camera

A multispectral camera offers multiple spectral bands across the electromagnetic spectrum. Most common airborne multispectral cameras have 4–5 bands which include rededge and NIR bands in addition to the visible bands, R-G-B (e.g., Figure 3a,c). Configurable filter placement of the spectral band is also available, which can potentially target certain physiological responses of horticultural crops [102]. Spectrally, the airborne multispectral camera has been reported to perform with consistency, producing reliable measurements following radiometric calibration and atmospheric correction [123–125]. Their spatial resolution has been found to be sufficient for horticultural applications enabling canopy level observation of the spectral response. For this reason, as well as relatively low cost, multispectral cameras are used more frequently in horticulture applications.

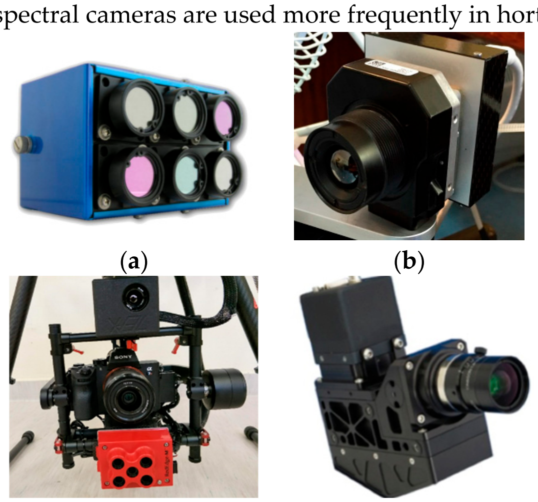

(**a**) (**b**) (**c**) (**d**)

Figure 3. Some examples of sensors used on a UAS platform to study water status of horticultural crops: **(a)** A multispectral camera (Tetracam Mini-MCA-6, Tetracam, Inc., Chatsworth, CA, USA) [126]. **(b)** A thermal camera (FLIR TAU II, FLIR Systems, Inc., USA) [100,108]. **(c)** A multi-sensor camera setup with an RGB (Sony α7R III, Sony Electronics, Inc., Minato, Tokyo, Japan), a multispectral (MicaSense RedEdge, MicaSense Inc., Seattle, WA, USA), and a thermal (FLIR TAU II 640, FLIR Systems, Inc., USA) camera. **(d)** A micro-hyperspectral camera (Micro-Hyperspec, Headwall Photonics, MA, USA) [110].

Chlorophyll and cellular structures of vegetation absorb most of the visible light and reflect infrared light. The rise in reflectance between the red and NIR band is unique to live green vegetation and is captured by vegetation spectral index called NDVI (Table 2, Equation (3). Once the vegetation starts to experience stress (biotic and abiotic), its reflectance in the NIR region is reduced, while the reflectance in the red band is increased. Thus, such stress is reflected in the vegetation profile and easily captured by indices, such as NDVI. For this reason, NDVI has shown correlations with a wide array of crops response including vigour, chlorophyll content, leaf area index (LAI), crop water stress, and occasionally yield [34,82–84,127].

The rededge band covers the portion of the electromagnetic spectrum between the red and NIR bands where reflectance increases drastically. Studies have suggested that the sharp transition between the red absorbance and NIR reflection is able to provide additional information about vegetation and its hydric characteristics [128]. Using the normalised difference red edge (NDRE) index, the rededge band was found to be useful in establishing a relative chlorophyll concentration map [127]. Given the sensitivity of NDRE, it can be used for applications, such as crops drought stress [107]. With regard to the water use efficiency, a combination of vegetation indices (VIs) along with structural physiological indices were found to be useful to study water stress in horticultural crops [34,82,129].

3.3. Hyperspectral

Hyperspectral sensors have contiguous spectral bands sampled at a narrower wavelength intervals spanning from visible to NIR spectrum at a high to ultra-high spectral resolution (Figure 3d). Scanning at contiguous narrow-band wavelengths, a hyperspectral sensor produces a three dimensional (two spatial dimensions and one spectral dimension) data called hyperspectral data cube. The hyperspectral data cube is a hyperspectral image where each pixel contain spatial information, as well as the entire spectral reflectance curve [130]. Based on the operating principle and output data cube, hyperspectral sensors for remote sensing can include a point spectrometer (aka spectroradiometer), whiskbroom scanner, pushbroom scanner, and 2D imager (Figure 4) [130,131]. A point spectrometer, samples within its field of view solid angle to produce an ultra-high spectral resolution spectral data of a point [130,132]. A whiskbroom scanner deploys a single detector onboard to scan one single pixel at a time. As the scanner rotates across-track, successive scans form a row of the data cube, and as the platform moves forward along-track, successive rows form a hyperspectral image [133]. A pushbroom scanner deploys a row of spatially contiguous detectors arranged in the perpendicular direction of travel and scans the entire row of pixels at a time. As the platform moves forward, the successive rows form a two-dimensional hyperspectral image [40,134]. The 2D imager using different scanning techniques [130] captures hyperspectral data across the image scene [135,136]. The point spectrometer offers the highest spectral resolution and lowest signal-to-noise ratio (SNR) among the UAS-compatible hyperspectral sensors [137,138].

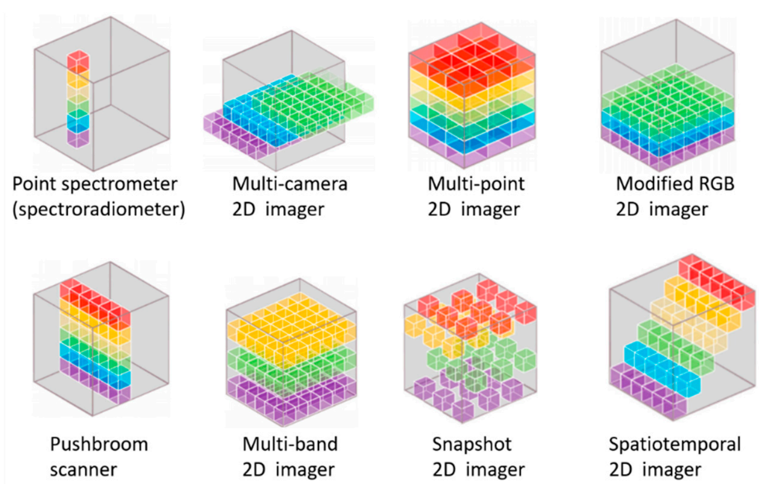

Figure 4. The data cube structure of different spectral sensors. The number of bands and resolution is shown as an example and does not indicate true sensor capability (adapted from [130]).

In horticultural applications, hyperspectral data, due to the high resolution contiguous spectral sampling, possesses tremendous potential to detect and monitor specific biotic and abiotic stresses [139]. Narrowband hyperspectral data was used to detect water stress using the measurement of fluorescence and PRI over a citrus orchard [110]. PRI was identified as one of the best predictors of water stress for a vineyard in a study that investigated numerous VIs using hyperspectral imaging [140]. High-resolution thermal imagery obtained from a hyperspectral scanner was used to map canopy stomatal conductance (g_s) and CWSI of olive orchards where different irrigation treatments were applied [18]. With the large volume of spatial/spectral data extracted from the hyperspectral data cube, machine learning will likely be adopted more widely in the horticultural environment to model water stress [141]. See Reference [54] for a comprehensive review of hyperspectral and thermal remote sensing to detect plant water status.

3.4. Thermal

Thermal cameras use microbolometers to read passive thermal signals in the spectral range of approximately 7–14 μm (Figure 3b). Small UAS are capable of carrying a small form-factor thermal camera with uncooled microbolometers, which does not use an internal cooling mechanism and, therefore, does not achieve the high SNR that can be found in cooled microbolometer-based thermal cameras. An array of microbolometer detectors in the thermal camera receives a thermal radiation signal and stores the signal on the corresponding image pixel as raw data number (DN) values. The result is a thermal image where each pixel has an associated DN value, which can be converted to absolute temperature. A representative list of commercial thermal cameras used on UAS platforms and their applications with regard to agricultural remote sensing is found in the literature [23,53,73]. Thermal imagery enables the measurement of the foliar temperature of plants. The foliar temperature difference between well-watered and water-stressed crops is the primary source of information for water stress prediction using a thermal sensor [142]. When mounted on a remote sensing platform, the canopy level assessment of crop water status can be performed on a large scale.

Thermal cameras are limited by their resolution (e.g., 640 × 512 is the maximum resolution of UAS compatible thermal cameras in the current market) and high price-tag [53]. The small number of pixels results in low spatial resolution limiting either the ability to resolve a single canopy or ability to fly higher and cover a larger area. If flown at a higher altitude, the effective spatial resolution may be inadequate for canopy level assessment of some horticultural crops. For example, a FLIR Tau2 640 thermal camera with a 13 mm focal length when flown at an altitude of approximately 120 m results in a spatial resolution of 15.7 cm. For relatively large horticultural crops, such as grapevine, almond, citrus, and avocado, the resolution at a maximum legal flying altitude of 120 m in Australia (for small-sized UAS) offers an adequate spatial resolution to observe a single canopy.

Another challenge with the use of thermal cameras is the temporal drift of the DN values within successive thermal images, especially with uncooled thermal cameras [143]. Due to the lack of an internal cooling mechanism for the microbolometer detectors, DN values registered by the microbolometers experience temporal drift i.e., the registered DN values for the same temperature target will drift temporally. Thus, the thermal image can be unreliable especially when the internal temperature of the camera is changing rapidly, such as during camera warmup period or during the flight when a gust of cool wind results in cooling of the camera. To overcome this challenge, the user may need to provide sufficient startup time before operation (preferably 30–60 min) [102,143–145], shield the camera to minimize the change in the internal temperature of the camera [142], calibrate the camera [146–153], and perform frequent flat-field corrections.

3.5. Multi-Sensor

To carry multiple sensors, the total UAS payload needs to be considered that includes, in addition to the sensors, an inertial measurement unit (IMU) and global navigation satellite system (GNSS) for the georeferencing purpose [40,154]. Higher accuracy sensors tend to be heavier, and in a multi-sensor scenario, the payload can quickly reach or even exceed the payload limit. This has limited contemporary measurements in earlier multirotor UAS requiring separate flights for each of sensor [126]. The use of fixed-wing UAS has allowed carrying higher payloads due to the much larger thrust-to-weight ratio as compared to a rotary-wing aircraft [155]. Similarly, recent advancement in UAS technology and lightweight sensors have enabled multirotor (payload 5–6 kg readily available) to onboard multi-sensors.

Water status of crops is a complex process influenced by a number of factors including the physiology of the crop, available soil moisture, the size and vigour of the crop, and meteorological factors [30,108,116,156,157]. For this reason, a multi-sensor platform is used to acquire measurements of the different aspects of the crop for water status assessment [34,102,108]. The most common combination of sensors found in the literature is the RGB, multispectral (including rededge and NIR bands) and thermal. Together, these sensors can be used to investigate the water status of the crop using various indicators, such as PRI, CWSI, fluorescence, and structural properties, with the aim of improving the water use efficiency [102,110,158–160].

4. Techniques of Remote Sensing in Horticulture

4.1. Georeferencing of Remotely Sensed Images

Georeferencing provides a spatial reference to the remotely sensed images such that the pixels representing crops or regions of interest on the images are correctly associated with their position on Earth. The georeferencing process generally uses surveyed coordinate points on the ground, known as ground control points (GCPs), to determine and apply scaling and transformation to the aerial images [161]. Alternatively, instead of GCPs, the user can georeference aerial images by using the accurate position of the camera, or by co-registration with the existing georeferenced map [105,162].

In the case of UAS-based images, the capture timing is scheduled to ensure a recommended forward overlap (>80%) between successive images. The flight path is designed to ensure the recommended side overlap (>70%) between images from successive flight strips. Thus, the captured series of images are processed using the Structure-from-Motion (SfM) technique to generate a 3D pointcloud and orthomosaic [73,130] (see Figure 5). Commonly used SfM software to process the remote sensing images are Agisoft PhotoScan and Pix4D. The commonly retrieved outputs from the SfM software for assessment of horticulture crops include the orthomosaic, digital surface model (DSM), DEM, and 3D pointcloud [113,126,163]. This technique of georeferencing can be applied to any sensor that produces images, e.g., RGB, thermal, or multispectral cameras [126,164,165].

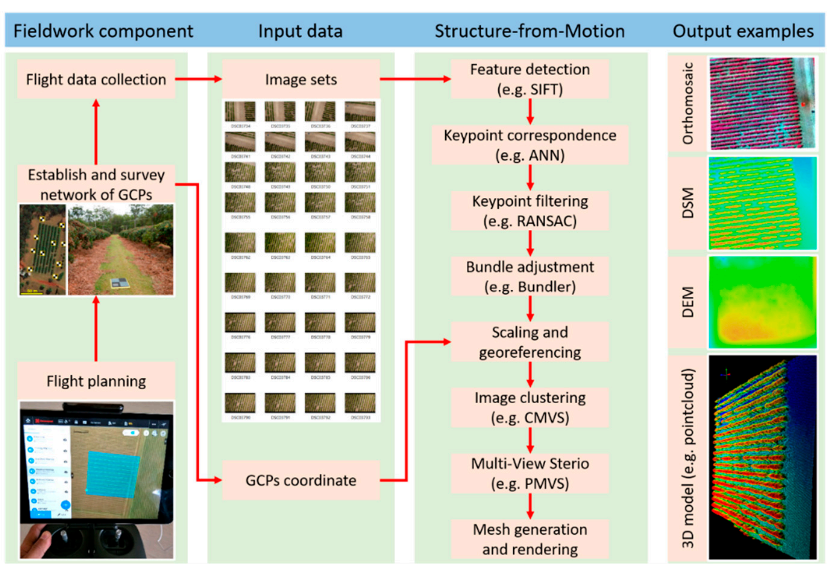

Figure 5. A typical workflow of structure-from-motion (SfM) to produce georeferenced products from UAS-based image sets and ground control points (adapted from [166,167]). SIFT = scale-invariant feature transform; ANN = approximate nearest neighbour; RANSAC = random sample consensus;

CMVS = clustering views for multi-view stereo; PMVS = patch-based multi-view stereo; GCP = ground control points.

The complexity of georeferencing of hyperspectral observations depends on the sensor type, i.e., imaging or non-imaging. A non-imaging spectroradiometer relies on the use of a GNSS antenna and an IMU for georeferencing the point observation [130,132,138,168]. An imaging hyperspectral camera, generally, in addition to GNSS and IMU measurement, uses the inter-pixel relation in SfM to produce a georeferenced orthomosaic [40,134,135,169,170].

4.2. Calibration and Correction of Remotely Sensed Images

Ensuring consistency, repeatability, and quality of the spectral observation requires stringent radiometric, spectral, and atmospheric corrections [123,171–177]. Spectral and radiometric calibration is performed in the spectral calibration facility in darkroom settings. The sensor's optical properties and shift in spectral band position are corrected during the spectral calibration process. Radiometric calibration enables conversion of the recorded digital values into physical units, such as radiance. Infield operation of the spectral sensor is influenced by variations in atmospheric transmittance from thin clouds, invisible to the human observer. Changes in atmospheric transmittance affect the radiance incident on the plant. As a result, the change in acquired spectral response by the sensor may not represent the change in plants response but the change in incident radiation on the plant. The most common method to convert the spectral data to reflectance is by generating an empirical line relationship between sensor values and spectral targets, such as a Spectralon® or calibration targets. The use of downwelling sensors, such as a cosine corrector [137], or the use of a ground-based PAR sensor enables absolute radiometric calibration to generate radiance [130].

The calibration of the broad wavelength multispectral sensor is generally less stringent than the hyperspectral. Generally, multispectral sensors are used to compute normalised indices such as NDVI. The normalised indices are relatively less influenced, although significant, by the change in illumination conditions which affect the entire spectrum proportionally [29,101]. In this regard, radiometric calibration of the multispectral camera has used a range of stringent to simplified, and vicarious approaches [123,125,171,173,178–180]. Some multispectral cameras are equipped with a downwelling light sensor, which is aimed at correcting for variations in atmospheric transmittance. However, the performance of such downwelling sensors (without a cosine corrector) on multispectral cameras have been reported to have directional variation resulting in unstable correction, indicating the inability of the sensor to incorporate the entire hemisphere of diffused light [124,137].

The radiometric calibration of the thermal images is typically based on the camera's DN to object temperature curve, which provides the relationship between the DN of a pixel and a known object temperature, usually of a black body radiator. Measurement accuracy and SNR of the camera under varying ambient temperatures can be improved by using calibration shutters, which are recently available commercially. Furthermore, for low measurement errors (under 1 °C), thermal data requires consideration to the atmospheric transmittance [18,102]. Flying over a few temperature reference targets placed on the ground reduces the temporal drift of the camera [142,143,181]. Temperature accuracy within a few degrees was achieved by flying over the targets three times (at the start, middle and end of UAS operation) and using three separate calibration equations for each overpass [142]. Additionally, using the redundant information from multiple overlapping images, drift correction models have been proposed, which lowered temperature error by 1 °C as compared to uncorrected orthomosaic [152]. The manufacturer stated accuracies (generally ±5 °C) can be sufficient to access the field variability and to detect "hotspots" of water status. However, the aforementioned calibration and correction of the thermal cameras are required for quantitative measurement as a goal [143]. In this regard, current challenges and best practices for the operation of thermal cameras onboard a UAS is provided in the literature [143].

4.3. Canopy Data Extraction

A key challenge in remote sensing of horticultural as compared to agricultural crops arises due to the proportion of inter-row ground/vegetation cover and resulting mixed pixels. The proportion of the mixed pixels increases with the decrease in spatial resolution of the image. Most of the pixels towards the edge of the canopy contain a blend of information originating from the sun-lit canopy, shadowed leaves, and inter-row bare soil/cover crop. A further challenge can arise for some crops, such as grapevine, due to overlapping of adjacent plants.

The canopy data from orthomosaic has been extracted using either a pixel-based or an object-based approach. Earlier studies manually sampled from the centre of crop row which most likely eliminated the mixed pixels [182]. In the pixel-based approach, techniques, such as applying global threshold and masking, have been used. Binary masks, such as NDVI, eliminates non-canopy pixels from the sampling [82,84]. Combining the NDVI mask with the canopy height mask can exclude the pixels associated with non-vegetation, as well as vegetation that does not meet the height threshold. The pixel-based approach, however, can result in inaccurate identification of some crops due to pixel heterogeneity, mixed pixels, spectral similarity, and crop pattern variability.

In the object-based approach, using object detection techniques, neighbouring pixels with homogenous information, such as spectral, textural, structural, and hierarchical features, are grouped into "objects". These objects are used as the basis of object-based image analysis (OBIA) classification using classifiers, such as k-nearest neighbour, decision tree, support vector machine, random forest, and maximum likelihood [122,183–185]. In the horticultural environment, OBIA has been adopted to classify and sample from pure canopy pixels [119,122,186]. Consideration should be provided on the number of features and their suitability for a specific application to reduce the computational burden, as well as to maintain the accuracies. The generalisation of these algorithms for transferability between study sites usually penalises the achievable accuracy. For details in object-based approach of segmentation and classification, readers are directed to literatures [122,183,185,187–189].

Other techniques found in the literature include algorithms, such as 'Watershed', which has been demonstrated in palm orchards [82,190]. Vine rows and plants have been isolated and classified using image processing techniques, such as clustering and skeletisation [188,191–193]. Similarly, the gridded polygon, available in common GIS software, such as ArcGIS and QGIS, can be used in combination with zonal statistics for this purpose. When working with the low-resolution images, co-registration with the high-resolution images has been proposed, whereby, the high-resolution images enable better delineation of the mixed pixels [194]. For this reason, spectral and thermal sensors, which are usually low in resolution, are generally employed along with high-resolution digital cameras.

4.4. Indicators of Crop Water Status

A crop's biophysical and biochemical attributes can be approximated using different indices and quantitative products. For example, CWSI is used to proxy leaf water potential (Ψ_{leaf}), stem water potential (Ψ_{stem}), g_s, and net photosynthesis (P_n) [83,100,195]. With regard to horticultural crops, water status has been assessed using a number of spectral and thermal indices (Table 2).

Table 2. Commonly used vegetation and thermal indices to study the water status of horticultural crops.

Indicators	Sensor	Purpose	References
T_c, ($T_c - T_a$)	Thermal	Ψ_{stem}, g_s, yield	[34,82,85,99,110]
I_g, I3	Thermal	Ψ_{stem}, g_s	[82,196]
CWSI	Thermal	Ψ_{leaf}, Ψ_{stem}, g_s, P_n, yield	[18,31,33,85,90,97,99,100,182,194,197–199]
($T_c - T_a$)/NDVI	Thermal + multispectral	Ψ_{stem}, g_s	[82,200]
NDVI	Multispectral	Ψ_{stem}, g_s, yield, LAI, vigour	[34,56,82,86,182,201]
GNDVI	Multispectral	Ψ_{stem}, g_s, yield	[34,82]

RDVI	Multispectral	Ψ_{stem}, g_s	[82,86,182]
PRI	Multispectral	Ψ_{leaf}, g_s	[86,110,182]
Fluorescence	Hyperspectral	Ψ_{leaf}, g_s	[110]
WBI	Hyperspectral	Ψ_{leaf}, g_s	[139,202,203]
SIF	Hyperspectral	Water stress	[204–206]

Note the acronyms: T_c = Canopy temperature, T_a = ambient temperature, I_g = conductance index, I3 = stomatal conductance index, CWSI = crop water stress index, NDVI = normalised difference vegetation index, GNDVI = green normalised difference vegetation index, RDVI = renormalized difference vegetation index, PRI = photochemical reflectance index, Fluorescence = chlorophyll fluorescence, WBI = water band index, SIF = solar-induced chlorophyll fluorescence, LAI = leaf area index.

4.4.1. Canopy Temperature

A plant maintains its temperature by transpiring through the stomata to balance the energy fluxes in and out of the canopy. As the plant experience stress (both biotic and abiotic), the rate of transpiration decreases, which results in higher canopy temperature (T_c), which can be a proxy to understand the water stress in the plant [207]. In this regard, crop water stress showed a correlation with canopy temperature extracted from the thermal image [208], which enables mapping the spatial variability in water status [209]. Leaf/canopy temperature alone, however, does not provide a complete characterisation of crop water status, for instance, an equally stressed canopy can be 25 °C or 35 °C, depending on the current ambient temperature (T_a). Thus, canopy-to-air temperature difference ($T_c - T_a$) was proposed, which showed a good correlation with the Ψ_{stem}, Ψ_{leaf}, and g_s in horticultural crops [85,99,182].

4.4.2. Normalised Thermal Indices

The CWSI, the conductance index (I_g) and the stomatal conductance index (I3) are thermal indices most commonly used to estimate crop water status and g_s [210–212]. These indices provide similar information, however, use a different range of numbers to represent the level of water stress. The CWSI is normalised within zero and one, whereas I_g and I3 represent stress using numbers between zero and infinity. CWSI has been adopted most widely in horticultural applications to assess the water status of crops, such as the grapevines [100,213], almond [91,198], citrus [85,110], and others [18,87,99,214]. By normalising between the lower and upper limits of ($T_c - T_a$), the CWSI of the canopy presents quantifiable relative water stress. The formula for CWSI computation is defined as in Equation (1) [208,212].

$$\mathrm{CWSI} = \frac{(T_c - T_a) - (T_c - T_a)_{LL}}{(T_c - T_a)_{UL} - (T_c - T_a)_{LL}}, \tag{1}$$

where $(T_c - T_a)_{UL}$ and $(T_c - T_a)_{LL}$ represent the upper and lower bound of ($T_c - T_a$) which are found in the water-stressed canopy and well-watered canopy transpiring at the full potential (or maximum) rate, respectively. Assuming a constant ambient temperature, Equation (1) can be simplified to Equation (2), which is the most widely reported formulation of CWSI with regard to the horticultural remote sensing.

$$\mathrm{CWSI} = \frac{(T_c - T_{wet})}{(T_{dry} - T_{wet})}, \tag{2}$$

where T_{wet} is the temperature of canopy transpiring at the maximum potential, and T_{dry} is the temperature of the non-transpiring canopy. CWSI has been shown to be well-correlated with direct measurements of crop water status in the horticultural environment [18,31,32,90,99]. In this regard, a correlation of CWSI with various ground measurements, such as Ψ_{leaf} [18,31,197], Ψ_{stem} [33,90,194], and g_s [18,90,100], have been established. Diurnal measurements of CWSI compared with Ψ_{leaf} showed the best correlation at noon [89,197,209].

CWSI is a normalised index, i.e., relative to a reference temperature range between T_{wet} and T_{dry}, which is specific to a region and crop type; thus, CWSI is not a universal quantitative indicator of crop water status. For instance, a CWSI of 0.5 for two different varieties of grapevines at different locations does not conclusively inform that they have equal or superior/inferior water status.

Furthermore, the degree of correlation can change depending on the isohydric/anisohydric response of crop [214] where early/late stomatal closure affects the indicators of water stress [110]. Moreover, phenological stage affects the relationship between remotely sensed CWSI and water stress [197]. Thus, water stress in a different crop, at a different location and at a different phenological stage, will have a unique correlation with CWSI and, therefore, needs to be established independently.

There are multiple methods to measure the two reference temperatures, T_{wet} and T_{dry}, which could result in variable CWSI values depending on the method used. The first method is to measure the two reference temperatures on the crop of interest. T_{dry} can be estimated by inducing stomatal closure, which is the leaf temperature approximately 30 min after applying a layer of petroleum jelly e.g., Vaseline to both sides of a leaf. This effectively blocks stomata and, therefore, impedes leaf transpiration. T_{wet} can be estimated by measuring leaf temperature approximately 30 s after spraying water on the leaf, which emulates maximum transpiration [23,83]. The advantage of this method is that the stress levels are normalised to actual plants response, whereas the necessity to repeat the measurement for every test site after each flight can be cumbersome. In an alternative (second) approach the range can be established based on meteorological data e.g., setting T_{dry} to 5 °C above air temperature and T_{wet} measured from an artificial surface. This method is also limited to local scale and presents a problem regarding the choice of material, which ideally needs to have similar to leaf emissivity, aerodynamic and optical properties [54,87]. The third method uses the actual temperature measurement range of the remote sensing image [33,97]. This method is simple to implement, however, works on the assumption that the field contains enough variability to contain a representative T_{wet} and T_{dry}. Fourth, the reference temperatures can be estimated by theoretically solving for the leaf surface energy balance equations, however, are limited by the necessity to compute the canopy aerodynamic resistance [87]. Standard and robust T_{wet} and T_{dry} measurements are needed to characterize CWSI with accuracy, especially for temporal analysis [85,87,211]. The level of uncertainty due to the adaptation of different approaches for T_{wet} and T_{dry} determination in the instantaneous and seasonal measurements of CWSI is not known. Nonetheless, adopting a consistent approach, CWSI has been shown to be suitable for monitoring the water status and making irrigation decisions of horticultural crops [31,85].

4.4.3. Spectral Indices

Crops reflectance properties convey information about the crop, for instance, a healthier crop has higher reflectance in the NIR band. Most often, the bands are mathematically combined to form VIs, which provide information on the crop’s health, growth stage, biophysical properties, leaf biochemistry, and water stress [29,215–218]. Using multispectral or hyperspectral data, several Vis, such as green normalised difference vegetation index (GNDVI), renormalised difference vegetation index (RDVI), optimized soil-adjusted vegetation index (OSAVI), transformed chlorophyll absorption in reflectance index (TCARI), and TCARI/OSAVI, amongst others [34,79,82], can be calculated that correlate with the water stress of horticultural crops (see Table 2). The most widely studied VI in horticulture, in this regard, is the NDVI (Equation (3)).

$$\mathrm{NDVI} = \frac{\mathrm{R}_{nir} - \mathrm{R}_{r}}{\mathrm{R}_{nir} + \mathrm{R}_{r}}, \tag{3}$$

where R_{nir} and R_{r} represent the spectral reflectance acquired at the NIR and red spectral regions, respectively. In horticulture, NDVI has been used as a proxy to estimate the vigour, biomass, and water status of the crop. A vigorous canopy with more leaves regulates more water, therefore remaining cooler when irrigated [200] and experiencing early water stress when unirrigated. With regard to irrigation, the broadband normalised spectral indices (such as NDVI) are suitable to detect spatial variability and to identify the area that is most vulnerable to water stress. However, these indices are not expected to change rapidly to reflect the instantaneous water status of plants that are needed to make decisions on irrigation scheduling.

The multispectral indices along with complementary information in thermal wavelengths have proven to be well suited to monitoring vegetation, specifically in relation to water stress [219]. The ratio of canopy surface temperature to NDVI, defined as temperature-vegetation dryness index

(TVDI), was found to be useful for the study of water status in horticultural crops. TVDI exploits the fact that vegetation with larger NDVI will have a lower surface temperature unless the vegetation is under stress. As most vegetation normally remains green after an initial bout of water stress, the TVDI is more suited than NDVI for early detection of water stress as the surface temperature can rise rapidly even during initial water stress [200].

Similarly, narrowband VIs that have been studied in relation to remote sensing of water status are PRI and chlorophyll fluorescence, which have been directly correlated to the crop Ψ_{leaf}, g_s [110,182,204]. Several hyperspectral indices to estimate water status have been identified [139]; however, their application in remote sensing of horticultural crops is at its infancy. Hyperspectral indices specific to water absorption bands around 900 nm, 1200 nm, 1400 nm, and 1900 nm may be used to detect the water status of horticultural crops. The absorption features were found to be highly correlated with plant water status [139]. Water band index (WBI), as defined in Equation (4), has been shown to closely track the changes in the plant water status of various crops [202,203].

$$\mathrm{WBI} = \frac{\mathrm{R}_{970}}{\mathrm{R}_{900}} \quad (4)$$

Other water-related hyperspectral indices with potential application for horticultural crops can be found in the literature [139,202,203]. Hyperspectral data possess the capability to reflect the instantaneous water status of the plant, which can be useful for quantitative decision-making on irrigation scheduling.

4.4.4. Soil Moisture

The moisture status of the soil provides an indication of the available water resource to the crop. Soil moisture is traditionally measured indirectly using soil moisture sensors placed below the surface of the soil. A key challenge with using soil moisture sensors are the spatial distribution of moisture, both vertically and horizontally, to account for inherent field-scale variability. For instance, the root system of some horticultural crops, such as grapevine, is capable of accessing water up to 30 m deep, while customer-grade soil moisture probes generally extend to 1.5 m in depth or less. Thus, soil moisture probes do not capture all the water available to the crop as they are point measures and not necessarily where the roots are located. Moreover, estimation of soil moisture across spatial and temporal scales is of interest for various agricultural and hydrological studies. Optical, thermal, and microwave remote sensing with their advantages relating to high spatial scale and temporal resolutions could potentially be used for soil moisture estimation [220–222]. L-band microwave radiometry, a component of synthetic aperture radar systems, has been shown to be a reliable approach to estimate soil moisture via satellite-based remote sensing [223], such as using the ESA's Soil Moisture and Ocean Salinity (SMOS) [224] and NASA's Soil Moisture Active Passive (SMAP) satellites [225,226]. The limitation of the SMOS and SMAP missions, with regard to horticultural application, is their depth of retrieval (up to 5 cm) and spatial resolution (in the order of tens of kilometre) [227–229]. As an airborne application, the volumetric soil moisture has been estimated by analysing the SNR of the GNSS interference signal [230,231]. With aforementioned capabilities, a combination of satellite and airborne remote sensing may, in the future, be a reliable tool to map soil moisture across spatial, temporal and depth scales.

4.4.5. Physiological Attributes

Using the SfM on remotely-sensed images, 3D canopy structure, terrain configurations, and canopy surface models can be derived [113,114,119,186,232]. By employing a delineation algorithm on the 3D models, the 3D attributes of the crops and macrostructure are determined more accurately [120,122,233]. Crop surface area and terrain configuration (e.g., slope and aspect) may help to develop an optimal resource management strategy. For example, crops located at a higher elevation within an irrigation zone may experience a level of water stress due to the gravitational flow of irrigated water.

Using the structural measurements, such as the canopy height, canopy size, the envelope of each row, LAI, and porosity, among others, the water demand of the crop may be estimated. Generally, larger canopies tend to require more water than smaller canopies with less leaf area [116,157]. Using the temporal measurement of the plant's 3D attributes, the vigour can be computed. Monitoring crop vigour over the season and over subsequent years can provide an indication of its health and performance, e.g., yield, within an irrigation zone. Canopy structure metrics are closely related to horticultural tree growth and provide strong indicators of water consumption, whereby canopy size can be used to determine its water requirements [234]. Other 3D attributes, such as the crown perimeter, width, height, area, and leaf density, have been shown to enable improved pruning of horticultural plants [116,119].

LAI can be estimated using the 3D attributes obtained from remote sensing [114,157,201], whereby, higher LAI is equivalent to more leaf layers, implying greater total leaf area and, consequently, canopy transpiration. Leaf density, LAI, and exposed leaf area of a crop drive its water requirement and productivity [235–237]. Knowledge of field attributes, such as row and plant spacing, may assist in inter-row surface energy balance to determine the irrigation need of the plant [238]. Combining the structural properties with spectral VIs provide an estimation of biomass [239], which can serve as another indicator of the plant's water requirements. Although physiological attributes have been used to understand plant water status and its spatial variability, they have not been directly applied to make quantitative decisions on irrigation.

4.4.6. Evapotranspiration

The estimation of ET via remote sensing, numerical modelling, and empirical methods have been extensively studied and reviewed in the literature [240–247]. These models are based on either surface energy balance (SEB), Penman-Monteith (PM), Maximum entropy production (MEP), water balance, water-carbon linkage, or empirical relationships.

SEB models are based on a surface energy budget in which the latent heat flux is estimated as a residual of the net radiation, soil heat flux, and sensible heat flux. The models are either one-source (canopy and soil treated as a single surface for the estimation of sensible heat flux) or two-source (canopy and soil surfaces treated separately). Improvements over the original one-source SEB models were in the form of Surface Energy Balance Algorithm for Land (SEBAL) algorithm [248,249] and Mapping EvapoTranspiration with high Resolution and Internalized Calibration (METRIC) [249,250]. SEBAL offers a simplified approach to collect ET data at both local and regional scales thereby increasing the spatial scope, while METRIC uses the same (SEBAL) technique but auto-calibrates the model using hourly ground-based reference ET (ET_r) data [251]. As such, these and other (e.g., MEP) models rely on accurate measurements of surface (e.g., canopy) and air temperatures, which can be erroneous under non-ideal conditions, e.g., cloudy days. There is also a reliance on ground-based sensors to capture ambient air temperatures required by the model.

Among the existing methods, FAO's PM is the most widely adopted model to estimate reference ET (ET_{ref} or ET_0) [252]. The PM method uses incident and reflected solar radiation, emitted thermal radiation, air temperature, wind speed, and vapour pressure to calculate ET_0 [253]. Remote sensing provides a cost-effective method to estimate the ET_0 at regional to global scales [241] by estimating reflected solar and emitted thermal radiation. One of the advantages of using the PM approach is that it is parametrised using micrometeorological data easily obtained from ground-based automatic weather stations. However, PM suffers from the drawback that canopy transpiration is not dynamic as influenced by soil moisture availability via stomatal regulation [241]. From a practical standpoint, PM-derived ET_0 estimates are used in conjunction with crop factors or crop coefficients (k_c), which are closely related to the light interception of the canopy [254].

Crop evapotranspiration (ET_c) is defined as the product of k_c and ET_0. In the absence of accurate ET_c measurements, k_c is an easy and practical means of getting reliable estimates of ET_c using ET_0 [255]. In this regard, studies have focused on the use of remote sensing to study spatial variability in k_c and ET_c [101,256–258]. Thermal and NIR imagery can be used to compute k_c and ET_c as transpiration rate is closely related to canopy temperature [259–261] and k_c has been shown to correlate with canopy reflectance [101,255]. Various thermal indices, such as CWSI, canopy temperature ratio, canopy temperature above non-stressed, and canopy temperature above canopy threshold, can be used to estimate ET_c, where CWSI- based ET_c was found to be the most accurate [24].

ET at a larger scale is typically estimated based on satellite remote sensing. The temporal resolution of satellites is, however, low and inadequate for horticultural applications, such as irrigation scheduling (e.g., Landsat has a 16-day revisit cycle). In contrast, high temporal resolution satellites are coarse in spatial resolution for field-scale observations [25]. The daily or even instantaneous estimation of ET_c at the field scale is crucial for irrigation scheduling and is expected to have great application prospects in the future [240,259,262,263]. In this regard, the future direction of satellite-based ET estimates may focus on temporal downscaling either by extrapolation of instantaneous measurement [264], interpolation between two successive observations [201], data fusion of multiple satellites [25,260], and spatial downscaling using multiple satellites [265–268]. An example of early satellite-based remote sensing for ET is the MODIS Global Evapotranspiration Project (MOD16), which was established in 1999 to provide daily estimates of global terrestrial evapotranspiration using data acquired from a pair of NASA satellites in conjunction with Algorithm Theoretical Based Documents (ATBDs) [269]. These estimates correlated well with ground-based eddy covariance flux tower estimates of ET despite differences in the uncertainties associated with each of these techniques.

UASs are being increasingly utilised to acquire multi-spectral and thermal imagery to compute ET at an unprecedented spatial resolution [270,271]. Using high-resolution images, filtering the shadowed-pixel is possible, which showed significant improvement in the estimation of ET in grapevine [101]. Using high-resolution thermal and/or multispectral imagery, ET has been derived for horticultural crops, such as grapevines [270] and olives [271]. The seasonal monitoring of ET_c at high spatial and temporal resolutions is of high importance for precision irrigation of horticultural crops in the future [259].

5. Case Studies on the Use of Remote Sensing for Crop Water Stress Detection

The increasing prevalence of UAS along with low-cost camera systems has brought about much interest in the characterisation of crop water status/stress during the growing season to inform orchard or farm management decisions, in particular, irrigation scheduling [272,273]. Traditional methodologies to assess crop water stress are constrained by limitations relating to large farm sizes and accompanying spatial variability, high labour costs to collect data, and access to instrumentation that is both inexpensive and portable [272]. The benefits of precision agriculture [274], including through precision irrigation practices [1], result in higher production efficiencies and economic returns through site-specific crop management [275,276]. This approach has motivated the use of high-resolution imagery acquired from remote sensing to identify irrigation zones [99,277]. The first horticultural applications of UAS platforms for crop water status measurement were in orange and peach orchards where both thermal and multispectral-derived VIs, specifically the PRI, were shown to be well-correlated to crop water status [102]. Here, we explore the use of remote sensing and accompanying image acquisition platforms to characterise the spatial and temporal patterns of the water status of two economically important horticultural crops, grapevine and almond.

5.1. Grapevine (Vitis *spp.*)

The characterisation of spatial variability in vine water status in a vineyard provides valuable guidance on irrigation scheduling decisions [82], and this spatial variability can be efficiently characterised by the use of remote sensing platforms [29]. The first use of remote sensing in vineyards for crop water stress detection was using manned aircraft flown over an irrigated vineyard in Hanwood (NSW) Australia where CWSI was mapped at a spatial resolution of 10 cm [278]. Subsequently, UAS platforms began to be used in vineyards for vine water stress characterisation. Early work in this crop used a fuel-based helicopter with a 29 cc engine and equipped with thermal (Thermovision A40M) and multispectral (Tetracam MCA-6) camera systems [102]. The study observed strong (inverse) relationships between ($T_c - T_a$) and g_s. A related study showed strong correlations between thermal and multispectral VIs, and traditional, ground-based measures of water status, such as Ψ_{leaf} and g_s [182]. In this study, normalised PRI was shown to have correlation coefficients exceeding 0.8 versus both Ψ_{leaf} and g_s, indicating that remotely-sensed VIs can be reliable indicators of vine water status. Thermal indices, such as ($T_c - T_a$) and CWSI, were also well-correlated to Ψ_{leaf} and g_s at specific times of the day. The use of thermal indices, such as CWSI or I_g, requires reference temperatures (T_{wet}, T_{dry}) or non-water stressed baselines (NWSB) [279]. Due to the difficulty of obtaining reference temperatures or NWSB using remote sensing, some authors have used the minimum temperature found from all canopy pixels as T_{wet} [199], and T_a + 5 °C as T_{dry} [213,280]. NWSB is typically obtained from well-watered canopies, measuring ($T_c - T_a$) under a range of vapour pressure deficit conditions [279]. Thermal water stress indices have also shown to be useful to distinguish between water use strategies of different grapevine cultivars [83,281], which is useful for customising irrigation scheduling based on the specific water needs of a given cultivar. More recently, studies have used UAS-based multispectral-based VIs to train an artificial neural network (ANN) models to predict spatial patterns of Ψ_{stem} [84,282]. Using UAS-based multispectral data, the authors showed that ANN estimated Ψ_{stem} with higher accuracy (RMSE lower than 0.15 MPa) as compared to the conventional multispectral indices based estimation (RMSE over 0.32 MPa).

5.2. Almond (Prunus Dulcis)

Almonds are perennial nut trees grown in semi-arid climates and are reliant on irrigation applications. Their water requirements are relatively high, with seasonal ET_c exceeding 1000 mm [283]. The requirement for prudent irrigation management in the face of decreased water availability is critical for maintaining tree productivity, yield, and nut quality [284]. Towards this goal, UAS-based remote sensing has been used to characterise the spatial patterns of tree water status in almond orchards. A UAS-based thermal camera was used to acquire tree the crown temperature data from a California almond orchard; this temperature was used to determine the temperature difference between crown and air ($T_c - T_a$) and compared to shaded leaf water potential (Ψ_{sl}) [92]. The study found a strong negative correlation ($R^2 = 0.72$) between ($T_c - T_a$) and Ψ_{sl}. The same authors conducted a follow on study in Spain on several fruit tree species including almond. The negative relationship (slope and offset) between ($T_c - T_a$) and Ψ_{stem} was observed to vary based on the time of observation; morning measurements had weak relationships, whereas afternoon measurements had stronger relationships [99]. Their proposed methodology allowed for the spatial characterisation of orchard water status on a single-tree basis, demonstrating the utility of UAS-based crop water stress data. Beyond the characterisation of crop water stress for irrigation scheduling, there is an opportunity to use this data to quantify the economic impact at a spatial level.

6. Future Prospective and Gaps in the Knowledge

Precision irrigation is a promising approach to increase farm water use efficiency for sustainable production, including for horticultural crops [3,5,9,10,274,285]. It is envisioned that the future of precision irrigation will incorporate UAS, manned aircraft, and satellite-based remote sensing platforms alongside ground-based proximal sensors coupled with wireless sensor networks. The automation of UAS technology will continue to develop further to a point that even novice users can adopt the technology with ease. It is also expected that the data processing pipeline of remote sensing images will become automated to be 'fit for purpose' for crop water status measurements. The ideal solution may lie in the use of satellites (or sometimes manned aircraft) for regional estimation and planning [55,260], UAS for seasonal monitoring and zoning [32,100,197,286], proximal sensors for continuous measurement [287], and artificial intelligence to derive decision-ready products [84,282] that can be used for making irrigation scheduling decisions [31,288–295]. Continued technological developments in this space will enable growers to acquire actionable data with ease, and eventually transition towards semi-automated or fully-automated irrigation applications.

Remote sensing and current irrigation application technologies are limited in temporal and spatial resolution, respectively. Although UAS technology can deliver sub-plant level spatially explicit information of water status, the size of the management block is much coarser, typically over

10 m. Hence, further improvements in variable rate application technologies, e.g., boom sprayers, or zoned drip irrigation, are required to fully exploit high-resolution UAS measurements. Nonetheless, the required resolution of remote sensing should be guided by the underlying spatial variability of the crop. For fields with relatively lower spatial variability, low/medium-resolution remote sensing imagery may suffice for crop water status assessment [278,296,297].

Remote sensing provides an indirect estimate of plant water status using the regression-based approach through several calculated reflectance indices. In comparison, physical and mechanistic models, e.g., radiative transfer models and energy balance models, incorporate both direct and indirect measures of the canopy, therefore establishing a basis for differences in plant water status. Using a similar approach, predictions of crop water status using regression-based remote sensing models can be improved by incorporating some direct auxiliary variables.

Further developments in thermal remote sensing are also expected, specifically, the advent of new thermal and hybrid thermal-multispectral water status/stress indices that are more sensitive to canopy transpiration. The most widely-adopted thermal index, CWSI, is an instantaneous measure that is normalised to local weather conditions and influenced by genotype and phenotype. For example, the relationship between CWSI and crop water status is influenced by environmental conditions (e.g., high incident radiation and low humidity vs low incident radiation and high humidity) and phenological stage [197,214,298]. As a result, corresponding ground-based measurements are required for each temporal remote measurement to determine the correlation with water status. Hence, temporal assessments of water status using thermal cameras will require the incorporation of meteorological data along with the thermal response using novel indices.

In the area of satellite remote sensing, we foresee further developments on temporal downscaling to achieve daily measurements. A higher temporal resolution may be achieved by fusion of multiple satellite observations, such as freely available Landsat and Sentinel. Further reductions of temporal resolution will require interpolation between two successive observations. Furthermore, temporal models of water status could be developed to assist the interpolation to eventually satisfy the requirements for irrigation scheduling [25,201,263]. The continued advancement and greater availability of Nanosat/Cubesat may provide an alternate method to capture high-resolution data at a higher a greater temporal resolution, which can be suitable to study the water status of horticultural crops [299–301].

Crop water status is a complex phenomenon, which can be interpreted with respect to a number of variables. These variables can include spectral response, thermal response, meteorological data, 3D attributes of the canopy, and macrostructure of the block (farm). Clearly, there is an opportunity for a multi-disciplinary approach, potentially incorporating artificial intelligence techniques which incorporate the aforementioned variables to provide a robust estimation of crop water status [84,141,282,302,303]. Furthermore, with machine learning algorithms, hyperspectral remote sensing will provide a wealth of data to estimate crop water status. A quantitative product, such as SIF, derived from hyperspectral data will have the potential for direct quantification of water stress [204,205,304]. In this regard, the upcoming FLEX satellite mission [305,306] and recent advances in aerial spectroradiometry [109,132,137,307–310] dedicated for observation of SIF may be unique and powerful tools for high-value horticultural crops.

Multi-temporal images represent an excellent resource for seasonal monitoring of changes in crop water status. Five to six temporal points of data acquisition at critical phenological stages of crop development have been recommended for irrigation scheduling [31,32]. However, for semi-arid or arid regions, irrigation is typically required multiple times per week. Acquisition and post-processing of remote sensing data for actionable products multiple times a week is currently logistically unfeasible. The fusion of UAS-based remote sensing data, continuous ground-based proximal or direct sensors, including weather station data, can potentially inform daily estimates of water status at canopy level. This approach will require predictive models, such as those based on machine learning algorithms, to estimate the current and future water status of the crop. Eventually, growers would benefit from the knowledge of crop water requirements for the determination of seasonal irrigation requirements to sustainably farm into the future.

One vision for the future of precision irrigation is in automated pipelines to explicitly manage irrigation water at the sub-block level. This automated pipeline would likely include remote and proximal data acquisition and processing, prediction and interpretation of crop water status and requirements, and subsequently, control of irrigation systems. Recent rapid developments in cloud computing and wireless technology could assist in the quasi-real-time processing of the remote sensing data soon after acquisition [311–313]. Eventually, automation and computational power will merge to develop smart technology in which artificial intelligence uses real-time data analysis for diagnosis and decision-making. Growers of the future will be able to take advantage of precise irrigation recommendations using information sourced from a fleet of UAS that map large farm blocks on a daily schedule, continuous ground-based proximal and direct sensors, and weather stations. This data can be stored on and accessed from the cloud almost instantaneously, used in conjunction with post-processing algorithms for decision-making on optimised irrigation applications [311,314].

7. Conclusions

This paper provides a comprehensive review of the use of remote sensing to determine the water status of horticultural crops. One of our objectives was to survey the range of remote sensing tools available for irrigation decision-making. Earth observation satellite systems possess the required bands to study the water status of vegetation and soil. Satellites are more suitable for scouting, planning, and management of irrigation applications that involve large areas, and where data acquisition is not time-constrained. Manned aircraft are sparingly used in horticultural applications due to the cost, logistics, and specific expertise needed for the operation of the platform. UAS-based remote sensing provides flexibility in spatial resolution (crop level observation achievable), coverage (over 25 ha achievable in a single flight), spectral bands, as well as temporal revisit. Routine monitoring of horticultural crops for water status characterisation is, therefore, best performed using a UAS platform. We envision a future for precision irrigation where satellites are used for planning, and UAS used in conjunction with a network of ground-based sensors to achieve actionable products on a timely basis.

The plant's instantaneous response to water stress can be captured using thermal cameras (via indices, such as CWSI) and potentially narrow-band hyperspectral sensors (via, for example, SIF), making them suitable to draw quantifiable decisions with regard to irrigation scheduling. Broadband multispectral and RGB cameras capture the non-instantaneous water status of crops, making them suitable for general assessment of crop water status. Integrated use of thermal and multispectral imagery may be the simplest yet effective sensor combinations to capture the overall as well as instantaneous water status of the plant. With regard to irrigation scheduling, further developments are required to establish crop-specific thresholds of remotely-sensed indices to decide when and how much to irrigate.

Author Contributions: performed the article review and prepared the original draft, D.G.; contributed to write the case studies, V.P., and together with D.G. contributed to review and edit the manuscript. All authors have read and agreed to the published version of the manuscript.

Funding: This research and the APC was funded by Wine Australia (Grant number: UA 1803-1.3).

Acknowledgments: The authors would like to acknowledge the funding body Wine Australia, The University of Adelaide, and anonymous reviewers for their contribution.

Conflicts of Interest: The authors declare no conflict of interest.

References

1. Monaghan, J.M.; Daccache, A.; Vickers, L.H.; Hess, T.M.; Weatherhead, E.K.; Grove, I.G.; Knox, J.W. More 'crop per drop': constraints and opportunities for precision irrigation in European agriculture. *J. Sci. Food Agric.* **2013**, *93*, 977–980.

2. Smith, R. *Review of precision irrigation technologies and their applications*; University of Southern Queensland Darling Heights: Queensland, Australia, 2011.
3. Piao, S.; Ciais, P.; Huang, Y.; Shen, Z.; Peng, S.; Li, J.; Zhou, L.; Liu, H.; Ma, Y.; Ding, Y.; et al. The impacts of climate change on water resources and agriculture in China. *Nature* **2010**, *467*, 43.
4. Howden, S.M.; Soussana, J.-F.; Tubiello, F.N.; Chhetri, N.; Dunlop, M.; Meinke, H. Adapting agriculture to climate change. *Proc. Natl. Acad. Sci. USA* **2007**, *104*, 19691–19696.
5. Webb, L.; Whiting, J.; Watt, A.; Hill, T.; Wigg, F.; Dunn, G.; Needs, S.; Barlow, E. Managing grapevines through severe heat: A survey of growers after the 2009 summer heatwave in south-eastern Australia. *J. Wine Res.* **2010**, *21*, 147–165.
6. Datta, S. Impact of climate change in Indian horticulture-a review. *Int J Sci Env. Technol* **2013**, *2*, 661–671.
7. Webb, L.; Whetton, P.; Barlow, E. Modelled impact of future climate change on the phenology of winegrapes in Australia. *Aust. J. Grape Wine Res.* **2007**, *13*, 165–175.
8. Wang, J.; Mendelsohn, R.; Dinar, A.; Huang, J.; Rozelle, S.; Zhang, L. The impact of climate change on China's agriculture. *Agric. Econ.* **2009**, *40*, 323–337.
9. Beare, S.; Heaney, A. Climate change and water resources in the Murray Darling Basin, Australia. In Proceedings of the 2002 World Congress of Environmental and Resource Economists, Monterey, CA, USA, 24-27 June 2002.
10. Khan, S.; Tariq, R.; Yuanlai, C.; Blackwell, J. Can irrigation be sustainable? *Agric. Water Manag.* **2006**, *80*, 87–99.
11. Droogers, P.; Bastiaanssen, W. Irrigation performance using hydrological and remote sensing modeling. *J. Irrig. Drain. Eng.* **2002**, *128*, 11–18.
12. Ray, S.; Dadhwal, V. Estimation of crop evapotranspiration of irrigation command area using remote sensing and GIS. *Agric. Water Manag.* **2001**, *49*, 239–249.
13. Kim, Y.; Evans, R.G.; Iversen, W.M. Remote sensing and control of an irrigation system using a distributed wireless sensor network. *IEEE Trans. Instrum. Meas.* **2008**, *57*, 1379–1387.
14. Ritchie, G.A.; Hinckley, T.M. The pressure chamber as an instrument for ecological research. In *Advances in ecological research*; Elsevier: Amsterdam, Netherlands, 1975; Vol. 9, pp. 165–254.
15. Smart, R.; Barrs, H. The effect of environment and irrigation interval on leaf water potential of four horticultural species. *Agric. Meteorol.* **1973**, *12*, 337–346.
16. Meron, M.; Grimes, D.; Phene, C.; Davis, K. Pressure chamber procedures for leaf water potential measurements of cotton. *Irrig. Sci.* **1987**, *8*, 215–222.
17. Santos, A.O.; Kaye, O. Grapevine leaf water potential based upon near infrared spectroscopy. *Sci. Agric.* **2009**, *66*, 287–292.
18. Berni, J.A.J.; Zarco-Tejada, P.J.; Sepulcre-Cantó, G.; Fereres, E.; Villalobos, F. Mapping canopy conductance and CWSI in olive orchards using high resolution thermal remote sensing imagery. *Remote Sens. Environ.* **2009**, *113*, 2380–2388.
19. Chaves, M.M.; Santos, T.P.; de Souza, C.; Ortuño, M.; Rodrigues, M.; Lopes, C.; Maroco, J.; Pereira, J.S. Deficit irrigation in grapevine improves water-use efficiency while controlling vigour and production quality. *Ann. Appl. Biol.* **2007**, *150*, 237–252.
20. Bravdo, B.; Hepner, Y.; Loinger, C.; Cohen, S.; Tabacman, H. Effect of irrigation and crop level on growth, yield and wine quality of Cabernet Sauvignon. *Am. J. Enol. Vitic.* **1985**, *36*, 132–139.
21. Matthews, M.; Ishii, R.; Anderson, M.; O'Mahony, M. Dependence of wine sensory attributes on vine water status. *J. Sci. Food Agric.* **1990**, *51*, 321–335.
22. Reynolds, A.G.; Naylor, A.P. 'Pinot noir'' and "Riesling'' grapevines respond to water stress duration and soil water-holding capacity."' *HortScience* **1994**, *29*, 1505–1510.
23. Alvino, A.; Marino, S. Remote sensing for irrigation of horticultural crops. *Horticulturae* **2017**, *3*, 40.
24. Kullberg, E.G.; DeJonge, K.C.; Chávez, J.L. Evaluation of thermal remote sensing indices to estimate crop evapotranspiration coefficients. *Agric. Water Manag.* **2017**, *179*, 64–73.
25. Semmens, K.A.; Anderson, M.C.; Kustas, W.P.; Gao, F.; Alfieri, J.G.; McKee, L.; Prueger, J.H.; Hain, C.R.; Cammalleri, C.; Yang, Y.; et al. Monitoring daily evapotranspiration over two California vineyards using Landsat 8 in a multi-sensor data fusion approach. *Remote Sens. Environ.* **2015**, *185*, 155–170.
26. Jackson, R.D. Remote sensing of biotic and abiotic plant stress. *Annu. Rev. Phytopathol.* **1986**, *24*, 265–287.
27. Moran, M.; Clarke, T.; Inoue, Y.; Vidal, A. Estimating crop water deficit using the relation between surface-air temperature and spectral vegetation index. *Remote Sens. Environ.* **1994**, *49*, 246–263.

28. Lamb, D.; Hall, A.; Louis, J. Airborne remote sensing of vines for canopy variability and productivity. *Aust. Grapegrow. Winemak.* **2001**, *449a*, 89–94.
29. Hall, A.; Lamb, D.; Holzapfel, B.; Louis, J. Optical remote sensing applications in viticulture-a review. *Aust. J. Grape Wine Res.* **2002**, *8*, 36–47.
30. De Bei, R.; Cozzolino, D.; Sullivan, W.; Cynkar, W.; Fuentes, S.; Dambergs, R.; Pech, J.; Tyerman, S. Non-destructive measurement of grapevine water potential using near infrared spectroscopy. *Aust. J. Grape Wine Res.* **2011**, *17*, 62–71.
31. Bellvert, J.; Zarco-Tejada, P.J.; Marsal, J.; Girona, J.; González-Dugo, V.; Fereres, E. Vineyard irrigation scheduling based on airborne thermal imagery and water potential thresholds. *Aust. J. Grape Wine Res.* **2016**, *22*, 307–315.
32. Bellvert, J.; Marsal, J.; Girona, J.; Gonzalez-Dugo, V.; Fereres, E.; Ustin, S.; Zarco-Tejada, P. Airborne thermal imagery to detect the seasonal evolution of crop water status in peach, nectarine and Saturn peach orchards. *Remote Sens.* **2016**, *8*, 39.
33. Park, S.; Ryu, D.; Fuentes, S.; Chung, H.; Hernández-Montes, E.; O'Connell, M. Adaptive estimation of crop water stress in nectarine and peach orchards using high-resolution imagery from an unmanned aerial vehicle (UAV). *Remote Sens.* **2017**, *9*, 828.
34. Espinoza, C.Z.; Khot, L.R.; Sankaran, S.; Jacoby, P.W. High resolution multispectral and thermal remote sensing-based water stress assessment in subsurface irrigated grapevines. *Remote Sens.* **2017**, *9*, 961.
35. Ezenne, G.I.; Jupp, L.; Mantel, S.K.; Tanner, J.L. Current and potential capabilities of UAS for crop water productivity in precision agriculture. *Agric. Water Manag.* **2019**, *218*, 158–164.
36. Oliver, M.A.; Webster, R. Kriging: A method of interpolation for geographical information systems. *Int. J. Geogr. Inf. Syst.* **1990**, *4*, 313–332.
37. Ha, W.; Gowda, P.H.; Howell, T.A. A review of downscaling methods for remote sensing-based irrigation management: Part I. *Irrig. Sci.* **2013**, *31*, 831–850.
38. Ha, W.; Gowda, P.H.; Howell, T.A. A review of potential image fusion methods for remote sensing-based irrigation management: Part II. *Irrig. Sci.* **2013**, *31*, 851–869.
39. Belward, A.S.; Skøien, J.O. Who launched what, when and why; trends in global land-cover observation capacity from civilian earth observation satellites. *ISPRS J. Photogramm. Remote Sens.* **2015**, *103*, 115–128.
40. Lucieer, A.; Malenovskỳ, Z.; Veness, T.; Wallace, L. HyperUAS—Imaging spectroscopy from a multirotor unmanned aircraft system. *J. Field Robot.* **2014**, *31*, 571–590.
41. McCabe, M.F.; Rodell, M.; Alsdorf, D.E.; Miralles, D.G.; Uijlenhoet, R.; Wagner, W.; Lucieer, A.; Houborg, R.; Verhoest, N.E.; Franz, T.E.; et al. The future of Earth observation in hydrology. *Hydrol. Earth Syst. Sci.* **2017**, *21*, 3879.
42. Matese, A.; Toscano, P.; Di Gennaro, S.; Genesio, L.; Vaccari, F.; Primicerio, J.; Belli, C.; Zaldei, A.; Bianconi, R.; Gioli, B. Intercomparison of UAV, aircraft and satellite remote sensing platforms for precision viticulture. *Remote Sens.* **2015**, *7*, 2971–2990.
43. Mancini, A.; Frontoni, E.; Zingaretti, P. Satellite and UAV data for Precision Agriculture Applications. In Proceedings of the 2019 International Conference on Unmanned Aircraft Systems (ICUAS 2019), Atlanta, GA, USA, 11–14 June 2019; pp. 491–497.
44. Diago, M.P.; Bellincontro, A.; Scheidweiler, M.; Tardáguila, J.; Tittmann, S.; Stoll, M. Future opportunities of proximal near infrared spectroscopy approaches to determine the variability of vineyard water status. *Aust. J. Grape Wine Res.* **2017**, *23*, 409–414.
45. Gutierrez, S.; Diago, M.P.; Fernández-Novales, J.; Tardaguila, J. Vineyard water status assessment using on-the-go thermal imaging and machine learning. *PloS One* **2018**, *13*, e0192037.
46. Fernández-Novales, J.; Tardaguila, J.; Gutiérrez, S.; Marañón, M.; Diago, M.P. In field quantification and discrimination of different vineyard water regimes by on-the-go NIR spectroscopy. *Biosyst. Eng.* **2018**, *165*, 47–58.
47. Diago, M.P.; Fernández-Novales, J.; Gutiérrez, S.; Marañón, M.; Tardaguila, J. Development and validation of a new methodology to assess the vineyard water status by on-the-go near infrared spectroscopy. *Front. Plant Sci.* **2018**, *9*, 59.
48. Aquino, A.; Millan, B.; Diago, M.-P.; Tardaguila, J. Automated early yield prediction in vineyards from on-the-go image acquisition. *Comput. Electron. Agric.* **2018**, *144*, 26–36.
49. Markham, B.L.; Helder, D.L. Forty-year calibrated record of earth-reflected radiance from Landsat: A review. *Remote Sens. Environ.* **2012**, *122*, 30–40.

50. Toth, C.; Jóźków, G. Remote sensing platforms and sensors: A survey. *ISPRS J. Photogramm. Remote Sens.* **2016**, *115*, 22–36.
51. Tyc, G.; Tulip, J.; Schulten, D.; Krischke, M.; Oxfort, M. The RapidEye mission design. *Acta Astronaut.* **2005**, *56*, 213–219.
52. Sweeting, M.N. Modern small satellites-changing the economics of space. *Proc. IEEE* **2018**, *106*, 343–361.
53. Khanal, S.; Fulton, J.; Shearer, S. An overview of current and potential applications of thermal remote sensing in precision agriculture. *Comput. Electron. Agric.* **2017**, *139*, 22–32.
54. Gerhards, M.; Schlerf, M.; Mallick, K.; Udelhoven, T. Challenges and Future Perspectives of Multi-/Hyperspectral Thermal Infrared Remote Sensing for Crop Water-Stress Detection: A Review. *Remote Sens.* **2019**, *11*, 1240.
55. Ryan, S.; Lewis, M. Mapping soils using high resolution airborne imagery, Barossa Valley, SA. In Proceedings of the Inaugural Australian Geospatial Information and Agriculture Conference Incorporating Precision Agriculture in Australasia 5th Annual Symposium, Orange, NSW, Australia, 17–19 July 2001.
56. Khaliq, A.; Comba, L.; Biglia, A.; Ricauda Aimonino, D.; Chiaberge, M.; Gay, P. Comparison of satellite and UAV-based multispectral imagery for vineyard variability assessment. *Remote Sens.* **2019**, *11*, 436.
57. Jones, H.G.; Vaughan, R.A. *Remote sensing of vegetation: principles, techniques, and applications*; Oxford University Press: Oxford, UK, 2010.
58. Thenkabail, P.S.; Lyon, J.G. *Hyperspectral remote sensing of vegetation*; CRC press: Boco Raton, FL, USA, 2016;
59. King, M.D.; Platnick, S.; Menzel, W.P.; Ackerman, S.A.; Hubanks, P.A. Spatial and temporal distribution of clouds observed by MODIS onboard the Terra and Aqua satellites. *IEEE Trans. Geosci. Remote Sens.* **2013**, *51*, 3826–3852.
60. Chen, X.; Liu, M.; Zhu, X.; Chen, J.; Zhong, Y.; Cao, X. " Blend-then-Index" or" Index-then-Blend": A Theoretical Analysis for Generating High-resolution NDVI Time Series by STARFM. *Photogramm. Eng. Remote Sens.* **2018**, *84*, 65–73.
61. Yin, T.; Inglada, J.; Osman, J. Time series image fusion: Application and improvement of STARFM for land cover map and production. In Proceedings of the 2012 IEEE International Geoscience and Remote Sensing Symposium, Munich, Germany, 22-27 July 2012; pp. 378–381.
62. Gevaert, C.M.; García-Haro, F.J. A comparison of STARFM and an unmixing-based algorithm for Landsat and MODIS data fusion. *Remote Sens. Environ.* **2015**, *156*, 34–44.
63. Li, L.; Wang, X.; Li, M. Study on the fusion of MODIS and TM images using the spectral response function and STARFM algorithm. In Proceedings of the 2011 International Conference on Image Analysis and Signal Processing, Hubei, China, 21–23 October 2011; pp. 171–176.
64. Pagay, V.; Kidman, C.M. Evaluating Remotely-Sensed Grapevine (*Vitis vinifera* L.) Water Stress Responses Across a Viticultural Region. *Agronomy* **2019**, *9*, 682.
65. Rascher, U.; Alonso, L.; Burkart, A.; Cilia, C.; Cogliati, S.; Colombo, R.; Damm, A.; Drusch, M.; Guanter, L.; Hanus, J.; et al. Sun-induced fluorescence—A new probe of photosynthesis: First maps from the imaging spectrometer HyPlant. *Glob. Change Biol.* **2015**, *21*, 4673–4684.
66. Buckley, S.; Vallet, J.; Braathen, A.; Wheeler, W. Oblique helicopter-based laser scanning for digital terrain modelling and visualisation of geological outcrops. *Int. Arch. Photogramm. Remote Sens. Spat. Inf. Sci.* **2008**, *37*, 1–6.
67. Pullanagari, R.; Kereszturi, G.; Yule, I. Mapping of macro and micro nutrients of mixed pastures using airborne AisaFENIX hyperspectral imagery. *ISPRS J. Photogramm. Remote Sens.* **2016**, *117*, 1–10.
68. Haboudane, D.; Miller, J.R.; Tremblay, N.; Zarco-Tejada, P.J.; Dextraze, L. Integrated narrow-band vegetation indices for prediction of crop chlorophyll content for application to precision agriculture. *Remote Sens. Environ.* **2002**, *81*, 416–426.
69. Miao, Y.; Mulla, D.J.; Randall, G.W.; Vetsch, J.A.; Vintila, R. Predicting chlorophyll meter readings with aerial hyperspectral remote sensing for in-season site-specific nitrogen management of corn. *Precis. Agric.* **2007**, *7*, 635–641.
70. Haboudane, D.; Miller, J.R.; Pattey, E.; Zarco-Tejada, P.J.; Strachan, I.B. Hyperspectral vegetation indices and novel algorithms for predicting green LAI of crop canopies: Modeling and validation in the context of precision agriculture. *Remote Sens. Environ.* **2004**, *90*, 337–352.
71. Sepulcre-Cantó, G.; Zarco-Tejada, P.J.; Jiménez-Muñoz, J.; Sobrino, J.; Soriano, M.; Fereres, E.; Vega, V.; Pastor, M. Monitoring yield and fruit quality parameters in open-canopy tree crops under water stress. Implications for ASTER. *Remote Sens. Environ.* **2007**, *107*, 455–470.

72. Sepulcre-Cantó, G.; Zarco-Tejada, P.J.; Jiménez-Muñoz, J.; Sobrino, J.; De Miguel, E.; Villalobos, F.J. Detection of water stress in an olive orchard with thermal remote sensing imagery. *Agric. For. Meteorol.* **2006**, *136*, 31–44.
73. Colomina, I.; Molina, P. Unmanned aerial systems for photogrammetry and remote sensing: A review. *ISPRS J. Photogramm. Remote Sens.* **2014**, *92*, 79–97.
74. Zecha, C.; Link, J.; Claupein, W. Mobile sensor platforms: Categorisation and research applications in precision farming. *J. Sens. Sens. Syst.* **2013**, *2*, 51–72.
75. Urbahs, A.; Jonaite, I. Features of the use of unmanned aerial vehicles for agriculture applications. *Aviation* **2013**, *17*, 170–175.
76. Gautam, D.; Ha, C. Control of a quadrotor using a smart self-tuning fuzzy PID controller. *Int. J. Adv. Robot. Syst.* **2013**, *10*, 380.
77. Shi, Y.; Thomasson, J.A.; Murray, S.C.; Pugh, N.A.; Rooney, W.L.; Shafian, S.; Rajan, N.; Rouze, G.; Morgan, C.L.; Neely, H.L.; et al. Unmanned aerial vehicles for high-throughput phenotyping and agronomic research. *PloS One* **2016**, *11*, e0159781.
78. Zhang, C.; Kovacs, J.M. The application of small unmanned aerial systems for precision agriculture: a review. *Precis. Agric.* **2012**, *13*, 693–712.
79. Mulla, D.J. Twenty five years of remote sensing in precision agriculture: Key advances and remaining knowledge gaps. *Biosyst. Eng.* **2013**, *114*, 358–371.
80. Huang, Y.; Thomson, S.J.; Hoffmann, W.C.; Lan, Y.; Fritz, B.K. Development and prospect of unmanned aerial vehicle technologies for agricultural production management. *Int. J. Agric. Biol. Eng.* **2013**, *6*, 1–10.
81. Zude-Sasse, M.; Fountas, S.; Gemtos, T.A.; Abu-Khalaf, N. Applications of precision agriculture in horticultural crops. *Eur. J. Hortic. Sci.* **2016**, *81*, 78–90.
82. Baluja, J.; Diago, M.P.; Balda, P.; Zorer, R.; Meggio, F.; Morales, F.; Tardaguila, J. Assessment of vineyard water status variability by thermal and multispectral imagery using an unmanned aerial vehicle (UAV). *Irrig. Sci.* **2012**, *30*, 511–522.
83. Matese, A.; Baraldi, R.; Berton, A.; Cesaraccio, C.; Di Gennaro, S.F.; Duce, P.; Facini, O.; Mameli, M.G.; Piga, A.; Zaldei, A. Estimation of water stress in grapevines using proximal and remote sensing methods. *Remote Sens.* **2018**, *10*, 1–17.
84. Poblete, T.; Ortega-Farías, S.; Moreno, M.; Bardeen, M. Artificial neural network to predict vine water status spatial variability using multispectral information obtained from an unmanned aerial vehicle (UAV). *Sensors* **2017**, *17*, 2488.
85. Gonzalez-Dugo, V.; Zarco-Tejada, P.J.; Fereres, E. Applicability and limitations of using the crop water stress index as an indicator of water deficits in citrus orchards. *Agric. For. Meteorol.* **2014**, *198*, 94–104.
86. Stagakis, S.; González-Dugo, V.; Cid, P.; Guillén-Climent, M.L.; Zarco-Tejada, P.J. Monitoring water stress and fruit quality in an orange orchard under regulated deficit irrigation using narrow-band structural and physiological remote sensing indices. *ISPRS J. Photogramm. Remote Sens.* **2012**, *71*, 47–61.
87. Agam, N.; Cohen, Y.; Berni, J.A.J.; Alchanatis, V.; Kool, D.; Dag, A.; Yermiyahu, U.; Ben-Gal, A. An insight to the performance of crop water stress index for olive trees. *Agric. Water Manag.* **2013**, *118*, 79–86.
88. Poblete-Echeverría, C.; Sepulveda-Reyes, D.; Ortega-Farias, S.; Zuñiga, M.; Fuentes, S. Plant water stress detection based on aerial and terrestrial infrared thermography: A study case from vineyard and olive orchard. In Proceedings of the XXIX International Horticultural congress on Horticulture: Sustaining Lives, Livelihoods and Landscapes (IHC2014): International Symposia on Water, Eco-Efficiency and Transformation of Organic Waste in Horticultural Production; Brisbane, Australia, 25 October 2016, pp. 141–146.
89. Testi, L.; Goldhamer, D.; Iniesta, F.; Salinas, M. Crop water stress index is a sensitive water stress indicator in pistachio trees. *Irrig. Sci.* **2008**, *26*, 395–405.
90. Gonzalez-Dugo, V.; Goldhamer, D.; Zarco-Tejada, P.J.; Fereres, E. Improving the precision of irrigation in a pistachio farm using an unmanned airborne thermal system. *Irrig. Sci.* **2015**, *33*, 43–52.
91. García-Tejero, I.F.; Rubio, A.E.; Viñuela, I.; Hernández, A.; Gutiérrez-Gordillo, S.; Rodríguez-Pleguezuelo, C.R.; Durán-Zuazo, V.H. Thermal imaging at plant level to assess the crop-water status in almond trees (cv. Guara) under deficit irrigation strategies. *Agric. Water Manag.* **2018**, *208*, 176–186.
92. Gonzalez-Dugo, V.; Zarco-Tejada, P.; Berni, J.A.; Suárez, L.; Goldhamer, D.; Fereres, E. Almond tree canopy temperature reveals intra-crown variability that is water stress-dependent. *Agric. For. Meteorol.* **2012**, *154*, 156–165.

93. Zhao, T.; Stark, B.; Chen, Y.; Ray, A.L.; Doll, D. Challenges in water stress quantification using small unmanned aerial system (sUAS): Lessons from a growing season of almond. *J. Intell. Robot. Syst.* **2017**, *88*, 721–735.
94. Zhao, T.; Doll, D.; Wang, D.; Chen, Y. A new framework for UAV-based remote sensing data processing and its application in almond water stress quantification. In Proceedings of the 2017 International Conference on Unmanned Aircraft Systems (ICUAS 2017), Miami, FL, USA, 13–16 June 2017; pp. 1794–1799.
95. Herwitz, S.; Johnson, L.; Dunagan, S.; Higgins, R.; Sullivan, D.; Zheng, J.; Lobitz, B.; Leung, J.; Gallmeyer, B.; Aoyagi, M.; et al. Imaging from an unmanned aerial vehicle: agricultural surveillance and decision support. *Comput. Electron. Agric.* **2004**, *44*, 49–61.
96. Furfaro, R.; Ganapol, B.D.; Johnson, L.; Herwitz, S. Model-based neural network algorithm for coffee ripeness prediction using Helios UAV aerial images. In *Remote Sensing for Agriculture, Ecosystems, and Hydrology VII*; International Society for Optics and Photonics: Bruges, Belgium, 2005; Vol. 5976, p. 59760X.
97. Park, S.; Nolan, A.; Ryu, D.; Fuentes, S.; Hernandez, E.; Chung, H.; O'connell, M. Estimation of crop water stress in a nectarine orchard using high-resolution imagery from unmanned aerial vehicle (UAV). In Proceedings of the 21st International Congress on Modelling and Simulation, Gold Coast, QLD, Australia, 29 November–4 December 2015; pp. 1413–1419.
98. Bulanon, D.M.; Lonai, J.; Skovgard, H.; Fallahi, E. Evaluation of different irrigation methods for an apple orchard using an aerial imaging system. *ISPRS Int. J. Geo-Inf.* **2016**, *5*, *79*.
99. Gonzalez-Dugo, V.; Zarco-Tejada, P.; Nicolás, E.; Nortes, P.A.; Alarcón, J.; Intrigliolo, D.S.; Fereres, E. Using high resolution UAV thermal imagery to assess the variability in the water status of five fruit tree species within a commercial orchard. *Precis. Agric.* **2013**, *14*, 660–678.
100. Santesteban, L.G.; Di Gennaro, S.F.; Herrero-Langreo, A.; Miranda, C.; Royo, J.B.; Matese, A. High-resolution UAV-based thermal imaging to estimate the instantaneous and seasonal variability of plant water status within a vineyard. *Agric. Water Manag.* **2017**, *183*, 49–59.
101. Aboutalebi, M.; Torres-Rua, A.F.; Kustas, W.P.; Nieto, H.; Coopmans, C.; McKee, M. Assessment of different methods for shadow detection in high-resolution optical imagery and evaluation of shadow impact on calculation of NDVI, and evapotranspiration. *Irrig. Sci.* **2018**, 1, 1–23.
102. Berni, J.A.; Zarco-Tejada, P.J.; Suárez, L.; Fereres, E. Thermal and narrowband multispectral remote sensing for vegetation monitoring from an unmanned aerial vehicle. *IEEE Trans. Geosci. Remote Sens.* **2009**, *47*, 722–738.
103. Candiago, S.; Remondino, F.; De Giglio, M.; Dubbini, M.; Gattelli, M. Evaluating multispectral images and vegetation indices for precision farming applications from UAV images. *Remote Sens.* **2015**, *7*, 4026–4047.
104. Thomasson, J.A.; Shi, Y.; Olsenholler, J.; Valasek, J.; Murray, S.C.; Bishop, M.P. Comprehensive UAV agricultural remote-sensing research at Texas AM University. In *Autonomous Air and Ground Sensing Systems for Agricultural Optimization and Phenotyping*; International Society for Optics and Photonics: Baltimore, Maryland, USA, 2016; Vol. 9866, p. 986602.
105. Turner, D.; Lucieer, A.; Wallace, L. Direct georeferencing of ultrahigh-resolution UAV imagery. *IEEE Trans. Geosci. Remote Sens.* **2014**, *52*, 2738–2745.
106. Primicerio, J.; Di Gennaro, S.F.; Fiorillo, E.; Genesio, L.; Lugato, E.; Matese, A.; Vaccari, F.P. A flexible unmanned aerial vehicle for precision agriculture. *Precis. Agric.* **2012**, *13*, 517–523.
107. Pajares, G. Overview and current status of remote sensing applications based on unmanned aerial vehicles (UAVs). *Photogramm. Eng. Remote Sens.* **2015**, *81*, 281–330.
108. Di Gennaro, S.F.; Matese, A.; Gioli, B.; Toscano, P.; Zaldei, A.; Palliotti, A.; Genesio, L. Multisensor approach to assess vineyard thermal dynamics combining high-resolution unmanned aerial vehicle (UAV) remote sensing and wireless sensor network (WSN) proximal sensing. *Sci. Hortic.* **2017**, *221*, 83–87.
109. Cendrero-Mateo, M.P.; Wieneke, S.; Damm, A.; Alonso, L.; Pinto, F.; Moreno, J.; Guanter, L.; Celesti, M.; Rossini, M.; Sabater, N.; et al. Sun-induced chlorophyll fluorescence III: Benchmarking retrieval methods and sensor characteristics for proximal sensing. *Remote Sens.* **2019**, *11*, 962.
110. Zarco-Tejada, P.J.; González-Dugo, V.; Berni, J.A.J. Fluorescence, temperature and narrow-band indices acquired from a UAV platform for water stress detection using a micro-hyperspectral imager and a thermal camera. *Remote Sens. Environ.* **2012**, *117*, 322–337.
111. Harwin, S.; Lucieer, A. Assessing the accuracy of georeferenced point clouds produced via multi-view stereopsis from Unmanned Aerial Vehicle (UAV) imagery. *Remote Sens.* **2012**, *4*, 1573–1599.

112. Wallace, L.; Lucieer, A.; Malenovskỳ, Z.; Turner, D.; Vopěnka, P. Assessment of forest structure using two UAV techniques: A comparison of airborne laser scanning and structure from motion (SfM) point clouds. *Forests* **2016**, *7*, 62.
113. Weiss, M.; Baret, F. Using 3D point clouds derived from UAV RGB imagery to describe vineyard 3D macro-structure. *Remote Sens.* **2017**, *9, 111*.
114. Mathews, A.; Jensen, J. Visualizing and quantifying vineyard canopy LAI using an unmanned aerial vehicle (UAV) collected high density structure from motion point cloud. *Remote Sens.* **2013**, *5*, 2164–2183.
115. Stone, C.; Webster, M.; Osborn, J.; Iqbal, I. Alternatives to LiDAR-derived canopy height models for softwood plantations: a review and example using photogrammetry. *Aust. For.* **2016**, *79*, 271–282.
116. Wu, D.; Phinn, S.; Johansen, K.; Robson, A.; Muir, J.; Searle, C. Estimating changes in leaf area, leaf area density, and vertical leaf area profile for mango, avocado, and macadamia tree crowns using terrestrial laser scanning. *Remote Sens.* **2018**, *10*, 1750.
117. Rosell, J.R.; Llorens, J.; Sanz, R.; Arno, J.; Ribes-Dasi, M.; Masip, J.; Escolà, A.; Camp, F.; Solanelles, F.; Gràcia, F.; et al. Obtaining the three-dimensional structure of tree orchards from remote 2D terrestrial LIDAR scanning. *Agric. For. Meteorol.* **2009**, *149*, 1505–1515.
118. Matese, A.; Di Gennaro, S.F. Technology in precision viticulture: A state of the art review. *Int J Wine Res* **2015**, *7*, 69–81.
119. Johansen, K.; Raharjo, T.; McCabe, M.F. Using multi-spectral UAV imagery to extract tree crop structural properties and assess pruning effects. *Remote Sens.* **2018**, 10, 854.
120. Tu, Y.-H.; Johansen, K.; Phinn, S.; Robson, A. Measuring canopy structure and condition using multi-spectral UAS imagery in a horticultural environment. *Remote Sens.* **2019**, *11*, 269.
121. Mu, Y.; Fujii, Y.; Takata, D.; Zheng, B.; Noshita, K.; Honda, K.; Ninomiya, S.; Guo, W. Characterization of peach tree crown by using high-resolution images from an unmanned aerial vehicle. *Hortic. Res.* **2018**, *5*, 74.
122. de Castro, A.I.; Jiménez-Brenes, F.M.; Torres-Sánchez, J.; Peña, J.M.; Borra-Serrano, I.; López-Granados, F. 3-D characterization of vineyards using a novel UAV imagery-based OBIA procedure for precision viticulture applications. *Remote Sens.* **2018**, *10, 584*.
123. Del Pozo, S.; Rodríguez-Gonzálvez, P.; Hernández-López, D.; Felipe-García, B. Vicarious radiometric calibration of a multispectral camera on board an unmanned aerial system. *Remote Sens.* **2014**, *6*, 1918–1937.
124. Tu, Y.-H.; Phinn, S.; Johansen, K.; Robson, A. Assessing radiometric correction approaches for multi-spectral UAS imagery for horticultural applications. *Remote Sens.* **2018**, *10*, 1684.
125. Stow, D.; Nichol, C.J.; Wade, T.; Assmann, J.J.; Simpson, G.; Helfter, C. Illumination geometry and flying height influence surface reflectance and NDVI derived from multispectral UAS imagery. *Drones* **2019**, *3*, 55.
126. Turner, D.; Lucieer, A.; Watson, C. Development of an unmanned aerial vehicle (UAV) for hyper resolution vineyard mapping based on visible, multispectral, and thermal imagery. In Proceedings of the 34th International symposium on remote sensing of environment, Sydney, Australia, 10–15 April 2011; p. 4.
127. Jorge, J.; Vallbé, M.; Soler, J.A. Detection of irrigation inhomogeneities in an olive grove using the NDRE vegetation index obtained from UAV images. *Eur. J. Remote Sens.* **2019**, *52*, 169–177.
128. Filella, I.; Penuelas, J. The red edge position and shape as indicators of plant chlorophyll content, biomass and hydric status. *Int. J. Remote Sens.* **1994**, *15*, 1459–1470.
129. Zúñiga, C.E.; Khot, L.R.; Jacoby, P.; Sankaran, S. Remote sensing based water-use efficiency evaluation in sub-surface irrigated wine grape vines. In *Autonomous Air and Ground Sensing Systems for Agricultural Optimization and Phenotyping*; International Society for Optics and Photonics: Baltimore, Maryland, USA, 2016; Vol. 9866, p. 98660O.
130. Aasen, H.; Honkavaara, E.; Lucieer, A.; Zarco-Tejada, P. Quantitative remote sensing at ultra-high resolution with uav spectroscopy: A review of sensor technology, measurement procedures, and data correction workflows. *Remote Sens.* **2018**, *10*, 1091.
131. Adão, T.; Hruška, J.; Pádua, L.; Bessa, J.; Peres, E.; Morais, R.; Sousa, J. Hyperspectral imaging: A review on UAV-based sensors, data processing and applications for agriculture and forestry. *Remote Sens.* **2017**, *9*, 1110.
132. Gautam, D.; Watson, C.; Lucieer, A.; Malenovský, Z. Error budget for geolocation of spectroradiometer point observations from an unmanned aircraft system. *Sens. Switz.* **2018**, *18*, 1–16.

133. Uto, K.; Seki, H.; Saito, G.; Kosugi, Y.; Komatsu, T. Development of a low-cost hyperspectral whiskbroom imager using an optical fiber bundle, a swing mirror, and compact spectrometers. *IEEE J. Sel. Top. Appl. Earth Obs. Remote Sens.* **2016**, *9*, 3909–3925.
134. Suomalainen, J.; Anders, N.; Iqbal, S.; Roerink, G.; Franke, J.; Wenting, P.; Hünniger, D.; Bartholomeus, H.; Becker, R.; Kooistra, L. A lightweight hyperspectral mapping system and photogrammetric processing chain for unmanned aerial vehicles. *Remote Sens.* **2014**, *6*, 11013–11030.
135. Iseli, C.; Lucieer, A. Tree species classification based on 3d spectral point clouds and orthomosaics acquired by snapshot hyperspectral UAS sensor. *ISPRS-Int. Arch. Photogramm. Remote Sens. Spat. Inf. Sci.* **2019**, *4213*, 379–384.
136. Hagen, N.A.; Kudenov, M.W. Review of snapshot spectral imaging technologies. *Opt. Eng.* **2013**, *52*, 090901.
137. Bendig, J.; Gautam, D.; Malenovsky, Z.; Lucieer, A. Influence of Cosine Corrector and UAS Platform Dynamics on Airborne Spectral Irradiance Measurements. In Proceedings of the 2018 IEEE International Geoscience and Remote Sensing Symposium (IGARSS 2018), Valencia, Spain, 22–27 July **2018**; pp. 8822–8825.
138. Gautam, D. Direct georeferencing and footprint characterisation of a non-imaging spectroradiometer mounted on an unmanned aircraft system. Ph.D. Thesis, University of Tasmania, Hobart, Tasmania, Australia, 2019.
139. Rodríguez-Pérez, J.R.; Riaño, D.; Carlisle, E.; Ustin, S.; Smart, D.R. Evaluation of hyperspectral reflectance indexes to detect grapevine water status in vineyards. *Am. J. Enol. Vitic.* **2007**, *58*, 302–317.
140. Hurley, S.P.; Horney, M.; Drake, A. Using hyperspectral imagery to detect water stress in vineyards. In *Autonomous Air and Ground Sensing Systems for Agricultural Optimization and Phenotyping IV*; International Society for Optics and Photonics: Baltimore, Maryland, USA, 2019; Vol. 11008, p. 1100807.
141. Loggenberg, K.; Strever, A.; Greyling, B.; Poona, N. Modelling water stress in a shiraz vineyard using hyperspectral imaging and machine learning. *Remote Sens.* **2018**, *10*, 1–15.
142. Gómez-Candón, D.; Virlet, N.; Labbé, S.; Jolivot, A.; Regnard, J.-L. Field phenotyping of water stress at tree scale by UAV-sensed imagery: new insights for thermal acquisition and calibration. *Precis. Agric.* **2016**, *17*, 786–800.
143. Kelly, J.; Kljun, N.; Olsson, P.-O.; Mihai, L.; Liljeblad, B.; Weslien, P.; Klemedtsson, L.; Eklundh, L. Challenges and best practices for deriving temperature data from an uncalibrated UAV thermal infrared camera. *Remote Sens.* **2019**, *11*, 567.
144. Smigaj, M.; Gaulton, R.; Suarez, J.; Barr, S. Use of miniature thermal cameras for detection of physiological stress in conifers. *Remote Sens.* **2017**, *9*, 957.
145. Clarke, I. Thermal infrared remote sensing from unmanned aircraft systems (UAS) for precision viticulture. Master's Thesis, University of Tasmania, Hobart, Tasmania, Australia, 2014.
146. Daakir, M.; Zhou, Y.; Pierrot Deseilligny, M.; Thom, C.; Martin, O.; Rupnik, E. Improvement of photogrammetric accuracy by modeling and correcting the thermal effect on camera calibration. *ISPRS J. Photogramm. Remote Sens.* **2019**, *148*, 142–155.
147. Nugent, P.W.; Shaw, J.A. Calibration of uncooled LWIR microbolometer imagers to enable long-term field deployment. In *Infrared Imaging Systems: Design, Analysis, Modeling, and Testing XXV*; International Society for Optics and Photonics: Baltimore, Maryland, USA, 2014; Vol. 9071, p. 90710V.
148. Budzier, H.; Gerlach, G. Calibration of uncooled thermal infrared cameras. *J. Sens. Sens. Syst.* **2015**, *4*, 187–197.
149. Lin, D.; Maas, H.-G.; Westfeld, P.; Budzier, H.; Gerlach, G. An advanced radiometric calibration approach for uncooled thermal cameras. *Photogramm. Rec.* **2018**, *33*, 30–48.
150. Ribeiro-Gomes, K.; Hernández-López, D.; Ortega, J.F.; Ballesteros, R.; Poblete, T.; Moreno, M.A. Uncooled thermal camera calibration and optimization of the photogrammetry process for UAV applications in agriculture. *Sensors* **2017**, *17*, 9–11.
151. Lin, D.; Westfeld, P.; Maas, H.G. Shutter-less temperature-dependent correction for uncooled thermal camera under fast changing FPA temperature. *Int. Arch. Photogramm. Remote Sens. Spat. Inf. Sci. - ISPRS Arch.* **2017**, *42*, 619–625.
152. Mesas-Carrascosa, F.J.; Pérez-Porras, F.; de Larriva, J.E.M.; Frau, C.M.; Agüera-Vega, F.; Carvajal-Ramírez, F.; Martínez-Carricondo, P.; García-Ferrer, A. Drift correction of lightweight microbolometer thermal sensors on-board unmanned aerial vehicles. *Remote Sens.* **2018**, *10*, 1–17.

153. Torres-Rua, A. Vicarious calibration of sUAS microbolometer temperature imagery for estimation of radiometric land surface temperature. *Sensors* **2017**, *17*, 1499.
154. Bendig, J.; Bolten, A.; Bareth, G. Introducing a low-cost mini-UAV for thermal-and multispectral-imaging. *Int Arch Photogramm Remote Sens Spat Inf Sci* **2012**, *39*, 345–349.
155. Raymer, D. *Aircraft design: a conceptual approach*; American Institute of Aeronautics and Astronautics, Inc.: Reston, VA, USA, 2018.
156. Tardieu, F.; Simonneau, T. Variability among species of stomatal control under fluctuating soil water status and evaporative demand: modelling isohydric and anisohydric behaviours. *J. Exp. Bot.* **1998**, 49, 419–432.
157. White, W.A.; Alsina, M.M.; Nieto, H.; McKee, L.G.; Gao, F.; Kustas, W.P. Determining a robust indirect measurement of leaf area index in California vineyards for validating remote sensing-based retrievals. *Irrig. Sci.* **2019**, *37*, 269–280.
158. Zarco-Tejada, P.J.; Berni, J.A.; Suárez, L.; Sepulcre-Cantó, G.; Morales, F.; Miller, J.R. Imaging chlorophyll fluorescence with an airborne narrow-band multispectral camera for vegetation stress detection. *Remote Sens. Environ.* **2009**, *113*, 1262–1275.
159. Gago, J.; Douthe, C.; Florez-Sarasa, I.; Escalona, J.M.; Galmes, J.; Fernie, A.R.; Flexas, J.; Medrano, H. Opportunities for improving leaf water use efficiency under climate change conditions. *Plant Sci.* **2014**, *226*, 108–119.
160. Suárez, L.; Zarco-Tejada, P.J.; Sepulcre-Cantó, G.; Pérez-Priego, O.; Miller, J.; Jiménez-Muñoz, J.; Sobrino, J. Assessing canopy PRI for water stress detection with diurnal airborne imagery. *Remote Sens. Environ.* **2008**, *112*, 560–575.
161. Eugenio, F.; Marqués, F. Automatic satellite image georeferencing using a contour-matching approach. *IEEE Trans. Geosci. Remote Sens.* **2003**, *41*, 2869–2880.
162. Hugenholtz, C.; Brown, O.; Walker, J.; Barchyn, T.; Nesbit, P.; Kucharczyk, M.; Myshak, S. Spatial accuracy of UAV-derived orthoimagery and topography: Comparing photogrammetric models processed with direct geo-referencing and ground control points. *Geomatica* **2016**, *70*, 21–30.
163. Matese, A.; Di Gennaro, S.F.; Berton, A. Assessment of a canopy height model (CHM) in a vineyard using UAV-based multispectral imaging. *Int. J. Remote Sens.* **2017**, *38*, 2150–2160.
164. Yahyanejad, S.; Misiorny, J.; Rinner, B. Lens distortion correction for thermal cameras to improve aerial imaging with small-scale UAVs. In Proceedings of the 2011 IEEE International Symposium on Robotic and Sensors Environments (ROSE 2011), Montreal, QC, Canada, 17–18 September 2011; pp. 231–236.
165. Maes, W.; Huete, A.; Steppe, K. Optimizing the processing of UAV-based thermal imagery. *Remote Sens.* **2017**, *9*, 476.
166. Smith, M.; Carrivick, J.; Quincey, D. Structure from motion photogrammetry in physical geography. *Prog. Phys. Geogr.* **2016**, *40*, 247–275.
167. Westoby, M.J.; Brasington, J.; Glasser, N.F.; Hambrey, M.J.; Reynolds, J.M. 'Structure-from-Motion'photogrammetry: A low-cost, effective tool for geoscience applications. *Geomorphology* **2012**, *179*, 300–314.
168. Gautam, D.; Lucieer, A.; Malenovský, Z.; Watson, C. Comparison of MEMS-based and FOG-based IMUs to determine sensor pose on an unmanned aircraft system. *J. Surv. Eng.* **2017**, *143*, doi: 10.1061/(ASCE)SU.1943-5428.0000225.
169. Turner, D.; Lucieer, A.; McCabe, M.; Parkes, S.; Clarke, I. Pushbroom hyperspectral imaging from an unmanned aircraft system (UAS)–geometric processingworkflow and accuracy assessment. *ISPRS-Int. Arch. Photogramm. Remote Sens. Spat. Inf. Sci.* **2017**, *XLII-2/W6*, 379–384.
170. Fang, J.; Wang, X.; Zhu, T.; Liu, X.; Zhang, X.; Zhao, D. A Novel Mosaic Method for UAV-Based Hyperspectral Images. In Proceedings of the 2019 IEEE International Geoscience and Remote Sensing Symposium (IGARSS 2019), Yokohama, Japan, 28 July–2 August 2019; pp. 9220–9223.
171. Tagle, X. Study of radiometric variations in unmanned aerial vehicle remote sensing imagery for vegetation mapping. Master's Thesis, Lund University, Lund, Sweden, 2017.
172. Kedzierski, M.; Wierzbicki, D.; Sekrecka, A.; Fryskowska, A.; Walczykowski, P.; Siewert, J. Influence of lower atmosphere on the radiometric quality of unmanned aerial vehicle imagery. *Remote Sens.* **2019**, *11*, 1214.
173. Kelcey, J.; Lucieer, A. Sensor correction of a 6-band multispectral imaging sensor for UAV remote sensing. *Remote Sens.* **2012**, *4*, 1462–1493.

174. Maes, W.H.; Steppe, K. Perspectives for remote sensing with unmanned aerial vehicles in precision agriculture. *Trends Plant Sci.* **2019**, *24*, 152–164.
175. McCabe, M.F.; Houborg, R.; Lucieer, A. High-resolution sensing for precision agriculture: from Earth-observing satellites to unmanned aerial vehicles. In *Remote Sensing for Agriculture, Ecosystems, and Hydrology XVIII*; International Society for Optics and Photonics: Edinbrugh, UK, 2016; Vol. 9998, p. 999811.
176. Dinguirard, M.; Slater, P.N. Calibration of space-multispectral imaging sensors: A review. *Remote Sens. Environ.* **1999**, *68*, 194–205.
177. Geladi, P.; Burger, J.; Lestander, T. Hyperspectral imaging: calibration problems and solutions. *Chemom. Intell. Lab. Syst.* **2004**, *72*, 209–217.
178. Iqbal, F.; Lucieer, A.; Barry, K. Simplified radiometric calibration for UAS-mounted multispectral sensor. *Eur. J. Remote Sens.* **2018**, *51*, 301–313.
179. Mamaghani, B.; Salvaggio, C. Multispectral Sensor Calibration and Characterization for sUAS Remote Sensing. *Sensors* **2019**, *19*, 4453.
180. Mamaghani, B.; Salvaggio, C. Comparative study of panel and panelless-based reflectance conversion techniques for agricultural remote sensing. *arXiv*, **2019**, arXiv191003734.
181. Jensen, A.M.; McKee, M.; Chen, Y. Calibrating thermal imagery from an unmanned aerial system-AggieAir. In Proceedings of the 2013 IEEE International Geoscience and Remote Sensing Symposium (IGARSS 2013), Melbourne, Australia, 21–26 July 2013; pp. 542–545.
182. Zarco-Tejada, P.J.; Victoria, G.-D.; Williams, L.; Suárez, L.; Berni, J.A.; Goldhamer, D.; Fereres, E. A PRI-based water stress index combining structural and chlorophyll effects: Assessment using diurnal narrow-band airborne imagery and the CWSI thermal index. *Remote Sens. Environ.* **2013**, *138*, 38–50.
183. Blaschke, T. Object based image analysis for remote sensing. *ISPRS J. Photogramm. Remote Sens.* **2010**, *65*, 2–16.
184. de Castro, A.; Torres-Sánchez, J.; Peña, J.; Jiménez-Brenes, F.; Csillik, O.; López-Granados, F. An automatic random forest-OBIA algorithm for early weed mapping between and within crop rows using UAV imagery. *Remote Sens.* **2018**, *10*, 285.
185. Peña-Barragán, J.M.; Ngugi, M.K.; Plant, R.E.; Six, J. Object-based crop identification using multiple vegetation indices, textural features and crop phenology. *Remote Sens. Environ.* **2011**, *115*, 1301–1316.
186. Johansen, K.; Raharjo, T. Multi-temporal assessment of lychee tree crop structure using multi-spectral RPAS imagery. *ISPRS Int. Arch. Photogramm. Remote Sens. Spat. Inf. Sci.* **2017**, *XLII-2/W6*, 165–170.
187. Ma, L.; Li, M.; Ma, X.; Cheng, L.; Du, P.; Liu, Y. A review of supervised object-based land-cover image classification. *ISPRS J. Photogramm. Remote Sens.* **2017**, *130*, 277–293.
188. Pádua, L.; Vanko, J.; Hruška, J.; Adão, T.; Sousa, J.J.; Peres, E.; Morais, R. UAS, sensors, and data processing in agroforestry: a review towards practical applications. *Int. J. Remote Sens.* **2017**, *38*, 2349–2391.
189. Torres-Sánchez, J.; López-Granados, F.; Peña, J.M. An automatic object-based method for optimal thresholding in UAV images: Application for vegetation detection in herbaceous crops. *Comput. Electron. Agric.* **2015**, *114*, 43–52.
190. Cohen, Y.; Alchanatis, V.; Prigojin, A.; Levi, A.; Soroker, V. Use of aerial thermal imaging to estimate water status of palm trees. *Precis. Agric.* **2012**, *13*, 123–140.
191. Comba, L.; Gay, P.; Primicerio, J.; Aimonino, D.R. Vineyard detection from unmanned aerial systems images. *Comput. Electron. Agric.* **2015**, *114*, 78–87.
192. Nolan, A.; Park, S.; Fuentes, S.; Ryu, D.; Chung, H. Automated detection and segmentation of vine rows using high resolution UAS imagery in a commercial vineyard. In Proceedings of the 21st International Congress on Modelling and Simulation, Gold Coast, QLD, Australia, 29 November–4 December 2015; Vol. 29, pp. 1406–1412.
193. Bobillet, W.; Da Costa, J.-P.; Germain, C.; Lavialle, O.; Grenier, G. Row detection in high resolution remote sensing images of vine fields. In Proceedings of the 4th European Conference on Precision Agriculture, Berlin, Germany, 15–19 June 2003; pp. 81–87.
194. Poblete, T.; Ortega-Farías, S.; Ryu, D. Automatic coregistration algorithm to remove canopy shaded pixels in UAV-borne thermal images to improve the estimation of crop water stress index of a drip-irrigated cabernet sauvignon vineyard. *Sensors* **2018**, *18*, 1–17.
195. Ihuoma, S.O.; Madramootoo, C.A. Recent advances in crop water stress detection. *Comput. Electron. Agric.* **2017**, *141*, 267–275.

196. Jones, H.G. Use of infrared thermometry for estimation of stomatal conductance as a possible aid to irrigation scheduling. *Agric. For. Meteorol.* **1999**, *95*, 139–149.
197. Bellvert, J.; Marsal, J.; Girona, J.; Zarco-Tejada, P.J. Seasonal evolution of crop water stress index in grapevine varieties determined with high-resolution remote sensing thermal imagery. *Irrig. Sci.* **2015**, *33*, 81–93.
198. García-Tejero, I.F.; Gutiérrez-Gordillo, S.; Ortega-Arévalo, C.; Iglesias-Contreras, M.; Moreno, J.M.; Souza-Ferreira, L.; Durán-Zuazo, V.H. Thermal imaging to monitor the crop-water status in almonds by using the non-water stress baselines. *Sci. Hortic.* **2018**, *238*, 91–97.
199. Alchanatis, V.; Cohen, Y.; Cohen, S.; Moller, M.; Sprinstin, M.; Meron, M.; Tsipris, J.; Saranga, Y.; Sela, E. Evaluation of different approaches for estimating and mapping crop water status in cotton with thermal imaging. *Precis. Agric.* **2010**, *11*, 27–41.
200. Goetz, S. Multi-sensor analysis of NDVI, surface temperature and biophysical variables at a mixed grassland site. *Int. J. Remote Sens.* **1997**, *18*, 71–94.
201. Sun, L.; Gao, F.; Anderson, M.; Kustas, W.; Alsina, M.; Sanchez, L.; Sams, B.; McKee, L.; Dulaney, W.; White, W.; et al. Daily mapping of 30 m LAI and NDVI for grape yield prediction in California Vineyards. *Remote Sens.* **2017**, *9*, 317.
202. Peñuelas, J.; Filella, I.; Biel, C.; Serrano, L.; Save, R. The reflectance at the 950–970 nm region as an indicator of plant water status. *Int. J. Remote Sens.* **1993**, *14*, 1887–1905.
203. Jones, C.L.; Weckler, P.R.; Maness, N.O.; Stone, M.L.; Jayasekara, R. Estimating water stress in plants using hyperspectral sensing. In Proceedings of the 2004 ASAE Annual Meeting, Ottawa, ON, Canada, 1–4 August 2004; p. 1.
204. Ač, A.; Malenovskỳ, Z.; Olejníčková, J.; Gallé, A.; Rascher, U.; Mohammed, G. Meta-analysis assessing potential of steady-state chlorophyll fluorescence for remote sensing detection of plant water, temperature and nitrogen stress. *Remote Sens. Environ.* **2015**, *168*, 420–436.
205. Mohammed, G.H.; Colombo, R.; Middleton, E.M.; Rascher, U.; van der Tol, C.; Nedbal, L.; Goulas, Y.; Pérez-Priego, O.; Damm, A.; Meroni, M.; et al. Remote sensing of solar-induced chlorophyll fluorescence (SIF) in vegetation: 50 years of progress. *Remote Sens. Environ.* **2019**, *231*, 111177.
206. Panigada, C.; Rossini, M.; Meroni, M.; Cilia, C.; Busetto, L.; Amaducci, S.; Boschetti, M.; Cogliati, S.; Picchi, V.; Pinto, F.; et al. Fluorescence, PRI and canopy temperature for water stress detection in cereal crops. *Int. J. Appl. Earth Obs. Geoinformation* **2014**, *30*, 167–178.
207. Jones, H.G.; Stoll, M.; Santos, T.; Sousa, C. de; Chaves, M.M.; Grant, O.M. Use of infrared thermography for monitoring stomatal closure in the field: application to grapevine. *J. Exp. Bot.* **2002**, *53*, 2249–2260.
208. Jackson, R.D.; Idso, S.B.; Reginato, R.J.; Pinter, P.J. Canopy temperature as a crop water stress indicator. *Water Resour. Res.* **1981**, *17*, 1133–1138.
209. Bellvert, J.; Zarco-Tejada, P.J.; Girona, J.; Fereres, E. Mapping crop water stress index in a 'Pinot-noir'vineyard: comparing ground measurements with thermal remote sensing imagery from an unmanned aerial vehicle. *Precis. Agric.* **2014**, *15*, 361–376.
210. Fuentes, S.; De Bei, R.; Pech, J.; Tyerman, S. Computational water stress indices obtained from thermal image analysis of grapevine canopies. *Irrig. Sci.* **2012**, *30*, 523–536.
211. Jackson, R.D. Canopy temperature and crop water stress. In *Advances in irrigation*; Elsevier: Amsterdam, The Netherlands, 1982; Vol. 1, pp. 43–85.
212. Idso, S.; Jackson, R.; Pinter Jr, P.; Reginato, R.; Hatfield, J. Normalizing the stress-degree-day parameter for environmental variability. *Agric. Meteorol.* **1981**, *24*, 45–55.
213. Möller, M.; Alchanatis, V.; Cohen, Y.; Meron, M.; Tsipris, J.; Naor, A.; Ostrovsky, V.; Sprintsin, M.; Cohen, S. Use of thermal and visible imagery for estimating crop water status of irrigated grapevine. *J. Exp. Bot.* **2006**, *58*, 827–838.
214. Egea, G.; Padilla-Díaz, C.M.; Martinez-Guanter, J.; Fernández, J.E.; Pérez-Ruiz, M. Assessing a crop water stress index derived from aerial thermal imaging and infrared thermometry in super-high density olive orchards. *Agric. Water Manag.* **2017**, *187*, 210–221.
215. Bannari, A.; Morin, D.; Bonn, F.; Huete, A. A review of vegetation indices. *Remote Sens. Rev.* **1995**, *13*, 95–120.
216. Ballester, C.; Zarco-Tejada, P.; Nicolas, E.; Alarcon, J.; Fereres, E.; Intrigliolo, D.; Gonzalez-Dugo, V. Evaluating the performance of xanthophyll, chlorophyll and structure-sensitive spectral indices to detect water stress in five fruit tree species. *Precis. Agric.* **2018**, *19*, 178–193.

217. Romero-Trigueros, C.; Nortes, P.A.; Alarcón, J.J.; Hunink, J.E.; Parra, M.; Contreras, S.; Droogers, P.; Nicolás, E. Effects of saline reclaimed waters and deficit irrigation on Citrus physiology assessed by UAV remote sensing. *Agric. Water Manag.* **2017**, *183*, 60–69.
218. Zhao, T.; Stark, B.; Chen, Y.; Ray, A.; Doll, D. More reliable crop water stress quantification using small unmanned aerial systems (sUAS). *IFAC-PapersOnLine.* **2016**, *49*, 409–414.
219. Sandholt, I.; Rasmussen, K.; Andersen, J. A simple interpretation of the surface temperature/vegetation index space for assessment of surface moisture status. *Remote Sens. Environ.* **2002**, *79*, 213–224.
220. Wang, L.; Qu, J.J. Satellite remote sensing applications for surface soil moisture monitoring: A review. *Front. Earth Sci. China* **2009**, *3*, 237–247.
221. Colaizzi, P.D.; Barnes, E.M.; Clarke, T.R.; Choi, C.Y.; Waller, P.M. Estimating soil moisture under low frequency surface irrigation using crop water stress index. *J. Irrig. Drain. Eng.* **2003**, *129*, 27–35.
222. Ahmed, A.; Zhang, Y.; Nichols, S. Review and evaluation of remote sensing methods for soil-moisture estimation. *SPIE Rev.* **2011**, *2*, 028001.
223. Kerr, Y.H. Soil moisture from space: Where are we? *Hydrogeol. J.* **2007**, *15*, 117–120.
224. Kerr, Y.H.; Waldteufel, P.; Wigneron, J.-P.; Delwart, S.; Cabot, F.; Boutin, J.; Escorihuela, M.-J.; Font, J.; Reul, N.; Gruhier, C.; et al. The SMOS mission: New tool for monitoring key elements ofthe global water cycle. *Proc. IEEE* **2010**, *98*, 666–687.
225. Entekhabi, D.; Njoku, E.G.; O'Neill, P.E.; Kellogg, K.H.; Crow, W.T.; Edelstein, W.N.; Entin, J.K.; Goodman, S.D.; Jackson, T.J.; Johnson, J.; et al. The soil moisture active passive (SMAP) mission. *Proc. IEEE* **2010**, *98*, 704–716.
226. Yueh, S.; Entekhabi, D.; O'Neill, P.; Njoku, E.; Entin, J. NASA soil moisture active passive mission status and science performance. In Proceedings of the 2016 IEEE International Geoscience and Remote Sensing Symposium (IGARSS 2016), Beijing, China, 10–16 July 2016; pp. 116–119.
227. Piles, M.; Sánchez, N.; Vall-llossera, M.; Camps, A.; Martínez-Fernández, J.; Martínez, J.; González-Gambau, V. A Downscaling Approach for SMOS Land Observations: Evaluation of High-Resolution Soil Moisture Maps Over the Iberian Peninsula. *IEEE J. Sel. Top. Appl. Earth Obs. Remote Sens.* **2014**, *7*, 3845–3857.
228. Cui, C.; Xu, J.; Zeng, J.; Chen, K.-S.; Bai, X.; Lu, H.; Chen, Q.; Zhao, T. Soil moisture mapping from satellites: An intercomparison of SMAP, SMOS, FY3B, AMSR2, and ESA CCI over two dense network regions at different spatial scales. *Remote Sens.* **2018**, *10*, 33.
229. Peng, J.; Loew, A.; Merlin, O.; Verhoest, N.E. A review of spatial downscaling of satellite remotely sensed soil moisture. *Rev. Geophys.* **2017**, *55*, 341–366.
230. Roussel, N.; Darrozes, J.; Ha, C.; Boniface, K.; Frappart, F.; Ramillien, G.; Gavart, M.; Van de Vyvere, L.; Desenfans, O.; Baup, F. Multi-scale volumetric soil moisture detection from GNSS SNR data: Ground-based and airborne applications. In Proceedings of the 2016 IEEE Metrology for Aerospace (MetroAeroSpace), Florence, Italy, 22–23 June 2016; pp. 573–578.
231. Yan, S.; Zhang, N.; Chen, N.; Gong, J. Feasibility of using signal strength indicator data to estimate soil moisture based on GNSS interference signal analysis. *Remote Sens. Lett.* **2018**, *9*, 61–70.
232. Johansen, K.; Sohlbach, M.; Sullivan, B.; Stringer, S.; Peasley, D.; Phinn, S. Mapping banana plants from high spatial resolution orthophotos to facilitate plant health assessment. *Remote Sens.* **2014**, 6, 8261–8286.
233. Hall, A.; Louis, J.; Lamb, D.W. Low-resolution remotely sensed images of winegrape vineyards map spatial variability in planimetric canopy area instead of leaf area index. *Aust. J. Grape Wine Res.* **2008**, *14*, 9–17.
234. Furness, G.; Magarey, P.; Miller, P.; Drew, H. Fruit tree and vine sprayer calibration based on canopy size and length of row: unit canopy row method. *Crop Prot.* **1998**, *17*, 639–644.
235. Rosell, J.; Sanz, R. A review of methods and applications of the geometric characterization of tree crops in agricultural activities. *Comput. Electron. Agric.* **2012**, *81*, 124–141.
236. Lee, K.; Ehsani, R. A laser scanner based measurement system for quantification of citrus tree geometric characteristics. *Appl. Eng. Agric.* **2009**, *25*, 777–788.
237. Li, F.; Cohen, S.; Naor, A.; Shaozong, K.; Erez, A. Studies of canopy structure and water use of apple trees on three rootstocks. *Agric. Water Manag.* **2002**, *55*, 1–14.
238. Kustas, W.; Agam, N.; Alfieri, J.; McKee, L.; Prueger, J.; Hipps, L.; Howard, A.; Heitman, J. Below canopy radiation divergence in a vineyard: Implications on interrow surface energy balance. *Irrig. Sci.* **2019**, *37*, 227–237.

239. Bendig, J.V. Unmanned aerial vehicles (UAVs) for multi-temporal crop surface modelling. A new method for plant height and biomass estimation based on RGB-imaging. Ph.D. Thesis, University of Cologne, Cologne, Germany, 2015.
240. Gowda, P.H.; Chavez, J.L.; Colaizzi, P.D.; Evett, S.R.; Howell, T.A.; Tolk, J.A. ET mapping for agricultural water management: present status and challenges. *Irrig. Sci.* **2008**, *26*, 223–237.
241. Zhang, K.; Kimball, J.S.; Running, S.W. A review of remote sensing based actual evapotranspiration estimation. *Wiley Interdiscip. Rev. Water* **2016**, *3*, 834–853.
242. Liou, Y.-A.; Kar, S. Evapotranspiration estimation with remote sensing and various surface energy balance algorithms—A review. *Energies* **2014**, *7*, 2821–2849.
243. Courault, D.; Seguin, B.; Olioso, A. Review on estimation of evapotranspiration from remote sensing data: From empirical to numerical modeling approaches. *Irrig. Drain. Syst.* **2005**, *19*, 223–249.
244. Kalma, J.D.; McVicar, T.R.; McCabe, M.F. Estimating land surface evaporation: A review of methods using remotely sensed surface temperature data. *Surv. Geophys.* **2008**, *29*, 421–469.
245. Li, Z.-L.; Tang, R.; Wan, Z.; Bi, Y.; Zhou, C.; Tang, B.; Yan, G.; Zhang, X. A review of current methodologies for regional evapotranspiration estimation from remotely sensed data. *Sensors* **2009**, *9*, 3801–3853.
246. Marshall, M.; Thenkabail, P.; Biggs, T.; Post, K. Hyperspectral narrowband and multispectral broadband indices for remote sensing of crop evapotranspiration and its components (transpiration and soil evaporation). *Agric. For. Meteorol.* **2016**, *218*, 122–134.
247. Maes, W.; Steppe, K. Estimating evapotranspiration and drought stress with ground-based thermal remote sensing in agriculture: a review. *J. Exp. Bot.* **2012**, *63*, 4671–4712.
248. Bastiaanssen, W.G.; Menenti, M.; Feddes, R.; Holtslag, A. A remote sensing surface energy balance algorithm for land (SEBAL). 1. Formulation. *J. Hydrol.* **1998**, *212*, 198–212.
249. Allen, R.; Irmak, A.; Trezza, R.; Hendrickx, J.M.; Bastiaanssen, W.; Kjaersgaard, J. Satellite-based ET estimation in agriculture using SEBAL and METRIC. *Hydrol. Process.* **2011**, *25*, 4011–4027.
250. Allen, R.G.; Tasumi, M.; Trezza, R. Satellite-based energy balance for mapping evapotranspiration with internalized calibration (METRIC)—Model. *J. Irrig. Drain. Eng.* **2007**, *133*, 380–394.
251. Allen, R.G.; Tasumi, M.; Morse, A.; Trezza, R.; Wright, J.L.; Bastiaanssen, W.; Kramber, W.; Lorite, I.; Robison, C.W. Satellite-Based Energy Balance for Mapping Evapotranspiration with Internalized Calibration (METRIC)-Applications. *J. Irrig. Drain. Eng.* **2007**, *133*, 395–406.
252. Allen, R.G.; Pereira, L.S.; Raes, D.; Smith, M. FAO Irrigation and drainage paper No. 56. *Rome Food Agric. Organ. U. N.* **1998**, *56*, e156.
253. Jackson, R.D.; Moran, M.S.; Gay, L.W.; Raymond, L.H. Evaluating evaporation from field crops using airborne radiometry and ground-based meteorological data. *Irrig. Sci.* **1987**, *8*, 81–90.
254. Williams, L.; Ayars, J. Grapevine water use and the crop coefficient are linear functions of the shaded area measured beneath the canopy. *Agric. For. Meteorol.* **2005**, *132*, 201–211.
255. Jayanthi, H.; Neale, C.M.; Wright, J.L. Development and validation of canopy reflectance-based crop coefficient for potato. *Agric. Water Manag.* **2007**, *88*, 235–246.
256. Samani, Z.; Bawazir, A.S.; Bleiweiss, M.; Skaggs, R.; Longworth, J.; Tran, V.D.; Pinon, A. Using remote sensing to evaluate the spatial variability of evapotranspiration and crop coefficient in the lower Rio Grande Valley, New Mexico. *Irrig. Sci.* **2009**, *28*, 93–100.
257. Kustas, W.P.; Anderson, M.C.; Alfieri, J.G.; Knipper, K.; Torres-Rua, A.; Parry, C.K.; Nieto, H.; Agam, N.; White, W.A.; Gao, F.; et al. The grape remote sensing atmospheric profile and evapotranspiration experiment. *Bull. Am. Meteorol. Soc.* **2018**, *99*, 1791–1812.
258. Kamble, B.; Kilic, A.; Hubbard, K. Estimating crop coefficients using remote sensing-based vegetation index. *Remote Sens.* **2013**, *5*, 1588–1602.
259. Hou, M.; Tian, F.; Zhang, L.; Li, S.; Du, T.; Huang, M.; Yuan, Y. Estimating crop transpiration of soybean under different irrigation treatments using thermal infrared remote sensing imagery. *Agronomy* **2019**, *9*, 8.
260. Knipper, K.R.; Kustas, W.P.; Anderson, M.C.; Alfieri, J.G.; Prueger, J.H.; Hain, C.R.; Gao, F.; Yang, Y.; McKee, L.G.; Nieto, H.; et al. Evapotranspiration estimates derived using thermal-based satellite remote sensing and data fusion for irrigation management in California vineyards. *Irrig. Sci.* **2019**, *37*, 431–449.
261. Hoffmann, H.; Nieto, H.; Jensen, R.; Guzinski, R.; Zarco-Tejada, P.; Friborg, T. Estimating evapotranspiration with thermal UAV data and two source energy balance models. *Hydrol. Earth Syst. Sci. Discuss.* **2016**, *20*, 697–713.

262. Cammalleri, C.; Anderson, M.; Kustas, W. Upscaling of evapotranspiration fluxes from instantaneous to daytime scales for thermal remote sensing applications. *Hydrol. Earth Syst. Sci.* **2014**, *18*, 1885–1894.
263. Biggs, T.W.; Marshall, M.; Messina, A. Mapping daily and seasonal evapotranspiration from irrigated crops using global climate grids and satellite imagery: Automation and methods comparison. *Water Resour. Res.* **2016**, *52*, 7311–7326.
264. Chávez, J.L.; Neale, C.M.; Prueger, J.H.; Kustas, W.P. Daily evapotranspiration estimates from extrapolating instantaneous airborne remote sensing ET values. *Irrig. Sci.* **2008**, *27*, 67–81.
265. McCabe, M.F.; Wood, E.F. Scale influences on the remote estimation of evapotranspiration using multiple satellite sensors. *Remote Sens. Environ.* **2006**, *105*, 271–285.
266. Kustas, W.; Li, F.; Jackson, T.; Prueger, J.; MacPherson, J.; Wolde, M. Effects of remote sensing pixel resolution on modeled energy flux variability of croplands in Iowa. *Remote Sens. Environ.* **2004**, *92*, 535–547.
267. Hong, S.; Hendrickx, J.M.; Borchers, B. Effect of scaling transfer between evapotranspiration maps derived from LandSat 7 and MODIS images. In *Targets and Backgrounds XI: Characterization and Representation*; International Society for Optics and Photonics: Orlando, Florida, USA, 2005; Vol. 5811, pp. 147–159.
268. Abiodun, O.O.; Guan, H.; Post, V.E.; Batelaan, O. Comparison of MODIS and SWAT evapotranspiration over a complex terrain at different spatial scales. *Hydrol. Earth Syst. Sci.* **2018**, *22*, 2775–2794.
269. Justice, C.; Townshend, J.; Vermote, E.; Masuoka, E.; Wolfe, R.; Saleous, N.; Roy, D.; Morisette, J. An overview of MODIS Land data processing and product status. *Remote Sens. Environ.* **2002**, *83*, 3–15.
270. Nieto, H.; Bellvert, J.; Kustas, W.P.; Alfieri, J.G.; Gao, F.; Prueger, J.; Torres-Rua, A.; Hipps, L.E.; Elarab, M.; Song, L. Unmanned airborne thermal and mutilspectral imagery for estimating evapotranspiration in irrigated vineyards. In Proceedings of the 2017 IEEE International Geoscience and Remote Sensing Symposium (IGARSS 2017), Fort Worth, TX, USA, 23–28 July 2017; pp. 5510–5513.
271. Ortega-Farías, S.; Ortega-Salazar, S.; Poblete, T.; Poblete-Echeverría, C.; Zúñiga, M.; Sepúlveda-Reyes, D.; Kilic, A.; Allen, R. Estimation of olive evapotranspiration using multispectral and thermal sensors placed aboard an unmanned aerial vehicle. *Acta Hortic.* **2017**, *1150*, 1–8.
272. Gago, J.; Douthe, C.; Coopman, R.E.; Gallego, P.P.; Ribas-Carbo, M.; Flexas, J.; Escalona, J.; Medrano, H. UAVs challenge to assess water stress for sustainable agriculture. *Agric. Water Manag.* **2015**, *153*, 9–19.
273. Sepúlveda-Reyes, D.; Ingram, B.; Bardeen, M.; Zúñiga, M.; Ortega-Farías, S.; Poblete-Echeverría, C. Selecting canopy zones and thresholding approaches to assess grapevine water status by using aerial and ground-based thermal imaging. *Remote Sens.* **2016**, *8*, 822.
274. McBratney, A.; Whelan, B.; Ancev, T.; Bouma, J. Future directions of precision agriculture. *Precis. Agric.* **2005**, *6*, 7–23.
275. Ferguson, R.; Rundquist, D. Remote sensing for site-specific crop management. In *Precision agriculture basics*; Shannon, D.K., Clay, D.E., Kitchen, N.R., Eds.; American Society of Agronomy: Madison, WI, USA; Crop Science Society of America: Madison, WI, USA; Soil Science Society of America: Madison, WI, USA, 2018; pp. 103–118.
276. Florin, M.J.; McBratney, A.B.; Whelan, B.M. Extending site-specific crop management from individual fields to an entire farm. In Proseedings of the Precision agriculture '05, Proceedings of the 5th European Conference on Precision Agriculture, Uppsala, Sweden, 9–12 June 2005; pp. 857–863.
277. Perea-Moreno, A.J.; Aguilera-Urena, M.J.; Merono-de Larriva, J.E.; Manzano-Agugliaro, F. Assessment of the potential of UAV video image analysis for planning irrigation needs of golf courses. *Water* **2016**, *8*, 584.
278. Meron, M.; Tsipris, J.; Charitt, D. Remote mapping of crop water status to assess spatial variability of crop stress. *Precis. Agric.* **2003**, 405–410.
279. Idso, S.B. Non-water-stressed baselines: A key to measuring and interpreting plant water stress. *Agric. Meteorol.* **1982**, *27*, 59–70.
280. Cohen, Y.; Alchanatis, V.; Meron, M.; Saranga, Y.; Tsipris, J. Estimation of leaf water potential by thermal imagery and spatial analysis. *J. Exp. Bot.* **2005**, *56*, 1843–1852.
281. Pagay, V.; Kidman, C.; Jenkins, A. Proximal and remote sensing tools for regional-scale characterisation of grapevine water and nitrogen status in Coonawarra. *Wine Vitic. J.* **2016**, *31*, 42–47.
282. Romero, M.; Luo, Y.; Su, B.; Fuentes, S. Vineyard water status estimation using multispectral imagery from an UAV platform and machine learning algorithms for irrigation scheduling management. *Comput. Electron. Agric.* **2018**, *147*, 109–117.
283. Goldhamer, D.A.; Viveros, M.; Salinas, M. Regulated deficit irrigation in almonds: effects of variations in applied water and stress timing on yield and yield components. *Irrig. Sci.* **2006**, *24*, 101–114.

284. Girona, J.; Marsal, J.; Cohen, M.; Mata, M.; Miravete, C. Physiological, growth and yield responses of almond (Prunus dulcis L) to different irrigation regimes. *Acta Hortic.* **1993**, 335, 389–398.
285. Sadler, E.; Evans, R.; Stone, K.; Camp, C. Opportunities for conservation with precision irrigation. *J. Soil Water Conserv.* **2005**, *60*, 371–378.
286. Corbane, C.; Jacob, F.; Raclot, D.; Albergel, J.; Andrieux, P. Multitemporal analysis of hydrological soil surface characteristics using aerial photos: A case study on a Mediterranean vineyard. *Int. J. Appl. Earth Obs. Geoinformation* **2012**, *18*, 356–367.
287. Osroosh, Y.; Peters, R.T.; Campbell, C.S. Daylight crop water stress index for continuous monitoring of water status in apple trees. *Irrig. Sci.* **2016**, *34*, 209–219.
288. Osroosh, Y.; Peters, R.T.; Campbell, C.S.; Zhang, Q. Comparison of irrigation automation algorithms for drip-irrigated apple trees. *Comput. Electron. Agric.* **2016**, *128*, 87–99.
289. Lamm, F.R.; Aiken, R.M. Comparison of temperature-time threshold-and ET-based irrigation scheduling for corn production. In Proceedings of the 2008 ASABE Annual International Meeting, Providence, RI, USA, 29 June–2 July 2008; p. 1.
290. O'Shaughnessy, S.A.; Evett, S.R.; Colaizzi, P.D.; Howell, T.A. A crop water stress index and time threshold for automatic irrigation scheduling of grain sorghum. *Agric. Water Manag.* **2012**, *107*, 122–132.
291. Bellvert, J.; Zarco-Tejada, P.; Gonzalez-Dugo, V.; Girona, J.; Fereres, E. Scheduling vineyard irrigation based on mapping leaf water potential from airborne thermal imagery. In *Precision agriculture'13*; Stafford, J.V., Ed.; Springer: Cham, Switzerland, 2013; pp. 699–704.
292. Bellvert, J.; Girona, J.; others The use of multispectral and thermal images as a tool for irrigation scheduling in vineyards. In *The use of remote sensing and geographic information systems for irrigation management in Southwest Europe;* Erena, M., López-Francos, A., Montesinos, S., Berthoumieu, J.-P., Eds.; Zaragoza, Spain, 2012; pp. 131–137.
293. Erdem, Y.; Şehirali, S.; Erdem, T.; Kenar, D. Determination of crop water stress index for irrigation scheduling of bean (Phaseolus vulgaris L.). *Turk. J. Agric. For.* **2006**, *30*, 195–202.
294. Osroosh, Y.; Troy Peters, R.; Campbell, C.S.; Zhang, Q. Automatic irrigation scheduling of apple trees using theoretical crop water stress index with an innovative dynamic threshold. *Comput. Electron. Agric.* **2015**, *118*, 193–203.
295. Irmak, S.; Haman, D.Z.; Bastug, R. Determination of crop water stress index for irrigation timing and yield estimation of corn. *Agron. J.* **2000**, *92*, 1221–1227.
296. Acevedo-Opazo, C.; Tisseyre, B.; Ojeda, H.; Ortega-Farias, S.; Guillaume, S. Is it possible to assess the spatial variability of vine water status? *OENO One* **2008**, *42*, 203–219.
297. Acevedo-Opazo, C.; Tisseyre, B.; Guillaume, S.; Ojeda, H. The potential of high spatial resolution information to define within-vineyard zones related to vine water status. *Precis. Agric.* **2008**, *9*, 285–302.
298. Petrie, P.R.; Wang, Y.; Liu, S.; Lam, S.; Whitty, M.A.; Skewes, M.A. The accuracy and utility of a low cost thermal camera and smartphone-based system to assess grapevine water status. *Biosyst. Eng.* **2019**, *179*, 126–139.
299. Woellert, K.; Ehrenfreund, P.; Ricco, A.J.; Hertzfeld, H. Cubesats: Cost-effective science and technology platforms for emerging and developing nations. *Adv. Space Res.* **2011**, *47*, 663–684.
300. Kramer, H.J.; Cracknell, A.P. An overview of small satellites in remote sensing. *Int. J. Remote Sens.* **2008**, *29*, 4285–4337.
301. McCabe, M.; Aragon, B.; Houborg, R.; Mascaro, J. CubeSats in Hydrology: Ultrahigh-Resolution Insights Into Vegetation Dynamics and Terrestrial Evaporation. *Water Resour. Res.* **2017**, *53*, 10017–10024.
302. Trombetti, M.; Riaño, D.; Rubio, M.; Cheng, Y.; Ustin, S. Multi-temporal vegetation canopy water content retrieval and interpretation using artificial neural networks for the continental USA. *Remote Sens. Environ.* **2008**, *112*, 203–215.
303. King, B.; Shellie, K. Evaluation of neural network modeling to predict non-water-stressed leaf temperature in wine grape for calculation of crop water stress index. *Agric. Water Manag.* **2016**, *167*, 38–52.
304. Shan, N.; Ju, W.; Migliavacca, M.; Martini, D.; Guanter, L.; Chen, J.; Goulas, Y.; Zhang, Y. Modeling canopy conductance and transpiration from solar-induced chlorophyll fluorescence. *Agric. For. Meteorol.* **2019**, *268*, 189–201.
305. Moreno, J.; Goulas, Y.; Huth, A.; Middelton, E.; Miglietta, F.; Mohammed, G.; Nebdal, L.; Rascher, U.; Verhof, W. Report for mission selection: CarbonSat flex–An earth explorer to observe vegetation fluorescence. *Euro. Space Agency* **2015**, *1330/2*, 179–185.

306. Drusch, M.; Moreno, J.; Del Bello, U.; Franco, R.; Goulas, Y.; Huth, A.; Kraft, S.; Middleton, E.M.; Miglietta, F.; Mohammed, G.; et al. The fluorescence explorer mission concept-ESA's Earth explorer 8. *IEEE Trans. Geosci. Remote Sens.* **2017**, *55*, 1273–1284.
307. Gautam, D.; Lucieer, A.; Watson, C.; McCoull, C. Lever-arm and boresight correction, and field of view determination of a spectroradiometer mounted on an unmanned aircraft system. *ISPRS J. Photogramm. Remote Sens.* **2019**, *155*, 25–36.
308. Garzonio, R.; Di Mauro, B.; Colombo, R.; Cogliati, S. Surface reflectance and sun-induced fluorescence spectroscopy measurements using a small hyperspectral UAS. *Remote Sens.* **2017**, *9*, 472.
309. Gautam, D.; Lucieer, A.; Bendig, J.; Malenovský, Z. Footprint Determination of a Spectroradiometer Mounted on an Unmanned Aircraft System. *IEEE Trans. Geosci. Remote Sens.* **2019**, 1–12.
310. Bendig, J.; Malenovskỳ, Z.; Gautam, D.; Lucieer, A. Solar-Induced Chlorophyll Fluorescence Measured From an Unmanned Aircraft System: Sensor Etaloning and Platform Motion Correction. *IEEE Trans. Geosci. Remote Sens*. **2019**, 1–8.
311. TongKe, F. Smart agriculture based on cloud computing and IOT. *J. Converg. Inf. Technol.* **2013**, *8*, 210–216.
312. Ojha, T.; Misra, S.; Raghuwanshi, N.S. Wireless sensor networks for agriculture: The state-of-the-art in practice and future challenges. *Comput. Electron. Agric.* **2015**, *118*, 66–84.
313. Hori, M.; Kawashima, E.; Yamazaki, T. Application of cloud computing to agriculture and prospects in other fields. *Fujitsu Sci Tech J* **2010**, *46*, 446–454.
314. Goap, A.; Sharma, D.; Shukla, A.; Krishna, C.R. An IoT based smart irrigation management system using Machine learning and open source technologies. *Comput. Electron. Agric.* **2018**, *155*, 41–49.

remote sensing

Article

Estimation of Grapevine Crop Coefficient Using a Multispectral Camera on an Unmanned Aerial Vehicle

Deepak Gautam [1,2], Bertram Ostendorf [3] and Vinay Pagay [1,*]

[1] School of Agriculture, Food and Wine, The University of Adelaide, PMB 1, Glen Osmond, SA 5064, Australia; Deepak.Gautam@adelaide.edu.au
[2] Research Institute for the Environment and Livelihoods, Charles Darwin University, Casuarina, NT 0810, Australia
[3] Oliphant Building, North Terrace Campus, School of Biological Science, The University of Adelaide, Adelaide, SA 5005, Australia; Bertram.Ostendorf@adelaide.edu.au
* Correspondence: Vinay.Pagay@adelaide.edu.au

Abstract: Crop water status and irrigation requirements are of great importance to the horticultural industry due to changing climatic conditions leading to high evaporative demands, drought and water scarcity in semi-arid and arid regions worldwide. Irrigation scheduling strategies based on evapotranspiration (ET), such as regulated deficit irrigation, requires the estimation of seasonal crop coefficients (k_c). The ET-driven irrigation decisions for grapevines rely on the sampling of several k_c values from each irrigation zone. Here, we present an unmanned aerial vehicle (UAV)-based technique to estimate k_c at the single vine level in order to capture the spatial variability of water requirements in a commercial vineyard located in South Australia. A UAV carrying a multispectral sensor is used to extract the spectral, as well as the structural, information of Cabernet Sauvignon grapevines. The spectral and structural information, acquired at the various phenological stages of the vine through two seasons, is used to model k_c using univariate (simple linear), multivariate (generalised linear and additive) and machine learning (convolution neural network and random forest) model frameworks. The structural information (e.g., canopy top view area) had the strongest correlation with k_c throughout the season ($p \leq 0.001$; Pearson R = 0.56), while the spectral indices (e.g., normalised indices) turned less-sensitive post véraison—the onset of ripening in grapes. Combining structural and spectral information improved the model's performance. Among the investigated predictive models, the random forest predicted k_c with the highest accuracy (R^2: 0.675, root mean square error: 0.062, and mean absolute error: 0.047). This UAV-based approach improves the precision of irrigation by capturing the spatial variability of k_c within a vineyard. Combined with an energy balance model, the water needs of a vineyard can be computed on a weekly or sub-weekly basis for precision irrigation. The UAV-based characterisation of k_c can further enhance the water management and irrigation zoning by matching the infrastructure with the spatial variability of the irrigation demand.

Keywords: UAV; UAS; drone; precision irrigation; remote sensing; spatial variability; random forest

check for updates

Citation: Gautam, D.; Ostendorf, B.; Pagay, V. Estimation of Grapevine Crop Coefficient Using a Multispectral Camera on an Unmanned Aerial Vehicle. *Remote Sens.* **2021**, *13*, 2639. https://doi.org/10.3390/rs13132639

Academic Editor: Javier J. Cancela

Received: 19 April 2021
Accepted: 28 June 2021
Published: 5 July 2021

1. Introduction

Water availability to horticultural crops in Australia is highly variable from season-to-season due to variable climatic conditions including evapotranspiration and precipitation patterns, extreme weather events, for example, heatwaves, and competing demand for freshwater. Climatic conditions are expected to deteriorate due to variability in the Indian Ocean Dipole, which is the key driver of ENSO outlook and the Australian climate [1,2]. The persistent drier conditions, combined with freshwater scarcities, will require a wider adaptation of precision irrigation to sustain the horticulture and agriculture of Australia [3,4]. As such, the horticultural industry needs to move from over-irrigation to stress management practices by adopting evidence-based precision irrigation [5–7].

One widely adopted irrigation strategy is evapotranspiration (ET)-based deficit irrigation, where a fraction of crop water requirement is replenished [8,9]. To improve the precision of the ET-based irrigation, accurate information of the crop coefficient (k_c) is required [10]. k_c is a highly variable parameter affected by the canopy structure, training system, pruning practices and vegetative growth. Within the same management vineyard block, spatial variation still exists due to the variation in resource availability, soil rooting depth, vine disease and terrain architecture. Due to this high spatiotemporal variability in the k_c, data, such as those from remote sensing, are required to make the irrigation decisions. Furthermore, mixed pixels arising from the inter-row bare/vegetated area specific to horticulture demands higher spatial resolution data, which can be achieved with an unmanned aerial vehicle (UAV) [6]. Unmanned aerial vehicle (UAV) remote sensing offers the potential to characterise ET [11,12], k_c and the irrigation needs spatially, as well as on a canopy level [13–15]. Canopy level irrigation requirements can be a basis on which to improve the precision of irrigation and irrigation scheduling by matching the timing, volume and location of irrigation with the crop water needs [16–19]. This, in turn, can sustain agriculture by optimising farm and crop water use efficiency and industry profitability.

The direct measurement of crop evapotranspiration (ET_c) can be made by lysimeter, eddy covariance, Bowen ratio and soil water balance methods [20,21]. These methods provide an accurate account of vegetation water balance; however, they are expensive, cumbersome, and provide low spatial representativeness of measurements. In the absence of direct ET_c measurements, an indirect estimation can be made from numerical modelling, empirical methods, and remote sensing, which use agronomic, biophysical, and meteorological elements as inputs [22–24]. The FAO Penman–Monteith method is the most widely adopted empirical model for estimating the reference ET (also known as ET_{ref} or ET_0) [10]. ET_0, when coupled with k_c (single or dual), yields ET_c, which is often the basis for deficit irrigation [25–29].

The similarity of k_c and the satellite-derived vegetation indices (VIs) resulted in the use of low-cost remote sensing technology for estimating k_c for a range of spatiotemporal scales [30–32]. The satellite-based VIs proxied the photosynthetically active vegetation cover, which in turn can be used to estimate both k_c and ET_c. For example, sources such as IrriSAT provide k_c estimates at 30 m resolution using a linear model based on the normalised difference vegetation index (NDVI) [33–36]. In similar studies, k_c has been estimated using several spectral/thermal indices such as NDVI and crop water stress index (CWSI) [37–39]. Similarly, structural properties ,such as canopy size, canopy area, leaf area index (LAI), and shaded area [40–43], have been utilised to estimate k_c. Using multiview stereo and structure-from-motion (SfM) techniques, UAV remote sensing can capture the 3D structure of the vegetation as well as the spectral bands [44,45]. Structural information and spectral reflectance on their own were used to estimate k_c from the aforementioned studies; however, combining the spectral and structural information could present an opportunity for the robust and precise estimation of k_c. Moreover, UAV-based estimation of k_c is a novel concept for grapevines, which, in the future, could potentially be used in lieu of field sampling.

In this paper, we present the UAV-based multispectral remote sensing technique for spatial estimation of the k_c of field-grown grapevines. Specifically, we combine the spectral reflectance and structural features of the grapevine in various modelling frameworks to provide an estimate of k_c. A workflow for canopy-level remote sensing data extraction, as well as modelling of k_c, is presented. Various predictive models (linear, non-linear and machine learning) are investigated for the canopy-specific estimation of k_c. This fine-scale canopy level k_c measurement can be used to estimate the canopy scale or irrigation zone level water requirements. k_c maps, which can be used to determine the spatial irrigation requirements, are generated by the best performing model for Cabernet Sauvignon at Wynns Coonawarra Estate, Coonawarra, SA, Australia.

2. Materials and Methods

2.1. Test Site

The test sites for this study are located in rural South Australia in the Coonawarra region (see Figure 1). Coonawarra is known for its premium quality red grape/wine attributed to the porous terrarossa soil, which generates moderate water stress [46,47]. The Cabernet Sauvignon vineyard at the Wynns Coonawarra Estate (37°17′8.5″S 140°49′37.9″E) at Coonawarra, which was planted over 17.3 ha in 1988, was used in this study. Two experimental blocks (each sized approximately 1 ha) were delineated at the two ends of the 700 m long row of the vineyard, which was planted in the east–west orientation. The grapevines had a bilateral cordon with a sprawling training system typical for the area. Conventional vineyard floor, canopy management and integrated pest management practices were conducted in this vineyard.

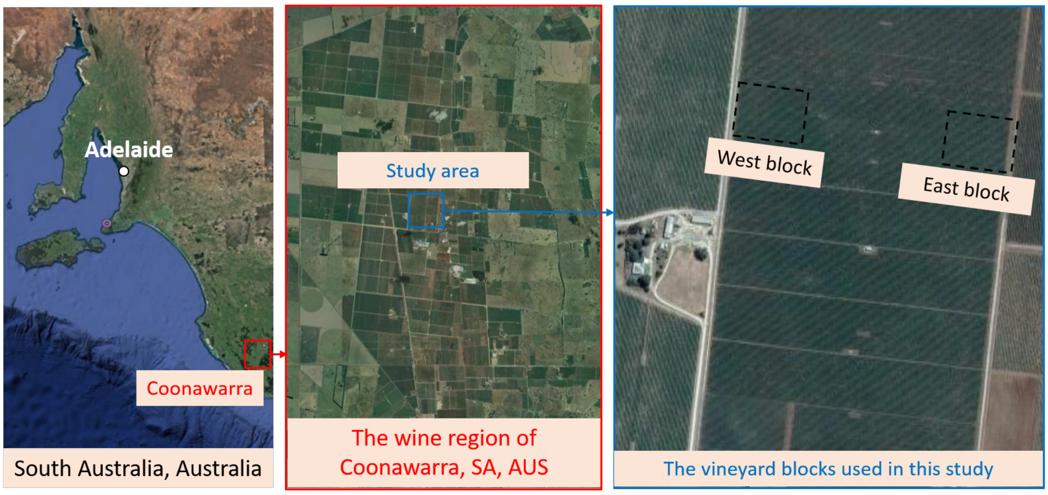

Figure 1. Two Cabernet Sauvignon vineyards at the Wynns Coonawarra Estate, Coonawarra, SA, Australia used in this study of crop coefficient and irrigation requirements.

2.2. Scientific Payload for Remote Sensing

A hexacopter multirotor (DJI Matrice 600 Pro, Dà-Jiāng Innovations Science and Technology Co., Ltd., Shenzhen, China) was deployed, which offered over 12 min of flight time and over 5 kg of scientific payload capability. The UAV carried trifecta cameras including a multispectral placed in a Gimbal (DJI Ronin, Dà-Jiāng Innovations Science and Technology Co., Ltd., Shenzhen, China). The gimbal allowed a stable platform for the cameras in order to acquire the images of the vines. The multispectral camera was equipped with a global navigation satellite system antenna to assist with the georeferencing and a downwelling light sensor (DLS) for reflectance calibration.

The RedEdge-MX captured five discrete images in blue, green, red, rededge and near infrared electromagnetic regions with bandwidths of 20 nm, 20 nm, 10 nm, 10 nm and 40 nm respectively. The bands had a centre wavelength of 475 nm, 560 nm, 668 nm, 717 nm and 840 nm, respectively. The camera had a field of view of 47.9 × 36.9 and a focal length of 5.4 mm. Each of the five discrete charge-coupled device chips had 1280 × 960 pixels with a radiometric resolution of 14 bit. The aerial images, captured from 30 m altitude, resulted in ground coverage of approximately 26.7 m × 20.0 m with a spatial resolution of 2.1 cm. This level of spatial detail is considered sufficient for single plant-level data acquisition, which resulted in several thousand multispectral pixels representing a single vine canopy.

A custom-built flexible solar panel (also known as 'Paso Panel'), sized 30 cm× 150 cm, was used for the ground sampling of k_c following an empirical formula [40]. Canopy LAI measurement was taken using an AccuPAR LP-80 Ceptometer (Meter Group, Inc., Pullman, WA, USA). Four greyscaled spectral panels were deployed during each flight to calibrate the canopy reflectance.

2.3. Data Acquisition

This study is comprised of the UAV-based and ground-based data collected during two grape growing seasons—2018/19 and 2019/20—and at five timepoints during the two seasons. The acquisition timepoints included early- to late-season, which captured a wider range of k_c values. Early season data include acquisition at EL-19 (flowering, 2019/20), and EL-31 (pea-size, 2019/20). The mid-season data were acquired around véraison at EL-34 (onset of véraison, 2018/19) and EL-35 (véraison 2019/20). Similarly, late season data were captured at EL-37 (pre-harvest, 2018/19) [48].

2.3.1. Aerial Data Acquisition

The UAV flight planning and multispectral image acquisition protocol were fixed for the entire two seasons of the field campaign. The UAV was flown at a height of 30 m above the ground at a speed of 3 m s^{-1} and in a regular mapping pattern flight, while the camera captured a multispectral image (5 band discrete images) every second. The flight parameter and camera setting together resulted in over 80% forward and side overlap, which is necessary for SfM processing [49,50].

Four greyscaled spectral panels (white, light-grey, dark-grey and black) were developed using a combination of barium sulphate and white paint [51]. These panels were deployed during each flight for atmospheric correction and reflectance calibration purposes. The MicaSence calibration panel and DLS were not utilised for four reasons: (a) the user manual recommended that the sampling method of the calibration panel was not feasible for the heavy UAV used in this study [52]; (b) the DLS without a cosine corrector could have directional variation [53,54]; (c) the use of four greyscaled spectral panels instead of one allowed more control during the empirical line correction; and (d) capturing the reflectance data of both plants and spectral panels from the same altitude potentially better corrected the atmospheric effects.

2.3.2. Reference Ground Data Acquisition

The ground reference data included the in-field k_c measurement using the Paso Panel. The Paso Panel measured the output current at full sun and when placed under the canopy. During the measurement, the panel was placed orthogonally to the cordon, approximately 10–15 cm from the ground. The final adjustment was made to make sure that the panel was level, that the vine shadow was approximately in the middle of the panel, and that no shadow was cast to the panel from the crew. For each vine, two under-vine measurements were made, one on each cordon. After measuring every four vines, the full sun measurement was repeated to accommodate for any changes in incident solar radiation. The k_c was computed analytically using Equation (1) [40].

$$k_c = 1.7 \times \frac{L_p}{W_r}(1 - \frac{I_c}{I_s}) - 0.008, \quad (1)$$

where L_p is the length of the Paso Panel, W_r is the row spacing, I_s and I_c are the current readings made under full sun and the canopy shade, respectively.

Thirty-two ground references were measured at both ends of the vineyard per timepoint (Figure 2). Note that this dataset is a part of a bigger irrigation trial. The irrigation trial tested several irrigation strategies using environmental, soil and plant-based sensors to schedule irrigation. The average seasonal irrigation for the block was approximately 0.5 ML ha^{-1} for the vine density of 1700 vines ha^{-1}. In the trial, the investigated irrigation strategies were limited to specific rows, resulting in the ground sampling vines for this k_c study being limited to specific rows throughout the season. Lacking the spatial distribution presented a risk of ground-based k_c values being clustered within a tight range. However, a wide range of k_c values was observed due to the distribution of sampling timepoints (early-, mid- and late-season), multiple seasons, and the different irrigation treatment-induced physiological responses.

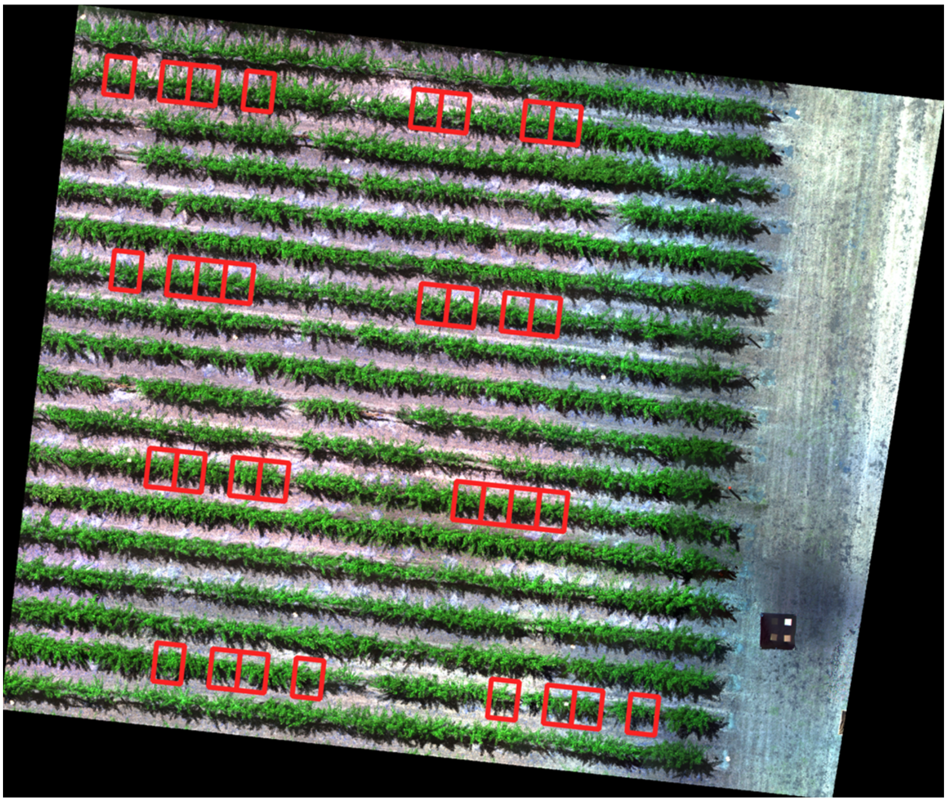

Figure 2. The ground data are sampled from 64 vines (32 on the east and 32 on the west end) of the vineyard (east end shown) per timepoint (EL-31 shown). Highlighted are the measurement vines that were measured throughout the two seasons.

2.4. Data Processing

2.4.1. Extraction of Canopy Level Data

The multispectral images were mosaicked using standard SfM workflow in Agisoft Metashape (Agisoft LLC, St. Petersburg, Russia) Professional Version 1.6.2. The products generated using the software included the digital elevation model (DEM), the digital surface model (DSM) and the orthomosaic, all expressed in projected coordinate frame MGA zone 54 (EPSG:28354). The temporal orthomosaics were processed using a custom-developed Python script routine that performed the radiometric/atmospheric calibration, masking, and data extraction from all individual canopies.

The radiometric/atmospheric calibration of the temporal orthomosaics was performed with respect to the reflectance of the four greyscaled spectral panels that were deployed during each flight (Figure 3). Using the reflectance of the four panels at five bands, the orthomosaics were converted to the reflectance by empirical line correction [55,56]. As the four greyscaled panels were used regularly in the field condition, the panels could degrade due to repeated handling, hence the panels were also calibrated regularly. The four panels were calibrated twice each season at the start and at the end (e.g., before budburst and after harvest) using an ASD HandHeld 2 spectroradiometer (Malvern Panalytical Ltd., Malvern, UK) and a calibrated Spectralon. The HandHeld 2 acquired the spectral signature of the panels within the spectral range of 325–1075 nm with a spectral resolution of 3 nm. The sampled spectral profile of the four panels was resampled using a Gaussian model to match the wavelength centre and wavelength bandwidth of the RedEdge-MX sensor.

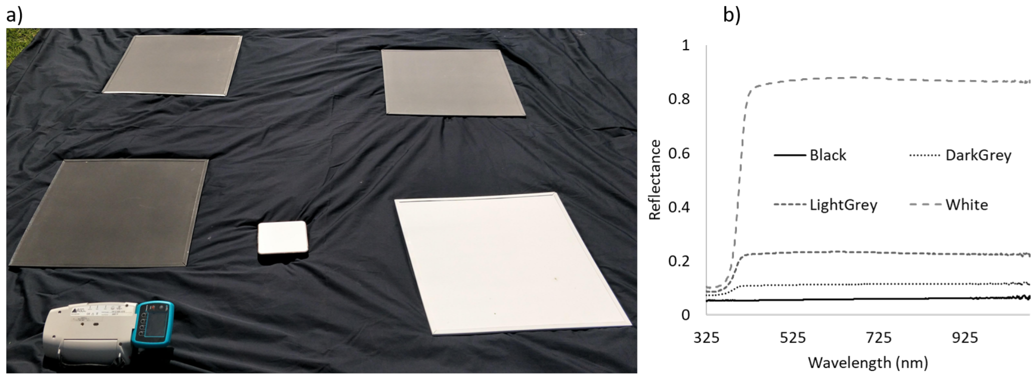

Figure 3. The four greyscaled spectral panels (**a**) were calibrated twice each season—before the start and after the end of the season. The reflectance curve (**b**) shows the sample reflectance of the four panels acquired using the ASD handheld spectroradiometer and the calibrated spectralon.

A canopy height mask and a normalised difference vegetation index (NDVI) mask were generated for each timepoint to mask out the non-canopy pixels including the inter-row, wooden post, and so forth. The canopy height mask was created by offsetting the DEM and DSM and applying a global threshold of 0.7 m (average height of the canopies was 1.7 m). The NDVI mask was created by computing the NDVI and a global threshold of 0.3 (average NDVI of the canopies was 0.6). The combination of the two masks effectively removed the inter-row vegetation, background soil and wooden posts, as well as diseased vines with significantly smaller canopies. Using the macrostructure information of the vineyard (i.e., vine spacing and row spacing), a spatial grid was created using QGIS version 3.16.2 and was approximately aligned with the vines—effectively placing a single canopy within each polygon of the grid. Each polygon of the grid was separated with a buffer of 20 cm to limit the crossover of the canopy to the adjacent polygon. Using the buffered and aligned grid over the masked orthomosaic, pure canopy data were extracted from every single vine and written in the attribute table. The extracted data included the mean spectral reflectance as well as canopy pixel count and height. Using the total pixels within a canopy, various structural information was derived including canopy area (c_area), canopy width, and canopy fraction cover within the ground area per vine (row spacing × vine spacing). Using the reflectance of five bands, several spectral indices were computed. This structural information and the spectral indices were then exported as a CSV file (see Figure 4).

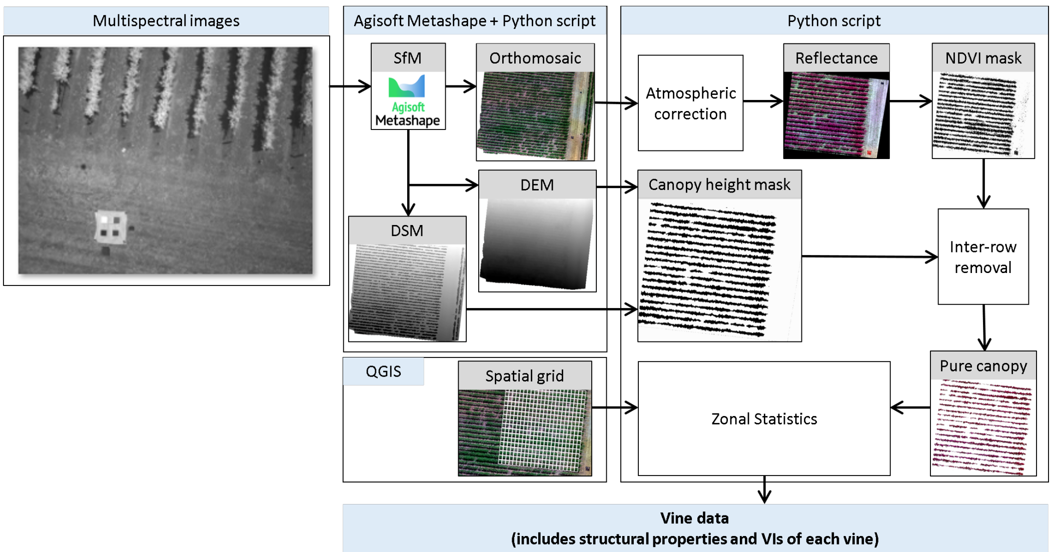

Figure 4. The workflow developed to process the UAV-based images and extract the canopy-specific structural information and spectral indices.

2.4.2. Spectral and Structural Feature Selection

This study incorporated numerous spectral features computed using the blue, green, red, rededge and near infrared bands (e.g., indices available at [57–60]), structural features (e.g., available at [44,61]) and canopy fraction cover [62], as well as a number of custom/adopted features (e.g., cummulative NDVI, canopy width, canopy area and canopy volume above cordon). A correlation analysis of each spectral and structural feature was performed with respect to the ground measured k_c for all the timepoints combined. The features that revealed no significant (Pearson test, *p*-value > 0.05) correlation with k_c were discarded for the modelling. Furthermore, the features with a high degree of collinearity (correlation coefficient > 0.95) were refined to select only one with the highest significance or correlation coefficient. These two steps of feature filtering eliminated most of the spectral/structural features that were initially computed for consideration. The features retained after the two elimination processes were taken as an input for developing k_c prediction models (see Table 1).

Table 1. The list of spectral and structural features retained after the feature filtering processes, i.e., the removal of non-significant and highly collinear features. Note: R, G, and NIR represent the spectral bands red, green and near infrared, respectively. n and r represent the number of pure-canopy pixels and the spatial resolution of the pixels, respectively.

Indices	Abbreviation	Formula	Reference
Greenness index	GI	$\frac{G}{R}$	[58,59]
Normalised difference vegetation index	NDVI	$\frac{NIR-R}{NIR+R}$	[60,63]
Visible-band difference vegetation index	VDVI	$\frac{2\times G-R-B}{2\times G+R+B}$	[64,65]
Enhanced NDVI #2	ENDVI2	$\frac{NIR+G-2\times R}{NIR+G+2\times R}$	modified [66,67]
Enhanced NDVI #3	ENDVI3	$\frac{NIR+G-R-B}{(NIR+G-R-B}$	modified [66,67]
Plant height	p_height	DEM-DSM	[44,61]
Cumulative NDVI	cum_NDVI	$\sum$NDVI	
Canopy top-view area	c_area	n × r	

2.4.3. Modelling

Within the five timepoints of the two seasons, a total of 320 datapoints were acquired, which included remotely sensed spectral/structural features and the corresponding ground-reference k_c. Outliers in the dataset were investigated and removed using Cook's distance (2/n), which reduced the number of datapoints to 231 [68,69]. The spectral/structural features synthesised in Table 1 were used to develop predictive models of k_c. The training and testing datasets were split randomly in the ratio of 3:1 (173 training and 58 testing datapoints). Using the training dataset and the leave-one-out cross-validation, k_c prediction models were developed. This leave-one-out approach of fit-control recursively develops a model and validates on one random datapoint until all the datapoints are used for validation [70]. Various models, such as the simple linear model (SLM), generalised linear model (GLM), generalised additive model (GAM), neural network model (NNM) and random forest model (RFM) were developed using the caret package in R programming languages (Version 4.0.4, RStudio Version 1.4.1106) [71–73]. The final refined model was tested on the testing dataset (58 datapoints). The model performance was evaluated using indicators including R squared (R^2), Root Mean Square Error (RMSE) and mean absolute error (MAE).

3. Results

The grape growing season in the Coonawarra region starts relatively late with budburst in late October, reaching flowering approximately in December, pea-sized berries in January, véraison in February and harvest in April. The cumulative growing degree days for the two seasons are computed by integrating the local weather station data (Australian Government, Bureau of Meteorology, weather station number 026091, Coonawarra, SA, Australia) starting from the budbrust up to the grape harvest (see Figure 5). The field data acquisition timepoints (3 timepoints in the 2018/19 season and 2 timepoints in the 2019/20 season) and the corresponding phenological stage of the grapevine are shown in the figure. In comparison, the 2019/20 season was cooler with fewer heatwaves and less extreme temperatures.

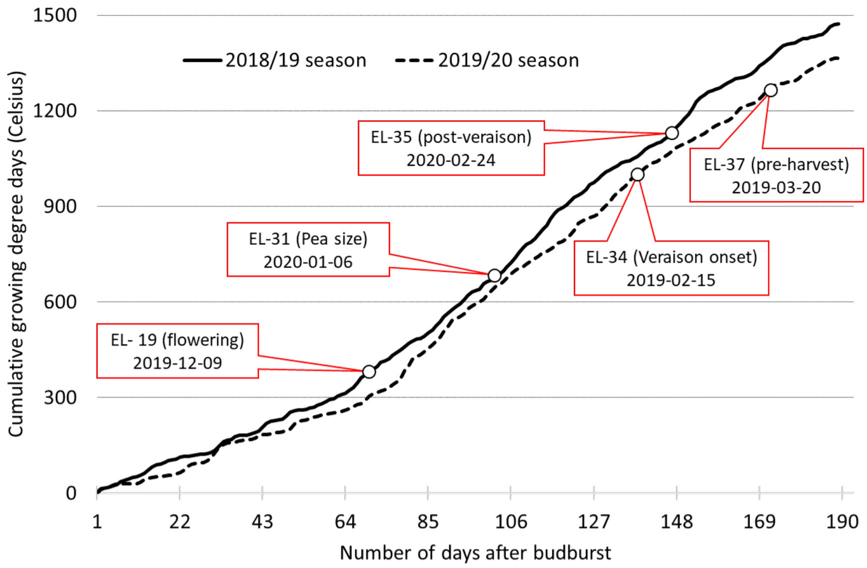

Figure 5. The cumulative growing degree days for the Cabernet Sauvignon at the Wynns Coonawarra Estate, Coonawarra for the two seasons, 2018/19 and 2019/20. The data acquisition stages for both seasons are shown.

The evolution of k_c, along with the most significant spectral/structural features, are presented in Figure 6. The displayed features had the highest significance and correlation coefficient with k_c. The seasonal k_c values followed the pattern, which was noted physically and observed in the canopy LAI measurements, of rapid canopy growth until the véraison and stability after that. The k_c started at a mean value of 0.48 at the start of the season and steadily increased to a mean value of 0.67 by the end of the season. The trends of NDVI and ENDVI2 appear to be less sensitive to canopy growth, while the c_area was the most sensitive, particularly in the early season between fruit set and pea-sized berries. Between the pea size and véraison, all of the remote sensing temporal trends do not appear to reflect the k_c trend. Post véraison, all the indices show a strong agreement with each other and reflect little to no changes in canopy development/growth. The decrease in spectral indices post véraison may be reflecting the depletion of nitrogen in the vine, including the leaves [74,75]. The seasonal evolution graph suggests that either the c_area alone or a combination of c_area and spectral features could be the best predictors of k_c at any timepoint. The best performing model for each timepoint could incorporate the timepoint specific data. However, this study assesses a holistic model to reduce the timepoint specific bias due to the small sample size, as well as to provide a robust predictor that is not limited by the growth stage of the plant.

Among various spectral indices and structural parameters (not listed exclusively here), few of the features were selected for modelling purposes following the removal of non-significant as well as collinear features. The correlogram in Figure 7 shows the selected indices, their statistical significance and correlation coefficients with the response variable, k_c. The c_area had the strongest correlation with k_c (highly significant and highest correlation coefficient). Composite feature cumulative NDVI and spectral features NDVI ENDVI2 were the second-tier features showing a strong correlation with k_c, while other features, such as the greenness index (GI), ENDVI3, visible-band difference vegetation index (VDVI) and plant height (p_height), had a weak but significant correlation.

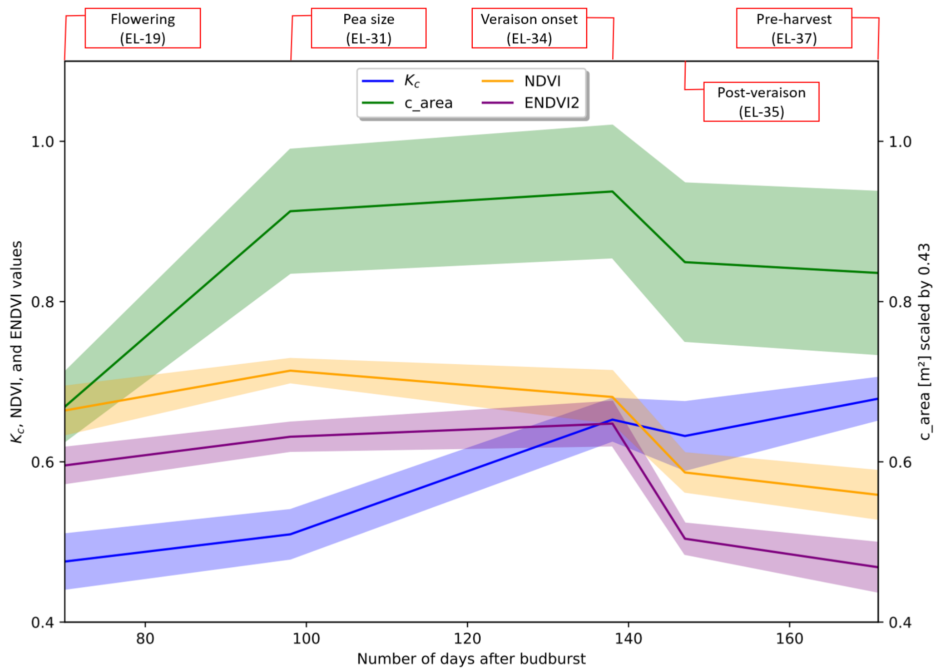

Figure 6. Seasonal evolution of the k_c along with the highly correlated and statistically significant spectral features, represented in the primary y-axis and canopy area (c_area) represented in the second y-axis. The shaded band on the seasonal evolution plot represents the $\pm 1\sigma$ around the mean.

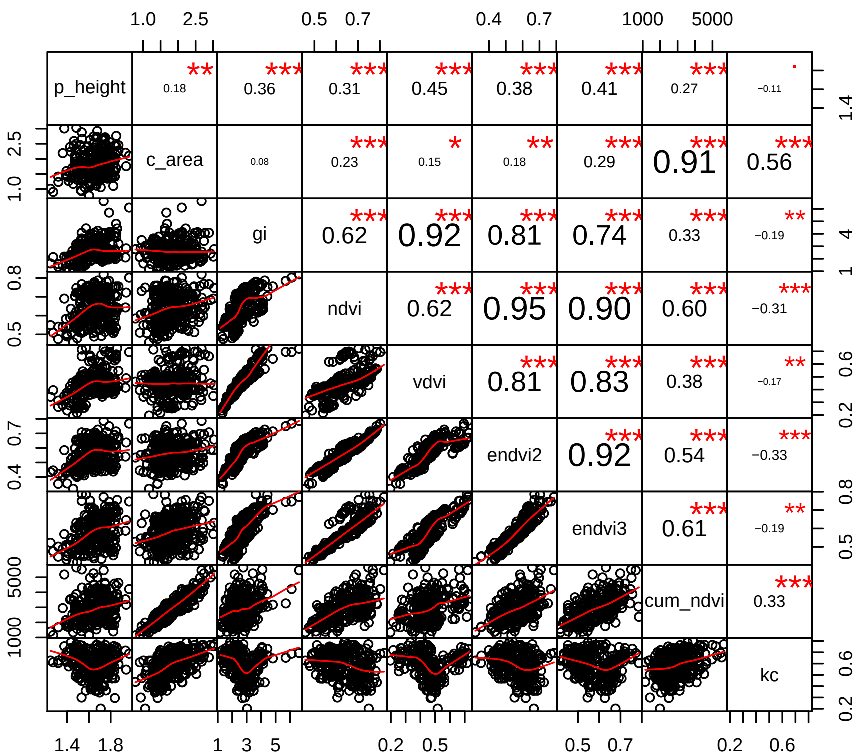

Figure 7. Correlogram showing the scatter plot, correlation coefficient values and statistical significance (Pearson test: p-value < 0.05 as *, p-value < 0.01 as **, and p-value < 0.001 as ***) between the selected features (spectral and structural) and the crop coefficient.

To develop k_c models, the dataset (231 datapoints) was split into training and testing on a ratio of 3:1. The training dataset was used to train the model while the testing dataset was used to access the performance accuracy. The leave-one-out cross-validation approach ensured that a large number of datapoints (172) were available for each of the model generations. The best univariate indicator of k_c was the c_area, which performed with reasonable accuracy (R^2 = 0.295, RMSE = 0.091, MAE = 0.076). Multidimensional regression using all the features substantially improved the prediction accuracy (e.g., GLM) with improved AIC (SLM AIC: −340.0, GLM AIC: −411.7). Further improvement in the prediction was achieved using non-linear-multidimensional models (e.g., GAM with AIC of −461.7) and machine learning models such as CNN (a 8-5-1 network with 51 weights) and RFM (ntree = 500, mtry = 3). While all the multidimensional models investigated used the same input features (listed in Table 1, the features that ended up being important in all the models were significantly different. For example, the RFM, which performed the best, had c_area as the most important feature whereas the CNN, which used cum_NDVI, performed relatively poorly. In addition to the leave-one-out, a k-fold cross-validation approach was tested, which resulted in a similar trend in the model accuracy—RFM performing the best of all the models evaluated in this study (see Table 2).

Table 2. Accuracy of various models used to predict the k_c using leave-one-out fit-control. Note the accuracy metrics were derived by applying the model to the unseen testing dataset. Note: AIC in the table heading is an abbreviation of the Akaike information criterion.

Models	R^2	RMSE	MAE	AIC	Most Influential Features
Generalised linear	0.528	0.074	0.061	−411.7	GI
Generalised additive	0.594	0.069	0.055	−461.7	c_area
Convolutional neural network	0.619	0.072	0.060	na	cum_NDVI
Random forest	0.675	0.062	0.047	na	c_area

The simple linear model provided the most straightforward model while the RFM provided the most accurate model for estimating k_c. The RFM model was used to further predict spatial k_c values at the vineyard scale at two key phenological stages of the vine (Figure 8). Using the estimated k_c values, along with the weather data (temperature, humidity, wind speed), the spatial irrigation requirements of the vineyard were computed on a per vine basis.

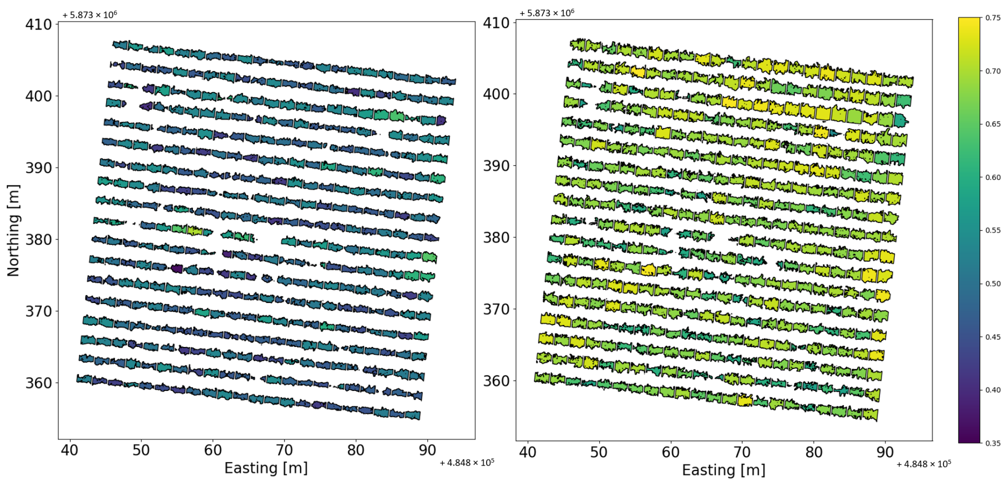

Figure 8. The map of estimated k_c values and at the early season ((**left**) pane, flowering stage, EL-19) and late season ((**right**) pane, post véraison, EL-35) of Cabernet Sauvignon.

4. Discussion

There exist differences in mesoclimate between different sites and within the site receiving uniform irrigation. For instance, the two sites used in this study received uniform irrigation despite highly variable soil depth. This variability presents a significant challenge for irrigation management that could be partly overcome by adopting high-resolution data capture. A significant advantage of UAV remote sensing in precision irrigation is the unprecedented spatial details that can reveal spatial variability within a vineyard receiving uniform irrigation. This detailed (canopy-specific) level of information is, however, not fully exploitable, that is, canopy-specific irrigation management is not practicable. The current irrigation management technology in vineyards generally has a fixed infrastructure, which makes the spatial control of the irrigation unfeasible or costly to incorporate. A potential benefit could lie in the improvement of the zoning of the vineyards such that zones receiving uniform irrigation have reduced spatial variability [76]. Using spatial clustering, irrigation zones can be set to minimise spatial variability whilst still maintaining economic viability [77].

The k_c is an evolving parameter that changes together with the development stage of the crop, canopy cover and architecture, and transpiration [10,40]. As such, different crops with different management practices will have a unique evolution of water requirements and k_c values throughout the various phenological stages [31,43,78]. Even for a single crop, such as a grapevine, a single k_c value may lead to over- or under-irrigation depending on the time of the year. This has numerous implications for management. The availability of a time series of k_c maps will allow spatially explicit parameterisation of models for irrigation management and this will facilitate improved realism in models (see [7] for a recent review of models). Spatio-temporal estimates of k_c will help with implementing regulated deficit irrigation (RDI). A typical RDI regime necessitates a minimum of two timepoints of k_c values. The temporal evolution of k_c seems to follow the thermal time (GDD) graph; however, it requires further temporally-intensive data at multiple seasons for verification. Such co-evolution of k_c and GDD, if established, could require only a few timepoints of k_c determination that can be extrapolated temporally based on the evolution of the thermal GDD.

This research could have limitations due to the study of just two seasons of data and the lack of spatial distribution of ground reference. Two seasons of data were considered sufficient as the investigated vines were mature and were managed using set management practices, which resulted in minimal seasonality effect on the canopy structure and architecture. However, there could still be some underlying seasonal variability requiring further data acquisition. The spatial distribution of the ground reference was set by a larger irrigation treatment study, which this research was a part of. The ground reference measurement vines were selected based on the physiology of the plant from set rows to minimise the inter-vine variability and to construct the irrigation system. As a result, only the selected vines that were located in certain rows were measured. However, despite this lack of spatial distribution, our dataset captured a wide extent of k_c measurement values, predominantly due to the data acquisition at early-, mid-, and late-season, as well as due to the application of various irrigation treatments. Moreover, the UAV-estimated range of k_c values was equivalent to the ground-observed range of k_c values.

The k_c is generally measured on the ground from several representative samples within each irrigation zone. This approach, however, does not capture the entire variability within a field and the selection of samples can be subjective to the user. UAV-based observation of the entire irrigation zone could provide a more unbiased and holistic view of the vineyard. Moreover, the UAV-based k_c estimation incorporates measurements from the entire canopy while the k_c measured on the ground using the Paso Panel incorporates a section of the canopy. For instance, we sampled k_c values once from each side of the cordon. This sampling strategy is equivalent to the incorporation of 0.6 m out of 2.1 m of the canopy cordon. As a result, the ground sampling is computed by observing less than 30% of the canopy foliage while the aerial sampling incorporates the entire canopy foliage. Hence, some errors associated with the UAV-based modelling of k_c could also be attributed to the Paso Panel acquired ground data. The UAV-based k_c values could, therefore, be more robust than is expressed in the model performance results (Table 2).

Preliminary economic calculations based on Australian standards, and excluding the Research and Development cost, revealed that the UAV-based approach could be profitable for the industry in the long run. Measuring on a small scale (e.g., 1 ha vineyard), the Paso Panel approach costs approximately AU$20/vine/season considering the measurement of 50 vines from the 1 ha at six timepoints throughout the season. The UAV-based approach costs approximately AU$5/vine/season considering the initial capital investment and the measurement of 2000 vines from 1 ha at six timepoints. When considering a larger vineyard, for example, 20 ha, the UAV-based approach was substantially cheaper (AU$0.45/vine/season) while the Paso Panel approach cost remained approximately the same. The total cost of the UAV-based approach was substantially high in the first year; however, it becomes progressively cheaper on a per-vine-per-season basis. In subsequent years, both the UAV and Paso Panel approaches had approximately similar year-on-year running costs. Hence, following the initial capital investment in the UAV and multispectral camera, the industry will be able to measure every vine by spending a similar amount as on the Paso Panel based approach. However, a detailed cost–benefit analysis in this regard is needed to establish a complete understanding of the costs associated with the adaptation of this technology and its benefits, both short- and long-term.

For non-horticultural homogenous field crops, the satellite-based estimation of k_c is very reliable [30,31,38]. Complexity in the horticultural setting specifically due to inter-row bare/vegetated areas reduces the estimation accuracies. In vineyards, R^2 of 0.177 and 0.426 was achieved using satellite-based SAR and NDVI images, respectively [79]. In a ground-based study of a vineyard, [43] showed a linear relationship between the ground-based LAI and the ground-based k_c in Cabernet Sauvignon with an R^2 of 0.66. In a similar study, [40] estimated the k_c of the Thompson Seedless table grape as a function of leaf area per vine (R^2 = 0.87), LAI (R^2 = 0.87) and shaded area (R^2 = 0.95). The higher estimation accuracy with the table grape canopies can be attributed to the overhead trellis systems as compared to the VSP trellis with the wine grapes [43]. Our study of k_c on sprawling Cabernet Sauvignon wine grapes is comparable to the ground-based study presented in [43]. Using UAV remote sensing, our study presented the capability of remotely measuring k_c with a similar accuracy to that of the ground-based measurements (R^2 = 0.675). This capability combined with the benefits of remote sensing in terms of efficiently and inexpensively sampling a much larger area (several hectares) could increase the use of UAV in lieu of field sampling.

The k_c in vineyards is highly variable and can be influenced by vine management practices, soil depth, rooting systems and vine training systems, among other factors. While there are k_c maps freely accessible to growers, these maps will require a site-, region-, and crop-specific ground calibration to establish their usability [30,33]. Using a UAV-based approach, the most practical solution from a grower's perspective could be with the use of a simple RGB camera on an autonomous UAV to compute the c_area as a proxy of k_c. Using just the c_area as an input, k_c was estimated, in this study, with an R^2 of 0.295, an RMSE of 0.091, and an MAE of 0.076. Given the improved level of autonomy of the UAVs and the increased efficiencies via data processing pipelines, estimating irrigation requirements at multiple timepoints of the season could be within reach for growers using a UAV-based RGB camera. This will improve the precision of the irrigation by computing spatially explicit irrigation requirements for each vine as well as for the entire irrigation zone. However, for the most accurate quantitative estimation, growers could consider sophisticated models such as GLM, GAM or machine learning.

5. Conclusions

In this article, we demonstrated the application of an unmanned aircraft system to estimating the crop coefficient and subsequent irrigation requirements of vineyards. The spectral indices were highly correlated to k_c until the véraison timepoint. After véraison, the correlation between the spectral indices and k_c value started to diverge. The structural features presented the highest correlation coefficient and statistical significance with k_c values throughout the season. Combining both the spectral reflectance and structural features of the grapevine provided a robust estimation of k_c for both early as well as late in the season. Incorporating k_c values with an energy balance model can provide an estimate of the irrigation requirements at different phenological stages. Preliminary economic analysis revealed that the proposed UAV-based method was the most cost effective and quickest method for estimating the k_c and subsequent crop water needs per vine. With the continued development of UAV and battery technology, we envision the increased use of UAV remote sensing for the estimation of irrigation requirements in both small and large vineyards. Future research directions could include irrigation thresholding and automated triggering based on the measured crop water needs and the monitoring of vines and their physiology. While ET_c provided a basis for evidence-based irrigation, more precise control of grapevine irrigation needs could require the use of plant-based sensors such as microtensiometers. A combination of both ET- and plant-based sensors could be a way forward to potentially maximise water use efficiency on a fine to a large scale.

Author Contributions: All authors conceived the initial design of the research. D.G. acquired the remote sensing and together with V.P. the ground data. D.G. processed/analysed the data and together with V.P. interpreted the results. D.G. prepared the manuscript. All authors contributed to the review of the manuscript. All authors have read and agreed to the published version of the manuscript.

Funding: This research was funded by Wine Australia (Grant number: UA 1803-1.3) bilateral project.

Acknowledgments: The authors would like to acknowledge Rochelle Schlank, Antoine Lespes, Caitlin Griffiths, Catherine Kidman, and Courtney Handford for their assistance in the field data collection at different stages; the Wynns Coonawarra Estate for providing test site for this study; the funding body Wine Australia; The University of Adelaide; and the anonymous reviewers for their contribution.

Conflicts of Interest: The authors declare no conflict of interest.

References

1. Ummenhofer, C.C.; England, M.H.; McIntosh, P.C.; Meyers, G.A.; Pook, M.J.; Risbey, J.S.; Gupta, A.S.; Taschetto, A.S. What causes southeast Australia's worst droughts? *Geophys. Res. Lett.* **2009**, *36*. [CrossRef]
2. King, A.D.; Pitman, A.J.; Henley, B.J.; Ukkola, A.M.; Brown, J.R. The role of climate variability in Australian drought. *Nat. Clim. Chang.* **2020**, *10*, 177–179. [CrossRef]
3. Paydar, Z.; Qureshi, M. Irrigation water management in uncertain conditions—Application of Modern Portfolio Theory. *Agric. Water Manag.* **2012**, *115*, 47–54. [CrossRef]
4. Smith, R. *Review of Precision Irrigation Technologies and Their Applications*; Technical Report; University of Southern Queensland: Toowoomba, Australia, 2011.
5. Mulla, D.J. Twenty five years of remote sensing in precision agriculture: Key advances and remaining knowledge gaps. *Biosyst. Eng.* **2013**, *114*, 358–371. [CrossRef]
6. Gautam, D.; Pagay, V. A Review of Current and Potential Applications of Remote Sensing to Study the Water Status of Horticultural Crops. *Agronomy* **2020**, *10*, 140. [CrossRef]
7. Knowling, M.; Bennett, B.; Ostendorf, B.; Westra, S.; Walker, R.; Pellegrino, A.; Edwards, E.; Collins, C.; Pagay, V.; Grigg, D. Bridging the gap between data and decisions in viticulture: A review of process-based models. *Agric. Syst.* **2021**, *193*. [CrossRef]
8. Fereres, E.; Soriano, M.A. Deficit irrigation for reducing agricultural water use. *J. Exp. Bot.* **2007**, *58*, 147–159. [CrossRef]
9. Iniesta, F.; Testi, L.; Orgaz, F.; Villalobos, F. The effects of regulated and continuous deficit irrigation on the water use, growth and yield of olive trees. *Eur. J. Agron.* **2009**, *30*, 258–265. [CrossRef]
10. Allen, R.G.; Pereira, L.S.; Raes, D.; Smith, M. Crop evapotranspiration-Guidelines for computing crop water requirements-FAO Irrigation and drainage paper 56. *Fao Rome* **1998**, *300*, D05109.
11. Hoffmann, H.; Nieto, H.; Jensen, R.; Guzinski, R.; Zarco-Tejada, P.; Friborg, T. Estimating evaporation with thermal UAV data and two-source energy balance models. *Hydrol. Earth Syst. Sci.* **2016**, *20*, 697–713. [CrossRef]
12. Nieto, H.; Bellvert, J.; Kustas, W.P.; Alfieri, J.G.; Gao, F.; Prueger, J.; Torres-Rua, A.; Hipps, L.E.; Elarab, M.; Song, L. Unmanned airborne thermal and mutilspectral imagery for estimating evapotranspiration in irrigated vineyards. In Proceedings of the 2017 IEEE International Geoscience and Remote Sensing Symposium (IGARSS), Fort Worth, TX, USA, 23–28 July 2017; pp. 5510–5513.
13. Niu, H.; Hollenbeck, D.; Zhao, T.; Wang, D.; Chen, Y. Evapotranspiration Estimation with Small UAVs in Precision Agriculture. *Sensors* **2020**, *20*, 6427. [CrossRef]

14. Niu, H.; Wang, D.; Chen, Y. Estimating actual crop evapotranspiration using deep stochastic configuration networks model and UAV-based crop coefficients in a pomegranate orchard. In *Autonomous Air and Ground Sensing Systems for Agricultural Optimization and Phenotyping V*; International Society for Optics and Photonics: San Diego, CA, USA, 2020; Volume 11414, p. 114140C.
15. Bellvert, J.; Adeline, K.; Baram, S.; Pierce, L.; Sanden, B.L.; Smart, D.R. Monitoring crop evapotranspiration and crop coefficients over an almond and pistachio orchard throughout remote sensing. *Remote Sens.* **2018**, *10*, 2001. [CrossRef]
16. Bellvert, J.; Zarco-Tejada, P.; Gonzalez-Dugo, V.; Girona, J.; Fereres, E. Scheduling vineyard irrigation based on mapping leaf water potential from airborne thermal imagery. In *Precision Agriculture'13*; Springer: Berlin/Heidelberg, Germany, 2013; pp. 699–704.
17. Bellvert, J.; Girona, J. The use of multispectral and thermal images as a tool for irrigation scheduling in vineyards. *Use Remote. Sens. Geogr. Inf. Syst. Irrig. Manag. Southwest Eur.* **2012**, *67*, 131–137.
18. Bellvert, J.; Zarco-Tejada, P.J.; Marsal, J.; Girona, J.; González-Dugo, V.; Fereres, E. Vineyard irrigation scheduling based on airborne thermal imagery and water potential thresholds. *Aust. J. Grape Wine Res.* **2016**, *22*, 307–315. [CrossRef]
19. Gonzalez-Dugo, V.; Goldhamer, D.; Zarco-Tejada, P.J.; Fereres, E. Improving the precision of irrigation in a pistachio farm using an unmanned airborne thermal system. *Irrig. Sci.* **2015**, *33*, 43–52. [CrossRef]
20. López-Urrea, R.; Montoro, A.; Mañas, F.; López-Fuster, P.; Fereres, E. Evapotranspiration and crop coefficients from lysimeter measurements of mature 'Tempranillo'wine grapes. *Agric. Water Manag.* **2012**, *112*, 13–20. [CrossRef]
21. Williams, L.; Phene, C.; Grimes, D.; Trout, T. Water use of mature Thompson Seedless grapevines in California. *Irrig. Sci.* **2003**, *22*, 11–18. [CrossRef]
22. Li, Z.L.; Tang, R.; Wan, Z.; Bi, Y.; Zhou, C.; Tang, B.; Yan, G.; Zhang, X. A review of current methodologies for regional evapotranspiration estimation from remotely sensed data. *Sensors* **2009**, *9*, 3801–3853. [CrossRef]
23. Liou, Y.A.; Kar, S.K. Evapotranspiration estimation with remote sensing and various surface energy balance algorithms—A review. *Energies* **2014**, *7*, 2821–2849. [CrossRef]
24. Zhang, K.; Kimball, J.S.; Running, S.W. A review of remote sensing based actual evapotranspiration estimation. *Wiley Interdiscip. Rev. Water* **2016**, *3*, 834–853. [CrossRef]
25. Kullberg, E.G.; DeJonge, K.C.; Chávez, J.L. Evaluation of thermal remote sensing indices to estimate crop evapotranspiration coefficients. *Agric. Water Manag.* **2017**, *179*, 64–73. [CrossRef]
26. Ihuoma, S.O.; Madramootoo, C.A. Recent advances in crop water stress detection. *Comput. Electron. Agric.* **2017**, *141*, 267–275. [CrossRef]
27. Tang, J.; Han, W.; Zhang, L. UAV Multispectral Imagery Combined with the FAO-56 Dual Approach for Maize Evapotranspiration Mapping in the North China Plain. *Remote Sens.* **2019**, *11*, 2519. [CrossRef]
28. Poblete-Echeverría, C.; Ortega-Farias, S. Evaluation of single and dual crop coefficients over a drip-irrigated M erlot vineyard (*Vitis vinifera* L.) using combined measurements of sap flow sensors and an eddy covariance system. *Aust. J. Grape Wine Res.* **2013**, *19*, 249–260. [CrossRef]
29. Cancela, J.; Fandiño, M.; Rey, B.; Martínez, E. Automatic irrigation system based on dual crop coefficient, soil and plant water status for Vitis vinifera (cv Godello and cv Mencía). *Agric. Water Manag.* **2015**, *151*, 52–63. [CrossRef]
30. Kamble, B.; Kilic, A.; Hubbard, K. Estimating crop coefficients using remote sensing-based vegetation index. *Remote Sens.* **2013**, *5*, 1588–1602. [CrossRef]
31. Zhang, H.; Anderson, R.G.; Wang, D. Satellite-based crop coefficient and regional water use estimates for Hawaiian sugarcane. *Field Crops Res.* **2015**, *180*, 143–154. [CrossRef]
32. Ramírez-Cuesta, J.M.; Mirás-Avalos, J.M.; Rubio-Asensio, J.S.; Intrigliolo, D.S. A novel ArcGIS toolbox for estimating crop water demands by integrating the dual crop coefficient approach with multi-satellite imagery. *Water* **2019**, *11*, 38. [CrossRef]
33. Montgomery, J.; Hornbuckle, J.; Hume, I.; Vleeshouwer, J. IrriSAT—Weather based scheduling and benchmarking technology. In Proceedings of the 17th ASA Conference, Hobart, Australia, 20–24 September 2015; pp. 20–24.
34. Trout, T.; Johnson, L. Estimating crop water use from remotely sensed NDVI, crop models, and reference ET. In Proceedings of the USCID Fourth International Conference on Irrigation and Drainage, Role of Irrigation and Drainage in a Sustainable Future, Sacramento, CA, USA, 3–6 October 2007; pp. 3–6.
35. Sanchez, L.; Sams, B.; Alsina, M.; Hinds, N.; Klein, L.; Dokoozlian, N. Improving vineyard water use efficiency and yield with variable rate irrigation in California. *Adv. Anim. Biosci.* **2017**, *8*, 574–577. [CrossRef]
36. Er-Raki, S.; Rodriguez, J.; Garatuza-Payan, J.; Watts, C.; Chehbouni, A. Determination of crop evapotranspiration of table grapes in a semi-arid region of Northwest Mexico using multi-spectral vegetation index. *Agric. Water Manag.* **2013**, *122*, 12–19. [CrossRef]
37. Choudhury, B.J.; Ahmed, N.U.; Idso, S.B.; Reginato, R.J.; Daughtry, C.S. Relations between evaporation coefficients and vegetation indices studied by model simulations. *Remote Sens. Environ.* **1994**, *50*, 1–17. [CrossRef]
38. Hunsaker, D.J.; Pinter, P.J.; Kimball, B.A. Wheat basal crop coefficients determined by normalized difference vegetation index. *Irrig. Sci.* **2005**, *24*, 1–14. [CrossRef]
39. Samani, Z.; Bawazir, A.S.; Bleiweiss, M.; Skaggs, R.; Longworth, J.; Tran, V.D.; Pinon, A. Using remote sensing to evaluate the spatial variability of evapotranspiration and crop coefficient in the lower Rio Grande Valley, New Mexico. *Irrig. Sci.* **2009**, *28*, 93. [CrossRef]
40. Williams, L.; Ayars, J. Grapevine water use and the crop coefficient are linear functions of the shaded area measured beneath the canopy. *Agric. For. Meteorol.* **2005**, *132*, 201–211. [CrossRef]

41. Picón-Toro, J.; González-Dugo, V.; Uriarte, D.; Mancha, L.; Testi, L. Effects of canopy size and water stress over the crop coefficient of a "Tempranillo" vineyard in south-western Spain. *Irrig. Sci.* **2012**, *30*, 419–432. [CrossRef]
42. Santos, L.; Ferraz, G.; Diotto, A.; Barbosa, B.; Maciel, D.; Andrade, M.; Ferraz, P.; Rossi, G. Coffee crop coefficient prediction as a function of biophysical variables identified from RGB UAS images. *Agron. Res.* **2020**, *18*, 1463–1471.
43. Munitz, S.; Schwartz, A.; Netzer, Y. Water consumption, crop coefficient and leaf area relations of a Vitis vinifera cv. 'Cabernet Sauvignon' vineyard. *Agric. Water Manag.* **2019**, *219*, 86–94. [CrossRef]
44. Matese, A.; Di Gennaro, S.F.; Berton, A. Assessment of a canopy height model (CHM) in a vineyard using UAV-based multispectral imaging. *Int. J. Remote Sens.* **2017**, *38*, 2150–2160. [CrossRef]
45. Jurado, J.M.; Ortega, L.; Cubillas, J.J.; Feito, F. Multispectral mapping on 3D models and multi-temporal monitoring for individual characterization of olive trees. *Remote Sens.* **2020**, *12*, 1106. [CrossRef]
46. Banks, G.; Sharpe, S. Wine, regions and the geographic imperative: The Coonawarra example. *N. Z. Geogr.* **2006**, *62*, 173–184. [CrossRef]
47. Mee, A.C.; Bestland, E.A.; Spooner, N.A. Age and origin of Terra Rossa soils in the Coonawarra area of South Australia. *Geomorphology* **2004**, *58*, 1–25. [CrossRef]
48. Coombe, B.G. Growth stages of the grapevine: Adoption of a system for identifying grapevine growth stages. *Aust. J. Grape Wine Res.* **1995**, *1*, 104–110. [CrossRef]
49. Mlambo, R.; Woodhouse, I.H.; Gerard, F.; Anderson, K. Structure from motion (SfM) photogrammetry with drone data: A low cost method for monitoring greenhouse gas emissions from forests in developing countries. *Forests* **2017**, *8*, 68. [CrossRef]
50. Dandois, J.P.; Olano, M.; Ellis, E.C. Optimal altitude, overlap, and weather conditions for computer vision UAV estimates of forest structure. *Remote Sens.* **2015**, *7*, 13895–13920. [CrossRef]
51. Sanches, I.; Tuohy, M.; Hedley, M.; Bretherton, M. Large, durable and low-cost reflectance standard for field remote sensing applications. *Int. J. Remote Sens.* **2009**, *30*, 2309–2319. [CrossRef]
52. RedEdge, M. *Multispectral Camera User Manual*; MicaSense Inc.: Seattle, WA, USA, 2015; p. 33.
53. Tu, Y.H.; Phinn, S.; Johansen, K.; Robson, A. Assessing radiometric correction approaches for multi-spectral UAS imagery for horticultural applications. *Remote Sens.* **2018**, *10*, 1684. [CrossRef]
54. Bendig, J.; Gautam, D.; Malenovskỳ, Z.; Lucieer, A. Influence of cosine corrector and UAS platform dynamics on airborne spectral irradiance measurements. In Proceedings of the IGARSS 2018-2018 IEEE International Geoscience and Remote Sensing Symposium, Valencia, Spain, 22–27 July 2018; pp. 8822–8825.
55. Smith, G.M.; Milton, E.J. The use of the empirical line method to calibrate remotely sensed data to reflectance. *Int. J. Remote Sens.* **1999**, *20*, 2653–2662. [CrossRef]
56. Wang, C.; Myint, S.W. A simplified empirical line method of radiometric calibration for small unmanned aircraft systems-based remote sensing. *IEEE J. Sel. Top. Appl. Earth Obs. Remote Sens.* **2015**, *8*, 1876–1885. [CrossRef]
57. Baluja, J.; Diago, M.P.; Balda, P.; Zorer, R.; Meggio, F.; Morales, F.; Tardaguila, J. Assessment of vineyard water status variability by thermal and multispectral imagery using an unmanned aerial vehicle (UAV). *Irrig. Sci.* **2012**, *30*, 511–522. [CrossRef]
58. Zarco-Tejada, P.J.; Berjón, A.; López-Lozano, R.; Miller, J.R.; Martín, P.; Cachorro, V.; González, M.; De Frutos, A. Assessing vineyard condition with hyperspectral indices: Leaf and canopy reflectance simulation in a row-structured discontinuous canopy. *Remote Sens. Environ.* **2005**, *99*, 271–287. [CrossRef]
59. Zarco-Tejada, P.J.; Ustin, S.; Whiting, M. Temporal and spatial relationships between within-field yield variability in cotton and high-spatial hyperspectral remote sensing imagery. *Agron. J.* **2005**, *97*, 641–653. [CrossRef]
60. Bannari, A.; Morin, D.; Bonn, F.; Huete, A. A review of vegetation indices. *Remote Sens. Rev.* **1995**, *13*, 95–120. [CrossRef]
61. Bendig, J.; Yu, K.; Aasen, H.; Bolten, A.; Bennertz, S.; Broscheit, J.; Gnyp, M.L.; Bareth, G. Combining UAV-based plant height from crop surface models, visible, and near infrared vegetation indices for biomass monitoring in barley. *Int. J. Appl. Earth Obs. Geoinf.* **2015**, *39*, 79–87. [CrossRef]
62. Pereira, L.; Paredes, P.; Melton, F.; Johnson, L.; Wang, T.; López-Urrea, R.; Cancela, J.; Allen, R. Prediction of crop coefficients from fraction of ground cover and height. Background and validation using ground and remote sensing data. *Agric. Water Manag.* **2020**, *241*, 106197. [CrossRef]
63. Rouse, J.W.; Haas, R.H.; Schell, J.A.; Deering, D.W.; Harlan, J.C. *Monitoring the Vernal Advancement and Retrogradation (Green Wave Effect) of Natural Vegetation*; NASA/GSFC Type III Final Report; NASA/GSFC: Greenbelt, MD, USA, 1974; Volume 371.
64. Tan, Y.; Wang, S.; Xu, B.; Zhang, J. An improved progressive morphological filter for UAV-based photogrammetric point clouds in river bank monitoring. *ISPRS J. Photogramm. Remote Sens.* **2018**, *146*, 421–429. [CrossRef]
65. Xiaoqin, W.; Miaomiao, W.; Shaoqiang, W.; Yundong, W. Extraction of vegetation information from visible unmanned aerial vehicle images. *Trans. Chin. Soc. Agric. Eng.* **2015**, *31*, 152–159.
66. Strong, C.J.; Burnside, N.G.; Llewellyn, D. The potential of small-Unmanned Aircraft Systems for the rapid detection of threatened unimproved grassland communities using an Enhanced Normalized Difference Vegetation Index. *PLoS ONE* **2017**, *12*, e0186193. [CrossRef] [PubMed]
67. Susantoro, T.M.; Wikantika, K.; Saepuloh, A.; Harsolumakso, A.H. Selection of vegetation indices for mapping the sugarcane condition around the oil and gas field of North West Java Basin, Indonesia. *IOP Conf. Ser. Earth Environ. Sci.* **2018**, *149*, 012001. [CrossRef]
68. Cook, R.D. Detection of influential observation in linear regression. *Technometrics* **1977**, *19*, 15–18.

69. Walfish, S. A review of statistical outlier methods. *Pharm. Technol.* **2006**, *30*, 82.
70. Vehtari, A.; Gelman, A.; Gabry, J. Practical Bayesian model evaluation using leave-one-out cross-validation and WAIC. *Stat. Comput.* **2017**, *27*, 1413–1432. [CrossRef]
71. Kuhn, M. The Caret Package. Available online: https://cran.r-project.org/web/packages/caret/index.html (accessed on 5 July 2020).
72. Kuhn, M. Building predictive models in R using the caret package. *J. Stat. Softw.* **2008**, *28*, 1–26. [CrossRef]
73. Bivand, R. Implementing spatial data analysis software tools in R. *Geogr. Anal.* **2006**, *38*, 23–40. [CrossRef]
74. Keller, M.; Hrazdina, G. Interaction of nitrogen availability during bloom and light intensity during veraison. II. Effects on anthocyanin and phenolic development during grape ripening. *Am. J. Enol. Vitic.* **1998**, *49*, 341–349.
75. BELL, S.J.; Henschke, P.A. Implications of nitrogen nutrition for grapes, fermentation and wine. *Aust. J. Grape Wine Res.* **2005**, *11*, 242–295. [CrossRef]
76. Bellvert, J.; Marsal, J.; Mata, M.; Girona, J. Identifying irrigation zones across a 7.5-ha 'Pinot noir'vineyard based on the variability of vine water status and multispectral images. *Irrig. Sci.* **2012**, *30*, 499–509. [CrossRef]
77. Ohana-Levi, N.; Bahat, I.; Peeters, A.; Shtein, A.; Netzer, Y.; Cohen, Y.; Ben-Gal, A. A weighted multivariate spatial clustering model to determine irrigation management zones. *Comput. Electron. Agric.* **2019**, *162*, 719–731. [CrossRef]
78. Davis, S.; Dukes, M. Irrigation scheduling performance by evapotranspiration-based controllers. *Agric. Water Manag.* **2010**, *98*, 19–28. [CrossRef]
79. Beeri, O.; Netzer, Y.; Munitz, S.; Mintz, D.F.; Pelta, R.; Shilo, T.; Horesh, A.; Mey-tal, S. Kc and LAI Estimations Using Optical and SAR Remote Sensing Imagery for Vineyards Plots. *Remote Sens.* **2020**, *12*, 3478. [CrossRef]

Irrigation Science
https://doi.org/10.1007/s00271-021-00758-8

TECHNICAL BRIEF

Evaluating a novel microtensiometer for continuous trunk water potential measurements in field-grown irrigated grapevines

Vinay Pagay[1]

Received: 24 June 2021 / Accepted: 8 October 2021

Abstract

Water potential (Ψ_w) is a fundamental thermodynamic parameter that describes the activity of water and is a key metric of plant water status. In this paper, we evaluate the continuous measurement of water potential in grapevine trunks using a novel in situ sensor known as a 'microtensiometer' under field conditions in two South Australian vineyards. We characterised the seasonal and diurnal dynamics of trunk water potentials (Ψ_{trunk}) obtained from microtensiometers installed in two grapevine cultivars, Shiraz and Cabernet Sauvignon, and compared these values to pressure chamber-derived stem (Ψ_{stem}) and leaf (Ψ_{leaf}) water potentials. Diurnal patterns of Ψ_{trunk} matched those of Ψ_{stem} and Ψ_{leaf} under low-vapour pressure deficit (VPD) conditions, but diverged under high-VPD conditions, where Ψ_{trunk} dropped below Ψ_{stem} in the late afternoon. Interestingly, under high-VPD conditions, Ψ_{trunk} values consistently dropped below Ψ_{stem} values around mid-afternoon with a recovery observed by early evening. The highest diurnal values of Ψ_{trunk} were observed shortly after dawn. Ψ_{stem} was better correlated with Ψ_{trunk} than was Ψ_{leaf} in both cultivars. Time cross-correlation analysis revealed that Shiraz Ψ_{trunk} lagged Cabernet Ψ_{trunk} in response to changing VPD. Microtensiometer-derived Ψ_{trunk} generally matched the seasonal and diurnal patterns of plant Ψ_w obtained with a pressure chamber except under high-VPD conditions. To be useful for irrigation scheduling, where absolute values of Ψ_w are required, crop- and cultivar-specific thresholds of Ψ_{trunk} need to be developed.

Introduction

Measurements of crop water status, which are essential for optimised irrigation scheduling, have historically relied on low throughput and high cost instruments, and labour intensive methods, that have decreased their utility and uptake by the farming community. One such method widely established to reliably quantify plant water status is the manual measurement of leaf or stem water potential (Shackel 2011; Williams and Baeza 2007), using a Scholander pressure chamber invented in the 1960s (Scholander et al. 1965). To overcome some of the limitations of such manual techniques, several electronic plant-based sensors to continuously measure crop water status have recently been developed that are based on various sensing modalities. These include sap flow sensors (Ginestar et al. 1998), thermal diffusivity sensors (Pagay and Skinner 2018), dendrometers (Corell et al. 2014), and thermal or infrared sensors (Jones 1999). A recent review of several of these sensors as applied in tree fruit crops can be found in Scalisi et al. (2017).

Given the prevalence of water potential as a reliable crop water status metric, sensors to measure plant water potential have also been developed. These sensors, known as hygrometers or psychrometers, provide continuous measurements of water potential either as contact sensors on leaves or in situ sensors embedded in stems (Dixon and Tyree 1984; McBurney and Costigan 1984; Michel 1977). Hygrometers measure the water potential of the vapour phase. They are prone to significant errors due to the requirement of isothermal conditions between the measurement junction and plant tissue (Dixon and Tyree 1984). A 1 °K temperature difference between the plant tissue and sensor can result in a water potential error of over 7.7 MPa (Dixon and Tyree 1984). Much like stem hygrometers, other in situ sensors embedded in the stems or trunks include those that measure the osmotic potential of the xylem tissue and calibrated to stem water potential (Meron et al. 2015). The osmotic potential sensor requires proper fluidic contact between the sensor and the plant tissue, as well has long transients (order hours) associated with the measurement.

✉ Vinay Pagay
vinay.pagay@adelaide.edu.au

[1] School of Agriculture, Food and Wine, Waite Research Institute, The University of Adelaide, PMB 1, Glen Osmond, Adelaide, SA 5064, Australia

Tensiometers measure the water potential of an external matrix by equilibrating an internal, constant volume of water whose hydrostatic pressure is taken as the negative of the external water potential. Tensiometers were originally developed for measurement of soil matric potential (Richards 1942) and have been used for irrigation scheduling of crops (Cormier et al. 2020). Based on this principle, Pagay et al. (2014) developed MEMS-based tensiometers, so-called 'microtensiometers' (MT), for rapid measurements of the water potential of an external matrix. The MTs were previously shown to operate reliably down to below − 10 MPa with short transients (equilibration or response times) of ~ 20 min. This measurement range and temporal resolution makes the sensors valuable for not only crop and soil water status monitoring, but also other contexts including meteorology, concrete curing and food processing, and other systems where the internal water status is required. Subsequent improvements on the original MT design for improved transients (faster response times) were made by Black et al. (2020). This second-generation microtensiometer was used for both in situ and ex situ measurements of water potential in a range of matrices, including foods.

This paper presents the first results of field experiments with MTs, embedded water potential sensors, in mature, irrigated grapevines in a Mediterranean climate. We compared the dynamic MT responses of plant water potential to values of leaf and stem water potentials as measured by the Scholander pressure chamber over both long-term and short-term (diurnal) periods. Our goal was to validate the use of MTs in a field context under dynamic environmental conditions.

Materials and methods

Experimental site and plant material

Two commercial vineyard blocks located in the Coonawarra region of South Australia (37.29° S, 140.83° E) were selected for the trial. One block was planted in 1988 to *Vitis vinifera* cv. Cabernet Sauvignon grafted onto Schwarzmann rootstock, while the second block was planted in 2013 to *V. vinifera* cv. Shiraz (syn. Syrah) grafted onto Teleki 5C rootstock. Both vineyards were situated within 5 km of each other and planted over the dominant 'terrarossa' soil, characterised by a distinctive red-brown, thick, clay B horizon soils overlying limestone, the depth to which is variable. In each vineyard, three adjacent vines per cultivar were selected for measurements, and additionally, the middle vine for continuous monitoring of soil and plant water status (see details below). Row and vine spacing was 2.75 m × 2.2 m. Vineyard management and integrated pest management were applied to both blocks as per convention in the region for premium wine grape production.

Irrigation was applied using a single drip line (ϕ = 21 mm) with pressure compensating emitters spaced 0.6 m apart, so each vine had approx. 3.7 drippers. The output of these emitters was 1.56 L h^{-1}. Therefore, each vine would receive approx. 5.7 L h^{-1}. Irrigation was applied weekly starting in mid-December and ranged from 3.3 mm to over 16 mm per week during the warmest period of the summer that typically included heatwaves. Irrigation decisions were made by the commercial vineyard operator that were based on a combination of historical experience, weather forecasts, and soil moisture capacitance probes where volumetric water content values were maintained over 22%. This threshold soil moisture level was based on historical experience in the vineyard block and soil type to minimise vine water stress, especially during heatwaves, which are common in the region during the growing season.

Environmental monitoring and climatic conditions

Environmental (weather) data for the vineyard blocks were obtained from the Coonawarra automatic weather station (AWS) maintained by the Australian Bureau of Meteorology (BOM), Station ID: 026091. The AWS was located approx. 200 m from the Cabernet Sauvignon vineyard and approx. 5 km from the Shiraz vineyard. Daily maximum air vapour pressure deficit (VPD) was calculated using maximum temperature and minimum relative humidity (RH) daily data. The long-term (20-year) mean January temperature (MJT) for Coonawarra is 19.3 °C and the growing degree days (GDD; base 10 °C; October–April) is 1511. The climate of the area is characterised as Mediterranean, with winter dominant rainfall and relative summer drought. Average annual rainfall for Coonawarra is approx. 569 mm (Bureau_of_Meteorology 2021). Supplemental irrigation is typically required from December until March. The elevation of the region is between 57 and 63 m above sea level.

Soil moisture measurements

Of the three sentinel adjacent vines in each cultivar/block, the middle vine was selected for continuous monitoring of soil moisture, temperature and electrical conductivity using a capacitance-based sensor (Model: Teros-12, Meter Group, Pullman, WA, USA) buried approx. 30 cm below the surface and approx. 10 cm from the trunk of the vine in the vine row. The hourly sensor data were wirelessly transmitted via telemetry to a Cloud-based server and visually displayed on a user interface (Greenbrain, Measurement Engineering Australia, Adelaide, SA, Australia).

Plant water status measurements

Leaf stomatal conductance

In each block, leaf stomatal conductance (g_s) was measured on the three sentinel vines per cultivar between 1200 and 1300 h. Measurements were performed on one fully expanded, healthy leaf per vine using an open system infrared gas analyser (IRGA; LI-6400XT, LI-COR Biosciences Inc., Lincoln, NE, USA) with a 6 cm^2 cuvette. An external LED light source (LI-6400-02B) attached to the cuvette was used at a fixed PAR value of 1500 µmol m^{-2} s^{-1} due to the sometimes variable ambient light levels. The cuvette gas flow rate was set at 400 µmol s^{-1} and reference CO_2 was set to 400 ppm. The cuvette and leaf temperatures were at ambient (uncontrolled), while cuvette relative humidity with the leaf inserted was maintained within a range of 35–55%. IRGA measurements were conducted diurnally (every 2 h between 0800 and 2000 h) on 2 days of contrasting VPDs—high VPD (February 17, 2021; max VPD ~ 6 kPa) and low VPD (January 26, 2021; max. VPD ~ 1.7 kPa)—that were typical of a Mediterranean region.

Leaf and stem water potentials

In each block, midday stem (Ψ_{stem}) and leaf water potentials (Ψ_{leaf}) were measured on adjacent mature leaves of the same shoot between the hours of 1200–1300 using a Scholander pressure chamber (Soil Moisture Equipment Corp., Santa Barbara, CA, USA). For Ψ_{stem} measurements, leaves were bagged using an opaque aluminium-lined bag for a minimum of 1 h prior to measurement to stop transpiration and allow for equilibration of water potentials between the leaf and shoot (stem). Measures of Ψ_{leaf} and Ψ_{stem} were performed on one leaf per vine from the three sentinel vines in each block/cultivar. Leaf and stem water potentials were measured diurnally on the two measurement days concurrently with IRGA measurements. The same leaf used for g_s measurement with the IRGA was used to measure Ψ_{leaf}.

Trunk water potentials

On December 12, 2020, a total of four microtensiometers (MT; FloraPulse, Davis, CA, USA) were embedded into the trunks of the grapevines, two MTs per vine per cultivar. Readers are referred to Pagay et al. (2014) for a detailed description of the theory of tensiometry, and to Black et al. (2020) for technical details of the MT sensor design, fabrication, calibration, and lab testing results (performance under controlled conditions). Two MTs (Fig. 1a) were embedded into each trunk of a woody, mature grapevine per cultivar. Sensor installation consisted of the following steps: (1) removal of bark on a flat section of the trunk; (2) removal

(a)
(b)
(c)

Fig. 1 **a** Close-up view of an individual microtensiometer showing the stainless steel packaging surrounding a protruding sensor chip. The tip of the chip consists of the nanoporous silicon membrane that allows for equilibration of water potentials between the exterior matrix and internal water; (**b**) MTs installed in a grapevine trunk within a stainless steel sleeve filled with kaolin mating compound; (**c**) background: MT batting and reflective film to minimise temperature effects on water potential measurements of the sensor; foreground: dataloggers and wireless transmitters of the MT (bottom unit, white box) and soil moisture sensor (top unit, red base)

of phloem tissue using a cork borer and spatula/blade; (3) insertion of a custom stainless steel sleeve (Fig. 1b; OD: 14 mm, ID: 9 mm) using a hammer; (4) drilling into the sleeve approx. 5 cm into the trunk (within xylem tissue) and

Fig. 2 Seasonal patterns of (**a**) vapour pressure deficit (VPD), (**b**, **c**) total water incident (irrigation + precipitation), (**d**) soil moisture (as volumetric water content, VWC), and (**e**) trunk water potentials (Ψ_{trunk}) for Cabernet Sauvignon and Shiraz grapevines during the 2020–21 season. Approximate phenological stages shown on top of VPD graph: *FL* = flowering; *BC* = bunch closure; *V* = veraison; *PH* = approx. one week pre-harvest ▸

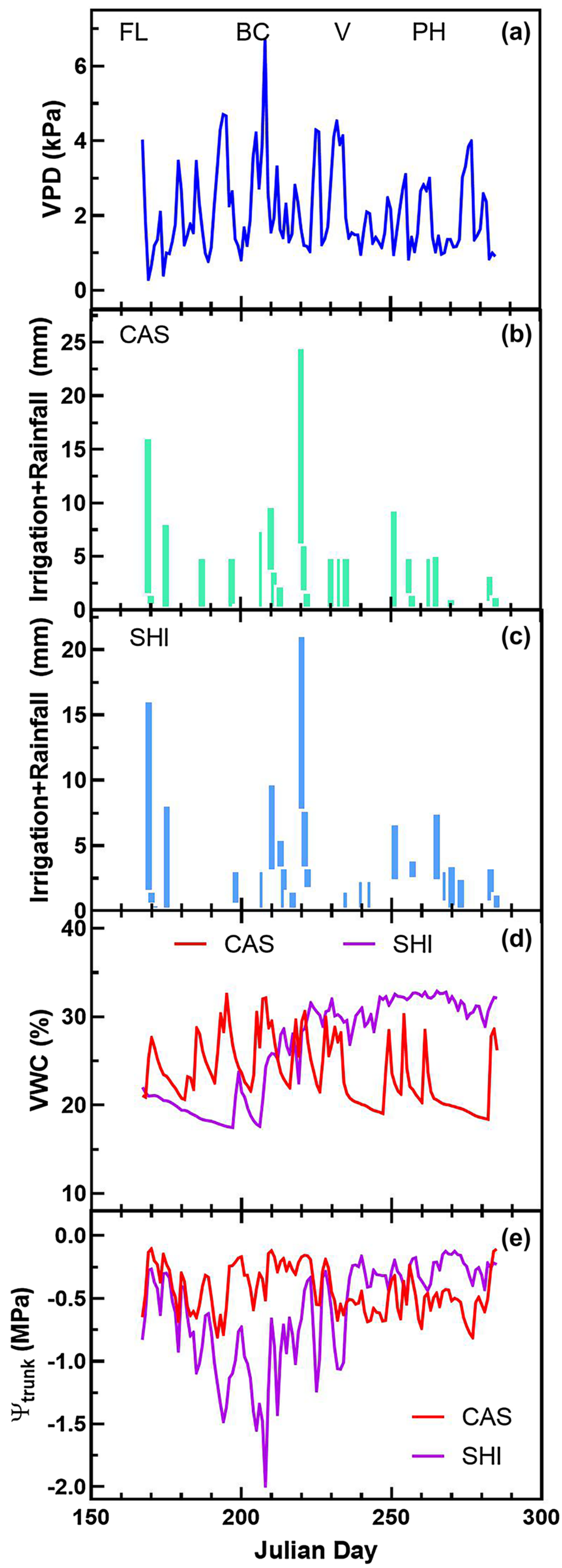

removing tissue; (5) filling the cavity with a kaolin-based mating compound; (6) inserting the hydrated MT into the mating compound; (7) placing a stainless steel cap to close the sleeve; (8) covering the sleeve exterior at the trunk with silicone to ensure air and water proofing; (9) wrapping plastic film around the sensor followed by a 25-mm-thick foam batting with reflective aluminium film to minimise exterior temperature fluctuations to the sensors (Fig. 1c). The sensors equilibrated with the vine (through the mating compound) within 2 days of installation. The MT data of trunk water potential (Ψ_{trunk}; value averaged for both sensors) were obtained every 20 min wirelessly transmitted via telemetry to a Cloud-based server (Amazon Web Services, USA) and visually displayed on a user interface (FloraPulse, Davis, CA, USA).

Statistical analyses

Time-lagged cross-correlation (TLCC) analysis was used in MATLAB programing software (v.9.8.0, R2020a, The MathWorks, Inc., Natick, MA, USA) to analyse the continuous (20-min interval) data of VPD and Ψ_{trunk} over the course of 2 days with contrasting VPDs: January 26, 2021 (low-VPD day; daily max. VPD ~ 1.6 kPa) and February 17, 2021 (high-VPD day; daily max. VPD ~ 6.7 kPa). TLCC analysis involves determining the correlations between two time series datasets that are shifted in time (Chatfield and Xing 2019), and repeatedly calculating Pearson Product Moment Correlation (cross-correlation) Coefficient (XCC) after each shift (Cheong 2020). Resulting 'offset' values, which when selected at the highest normalised XCC in the series, indicate the time shift (lag or advancement) of a particular time series compared to the other. Time shifts were selected such that they aligned with the VPD and Ψ_{trunk} measurement interval of 20 min; therefore, each offset represented 20 min.

Results

Seasonal patterns

Seasonal patterns of environmental conditions (VPD, rainfall + irrigation), soil moisture, and vine water status (Ψ_{trunk}), as measured by the microtensiometers, are shown in Fig. 2. In general, soil moisture levels correlated strongly to water incident in both vineyard, and in many cases inversely with

VPD. Microtensiometer responses (Ψ_{trunk}) reflected both soil moisture and atmospheric demand. Under high-VPD conditions, e.g. Julian Day (JD) 208 when the maximum VPD was approx. 6.7 kPa, Ψ_{trunk} values dropped by 0.2 and 0.5 MPa in Cabernet and Shiraz grapevines, respectively, despite stable or even higher soil moisture levels. Based on linear regression modelling using the same dataset to predict Ψ_{trunk} from VWC and VPD, the following relationships were obtained for CAS and SHI ($n = 119$):

$$\Psi_{trunk,CAS} = -0.983 - (0.109 \times VPD) + (0.033 \times VWC)\ (P < 0.0001)$$

$$\Psi_{trunk,SHI} = -1.187 - (0.212 \times VPD) + (0.039 \times VWC)\ (P < 0.0001)$$

The model results indicate that, while soil moisture has a similar influence on Ψ_{trunk} in both cultivars, Shiraz was more sensitive to VPD than Cabernet Sauvignon.

Seasonal courses of pre-dawn (leaf), stem and trunk water potentials are shown in Fig. 3 for Shiraz and Cabernet grapevines. In Shiraz, Ψ_{pd} values showed a declining trend over the season from JD 167, coinciding with the fruit set phenological stage until bunch closure (JD 196) followed by a recovery until harvest (Fig. 3a). This trend was matched by both Ψ_{trunk} and Ψ_{stem} albeit at lower absolute values of water potential. The lowest value of Ψ_{trunk} was observed around bunch closure at approx. −0.7 MPa. For Cabernet, the Ψ_{pd} value remained relatively stable until veraison (JD 261) when the value dropped from −0.2 MPa to −0.5 MPa by harvest (Fig. 3b). This was matched by a continually declining Ψ_{stem}, which reached a minimum of −0.9 MPa by harvest. Interestingly, the trend in Ψ_{trunk} appeared to remain fairly stable until JD 260 and then stabilised in the post-veraison period.

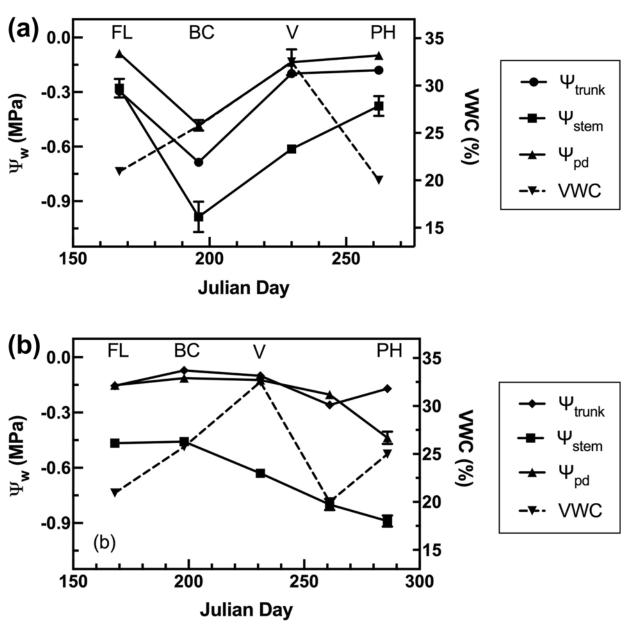

Fig. 3 Seasonal patterns of trunk (Ψ_{trunk}), stem (Ψ_{stem}), pre-dawn leaf (Ψ_{pd}) water potentials, and soil volumetric water content for (**a**) Shiraz and (**b**) Cabernet Sauvignon grapevines during the 2020–21 season. Data shown are for a single measurement vine per cultivar in which the pair of MTs was installed. Approximate phenological stages shown on top of each graph: *FL* = flowering; *BC* = bunch closure; *V* = veraison; *PH* = approx. 1 week pre-harvest

Diurnal patterns of environment and vine water status

Measurements of environmental conditions and vine water status were made over the course of 2 days, one with high vapour pressure deficit (VPD) and the other with low VPD, during the 2020–21 growing season from 0800 to 2000 h. The low-VPD day, January 26, 2021, was characterised by sunny and cool conditions, with the daily maximum temperature reaching just over 23 °C with a maximum VPD of 1.7 kPa at around 1400 h (Fig. 4a, g). On the high-VPD day, February 17, 2021, maximum daily temperature was nearly 37 °C and maximum VPD was approx. 6.0 kPa (Fig. 4d, j). The average soil volumetric water content (VWC) on the two measurement days were 24.0% and 30.6% on January 26 and February 17, respectively, in Shiraz; in Cabernet Sauvignon the VWC values were 28.3% and 30.3% on January 26 and February 17, respectively.

Under low-VPD (~ 1.7 kPa) conditions, Shiraz grapevines had Ψ_{trunk}, Ψ_{stem}, and Ψ_{leaf} daily average minimum values of −0.66, −0.96, and −1.30 MPa, respectively (Fig. 4b). Under high-VPD (~ 6 kPa) conditions, Shiraz grapevines dropped their Ψ_{trunk}, Ψ_{stem} and Ψ_{leaf} values to −1.1, −0.7, −1.5 MPa, respectively (Fig. 4e), which were considerably lower than during the low-VPD day. Under high-VPD conditions in both cultivars, patterns of plant water potential (Ψ_w) early in the day were similar to the patterns observed during the low-VPD day; the values of Ψ_w followed the expected order of $\Psi_{trunk} > \Psi_{stem} > \Psi_{leaf}$ during the morning. However, a distinct shift in the pattern of Ψ_{trunk} was observed after approx. 1400 h: Ψ_{trunk} dropped below Ψ_{stem}, reaching a minimum of −1.06 MPa around 1800 h, matching values observed for Ψ_{leaf}. In comparison, Ψ_{stem} at the same time (1800 h) was −0.47 MPa. There was a noticeable recovery (increase) in Ψ_{trunk} that started soon after 1800 h, matching the values of Ψ_{leaf} during this period late in the day (1800 h–2000 h). Under the same (high VPD) conditions, patterns of Cabernet Sauvignon Ψ_w were similar to that of Shiraz. Cabernet had large differences between Ψ_{trunk}, Ψ_{stem} and Ψ_{leaf} early in the day, and these reached their minimum values of − 0.67, − 0.76, and − 1.5 MPa, respectively, between 1400 and 1600 h (Fig. 4k). Much like Shiraz under similar (high VPD) conditions, there was a distinct crossing over of Ψ_{trunk}

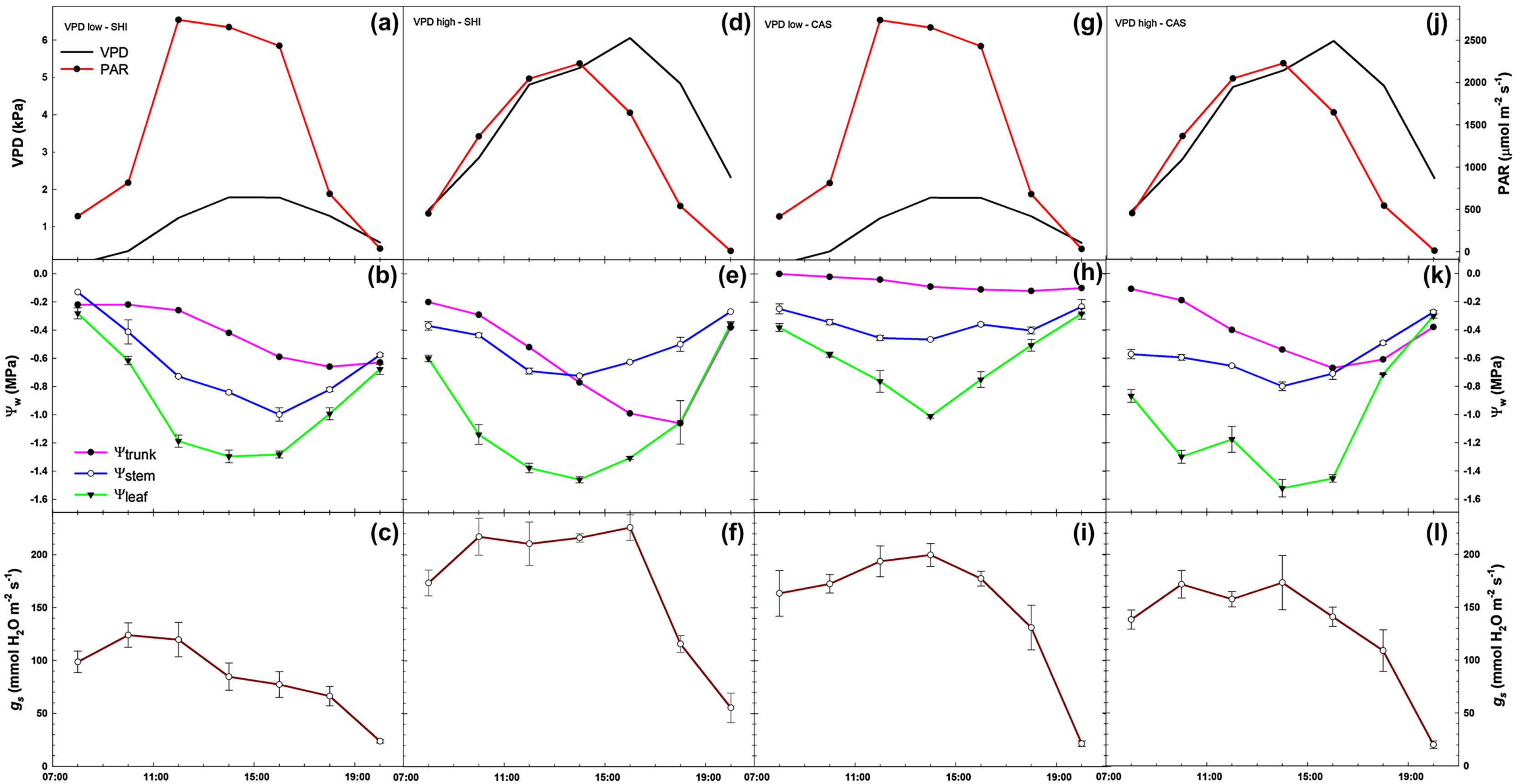

Fig. 4 Diurnal patterns of VPD, PAR, trunk (Ψ_{trunk}), stem (Ψ_{stem}), leaf (Ψ_{leaf}) water potentials, and leaf stomatal conductance (g_s) on low- and high-VPD days for Shiraz (SHI) and Cabernet Sauvignon (CAS) grapevines

and Ψ_{stem} around 1600 h; Ψ_{trunk} dropped to values below Ψ_{stem}, remaining in this position until the end of the day.

Leaf stomatal conductance (g_s) was measured concurrently with Ψ_w measurements, and on the same leaf used to measure Ψ_{leaf}. Patterns of g_s mirrored Ψ_w in both cultivars and across both measurement days under contrasting environmental conditions. In Shiraz, average g_s values were highest early in the day, peaking around 124 mmol H_2O m^{-2} s^{-1} at 1000 h under low-VPD conditions, and considerably higher around 235 mmol H_2O m^{-2} s^{-1} also at 1000 h under high-VPD conditions (Fig. 4c,d). Under high-VPD conditions, however, there was a precipitous decline in g_s after 1600 h down to similar values observed under low-VPD conditions by late day (2000 h).

Relationships between leaf, stem and trunk water potentials

Correlation analysis between various vine water potential metrics was performed to validate the Ψ_{trunk} data from the microtensiometers versus the pressure chamber-derived established metrics, Ψ_{leaf} and Ψ_{stem}. To search for robust relationships between water potential metrics for the individual cultivars, linear regression analysis was done for the combined dataset of both cultivars (Fig. 5). For Ψ_{trunk} vs. Ψ_{leaf} (Fig. 5a), the slope was approx. 0.4 ($R^2 = 0.21$), while for Ψ_{trunk} vs. Ψ_{stem} (Fig. 5b), the slope was higher at approx. 0.95 with higher correlation coefficients ($R^2 = 0.45$) and a greater agreement between the two metrics compared to Ψ_{trunk} vs. Ψ_{leaf} as indicated by the slope similarity to the 1:1 line.

Trunk water potential sensitivity to VPD

The relationships between VPD and Ψ_{trunk} for Cabernet and Shiraz for the period December 14, 2020 to February 10, 2021 (0600–2000 h) are presented in Fig. 6. There was a significant difference between cultivars in the sensitivity of vine water status to VPD (as indicated by the slopes of the regression lines) during the 2-month peak summer period. Shiraz was more sensitive than Cabernet to changes in atmospheric conditions, dropping its Ψ_{trunk} by approx. 0.17 MPa kPa^{-1}. In comparison, Cabernet reduced its Ψ_{trunk} by approx. 0.07 MPa kPa^{-1}.

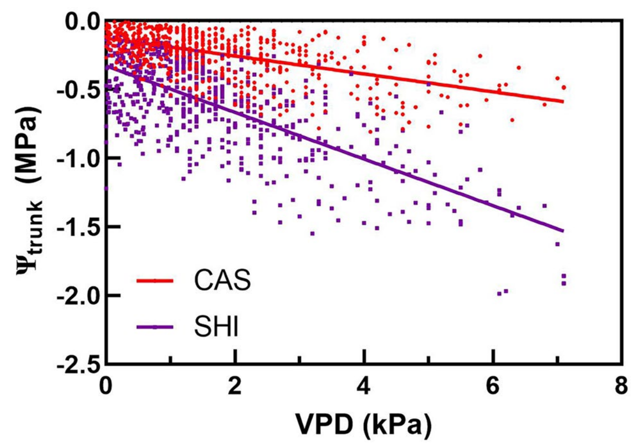

Fig. 6 Linear regression analysis of VPD vs. Ψ_{trunk} of Shiraz and Cabernet Sauvignon grapevines over the measurement period. Regression equations: Shiraz: $\Psi_{trunk} = -0.3272 - 0.1696 * VPD$, $R^2 = 0.51$; Cabernet Sauvignon: $\Psi_{trunk} = -0.1247 - 0.065 * VPD$, $R^2 = 0.33$. P value for differences between the slopes: < 0.001

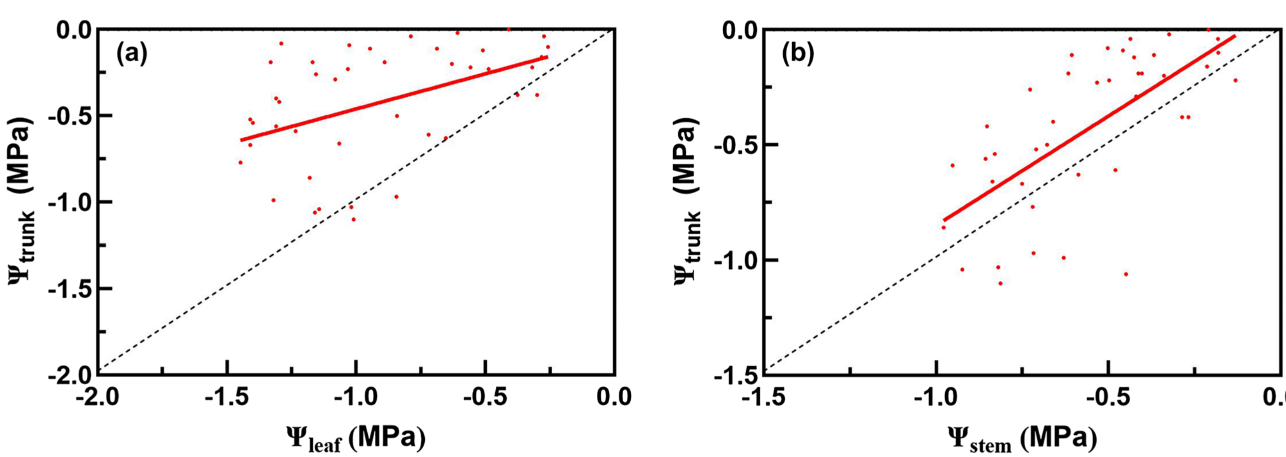

Fig. 5 Correlation analysis between trunk water potential (Ψ_{trunk}) and (**a**) leaf water potential (Ψ_{leaf}) and (**b**) stem (Ψ_{stem}) water potentials for both cultivars combined (slopes of individual cultivar regressions not significantly different). Regression equations: $\Psi_{trunk} = (\Psi_{leaf} * 0.4072) - 0.0531$, $R^2 = 0.21$ ($P = 0.0022$); $\Psi_{trunk} = (\Psi_{stem} * 0.9505) + 0.1003$, $R^2 = 0.45$ ($P < 0.0001$). Diagonal dotted line represents 1:1 line

Time-lagged cross-correlation analysis (TLCC) was used to analyse the time series datasets of VPD and Ψ_{trunk} across 2 days with contrasting environmental conditions or VPDs. Under low-VPD conditions (January 26, 2021; VPD ~ 1.7 kPa), TLCC analysis between VPD and Ψ_{trunk} revealed that CAS had the minimum Pearson Product Moment (normalised cross-correlation) coefficient of −180 min indicating that Ψ_{trunk} lagged VPD by 180 min. under similar (low VPD) conditions, Shiraz Ψ_{trunk} lagged VPD by 220 min. On the high-VPD day (February 17, 2021; VPD ~ 6.7 kPa), TLCC analysis revealed that CAS Ψ_{trunk} lagged VPD by 80 min while Shiraz Ψ_{trunk} lagged VPD by 120 min, both lower than the time lags observed on the low-VPD day.

Discussion

Seasonal and diurnal patterns of vine water status

In the present study, seasonal and diurnal measurements were made using MTs in Shiraz and Cabernet Sauvignon field-grown grapevines. Seasonal patterns of Ψ_{trunk} were typical of crop water potentials observed in several Mediterranean crops under supplemental irrigation (McCutchan and Shackel 1992; Williams et al. 2012) with a gradual increase of vine water stress over time. In the case of Shiraz, the steep decline observed leading up to JD 196 (Fig. 3a) resulted from a faulty valve in the sub-main irrigation line, which upon subsequent repair improved soil moisture levels and vine water status. Cabernet Ψ_{trunk} stabilised after veraison and could be related to the increase in soil moisture during this period coupled with warmer and drier conditions.

Our diurnal observations indicated that the lowest Ψ_{leaf}, Ψ_{stem}, and Ψ_{trunk} were reached around 1400 h, 1600 h and 1800 h, respectively, on low-VPD days, whereas these times were advanced on the high-VPD day, particularly for Ψ_{stem} and Ψ_{trunk}. Williams and Baeza (2007) suggested that the influence of VPD on Ψ_{leaf} decreases as soil moisture decreases. Modelling of diurnal patterns of Ψ_{leaf} predicted that the lowest values are likely to be reached around 1400 h, approx. 2 h after the highest leaf transpiration rates are reached (Katerji et al. 1986). This transient (or delay) in Ψ_{leaf} response can be attributed to the contributions of both plant tissue water and root uptake of soil moisture to the transpiration stream. These modelled patterns compare favourably with those obtained from lysimeters; maximum transpiration rates were reached between 1200 and 1400 h (Williams et al., 2012). The same study found that higher vine sizes or crop factors result in not only increased transpiration rates, as expected, but also a delayed peak by as much as 2 h. Similar patterns of vine transpiration were observed in studies using sap flow and thermal dissipation sensors (Braun and Schmid 1999; Pagay and Skinner 2018). The diurnal measurements of leaf stomatal conductance (g_s) in the present study indicated that the highest values were reached in the afternoon on low-VPD days and late morning on high-VPD days. Reductions in g_s following this peak resulted in increases in Ψ_{leaf} and Ψ_{stem}, but not Ψ_{trunk}. This lack of response from Ψ_{trunk} might indicate a level of buffering of water potential in the woody organs of the plant, in this case the trunk, where xylem vessels are surrounded by parenchymal cells that can contribute water to the transpiration stream, the so-called ‘capacitance effect’ (Salomón et al. 2017; Waring and Running 1978).

The highest diurnal Ψ_{trunk} observed in the present study was reached in the early morning, between 0700 and 0800 h, which is consistent with another study reporting that Ψ_{stem} does not start decreasing from its maximum diurnal value until the early morning, approx. 0700 h (Cole and Pagay 2015), but in contrast to another report that Ψ_{pd} decreases from 0330 h (Carbonneau et al. 2004). The observation has implications for the timing of measurement of Ψ_{pd}, if used as a metric for crop irrigation scheduling as recommended previously (Stricevic and Caki 1997). Donovan et al. (2001) found that Ψ_{pd} and Ψ_{p} in several woody plants may not reflect Ψ_{m} even under well-watered conditions without nocturnal transpiration. This was hypothesised to be due to the accumulation of high concentrations of solutes in the leaves, although grapevines have only modest levels of osmotic adjustment compared to many other woody horticultural crops (Rodrigues et al. 1993).

The use of trunk water potential for irrigation scheduling

MTs offer yet another plant water status metric, Ψ_{trunk}, that has been shown in this study to have a different range of values compared to conventional measures of Ψ_{leaf} and Ψ_{stem}. These conventional metrics have been well characterised for irrigation scheduling and thresholds have been suggested in the literature (Deloire and Heyns 2011; Romero et al. 2010). Trunk water potential is arguably the most stable of these three metrics, integrating all the leaves of the plant in a stable tissue that is relatively unaffected by external factors as are Ψ_{leaf} and Ψ_{stem}. Our measurements of these three vine Ψ_{w} metrics indicated that, in some instances, Ψ_{trunk} tended to be nearly 1 MPa higher than Ψ_{leaf}, indicative of the high hydraulic resistances between the trunk and leaves. Previous reports have shown that the highest hydraulic resistance in this pathway lies in the leaf, representing as much as 30% of the overall resistance in the plant (Sack et al. 2003), likely due to the fewer and narrower xylem vessels in this section of the pathway compared to distal sections. We found a weak agreement between the absolute values of Ψ_{trunk} and Ψ_{leaf} and a slightly better agreement versus Ψ_{stem}. This indicates that practitioners require new thresholds of Ψ_{trunk} to use for irrigation scheduling. The Ψ_{trunk} was also susceptible to the least fluctuations diurnally, although this was only shown to be true under low-VPD conditions (Fig. 4). Its central location in the plant between the roots and leaves, as well as buffering of xylem water status (pressure potential) via capacitance from adjoining parenchymal cells and secondary xylem (Meinzer et al. 2009) would be plausible reasons for the stability of the trunk's water status. However, we observed that Ψ_{trunk} responded to changes in soil moisture (via irrigations) less rapidly than to changes in VPD (data not shown), which suggests that the trunk may be well-coupled to the leaves despite the high hydraulic resistances in the leaf petioles. A related and somewhat surprising observation was made under high-VPD conditions: we consistently observed the crossing over of the Ψ_{trunk} and Ψ_{stem} lines in the mid-afternoon (Fig. 4e, k). The lower Ψ_{trunk} value (compared to Ψ_{stem}) during warm afternoons indicates that the trunks of both cultivars were considerably more water stressed than the stems and similar to the leaves in the late afternoon. A plausible explanation for this response is that the roots may be under water stress owing to transient water deficits at the soil-root interface due to high transpiration rates under high-VPD conditions, as well a relatively significant hydraulic resistance between the trunk and stem. Pagay et al. (2016) reported that, under high-VPD conditions, low plant water potentials could result, if the capillary conductivity of soils in the rhizosphere is inadequate to support high canopy transpiration rates. Recent reports on the existence of localised positive pressures in the xylem due to a variety of factors including osmotic exudation and/or water contributed from neighbouring parenchymal cells (Schenk et al. 2020) further support the possibility that higher water potentials in the stem compared to the trunk may exist transiently and in a localised manner, particularly when transpiration rates are low. This hypothesis needs to be tested with additional experimentation.

Continuous measurements of Ψ_{trunk} using in situ microtensiometers, which were demonstrated in field-grown plants for the first time in this study, offers a convenient measurement of plant water status for irrigation scheduling. Furthermore, these in situ measurements of plant water potential provide a useful tool for physiological studies of plant hydraulics in a dynamic environment, for example, studies on the limiting water potentials of plants as well as those involving cavitation and embolism recovery dynamics. Microtensiometers are also amenable to automation, for example, to automate irrigation scheduling via a decision support system in which thresholds of Ψ_{trunk} are pre-programmed in irrigation controllers for various crop phenological stages and that also incorporate other relevant environmental parameters such as weather forecast and soil moisture data for precision irrigation. The use of published Ψ_{stem} or Ψ_{leaf} thresholds to drive irrigation decisions should be based on measurements of the specific metric for which the threshold has been developed; a translation of those values to Ψ_{trunk} would not be appropriate due to physiological, hydraulic and anatomical differences between plants. Further research is required to validate inter-sensor variation of Ψ_{trunk} within the same plant, long-term sensor performance and stability, as well as determining Ψ_{trunk} thresholds for irrigation scheduling.

Acknowledgements The author thanks the following individuals for assistance with the project: Dr Franziska Doerflinger (Plant and Food Research Australia), Dr Michael Santiago (FloraPulse), Mr Popolopoulos, Felipe Canela, and Rochelle Schlank. The project was supported by funding from Wine Australia (project: UA 1803-1.3), and in-kind support by Katnook Estate and Wynns Coonawarra Estate.

Data availability The data supporting the findings of this study are available upon request from the author.

Declarations

Conflict of interest The author declares that no conflict of interest exists.

References

Black WL, Santiago M, Zhu SY, Stroock AD (2020) Ex situ and in situ measurement of water activity with a MEMS tensiometer. Anal Chem 92:716–723

Braun P, Schmid J (1999) Sap flow measurements in grapevines (*Vitis vinifera* L.) - 1. Stem morphology and use of the heat balance method. Plant Soil 215:39–45

Bureau_of_Meteorology (2021) http://www.bom.gov.au/climate/averages/tables/cw_026091.shtml. (Date accessed: 03/04/2021). http://www.bom.gov.au/climate/averages/tables/cw_026091.shtml. (Accessed 03/04/2021)

Carbonneau A, Deloire A, Costanza P (2004) Leaf water potential meaning of different modalities of measurements. J Int Sci Vigne Vin 38:15–19

Chatfield C, Xing H (2019) The analysis of time series: an introduction with R. Chapman & Hall/CRC texts in statistical science series, Seventh edition. edn. CRC Press, Taylor & Francis Group, Boca Raton

Cole J, Pagay V (2015) Usefulness of early morning stem water potential as a sensitive indicator of water status of deficit-irrigated grapevines (*Vitis vinifera* L.). Sci Hortic-Amsterdam 191:10–14

Corell M et al (2014) Using band dendrometers in irrigation scheduling Influence of the location inside the tree and comparison with point dendrometer. AgricWater Manag 142:29–37

Deloire A, Heyns D (2011) The leaf water potentials principles, method and thresholds. Wineland Magazine technical yearbook, pp 129–131

Dixon MA, Tyree MT (1984) A new stem hygrometer, corrected for temperature gradients and calibrated against the pressure bomb. Plant Cell Environ 7:693–697

Donovan LA, Linton MJ, Richards JH (2001) Predawn plant water potential does not necessarily equilibrate with soil water potential under well-watered conditions. Oecologia 129:328–335

Ginestar C, Eastham J, Gray S, Iland P (1998) Use of sap-flow sensors to schedule vineyard irrigation. I. Effects of post-veraison water deficits on water relations, vine growth, and yield of Shiraz grapevines. Am J Enol Vitic 49:413–420

Jones HG (1999) Use of infrared thermometry for estimation of stomatal conductance as a possible aid to irrigation scheduling. Agric for Meteorol 95:139–149

McBurney T, Costigan PA (1984) Rapid oscillations in plant water potential measured with a stem psychrometer. Ann Bot-London 54:851–853

McCutchan H, Shackel KA (1992) Stem water potential as a sensitive indicator of water stress in prune trees (*Prunus domestica* L cv French). J Am Soc Hortic Sci 117:607–611

Meinzer FC, Johnson DM, Lachenbruch B, McCulloh KA, Woodruff DR (2009) Xylem hydraulic safety margins in woody plants: coordination of stomatal control of xylem tension with hydraulic capacitance. Funct Ecol 23:922–930

Meron M, Goldberg SY, Solomon-Halgoa A, Ramon G (2015) Embedded stem water potential sensor. In: Stafford (ed) Precision agriculture. Wageningen Academic Publishers, pp 527–532

Michel BE (1977) Miniature stem thermocouple hygrometer. Plant Physiol 60:645–647

Pagay V (2016) Effects of irrigation regime on canopy water use and dry matter production of 'Tempranillo' grapevines in the semi-arid climate of Southern Oregon, USA. Agric Water Manag 178:271–280

Pagay V et al (2014) A microtensiometer capable of measuring water potentials below-10 MPa. Lab Chip 14:2806–2817

Pagay V, Zufferey V, Lakso AN (2016) The influence of water stress on grapevine (*Vitis vinifera* L.) shoots in a cool, humid climate: growth, gas exchange and hydraulics. Funct Plant Biol 43:827–837

Pagay V, Skinner A (2018) Continuous *in situ* measurements of crop water stress in 'Shiraz' grapevines using a thermal diffusivity sensor. In: Herppich WB (ed) International symposium on sensing plant water status - methods and applications in horticultural science, vol 1197. Acta Hort pp 83–88

Podobnik B, Stanley HE (2008) Detrended cross-correlation analysis: a new method for analyzing two nonstationary time series. Phys Rev Lett 100

Richards LA (1942) Soil moisture tensiometer materials and construction. Soil Sci 53:241–248

Rodrigues ML et al (1993) Osmotic adjustment in water-stressed grapevine leaves in relation to carbon assimilation. Aust J Plant Physiol 20:309–321

Romero P, Fernandez-Fernandez JI, Martinez-Cutillas A (2010) Physiological thresholds for efficient regulated deficit irrigation management in winegrapes grown under semiarid conditions. Am J Enol Vitic 61:300–312

Sack L, Cowan PD, Jaikumar N, Holbrook NM (2003) The "hydrology" of leaves: co-ordination of structure and function in temperate woody species. Plant Cell Environ 26:1343–1356

Scalisi A, Bresilla K, Grilo F (2017) Continuous determination of fruit tree water-status by plant-based sensors. Italus Hortus 24:39–50

Schenk HJ, Jansen S, Hölttä T (2020) Positive pressure in xylem and its role in hydraulic function. New Phytol 230:27–45

Scholander PF, Hammel HT, Bradstreet ED, Hemmingsen EA (1965) Sap pressure in vascular plants: negative hydrostatic pressure can be measured in plants. Science 148:339–346

Shackel K (2011) A plant-based approach to deficit irrigation in trees and vines. HortScience 46:173–177

Stricevic R, Caki E (1997) Relationships between available soil water and indicators of plant water status of sweet sorghum to be applied in irrigation scheduling. Irrig Sci 18:17–21

Waring RH, Running SW (1978) Sapwood water storage: its contribution to transpiration and effect upon water conductance through the stems of old-growth Douglas fir. Plant Cell Environ 1:131–140

Williams LE, Baeza P (2007) Relationships among ambient temperature and vapor pressure deficit and leaf and stem water potentials of fully irrigated, field-grown grapevines. Am J Enol Vitic 58:173–181

Williams LE, Baeza P, Vaughn P (2012) Midday measurements of leaf water potential and stomatal conductance are highly correlated with daily water use of thompson seedless grapevines. Irrig Sci 30:201–212

Ground, Proximal and Remote Sensing Techniques for Precision Irrigation of Vineyards

Deepak Gautam [1], Vinay Pagay [1], Catherine Kidman [2], Stephen Tyerman [1], Bertram Ostendorf [3], Chris Brodie [4], Richard Muhlack [1], Kerry Wilkinson [1] and David Jeffery [1]

[1] School of Agriculture, Food and Wine , Waite Campus, the University of Adelaide, SA., [2] Treasury Wine Estates, Wynns Coonawarra Estate, Coonawarra, SA., [3] School of Biological Sciences, North Terrace Campus, the University of Adelaide., [4] Wingara Wine Group Pty Ltd, Katnook Coonawarra Estate, Coonawarra, SA.

THE UNIVERSITY of ADELAIDE

Australian Government

Wine Australia

Introduction

Precision irrigation to save water, make better wine, and increase the profitability of vineyards.

Test sites

Cabernet Sauvignon and Shiraz at Coonawarra, the premium wine region of South Australia, are studied.

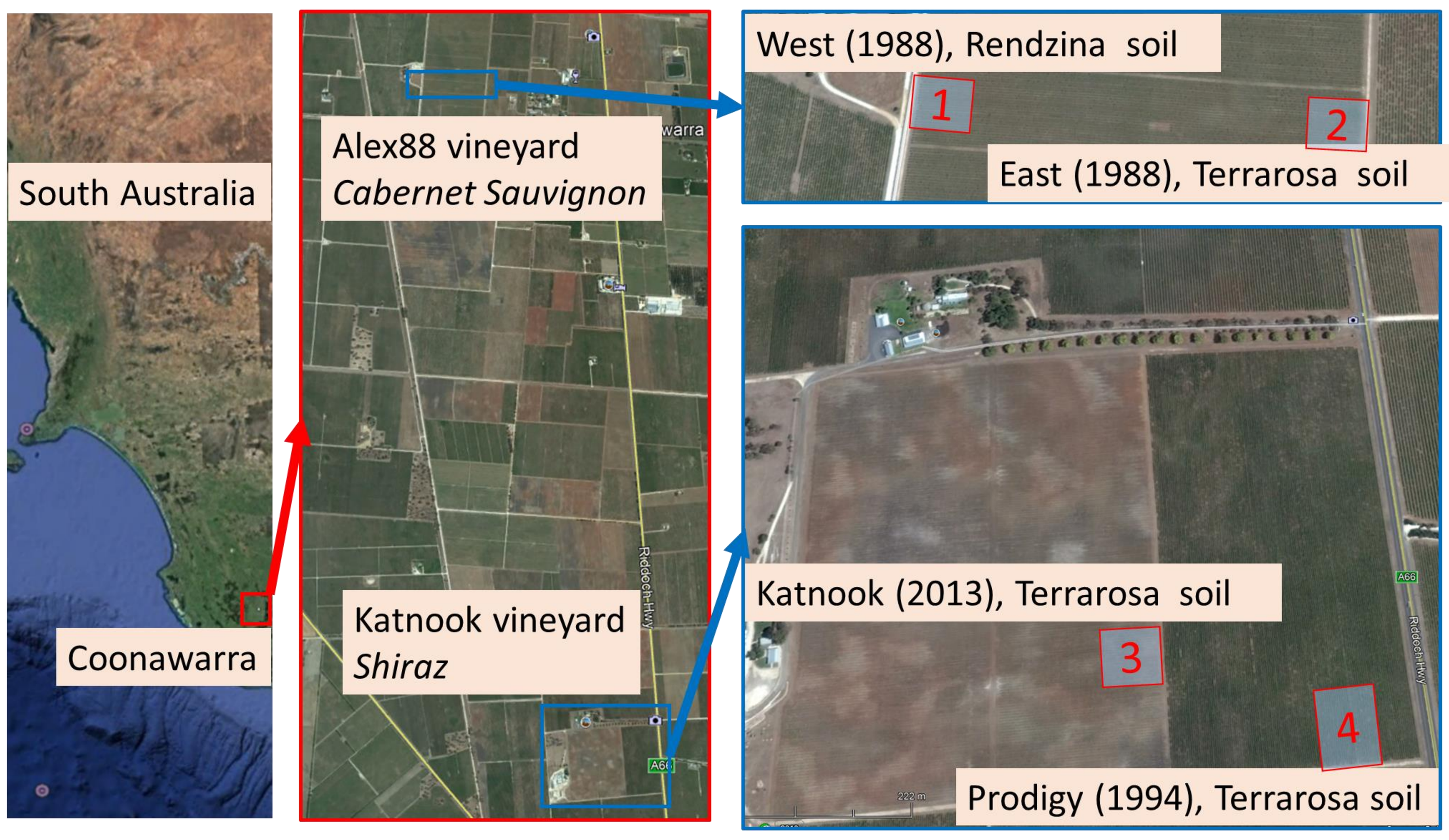

Experimental design

Each test site includes four irrigation treatments with two replication blocks.

Precision irrigation experimental design

Rows		Replication block #1								Replication block #2							
1																	
2		W	*	M	M	M	M					M	M	M	M		
3																	
4																	
5																	
6		W	*	M	M	M	M					M	M	M	M		
7																	
8																	
9																	
10		W	*	M	M	M	M					M	M	M	M		
11																	
12																	
13																	
14		W	*	M	M	M	M					M	M	M	M		
15																	
Vines->	1	2	3	4	5	6	7	8	9	10	11	12	13	14	15	16	17

M Measurement/sentinel vine
W Water meter
* Soil moisture sensor
Conventional treatment
Evapotranspiration treatment
Plant water status treatment
Soil water status treatment

The terrarossa soil type

Proximal and ground sensing

Using proximal and ground sensors, following measurements are made throughout the season: pre-dawn leaf water potential (ψ_{pd}), mid-day stem water potential (ψ_{stem}), canopy conductance (g_s), net photosynthesis (p_n), soil moisture, leaf area index (LAI), crop coefficient (k_c), porosity, canopy temperature, in bunch temperature, and meteorological data (daily temperature, humidity, precipitation, wind, solar radiation), etc.

Plant water status

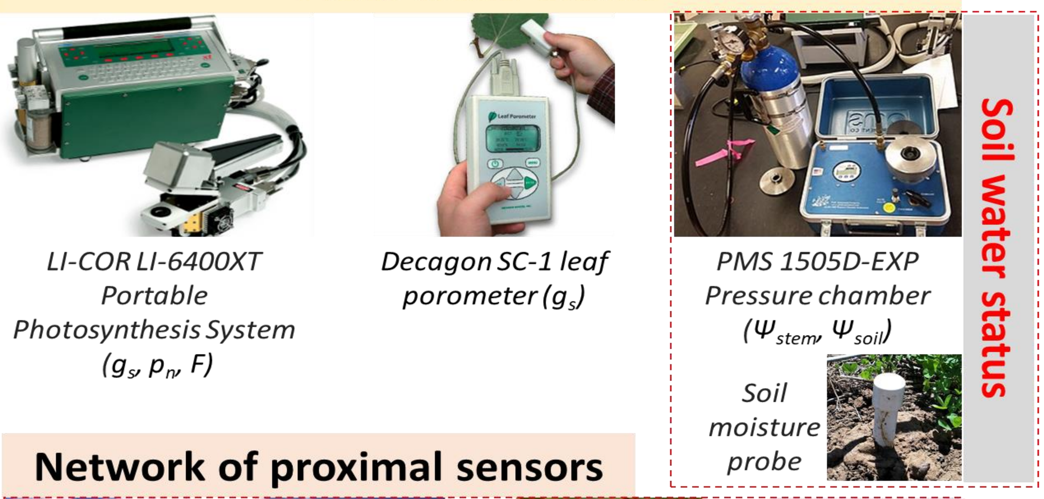

LI-COR LI-6400XT Portable Photosynthesis System (g_s, p_n, F)

Decagon SC-1 leaf porometer (g_s)

PMS 1505D-EXP Pressure chamber (Ψ_{stem}, Ψ_{soil})

Soil moisture probe

Soil water status

Light measurement

AccuPAR LP-80 ceptometer (porosity)

Paso panel (LAI, k_c)

Network of proximal sensors

Ground network of thermography towers via LoRaWAN gateway for cloud-based monitoring (RH%, Ambient T, Shade T)

Meteorological

Weather station (T, RH%, PAR, rain, wind)

Tinytag (RH%, T)

Remote sensing

Remote thermal and multispectral (including visible) data is acquired at critical phenology stages of the plant.

Platforms

DJI Matrice 600 Pro

Remote sensors

Sony Alpha 7R III

MicaSense RedEdge-M

FLIR Tau2 640

Map georeferencing

Custom GCPs

Surveying pegs

Multispectral/Thermal calibration

FFC blackbody

FLIR Fluke gun

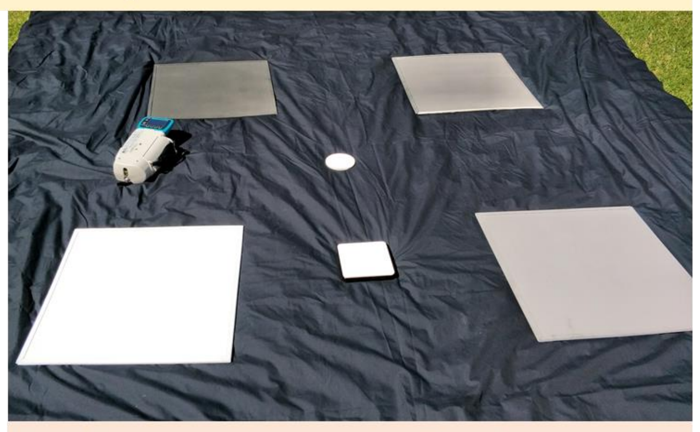

Multispectral/thermal calibration panels, spectralon and spectroradiometer

Data collection stages

1. Flowering

2. Peppercorn

3. Pea size

4. Pre-veraison

5. Veraison

6. Post-veraison#1

7. Post-veraison#2

8. Pre-harvest

Preliminary results (season 1)

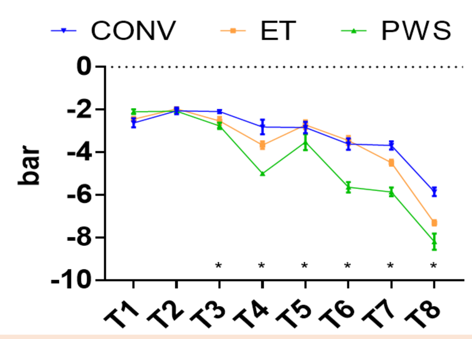

Seasonal pre-dawn ψ_{leaf}

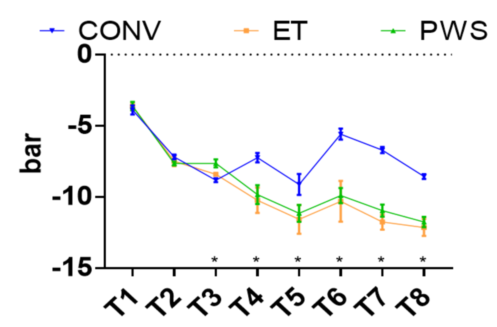

Seasonal mid-day ψ_{stem}

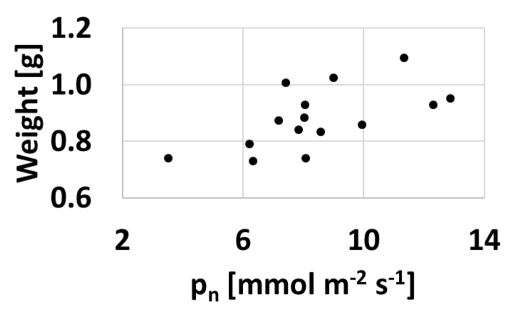

p_n vs berry weight

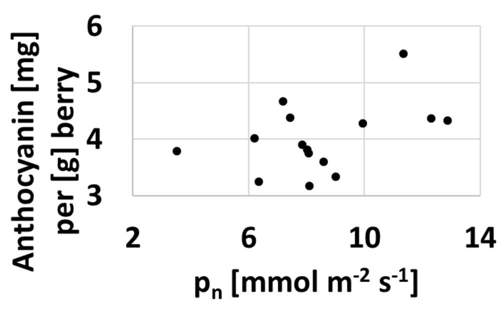

p_n vs berry anthocyanin

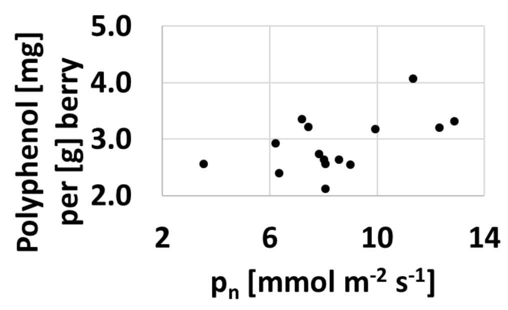

p_n vs berry polyphenol

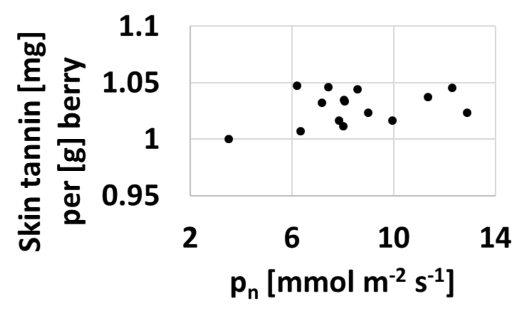

p_n vs berry skin tannin

Conclusion and future work

- The irrigation treatment appears to stand out at later season.
- The post-veraison net photosynthesis appears to be strong covariate of berry size and berry quality parameters.
- Thermal and multispectral remote sensing will be used to predict the water status, yield, and wine quality parameters
- Mechanistic and/or machine learning models will be incorporated with remote sensing for spatial/temporal prediction.

Get in touch

Dr Deepak Gautam
Email: Deepak.Gautam@adelaide.edu.au

References

1. Bellvert, J., Zarco-Tejada, P.J., Marsal, J., Girona, J., González-Dugo, V. and Fereres, E., 2016. Vineyard irrigation scheduling based on airborne thermal imagery and water potential thresholds. *Australian Journal of Grape and Wine Research*, *22*(2), pp.307-315.
2. Espinoza, C.Z., Khot, L.R., Sankaran, S. and Jacoby, P.W., 2017. High resolution multispectral and thermal remote sensing-based water stress assessment in subsurface irrigated grapevines. *Remote Sensing*, *9*(9), p.961.

Financial analysis of implementing different irrigation scheduling strategies in premium Cabernet Sauvignon grapevine in a cool climate Australian vineyard

Rochelle Schlank[1], Ying Xu[2] and Vinay Pagay[1*]

[1] School of Agriculture, Food and Wine, The University of Adelaide, Waite Research Institute, PMB 1, Glen Osmond, SA 5064, Australia

[2] School of Economics and Public Policy, The University of Adelaide, Adelaide, SA 5000, Australia

Acknowledgements: We thank Antoine Lespes, Caitlin Griffiths, Felipe Canela and Dilrukshi Nagahatenna for their assistance in the field data collection. R. S. acknowledges the financial support from the University of Adelaide in the form of a Research Training Stipend scholarship. This study was financially supported by Wine Australia (Grant number: UA 1803-1.3).

Short running title: Financial analysis of irrigation scheduling in vineyards

*Corresponding author.

Email address: vinay.pagay@adelaide.edu.au

Abstract

Background and Aims: To improve vineyard sustainability in increasingly arid conditions, optimising water use efficiency (WUE) has been proposed as an important target in scientific literature, and irrigation scheduling is another means by which WUE may be improved. To schedule irrigation, there are a wide variety of strategies available to vineyard operators. However, there is a need to investigate the costs associated with each of these approaches, particularly when considering the adoption of new technology.

Methods and Results: The financial returns associated with four different approaches (GROW, ET, PWS and SWS) to irrigation scheduling was investigated in a premium Cabernet Sauvignon vineyard in Coonawarra, South Australia over three growing seasons. Financial analysis showed scheduling using data driven metrics (ET, PWS and SWS) as having similar returns compared with scheduling carried out in the conventional (GROW) treatment, as demonstrated by statistically similar net present values (NPV). Though despite the lack of statistical significance, all financial indicators investigated in this study suggested scheduling using either an ET or PWS based approach to be associated with higher farm returns (compared with GROW). The impact of including a gross water price into production costs was also discussed, as water is principally sourced from underground aquifers in Coonawarra.

Conclusions: Data driven strategies were preferred when carrying out irrigation scheduling, as these strategies were associated with irrigation reductions, improvements in WUE and similar financial returns compared with the conventional approach.

Significance of the Study: This study highlights data driven strategies as financially feasible alternatives for irrigation scheduling in cool climate Australian vineyards.

Keywords: capacitance probe, evapotranspiration, infrared thermography, vitis vinifera, water use efficiency,

1. Introduction

Vineyard management strategies that enable grape growers to adapt to changing climatic conditions are essential for safeguarding the future of wine production in Australia. The wine industry plays an important role in the Australian economy, having contributed approximately $45 billion dollars in 2020. However, this contribution required over 496,300 ML of irrigation, representing just over 8% of Australia's agricultural water usage in 2019/2020 (Australian Bureau of Statistics, 2020). Modifying irrigation has previously been stated as one of the most effective tools to lessen the impact of reduced water availability and increase water use efficiency (WUE) in agriculture (Medrano et al., 2015, Naulleau et al., 2021). For this reason, as well as often observed improvements to berry quality and resulting wine (Chaves et al., 2010, Torres et al., 2022), deficit irrigation (DI) strategies are a common aspect of irrigation management in most Australian vineyards. DI refers to strategies that apply irrigation below a crop's full water requirements (Fereres and Soriano, 2007), and refers to approaches such as sustained deficit irrigation (SDI) (Fereres and Soriano, 2007), regulated deficit irrigation (RDI) (McCarthy et al., 2002) and partial rootzone drying (PRD) (Dry and Loveys, 1999). However, DI strategies need to be managed with appropriate plant water stress and irrigation thresholds in mind (i.e. irrigation scheduling) (Romero et al., 2010), in order to realise the full benefits associated with these techniques. Irrigation scheduling refers to the timing and volume of irrigation application and has been proposed as another means of improving WUE (Koech and Langat, 2018), particularly in horticultural crops, including grapevine (Fernández, 2017). Vineyard irrigation scheduling can be undertaken using several different strategies, and these strategies can be broadly categorised as those based on i) historical applications or experiential, ii) evaporative demand (e.g., crop evapotranspiration, ET_c), iii) plant water status thresholds, and iv) soil moisture (matric potential or volumetric water content) thresholds.

In Australian vineyards, carrying out irrigation scheduling using soil moisture thresholds is widely popular, particularly when it involves measuring volumetric water content (%VWC) (Nordestgaard, 2019). Monitoring %VWC typically involves using a variety of commercially available sensors and probes that can function either continuously or as a static measurement. The crucial challenge when using soil-based approaches for irrigation scheduling is in ensuring measurements are representative of the large spatial variation (i.e. differences in rooting depths or soil characteristics) that is often present in vineyards (Lebon et al., 2003). To overcome this variability, a large network of sensors (or probes) are often required, which may become cost prohibitive for some grape growers. Alternatively, irrigation scheduling using plant-based thresholds requires the irrigator to measure an aspect of plant physiology responsive to changes in plant water status. As an example, recent investigations highlighted stomatal conductance (g_s) as a highly sensitive indictor of water stress (Tuccio et al., 2019), a finding which has been emphasised previously (Jones, 2004). Canopy temperature has also been shown to be highly related to g_s due to the effect stomatal aperture has on leaf temperature (Jones et al., 2002) and techniques such as infrared thermography enable canopy temperature to be accurately monitored (Belfiore et al., 2019), with specific indexes that relate g_s to canopy temperature also available (Petrie et al., 2019). Similar to other plant-based approaches, adequately capturing vine-vine variability while avoiding the need for labour intensive measurements and high equipment costs can pose a challenge when using these methods. Though despite this, plant-based methods are still considered to be the most accurate representation of plant water status compared with other forms of irrigation scheduling (Shackel, 2011). As an alternative to sensor driven approaches, irrigation scheduling based on evaporative demand (evapotranspiration, ET) is another method available to growers. ET-based scheduling involves the estimation of a crop's water loss (crop evapotranspiration, ET_c) over a specific period of time (either daily or weekly) and then replacing a fraction of or all of this water. Calculating this water loss is most commonly undertaken using the Penman-Monteith energy balance model (Allen et al., 1998). The major benefit in using this approach is the ability to numerically determine how much irrigation water is required, while the biggest challenge is typically in obtaining and using accurate crop factors (k_c values) (Gautam et al., 2021).

Each of these scheduling approaches (historical or experiential knowledge, soil moisture thresholds, evaporative demand based, plant water status thresholds) pose a range of benefits and challenges, however, understanding the costs involved is also an important consideration when carrying out irrigation scheduling. Furthermore, the adoption of new technology or the implementation of an altered practice change can be hindered by an incomplete understanding of the economic implications of these decisions (i.e., introducing new technology) (Alcon et al., 2013). It therefore follows that adoption is more likely to be made, if the technology (or practice change) generates a positive net benefit. This is critically important when investigating ways to improve water use efficiency in irrigated agriculture. Financial analysis and discounted cash flow analysis (DCFA) have previously been used to assess the financial feasibility of different irrigation technologies and strategies in a range of horticultural crops, including almonds (García et al., 2004, Romero et al., 2006, Alcon et al., 2013), citrus (Pérez-Pérez et al., 2010, Maestre-Valero et al., 2016, Panigrahi et al., 2013), olives (Egea et al., 2017), and winegrapes (García García et al., 2012, Romero et al., 2016, Bellvert et al., 2021). In its simplest form, a financial analysis involves summing the total monetary benefits and costs of a project and, if the total benefits exceed the costs, the project is considered economically viable (Griffin, 1998). As an extension of this, a DCFA can be used to assess the future profitability associated with adopting new technology by considering the total lifespan of the investment in question. Additional indices that explore the relationship between various parameters such as profit, yield and water applied can also be calculated during a CBA (Romero et al., 2016). Therefore, the primary objective of this work was to apply financial analysis in order to evaluate the financial costs and benefits involved with adopting different forms of irrigation scheduling in premium Coonawarra Cabernet Sauvignon.

2. Materials and Methods

2.1 Field conditions, vineyard description and management

This research was carried out over three growing seasons (2018/2019, 2019/2020 and 2021/2022) at a commercial vineyard planted in 1988 in Coonawarra, South Australia (-37°28'52" S, 140°83'00" E). *Vitis vinifera* L. cv. Cabernet Sauvignon on Schwarzmann rootstock (*V. riparia* × *V. rupestris*) was grown on Terra Rossa, a red clay loam common to the region (Longbottom et al., 2011). Analysis showed the soil as posessing 25% clay, 56% sand and 19% silt. Vine rows were orientated east-west and had a row and vine spacing of 2.75 m and 2.2 m, respectively, generating a vine density of 1,653 vine ha^{-1}. Vines were spur pruned to two-node spurs with 5 to 6 spurs per linear metre of cordon, and were trained according to a sprawl type canopy. According to this canopy structure, shoots grow vertically early in the season and are allowed to drop after mid-season, therefore providing shade to the fruit. Canopy management followed the practices of the commercial vineyard and varied depending on the season, but generally included at least one pass of shoot trimming (average shoot length ~1 m) to minimise canopy vegetative growth. Nutrition and integrated pest management were applied as per regional convention.

2.2 Experimental design and irrigation treatments

The experimental layout was a randomised complete block design where each treatment was replicated twice in two blocks. Within each block, treatments consisted of three rows, with two rows separating each treatment block. Four vines from the middle row (of the three rows) were evaluated for a maximum of eight vines per treatment each season. Irrigation treatments were defined by the types of irrigation thresholds/decision making involved with using each metric. Four different irrigation scheduling treatments were applied 1) irrigation decisions that were grower driven (GROW), 2) decisions that were driven by assessments of plant water status thresholds (PWS), 3) decisions based on crop evapotranspiration (ET_c) and 4) scheduling based on measurements of soil volumetric water content using soil water status thresholds (SWS); see below for description of specific thresholds.

The GROW treatment was conducted according to experiential/historical grower knowledge and was assigned as the control treatment. Grower decision making typically included the use of historical irrigation records, weather forecasts, and visual canopy assessment of vine water status. The grower also had access to one soil moisture probe in an adjacent block with the same soil type. The frequency and amount of seasonal irrigation typically received by these blocks vary from season to season, however generally falls within 0.5-0.6 ML ha^{-1}. The ET treatment included a weekly calculation of crop evapotranspiration (ET_c). The single k_c approach was used to estimate ET_c, with k_c values derived from measurements of intercepted light beneath the canopy (Williams and Ayars, 2005), whilst reference evapotranspiration (ET_0) was calculated using the Penman-Monteith equation (Allen et al., 1998). The climatic variables required for the equation were obtained from a nearby weather station (Bureau of Meteorology weather station, Coonawarra, station ID 026091). The PWS treatment was based on measurements of g_s carried out with a portable infrared gas analyser (LI-6400XT; LI-COR, Inc., Lincoln, Nebraska USA) in the first two seasons (2018/2019 and 2019/2020), then fully transitioned to proximal sensing using infrared thermography towers (Transp-IR, Athena Irrigation, Adelaide, South Australia) in the last season (2020/2021). One infrared thermography tower was placed between the second and third vine in each PWS block. The vine water index (VWI), which is based on g_s, was calculated in the Cloud daily and was remotely accsssible. Lastly, vines in the SWS treatment were irrigated according to measurements of volumetric water content from capacitance-based soil moisture sensors (Teros 12, Meter Group, Pullman, USA). The sensors were situated 10 cm away from the trunk in the under vine area and buried at a depth of 30 cm. Data from these sensors were also remotely accessible and continuously logged every hour.

For each data-driven treatment (ET, PWS, SWS), the decision to irrigate was triggered when a reference parameter (% ET_c, g_s and % VWC) fell below predetermined thresholds. Historical soil moisture in the growing season over the previous five years was 32% and the SWS treatment imposed a 30% deficit on this historical value to follow an SDI strategy consistent with premium Cabernet Sauvignon wine grape production in the region. ET and PWS thresholds were established using data from preliminary studies in the vineyard block during the 2017/2018 season. Target thresholds for the ET treatment were based on RDI; fruit set to veraison 25% ET_c, and veraison to harvest 50% ET_c, targeted at controlling canopy and berry size. PWS thresholds were based on an empirical relationship between *an* and g_s and established in a preliminary study. The optimum g_s (to maximise WUE_i) corresponded to approx. 75% of maximum A_n, which was found to be between g_s values of 0.12 – 0.15 mol H_2O m^{-2} s^{-1} (VWI of 0.4 – 0.6). This threshold was maintained from fruit set to harvest.

2.3 Yield and water use efficiency measurements

Grape bunches were hand-harvested in line with commercial harvest dates in early April of all seasons (11th April 2019, 8th April 2020 and 14th April 2021) and weighed on a per vine basis to determine t ha^{-1}. To assist in accounting for the high variability in the trial blocks, irrigation amounts and WUE_c were adjusted according to vine length. It was assumed that vines 2.2m or less in length would have received the full amount of irrigation as determined by the thresholds each week. However, vines that exceeded 2.2m in length were assumed to have received a higher irrigation entitlement compared to the shorter vines. This was achieved by multiplying the vine length by total water output (L m^{-1}) as dictated by the number of drippers in a row.

As an additional measure to account for high vine-vine variability, an outlier test was applied in to assess whether variations in bunch number unfairly influenced gross margin (gross revenue before tax minus costs) (GM) via effects on yield. All 32 vines (including all treatments) were sorted according to bunch number each season (bunch numbers per vine and bunch m^{-1}), with vines repeatedly found outside the 2nd and 3rd quartiles highlighted for further inspection (i.e. found to be an outlier in 2018/2019, and continued to be an outlier in 2019/2020 and 2020/2021). All vines were then sorted according to yield, if the same vines that were identified in the whole bunch number and bunch m^{-1} outlier tests were identified in the yield outlier test, these vines were removed from the analysis. 1 vine was identified in each of the GROW, ET and PWS treatments that satisfied these criteria.

2.4 Financial analysis – discounted cash flow analysis

To carry out the financial analysis, the approach that was used closely follows that of Egea et al. (2017). Production and irrigation data were assessed within the experimental period using GM, as well as a range of financial performance indices: economic productivity (EP), economic water productivity (EWP) and breakeven point (BP).

$$EP = \frac{Gross\ margin\ (\$)}{Total\ yield\ (t)}$$

$$EWP = \frac{Gross\ margin\ (\$)}{Total\ irrigation\ water\ (ML)}$$

$$BP = \frac{Total\ operational\ costs\ (\$)}{Total\ yield\ (t)}$$

DCFA was also undertaken in order to investigate each strategy based on estimated future farm returns. A DCFA facilitates this by evaluating future cash flows in relation to the size of the initial investment (Finnerty, 2012), and involves estimating the expected future cash flows (CF_n) over a specific time period, discounting these cash flows using an appropriate discount rate (i), and calculating the value of these cash flows (minus investment costs, k), also known as the net present value (NPV). In addition to NPV, the internal rate of return (IRR) were also calculated. The IRR is the discount rate in which NPV equals 0, and reflects an estimated return on investment as a percentage rather than a dollar value.

$$NPV = -k + \sum_{t=1}^{n} \frac{CF_n}{(1+i)^n}$$

$$0 = NPV = \sum_{t=1}^{t} \frac{CF_n}{(1+IRR)^t} - k$$

The discount rate chosen to carry out the DCFA in this study was 5% and the time horizon for the DCFA was fixed at 20 years. Although vineyards can be productive beyond 20 years, scheduling technology may evolve beyond what was investigated here when considering a time period outside 20 years. In addition to this, a time horizon of 20 years been used previously in similar horticulturally based irrigation studies (Maestre-Valero et al., 2016, Egea et al., 2017). Investment costs for vineyard establishment were estimated to be \$60,000 ha^{-1}, and is reflective of a replanting approach using grafted vines in an already established vineyard (Logan, 2018) (which includes removing existing vines, replacing irrigation infrastructure and trellising; this approach was estimated to be more common in Australia), rather than establishing a new vineyard on previously unplanted land. Investment costs for vineyard establishment were taken to be the same for each strategy. For the purpose of carrying out the DCFA, a non-productive and 50% full production phase was included as part of a replanting approach. It was assumed vineyard establishment costs would be incurred at the beginning of year 1 (time 0), further negative cash flows would be incurred in years 1 (the end of) and 2 (representing the non-productive phase of a new vineyard), 50% of full production would be reached in year 3 and full production would be reached in year 4. Cash flows from each experimental season were averaged for each strategy (to represent full production), with this average value being extrapolated out for a 20 year investment. It should be noted the DCFA was undertaken assuming i) grape price would remain stable, ii) berry quality would remain unchanged, and iii) average gross margins would remain consistent across the 20-year simulated period. As part of the financial analysis, a sensitivity analysis was applied in order to assess the impact of different factors (i.e., grape and electricity prices), including discount rate (3% and 7%), on measures of farm return. In addition to the sensitivity analysis, scenario analysis was also undertaken to evaluate a situation in which growers would need to factor in a gross water price as part of production costs. A gross water price of of \$1000 ML^{-1} was chosen as this represented the highest monthly allocation price of water attained in the souther Murray Darling Basin (MBD) during the Millennium drought (Aither, 2020).

2.4.1 Costs

2.4.1.1 Irrigation scheduling technologies

Developing the initial financial model required establishing the costs and benefits associated with strategy. Costs of interest included those either directly related to the strategy itself (i.e., equipment costs), or costs indirectly related via the strategy's impacts on water usage and vine performance (i.e., electricity costs). Investment and ongoing operational and maintenance costs were separately established for each irrigation strategy according to a 15ha vineyard (Table 1). The GROW treatment reflected the equipment the commercial grower used at each site, which included a singular soil moisture probe and access to a local BOM weather station (Bureau of Meteorology weather station, Coonawarra, station ID 026091). In this GROW scenario, the soil moisture probe incurred a cost, however, access to the local weather station data was free. It was assumed an experienced Vineyard Manager would be making weekly irrigation decisions over an 18 week irrigation season (Middle of December to the middle of April), and that the Vineyard Manager would spend approximately half an hour each week making these decisions. The time cost associated with these decisions was calculated and reflected the average yearly wage of an experienced Vineyard Manager. For the ET treatment, as crop factors were obtained through measurements of intercepted light beneath the canopy (Williams and Ayars, 2005), construction of the panel required for those measurements was included as an initial cost (Table 1). To reflect the panel's potential usage in a vineyard setting, it was assumed a grade 5 vineyard worker (Fair Work Commission, 2000) would require one season to measure and establish crop factors that could be used in future seasons (provided the season measured was generally reflective of previous seasons), and was therefore considered as an initial cost. However, crop factors can also be obtained through use of remote sensing techniques (Gautam et al., 2021), but this was not investigated as part of the current study. Operational costs associated with the ET treatment was taken as the time cost of a grade 5 vineyard worker (Fair Work Commission, 2000) requiring one hour each week to calculate ET_c values using ET_o values obtained from the nearby BOM weather station (access to weather station did not incur a cost). However, ET_o can also be manually calculated using climatic variables sourced from an onsite weather station. Though this may constitute an additional labour cost, with the weather station itself also an additional investment cost that must be considered. For each of the sensor driven approaches (PWS and SWS), it was assumed a 15ha vineyard would have 6 sampling sites (6 sensors), and would require a grade 5 vineyard ½ hour each week to evaluate sensor data in line with established threshold ranges. Ongoing data subscriptions and maintenance costs were included as per company guidelines (Table 1). The lifespan of each technology was also established in conjunction with company guidelines, however, it was assumed crop factors would need to be recalculated every 10 years. There was no lifespan value attributed to the GROW approach.

2.4.1.2 Vineyard

Costs associated with each irrigation scheduling approach were then integrated into a general model which included both the costs accumulated during the vineyard growing season, and investments costs required for vineyard establishment. General vineyard operating costs such as chemical spray programs, pruning and harvesting etc. were taken to be the same for each strategy, as were the fixed overhead costs which included aspects such as management wages, land tax, insurance and debt servicing etc. Both the fixed and general vineyard operating costs were set at a value of \$9,000 ha^{-1}, a figure which is reflective of a corporately owned vineyard operating in a cool climate region. This value was established during conversations with local growers and vineyard contractors. As water is principally sourced using groundwater in the Coonawarra region, the cost of water was calculated as the electricity required to pump the water from bore sites in close proximity to the trial blocks, as per Egea et al. (2017). To calculate pumping costs, kWh ML^{-1} was determined, and then converted to \$ ML^{-1} using an appropriate electricity rate (incorporating both raw energy costs and supply charges):

$$kWh\,ML^{-1} = kW \div (Q \times 0.0036)$$

$$\$\,ML^{-1} = \$\,kWh^{-1} \times kWh\,ML^{-1}$$

2.4.2 Benefits

Benefits were taken to be the pre-tax income received if growers on sold the grapes to a winery (with wine grape production volume influenced by the irrigation strategy applied). Income was grade based, and the specific grade chosen for the fruit that resulted in this study was conceptualised based on discussions with growers, assessing pricing surveys, and statistical tests to determine whether fruit quality differed between treatments (data not shown).

2.5 Statistical analysis

Statistical analysis was carried out using Prism software (version 9.0.0, GraphPad Software, San Diego, CA). One-way ANOVA was used to compare all treatments and the Tukey multiple comparisons posthoc test ($\alpha = 0.05$) was applied to assess differences between specific treatments.

3. Results

When considering initial investment requirements for a 15ha vineyard, the sensor driven treatments were associated with the highest initial costs (SWS being the highest, \$13,577), whereas the ET treatment had the lowest (\$1,172) (Table 1). Alternatively, in other vineyards where the GROW treatment is more closely defined by a purely non-data driven approach (i.e. encompassing a heavy reliance of visual assessments, local weather reports and historical knowledge), this treatment would arguably have no investment requirements in comparison to what has been shown here, and would therefore have the lowest initial cost. Operational costs for the GROW and ET treatment were predominantly driven by the cost of labour, whereas operational costs for the PWS and SWS treatments were heavily influenced by the cost of data subscriptions and equipment maintenance.

Across all seasons, reductions in water were observed for each of the data driven strategies (ET, PWS and SWS) in comparison with the GROW treatment (with an average reduction of between 28% and 43%) (Table 2). Irrigation for both the ET and PWS treatments were found to be similar and significantly lower than either of the SWS and

GROW treatments (Table 2). In connection with water applied, total pumping costs (TPC) were also found to be significantly lower for both the ET and PWS treatments in comparison with GROW (with TPC reductions of 45% and 42%, respectively). Mean yields were similar across all treatments, however, SWS was associated with the lowest yield (5.09 t ha^{-1}) and the ET treatment, the highest (6.41 t ha^{-1}). WUE was also found to be highest for the PWS treatment (2.96 t ML^{-1}), and lowest for the GROW treatment (2.31 t ML^{-1}), however, these weren't found to be significant differences (PWS v GROW, $P < 0.1552$) (Table 2).

Following trends observed for yield, the ET and PWS treatment obtained the highest GM values (16,578 $ ha^{-1} and 16,515 $ t^{-1}, respectively), followed by GROW (15,201 $ t^{-1}) and SWS (11,188 $ t^{-1}) (Table 3). Economic water productivity (EWP) was significantly higher for the PWS treatment compared with GROW and SWS, but was similar to ET. However, these same differences were not observed for economic productivyt values (EP), which were found to be similar between treatments. With regards to breakeven point (BP), BP was lowest for the ET and PWS treatments (1,553 $ t^{-1} and 1,588 $ t^{-1}, respectively), and highest for the GROW and SWS strategies ($1,655 and $1,845, respectively). When considering long-term profitability as a result of the DCFA, trends closely followed those observed for GM within the experimental period. This meant the ET and PWS treatments showed the highest net present value (NPV) (86,676 $ ha^{-1} and 84,834 $ ha^{-1}, respectively), and SWS, the lowest (30,201 $ ha^{-1}) (Table 4), with NPV BP following a similar ranking (Figure 1 A). The internal rate of return (IRR), which is an indicator of return on investment was also consistent with NPV in each treatment.

When considering changes in NPV as a result of fluctuating grape price, the SWS treatment was found to be the most sensitive (slope of 6.8) (Figure 1 B), followed by the GROW treatment (slope of 3.3). Similar trends were also observed when comparing the sensitivity of NPV to changes in discount rate (slopes ranged between 2.5 (SWS) and 1.9 (ET)). When considering the effect of a 50% increase to electricity price, impact on NPV and BP values were negligible (>1% change). However, when considering a scenario in which growers paid for water similarily to what occurs in warm climate regions (i.e. the Murray Darling Basin), an additional production cost of $1000 ML^{-1} (representing a gross water price) was associated with NPV and BP reductions of 9% and 7%, respectively for the GROW treatment.

4. Discussion

During the course of investigation, reductions in irrigation were observed for all data driven interventions across each season, with reductions in water requirements also associated with reduced costs (Tables 2 and 3). In particular, TPC which reflects the cost of electricial energy for irrigation supply, mirrored differences in water application observed between each treatment. However, the similarities between the ET and PWS treatments (when considering TPC) were no longer evident when exploring total operational costs (TOC), suggesting the higher scheduling costs associated with the PWS treatment reduced its costing similarity to ET (Table 3). The GROW treatment was observed to have a sigifncaitly higher TOC compared with each of the data driven strategies despite noticeably minor differences between absolute values (less than 1%), indicating trends in TOC were highly conserved among seasons. Differences between absolute values of treatment TOC may have been slightly larger had vine size and yield been accounted for, as both these parameters would have been influenced by differences in water application, and consequently harvest and pruning operations. However, when carrying out the intial financial assessment, a machine-based approach to harvesting and pruning was chosen as opposed to carrying out these tasks by hand. When considering these costs, the cost of a machine based approach is rarely affected by the size of a vine, but rather, is largely based on a cost per linear metre of vine cordon (Fisher, 2005), or the layout of the vineyard itself. Additionally, in a previous study considering wine grapes, García García et al. (2012) determined that differences in pruning expenses had a negligible impact on the total costs associated with each of the deficit irrigation strategies investigated in that study, despite large differences in water application (up to 54% reduction in irrigation compared with a 60% ET_c SDI control). Consequently, the difference in harvesting and pruning costs between treatments was considered to be negligible and was not considered as part of the model. Therefore, the main driver behind differences in treatment costs throughout this study was associated wth irrigation supply itself.

To establish the financial benefits associated with each treatment, the value of the crop produced using each strategy was determined by investigating yield and quality differences. However, as berry quality was found to be similar between treatments (data not shown) and trends in GM were closely related with yield, the ET and PWS treatments were associated with the highest farm returns (in comparison with GROW and SWS), though these differences were not found to be significant (Table 2 and 3). The similarties between average GM for each strategy was likely the result of statistically similar yields, indicating differences in TOC did not have a signficant influence on resulting cash flows. This is particualty evident for the SWS treatment, where lower yields became a more important driving force behind overall profitability, rather than the cost savings associated with reduced water application. Incidentally, even though differences in quality were not observed in this study, the effect of berry quality on the financial desirability of different irrigation stratgies has previously been demonstrated by García García et al. (2012). The authors noted that RDI and PRD strategies previously thought unviable (due to harsh deficits reducing yield), became financially viable when considering the increase in berry quality associated with these strategies, highlighting an additional benefit that needed to be included in the financial analysis. However, interestingly in that study, the control treatment which provided 60% ET_c was still considered to be the most profitable due to higher yield. This phenonomen of yields driving profitability rather than reduced water costs has similarily been observed in other studies investigating deficit irrigation . Though contrastingly, in this study, both the ET and PWS treatments which provided lower water application compared with GROW produced higher yields. This may potentially be due to improved canopy characteristics, which may constitute an additional benefit using when these types of strategies.

Other benefits when using data driven interventions (or deficit irrigation strategies generally) may also be associated with improved WUE and EWP. EWP which reflects the economic return on water applied, was highest for the ET treatment (Table 3), and this is likely due to the negative correlation that was observed between EWP and irrigation, indicating a greater economic return on water applied was achieved with reduced irrigation. This relationship was similarly observed by Alcon et al. (2013) when comparing deficit irrigation practices in almonds at sales prices of 3 € kg^{-1} (or 3000 € t^{-1}). Trends in EWP showed a positive correlation with WUE values, and improvements to WUE were also related to reductions in TOC (Tables 2 & 3). This association between WUE and TOC was also observed by Bellvert et al. (2021), indicating a target of high WUE was also associated high EWP and lower TOC in this study. The positive relationship between WUE and EWP is in contrast with Romero et al. (2016) who when comparing different deficit irrigation strategies in Monastrell grapevine found a negative relationship between EWP (denoted as financial efficiency, € m^{-3}) and WUE. In that study, a regression coefficient relating the two parameters was not provided, so the relationship's statistical significance cannot be fully assessed. However, despite this, the authors noted that severe water deficits resulted in elevated WUE values, but low and negative EWP values due to the steep reductions in yield, and consequently GM. The authors also noted a positive correlation between EWP and irrigation, a relationship that was also observed by García García et al. (2012) (and opposite to what was observed here). However, it is important to note that yields in both these studies were between 40% - 170% higher than what was obtained under the current trial, and that grape sales prices were also 12-16 fold lower, likely leading to comparatively lower GM values than what was achieved in this study. These results would suggest that for premium winegrapes, reduced irrigation is associated with high economic returns on water. Whereas for winegrapes coupled with a lower grape price, deficit irrigation is not associated with these same high returns on water, as GM is greatly reduced by any reductions in yield. However, for premium winegrape production, this effect is buffered by high grape prices as long as yields aren't drastically reduced.

Following trends observed for GM values, NPV was also found to be similar between all treatments, however, the ET treatment was observed to have the highest long-term financial return. This is in contrast with Egea et al. (2017) who when comparing irrigation scheduling strategies in a super high density olive orchard, found a plant-based method (leaf turgor pressure measurements) to have a more positive long-term economic view than the approach that used ET-based scheduling. However, this conclusion was made on the basis of the ET-based treatment receiving a significantly lower NPV compared with the full irrigation treatment in that study, as both the plant-based and ET-based treatment were found to be similar to one another, likewise to what was observed here. The observed range IRR values (Table 4) are within the range previously reported to be common for Australian vineyards (Davidson, 2001). The sensitivity of NPV to fluctuating grape price and discount rate was likely driven by differences in yield, as the SWS treatment was the most sensitive. The individual investment costs associated with each treatment, and particularly the sensors themselves did not have a large impact on final NPV or IRR values, with changes in each these parameters being largely driven by GM, which was closely associated with yield. Reasons for the high degree of similarity between treatments may stem from the fact that the GROW treatment in this study represented premium Cabernet Sauvignon production in a cool climate region, therefore, traditional irrigation requirements in this vineyard were already quite low. As the thresholds used for each of the interventions were devised with the aim of providing a further deficit on the GROW treatment, absolute differences in water application were only on the order of 0.1 ML ha^{-1} to 0.25 ML ha^{-1}. So while reductions in water were achieved, this may have led to the high similarities observed between treatments, notwithstanding the high soil variability also present in this region (Longbottom et al., 2011). Given irrigation requirements were low, the effect of increasing electricity only had a marginal effect on farm returns. Inclusion of an additional production cost of \$1000 ML^{-1}, while decreasing both NPV and BP up to 9% and 7% respectively, also did not result in a signficiant reduction according to statistical analysis. This is in stark contrast to vineyards in warm climate regions, where even a 50% increase in water price (using an averaged annual allocation price of \$417 averaged over each season of the trial in the southern MBD, (Aither, 2021)) could result in a BP increase of approximately 14% under current irrigation rates (Dixon, 2021).

In light of the similarities observed between in this study, an additional matter of interest when implementing a specific irrigation strategy is its ability to be adapted for use in precision irrigation (PI). It is widely recognised that spatial variability (i.e. soil type and topography) can lead to differences in vine vigour, therefore, supporting the concept of zoned irrigation management (Bramley, 2005). In the current study, soil depth to limestone is highly variable throughout the region (Longbottom et al., 2011), and so implementing a PI system is an attractive alternative to the approach used in this study (which relied on weekly uniform irrigation application). Implementing such a system would not represent a huge cost to the grower, as additional main costs to be considered include: the cost of obtaining an NDVI map (to assess variations in vineyard vigour and delineate irrigation zones), programmable solenoid valves to enable variable control of irrigation and an irrigation controller to program solenoids. Each of the ET, PWS and SWS treatments in this study could be adapted for use in such a system, particularly the PWS and SWS methods. However, an ET approach could also be used alongside sensor driven strategies to determine how much irrigation to apply. Calculating the opportunity costs associated with implementing a non-precision irrigation (NPI) over a PI one in the current study is difficult, however, previous research has suggested that there is in fact an opportunity cost associated with this decision. In Temperanillo, Cabernet Sauvignon and Syrah, Bellvert et al. (2021) compared the cost of using PI with NPI using an integrated vine water consumption model and remote sensing approach. The authors found choosing a NPI over a PI approach meant forgoing cost savings of between 32 \$ ha^{-1} and 77 \$ ha^{-1} (which was associated with irrigation water reductions of between 1 ML ha^{-1} and 1.4 ML ha^{-1}), suggesting further water savings are a possibility when using a PI approach. However, in relation to the current study, the vines were already minimally irrigated, so any further water savings would likely be negligible. Though conversely, if this trial had been undertaken in a region that had higher irrigation requirements, water savings may likely have been higher.

5. Conclusion

Following the conditions explored in this study, data driven interventions were found to have equivalent financial returns compared with the GROW treatment, despite differences observed in water application. However, as reduced irrigation requirements are critically important in the context of water security, each of the data driven strategies were preferable to the GROW treatment which was associated with the highest water needs. This study also highlighted that inclusion of a gross water price into production costs would have a negligible impact on GM for producers in this region, however, this would not be the case in warmer regions with increased irrigation requirements. As a result of the information gleaned from this study, the author’s recommendation would be to carry out irrigation scheduling using data driven strategies, as this typically led to water reductions, improvements in WUE and similar financial returns compared with GROW driven strategies.

References

Aither 2020. *Australian Water Markets Report: 2019-20 Review and 2020-21 Outlook*. Melbourne, Aither Pty Ltd.

Aither 2021. *Australian water markets report: 2020-21 review and 2021-22 outlook*. Aither Pty Ltd; Melbourne

Alcon, F., Egea, G. & Nortes, P. 2013. Financial feasibility of implementing regulated and sustained deficit irrigation in almond orchards. *Irrig. Sci.,* 31**,** 931-941.

Allen, R. G., Pereira, L. S., Raes, D. & Smith, M. 1998. *Crop Evapotranspiration. Guidelines for Computing Crop Water Requirements. FAO irrigation and drainage paper no. 56.,* Rome; Rome, Italy

Australian Bureau of Statistics. 2020. *Water use of on Australian farms-2019-20* [Online].' Available: https://www.abs.gov.au/statistics/industry/agriculture/water-use-australian-farms/2019-20.

Belfiore, N., Vinti, R., Lovat, L., Chitarra, W., Tomasi, D., de Bei, R., Meggio, F. & Gaiotti, F. 2019. Infrared Thermography to Estimate Vine Water Status: Optimizing Canopy Measurements and Thermal Indices for the Varieties Merlot and Moscato in Northern Italy. *Agron.,* 9**,** 821.

Bellvert, J., Mata, M., Vallverdú, X., Paris, C. & Marsal, J. 2021. Optimizing precision irrigation of a vineyard to improve water use efficiency and profitability by using a decision-oriented vine water consumption model. *Precis. Agric.,* 22**,** 319-341.

Bramley, R. G. V. 2005. Understanding variability in winegrape production systems 2. Within vineyard variation in quality over several vintages. *Aust. J. Grape Wine Res.,* 11**,** 33-42.

Chaves, M. M., Zarrouk, O., Francisco, R., Costa, J. M., Santos, T., Regalado, A. P., Rodrigues, M. L. & Lopes, C. M. 2010. Grapevine under deficit irrigation: hints from physiological and molecular data. *Ann. Bot.,* 105**,** 661-676.

Davidson, D. 2001. *The business of vineyards,* Adelaide, South Australia, Davidson Viticultural Consulting Services. 1-38.

Dixon, R. 2021. *AWRI Irrigation Efficiency and Practice Change Survey March 2021* [Online]. South Australia: The Australian Wine and Research Institute.' Available: https://www.awri.com.au/wp-content/uploads/2021/03/awri-irrigation-efficiency-practice-change-survey-2021.pdf.

Dry, P. R. & Loveys, B. R. 1999. Grapevine shoot growth and stomatal conductance are reduced when part of the root system is dried. *Vitis*, 151-156.

Egea, G., Fernández, J. E. & Alcon, F. 2017. Financial assessment of adopting irrigation technology for plant-based regulated deficit irrigation scheduling in super high-density olive orchards. *Agric. Water Manage.,* 187**,** 47-56.

Fair Work Commission. 2000. *Wine Industry Award [MA000090]* [Online].' Available: https://awardviewer.fwo.gov.au/award/show/MA000090#P899_82037.

Fereres, E. & Soriano, M. A. 2007. Deficit irrigation for reducing agricultural water use. *J. Exp. Bot.,* 58**,** 147-59.

Fernández, J. 2017. Plant-based methods for irrigation scheduling of woody crops. *Horticulturae,* 3**,** 35.

Finnerty, J. D. 2012. Discounted Cash Flow Analysis. *Project Financing.* Hoboken, NJ, USA: John Wiley & Sons, Inc. 169-191.

Fisher, M. 2005. Comparing the costs of machine and hand harvesting. *Australian Viticulture*, May/June: 72-73

García García, J., Martínez-Cutillas, A. & Romero, P. 2012. Financial analysis of wine grape production using regulated deficit irrigation and partial-root zone drying strategies. *Irrig. Sci.,* 30**,** 179-188.

García, J., Romero, P., Botía, P. & García, F. 2004. Cost-benefit analysis of almond orchard under regulated deficit irrigation (RDI) in SE Spain. *Span. J. Agric. Res.*, 157-165.

Gautam, D., Ostendorf, B. & Pagay, V. 2021. Estimation of grapevine crop coefficient using a multispectral camera on an unmanned aerial vehicle. *Remote Sens.,* 13**,** 2639.

Jones, H. G. 2004. Irrigation scheduling: advantages and pitfalls of plant-based methods. *J. Exp. Bot.,* 55**,** 2427-36.

Jones, H. G., Stoll, M., Santos, T., Sousa, C. d., Chaves, M. M. & Grant, O. M. 2002. Use of infrared thermography for monitoring stomatal closure in the field: application to grapevine. *J. Exp. Bot.,* 53**,** 2249-2260.

Koech, R. & Langat, P. 2018. Improving irrigation water use efficiency: A review of advances, challenges and opportunities in the australian context. *Water,* 10**,** 1771.

Lebon, E., Dumas, V., Pieri, P. & Schultz, H. R. 2003. Modelling the seasonal dynamics of the soil water balance of vineyards. *Funct. Plant Biol.,* 30**,** 699-710.

Logan, S. 2018. Rootstock resistance – why isn't Australia doing better in its uptake of rootstocks for phylloxera control? *Wine & Viticulture Journal March/April,* V33N2**,** 40-42.

Longbottom, M., Maschmedt, D. J. & Pichler, M. 2011. *The climate, geology, soils, hydrology and environment of South Australia's Limestone Coast,* Coonawarra, Limestone Coast Grape and Wine Industry Council. 288 pp.

Maestre-Valero, J. F., Martin-Gorriz, B., Alarcón, J. J., Nicolas, E. & Martinez-Alvarez, V. 2016. Economic feasibility of implementing regulated deficit irrigation with reclaimed water in a grapefruit orchard. *Agric. Water Manage.,* 178**,** 119-125.

McCarthy, M. G., Loveys, B. R., Dry, P. R. & Stoll, M. 2002. Regulated deficit irrigation and partial rootzone drying as irrigation management techniques for grapevines. *Water Reports (FAO)*, 79–87.

Medrano, H., Tomás, M., Martorell, S., Escalona, J.-M., Pou, A., Fuentes, S., Flexas, J. & Bota, J. 2015. Improving water use efficiency of vineyards in semi-arid regions. A review. *Agron. Sustain. Dev.,* 35**,** 499-517.

Naulleau, A., Gary, C., Prévot, L. & Hossard, L. 2021. Evaluating strategies for adaptation to climate change in grapevine production - A systematic review. *Front. Plant Sci.,* 11:607859.

Nordestgaard, S. 2019. *AWRI Vineyard & Winery Practices Survey* [Online]. The Australian Wine Research Institute.' Available: https://www.awri.com.au/wp-content/uploads/2019/05/AWRI_Practices_Survey_Final_Report.pdf.

Panigrahi, P., Sharma, R. K., Parihar, S. S., Hasan, M. & Rana, D. S. 2013. Economic analysis of drip-irrigated kinnow andarin orchard under deficit irrigation and partial root zone drying. *Irrig. Drain,* 62**,** 67-73.

Pérez-Pérez, J. G., García, J., Robles, J. M. & Botía, P. 2010. Economic analysis of navel orange cv. 'Lane late' grown on two different drought-tolerant rootstocks under deficit irrigation in South-eastern Spain. *Agric. Water Manage.,* 97**,** 157-164.

Petrie, P. R., Wang, Y., Scareltt, L., Stanley, L., Whitty, M. A. & Skewe, M. A. 2019. The accuracy and utility of a low cost thernal camera and smartphone-based system to assess grapevine water status. *Biosyst. Eng.,* 179**,** 126-139.

Romero, P., Fernández-Fernández, J. I. & Martinez-Cutillas, A. 2010. Physiological thresholds for efficient regulated deficit-irrigation management in winegrapes grown under semiarid conditions. *Am. J. Enol. Vitic.,* 61**,** 300-312.

Romero, P., García García, J., Fernández-Fernández, J. I., Munoz, R. G., Amor Saavedra, F. & Martinez-Cutillas, A. 2016. Improving berry and wine quality attributes and vineyard economic efficiency by long-term deficit irrigation practices under semiarid conditions. *Sci. Hortic.,* 203**,** 69-85.

Romero, P., García, J. & Botia, P. 2006. Cost-benefit analysis of a regulated deficit-irrigated almond orhcard under subsurface drip irrigation conditions in Southeastern Spain. *Irrig. Sci.,* 24**,** 175-184.

Shackel, K. 2011. Plant-based approach to deficit irrigation in trees and vines. *HortScience,* 46**,** 173-177.

Torres, N., Yu, R., Martinez-Luscher, J., Girardello, R. C., Kostaki, E., Oberholster, A. & Kaan Kurtural, S. 2022. Shifts in the phenolic composition and aromatic profiles of Cabernet Sauvignon (Vitis vinifera L.) wines are driven by different irrigation amounts in a hot climate. *Food Chem.,* 371**,** 131163-131163.

Tuccio, L., Lo Piccolo, E., Battelli, R., Matteoli, S., Massai, R., Scalabrelli, G. & Remorini, D. 2019. Physiological indicators to assess water status in potted grapevine (Vitis vinifera L.). *Sci. Hort.,* 255**,** 8-13.

Williams, L. E. & Ayars, J. E. 2005. Grapevine water use and the crop coefficient are linear functions of the shaded area measured beneath the canopy. *Agric. For. Meteorol.,* 132**,** 201-211.

Table 1. Approximate investment and operational costs for each irrigation scheduling strategy investigated in this study. Operational costs for the GROW and ET treatments were calculated on a per season basis, whereas PWS and SWS operational costs were considered over a year as data subscription plans occur in 12 month cycles. Costs were considered for a 15 ha vineyard considering an 18 week irrigation period.

	Investment concept	Initial cost ($)	Lifespan (years)	Operational concept	Yearly operational cost ($)	Benefits
GROW	Experienced Vineyard Manager and one soil moisture sensor	3,453	10	Cost of wages involved in making decisions, ongoing maintenance of soil moisture probe	479	Minimal equipment requirements and interpretation of complex data
ET	Paso panel and labour required to establish crop factor values over one season	1,172	10	Cost of wages required to calculate ET_c	440	Ability to numerically calculate irrigation needs
PWS	Thermography towers (thermal camera, gateway, waterproof outdoor boxes, pole, self-installation)	6,000	5	Data subscription each month, ongoing annual maintenance, cost of wages to analyse data	580	Integrates data from the whole canopy with measurements directly related to vine transpiration
SWS	Multiple depth capacitance probe (probes, installation cost and irrimax software)	13,577	10	Data subscription each month, ongoing maintenance of soil moisture probe, cost of wages to analyse data	357	Well-established methodology with a high degree of support for troubleshooting equipment and data problems

Table 2. Yield, water applied and crop water use efficiency for each irrigation treatment. Mean ± SEM (n = 10 → 21)

	GROW	ET	PWS	SWS
Water applied (ML ha^{-1})	0.61 ± 0.02 a	0.35 ± 0.03 c	0.35 ± 0.02 c	0.44 ± 0.03 b
Yield (t ha^{-1})	6.08 ± 0.39	6.41 ± 0.62	6.14 ± 0.46	5.09 ± 0.23

WUE (t ML^{-1})	2.31 ± 0.20	2.76 ± 0.26	2.96 ± 0.28	2.08 ± 0.13

One-way ANOVA and Tukey's multiple comparison test (α = 0.05) was used to compare treatments found to be normally distributed. Data that was not found to pass the D'Agostino-Pearson omnibus (K2) normality test underwent statistical testing using the Kruskal-Wallis and Dunn's multiple comparison test (α = 0.05). Significant differences between treatments are denoted by lowercase letters.

Table 3. Mean cost considerations, gross margins and economic indices calculated for a 15 ha vineyard undergoing irrigation scheduling according to each of the investigated strategies. Production Vineyard operating and fixed overhead costs included: chemical application, winter pruning (machine), harvesting (machine), vineyard row and floor management, permanent management, general repairs and maintenance, debt servicing and general power.

Variable	GROW	ET	PWS	SWS
Vineyard operating and fixed overhead costs ($ ha^{-1})	9,000	9,000	9,000	9,000
Scheduling operating costs ($ ha^{-1})	31.9	14.7	38.7	23.8
Pumping cost ($ ML^{-1})	141	141	141	141
Total pumping costs ($ ha^{-1})	85.2 a	46.6 c	49.1 c	61.9 b
Total operational costs ($ ha^{-1})	9,117 a	9,063 c	9,088 b	9,086 b
Gross margin ($ ha^{-1})	15,201	16,578	16,515	11,188
Economic productivity ($ t^{-1})	2,335	2,447	2,412	2,155
Economic water productivity ($ ML^{-1})	24,983 b	55,309 a	51,345 a	26,219 ab
Breakeven point ($ t^{-1})	1,665	1,553	1,588	1,845

Table 4. The net present value (NPV) and internal rate of return (IRR) calculated for each strategy considering a time horizon of 20 years. Scenario analysis was undertaken to evaluate figures according to a situation in which the price of water was considered to be pumping costs, and a situation where growers would have to pay for per megalitre (ML) water they used. Means were calculated on a per vine basis for each season and averaged according to irrigation treatment

	Pumping costs			
Indicator	**GROW**	**ET**	**PWS**	**SWS**
NPV ($ ha^{-1})	72,343	86,676	84,834	30,201
IRR (%)	11.1	12.7	12.3	8.08

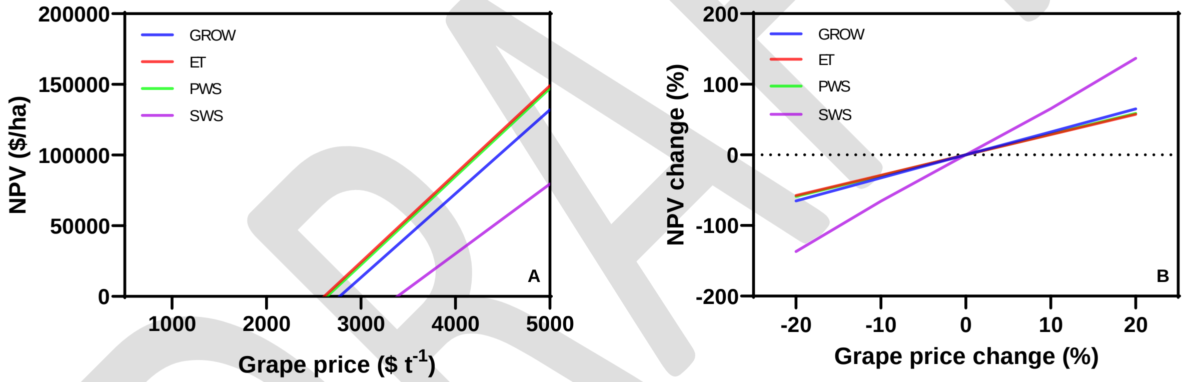

Figure 1. Panel A represents the relationship between NPV and grape price, with the break-even grape price (when NPV equals 0) also represented along the x-axis. Panel B represents NPV % change as a function of % change in grape price.